Characterizing Transiting Extrasolar Planets

Simona Ciceri
Max-Planck-Institut für Astronomie

Heidelberg 2015

Dissertation in Astronomy
submitted to the
Combined Faculties of the Natural Sciences and Mathematics
of the Ruperto-Carola-University of Heidelberg, Germany,
for the degree of
Doctor of Natural Sciences

Put forward by
M.Sc. *Simona Ciceri*
born in Treviglio (BG), Italy

Oral examination: 07.12.15

Characterizing Transiting Extrasolar Planets

Simona Ciceri
Max-Planck-Institut für Astronomie

Referees: **Prof. Dr. Thomas Henning**
Prof. Dr. Joachim Wambsganß

A l'alta fantasia qui mancó possa;
ma già volgeva il mio disio e 'l velle,
sí come rota ch'igualmente é mossa,
l'amor che move il sole e l'altre stelle.

Paradiso XXXIII, Divina Commedia, Dante

Abstrakt

Die Entdeckung der ersten Planeten außerhalb unseres Sonnensystems vor zwei Jahrzehnten setzte immer größere Bemühungen in Gang, neue Planeten aufzuspüren. Dank des Fortschritts in der Spektroskopie- und Photometrietechnologie, erzielt in zehnjähriger Erfahrung, wurden mehr und mehr Planeten mit einer erstaunlichen Vielfalt hinsichtlich ihrer physikalischen Eigenschaften und in den Eigenschaften ihrer Umlaufbahn gefunden. Gleichzeitig wurden große Anstrengungen zur Charakterisierung bekannter Planeten unternommen, um deren Zusammensetzung zu verstehen. Dadurch wird es möglich, Einsicht in die Entstehungsprozesse eines Planeten zu bekommen. Die Forschungsarbeit, die in dieser Promotionsschrift vorgestellt wird, konzentriert sich zum einen auf die Identifizierung und den Nachweis neuer Exoplaneten, zum anderen auf die Charakterisierung bekannter extrasolarer Planetensysteme, die mithilfe der Transitmethode entdeckt wurden.

Zum ersten Thema werden zwei Forschungsarbeiten vorgestellt: Die Entdeckung zweier neuer Planetensysteme im Rahmen der HATSouth Kollaboration (HATS-15 und HATS-16), und der Nachweis der Planeteneigenschaften des Kepler Planetenkandidaten Kepler-4320 b. HATS-15 b und HATS-16 b sind zwei massereiche Planeten (mit einer Masse von $\sim 2.2\,M_{Jup}$ bzw. $\sim 3.3\,M_{Jup}$), die zwei alte Sterne der Spektralklasse G (Alter ~10 Gyr) umkreisen. Die kurze Umlaufdauer von HATS-16 weist auf Gezeitenwechselwirkung mit dem Planeten hin, die zu einer Beschleunigung der Rotation des Sterns geführt haben könnte. Kepler-432 ist ein Unterriese, der sich auf dem aufsteigenden Roten Riesenast befindet. Er wird von einem massereichen Planeten ($\sim 5\,M_{Jup}$) auf einer moderat exzentrischen Umlaufbahn umkreist. Unter den Planeten von Sternen in entwickelten Stadien ist Kepler-432 b außerordentlich einzigartig, da er einer der wenigen ist, der sich auf einer engen Umlaufbahn ($a < 0.5$ au) befindet und so Theorien zur Planetenentstehung und ihrer Dynamik in Frage stellt.

Der Leitgedanke des zweiten Themas besteht darin, Folgebeobachtungen extrasolarer Transitplaneten zur genauen Charakterisierung ihrer Systeme durchzuführen. Mit verschiedenen Beobachtungsstrategien können weitere Informationen gewonnen werden, sei es über die Zusammensetzung der Planetenatmosphäre oder über die Ausrichtung von Sternspin und Planetenorbit: Durch die Aufnahme desselben Transits mit zwei verschiedenen Instrumenten, oder durch gleichzeitige Beobachtung in verschiedenen Spektralbändern mit Instrumenten wie BUSCA (CAHA) oder mit GROND (LaSilla). Die Charakterisierung von sechs Planetensystemen und die erfolgreiche Anwendung beider Beobachtungsstrategien werden in dieser Arbeit präsentiert.

Abstract

The detection of the first planets outside our solar system two decades ago has spurred growing efforts to detect new planets. Thanks to improvements in spectroscopic and photometric technology fed by ten years experience, more and more planets have been found showing an astounding diversity of physical and orbital characteristics. At the same time, great efforts are spent on the characterization of the known planets in order to understand their composition, especially as this can give insights into planet formation processes.

The work presented in this thesis is pointed on one side towards the identification and confirmation of new exoplanets, on the other side towards the characterization of known transiting exoplanetary systems.

Regarding the first science case, two different works are reported: the discovery of two new planetary systems within the HATSouth (HATS-15 and HATS-16) collaboration and the confirmation of the planetary nature of the *Kepler* candidate Kepler-432 b.

HATS-15 b and HATS-16 b are two massive planets (with masses of $\sim 2.2\,M_{\rm Jup}$ and $\sim 3.3\,M_{\rm Jup}$ respectively) orbiting around two old G-type stars (age ~ 10 Gyr). The short rotation period of HATS-16 points towards a tidal interaction with the planet that resulted in a spun-up.

Kepler-432 is a sub-giant star ascending the red-giant branch. It hosts a massive planet ($\sim 5\,M_{\rm Jup}$) orbiting on a moderately eccentric orbit. Among other planets around evolved stars, Kepler-432 b is extremely rare being one of the few on a tight orbit ($a < 0.5$ au), challenging evolution and dynamical theories.

The main idea of the latter project is to perform follow-up observations of known transiting extrasolar planets in order to accurately characterize their systems. Further information, such as planetary atmosphere composition or stellar spin-orbit alignment, can be achieved by using different observing strategies: monitoring the same transit with two different facilities or perform simultaneous observations in different bands with instruments as BUSCA (CAHA) or GROND (La Silla). The characterization of six planetary systems and the successful exploit of the two observing strategies are presented. Two planetary systems were observed simultaneously from two sites: HAT-P-16 and WASP-21. For HAT-P-23, WASP-45, WASP-46 and WASP-48 we obtained multi-band observations. For all the systems studied, a preciser measurements for the physical parameters was obtained. Moreover, all the planets are smaller than previously known. The planetary densities are therefore higher and in some cases the variation is significant (e.g. WASP-45 b), leading to a planet's size compatible with a model predicting a core $50\,M_{\oplus}$.

Contents

Chapter 1

Introduction

'*Why do stars shine?*','*What are the Sun and planets made of and where do they come from?*', '*Are we alone in the universe?*' Ancient questions like these are some of the underlying questions that have motivated and spurred man throughout the centuries to gaze at the starry night sky and try to grasp its secrets.

Over time, scientists gained a better understanding of the mechanisms and laws that control the universe and their questions became more sophisticated and focused on certain aspects. For instance, the initial query on the presence of other life has evolved into more detailed questions. 'What are the conditions required to sustain an environment suitable for lifeforms?' 'What are the signatures that a living being would leave on the atmosphere of its planet?' And now that we have found other planets: 'Is our Solar system peculiar or are the other planetary systems similar to ours?' and 'How do they become how they are now from dust and gas?'

In the year of the 20^{th} anniversary of the discovery of the first extrasolar planet orbiting around a main sequence star by Mayor & Queloz (1995), almost two thousand exoplanets[1] have been found and thousands are candidates awaiting for confirmation. By this time some of the initial questions have found an answer but several others have risen thanks to the unexpected variety of properties that the exoplanetary systems found to date have shown.

Great strides have been made and nowadays we are able to detect planets small as Mercury (e.g. Kepler-37 b, Barclay et al. 2013) and detect the presence of molecules in the planet's atmosphere (e.g. sodium in HD 189733 b, Wyttenbach et al. 2015). Nevertheless, an Earth twin or a solar system analog hasn't been found yet, driving astronomers to improve their techniques and instruments.

As said, one of he main drivers for building new instrumentation, and start new survey is the desire to look for planets that can possibly host life. One of the condition necessary for the support and evolution of life as we know is the presence of liquid water on the planet. In this context the definition of habitable zone (HZ) plays an important role. In general one refers to HZ as to the annular region around a star where the irradiation flux that a planet receives is so that its temperature allows water to be in the liquid phase. This general definition can be further refined by taking into account the way the planetary atmosphere reacts to the stellar irradiation reflecting or absorbing it in different ways. A proper and preciser definition of HZ will therefore take into account also the albedo and greenhouse effect (e.g. Kasting et al. 1993; Kaltenegger & Sasselov 2011; Kopparapu et al. 2013). Finding a planet in the HZ of a star doesn't guarantee its habitability. For biological organisms to evolve, a solid

[1] number obtained from *http://exoplanet.eu*, by August 2015

surface on the planet is essential. Planets such as Kepler-22 b (Borucki et al. 2012) or PH2 b (Wang et al. 2013) are therefore not suitable to host life: even though they lay in the HZ of their respective host stars, they are gaseous Jupiter-like planets possibly with no solid surface. Nonetheless, finding giant gaseous planets in the HZ can be interesting as they might arbor rocky exomoons circling around them, that can therefore support life (e.g. Tusnski & Valio 2014). Measuring only the mass or the radius of a planet in the HZ is not sufficient to determine its habitability. Rogers (2015) found indeed that measuring a small planet size, of the order of 1.5-1.6 $R_\oplus$, doesn't necessary lead to find a rocky planet. For instance Kepler-138 b having a radius of $\sim$ 1.6 $R_\oplus$ and a mass of $\sim$ 3.8 $M_\oplus$ has an Earth like density, while its companion Kepler-138 c, despite having the same radius, has a lower mass of $\sim$ 1.0 $M_\oplus$ leading to a much lower density compatible with gaseous planet models (Kipping et al. 2014). It goes without saying that knowing the bulk densities of a planet is essential in discerning gaseous planets form the rocky ones. Hence the extreme importance of follow-up observations that can provide these necessary information.

Finding planets that can possibly host life usually requires to look for small sized planets orbiting far enough from their star to be in the HZ. For a typical sun-like star, regardless of the definition used, the HZ is about at an astronomical unit. This means that the average period for such a planet would be of the order of years. In addition, the radii ratio between host star and a super-Earth-like planet is very small causing a possible transit to be very shallow and challenging to detect.
To overcome these problems in recent years the exoplanet community has started to look at M-dwarfs stars. Being intrinsically fainter than solar-like stars, the HZ of M-dwarfs lay at smaller orbital radii going from 0.2 to 0.02 au for M3 or M8 stars (Kasting & Catling 2003), resulting in planets with shorter periods. M-dwarfs have smaller sizes than F-, G-, K-type stars and given a certain planetary size and orbit, the transit depth is deeper, making it easier to detected such planets. Several are the projects targeting M-dwarfs using available instruments such as UVES (Kürster & Endl 2004) on the ground, or the K2 space mission (Crossfield et al. 2015a; Demory et al. 2013). New instrumentation has also been developed e.g. CARMENES (Quirrenbach et al. 2014), HZPF (Mahadevan et al. 2010), iLOCATER (Crepp et al. 2014) or SPECULOOS (Gillon et al. 2013).

If on one side astronomers are looking for smaller and smaller planets that may harbor life, on the other side one of the other big open questions in the exoplanet field is how planets form and what are they made of. Up to now, the only planets for which we have detailed information on their characteristics and composition are those belonging to our solar system, and even in this cases, several open questions remain. However, already from the discovery of the first extrasolar planets, it was clear that the solar system planets were not standard, but several different scenarios are possible. To understand how planetary systems form and evolve, and pose some constraints on the different theories, on one side is necessary to enlarge our sample by looking for more planets, but on the other hand it is necessary to characterize the already known ones, properly measuring their sizes, masses, densities and investigate their composition.

The detailed study of exoplanet interiors and compositions is the key to be able to answer the aforementioned questions. The only way, to date, to gain this knowledge is to derive the planetary mean density from the measure of their mass and radius, and try to obtain information on the atmosphere, which is the only part of the planet we can directly probe. Nowadays, the only planets for which both the mass and the size are measured, are the transiting ones. The probability for a planet to transit its

host star is pretty low, and depends on the star-planet relative dimension and the orbital semi-major axis (see Section 1.1.4). Given the great importance of the transiting planets and the low probability to observe one, several surveys, both ground and space based, are now targeting thousands and thousands of stars, and others are in development (for examples of current and future surveys see Section 1.1.4). The class of planets that has the highest probability to be seen in transit is the hot Jupiter's one. In addition, hot Jupiters can be detected with more precision than for smaller and farther away planets, as both the photometric and spectroscopic signals are larger. Orbiting very close to their host star, hot Jupiters are extremely irradiated and have therefore high temperature leading to an inflated atmosphere compared to Jupiter. The large and relatively low density atmosphere of these giant gaseous planets are particularly suited for the study of their atmosphere during a transit 1.2.2).

The work presented in this thesis takes place in the context of the latter open question. The discovery and confirmation of three new transiting planetary system hosting a hot Jupiter go to swell the ranks of planets well suited for follow-up studies. In particular these discoveries were made in the framework of two transiting survey: HATSouth and *Kepler* (for an introduction on the instruments and functioning of the two surveys see Section 2.2 and 2.3 respectively). Furthermore, the characterization of six already known hot-Jupiters is also presented: the measurements of the planets radii and masses have been refined and some hints on the planets atmospheric composition are given.

Thesis outline

In this first chapter are outlined the diverse methods employed to discover planetary systems. Particular attention is payed to the transit technique, which has been employed in the detection and characterization of the planetary systems presented in this thesis. In the last part of the chapter is described a particular class of exoplanets: the hot Jupiters. All the planets studied and analyzed in the following chapters belong indeed to this class.

In the second chapter are introduced and described two transit surveys, HATSouth and *Kepler*, whose instruments and data underpin the discovery and confirmation of three of the planetary systems discussed in this thesis. At last, it is described an ongoing project: the *Homogeneous studies of transiting extrasolar planets* aimed to characterize known planetary systems through an extensive photometric follow-up campaign. Within this latter project are located the works on six planetary systems considered in this thesis.

Chapter 3 presents the work that lead to the discovery of two massive hot Jupiters, HATS-15 and HATS-16, within the HATSouth collaboration. Subsequently, the confirmation of the planetary nature of Kepler-432 b is described in Chapter 4. This is a massive planet orbiting around an evolved star discovered by the *Kepler* satellite.

In Chapters 5, 6 and 7 report the results of the follow-up observations of six planetary systems (HAT-P-16, HATS-P-23, WASP-21, WASP-45, WASP-46 and WASP-48). In particular the planetary systems HAT-P-16 and WASP-21 have multi-site observations, while the others have simultaneous multi-band light curves.

Finally, in Chapter 8, we discuss and summarize the work presented in this thesis.

1.1 Detection methods

In order to find an answer to the aforementioned and a myriad of similar questions, diverse techniques to look for extrasolar planets have been developed. Almost all of these methods are indirect and rely on the observation and measurement of the effects that the presence of a planet has on its host star or other planetary companions. The methods and techniques used to discover exoplanets are described in the following sections, specifically the radial velocity, microlensing, direct imaging and transit techinques.

1.1.1 Radial velocity

The method used to discover the first planet orbiting around a sun-like star was the radial velocity (RV) technique. This technique is based on the measure of the motion of the parent star due to the interaction with a planetary companion. When two or more objects are gravitationally bound, they orbit around the common center of mass. The presence of an exoplanet around a star causes a motion towards and away from an observer.

Combining the Keplerian and Newton's laws, specifically the relation between semi major axes and period, conservation of energy and the definition of center of mass, it is possible to describe the motion of two or more bodies of a planetary system. In particular, quantities such as the stellar and planetary mass ($M_\star$ and M_p) and observables such as the period P and the projected velocity variation along the line of sight can be related:

$$\frac{\left(M_p \sin i\right)^3}{\left(M_\star + M_p\right)^2} = \frac{P}{2\pi G} K^3 \left(1 - e^2\right)^{\frac{3}{2}}, \tag{1.1}$$

where i is the inclination of the orbit with respect to the observer's line of sight, G the gravitational constant, K the semi-amplitude of the sinusoidal oscillation of the radial velocity and e the eccentricity of the orbit. For most of the planetary systems $M_p \ll M_\star$, hence, the mass function (the term on the left side of the equal sign in the previous equation) can be re-written as:

$$\frac{M_p \sin i}{M_\star^{\frac{2}{3}}} = \left(\frac{P}{2\pi G}\right)^{\frac{1}{3}} K \left(1 - e^2\right)^{\frac{1}{2}}. \tag{1.2}$$

Given that the inclination of the orbit is an unknown, the planetary mass cannot be exactly constrained, thus only a lower limit can be measured.

To find planetary systems with the RV method, one has to measure the variation of the projected velocity by means of the Doppler effect. When the star is moving towards the observer its light is blue-shifted, while when moving away it is red-shifted (see sketch in Figure 1.1). The doppler shift is described as:

$$\frac{\Delta\lambda}{\lambda_0} = \frac{v_\star}{c}, \tag{1.3}$$

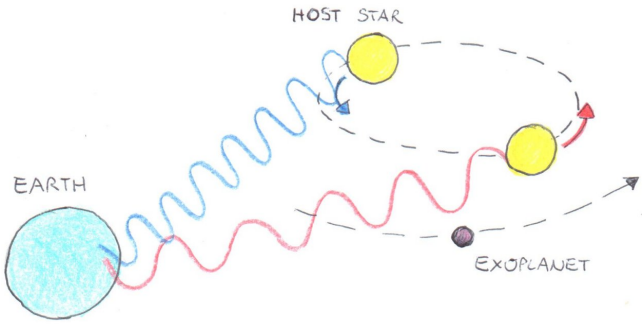

Figure 1.1: Sketch of the Doppler shifted light coming from a star hosting an exoplanet.

where $\Delta\lambda = \lambda_0 - \lambda_1$ is the difference of the emitted wavelength λ_0 and the received one λ_1. In practice, the shift over time of the spectral lines of the parent star is measured with respect to a chosen reference position.
Given the large difference in mass between star and planet, the star motion is usually small. Moreover, as can be deduced from Eq. 1.2, the amplitude of the RV signal diminishes with increasing distance of the planet. For example, the amplitude of the Sun's motion due to the presence of the Earth is $\sim 0.09\,\mathrm{m\,s^{-1}}$, while for Jupiter it is about $\sim 12.4\,\mathrm{m\,s^{-1}}$. The signal to be detected is therefore very small, so good precision and proper treatment of the instrumental systematics is needed (see Figure 1.2). The RV method is biased towards finding planets with high masses at close distance from their host, as they have a larger RV signal. The ease in finding planets very close-in has twofold reasons. On one side the gravitational interaction between the star and its planet is stronger, on the other side, if the period is shorter, less time is required before the data for a complete period can be acquired.

The periodic motion of the planetary host is measured by taking several spectra of the star during the orbital period. This is done using a spectrograph that splits the different wavelength of the light collected through grating or grisms. A high wavelength resolution, defined as $R = \lambda/\Delta\lambda$, is required in order to resolve the spectral lines and be able to measure their movement in time. The intrinsic resolution is determined by the slit or fiber aperture, while the disperser governs the spread in wavelength.

The motion of the spectral lines in a host star spectrum is, as stated, very small and corresponds to a shift on the CCD of a fraction of a pixel. It is self-evident that proper knowledge of the wavelentgh solution and CCD response is required.

There are three different ways to calibrate in wavelength the spectra obtained, which correspond to different hardware setup of the spectrograph. One first way is to obtain a spectra of a known source, such as a ThAr lamp, in the same condition as the target is observed. The second option is to introduce along the light path a iodine cell containing a specific, and well known, amount of gas that will produce a forest of absorption lines superimposed to the star's spectrum. The last way to calibrate the spectra is to use the laser comb technique (Wilken et al. 2010).

Once the spectra are reduced and extracted, the RV measurement is usually performed by cross-correlating the observed spectrum with a reference. The reference spectrum can be a very high signal-to-noise observed spectrum of the same target, a synthetic one or a properly constructed binary mask.

When doing very high precision RV measurements, even if all the sources of instrumental and at-

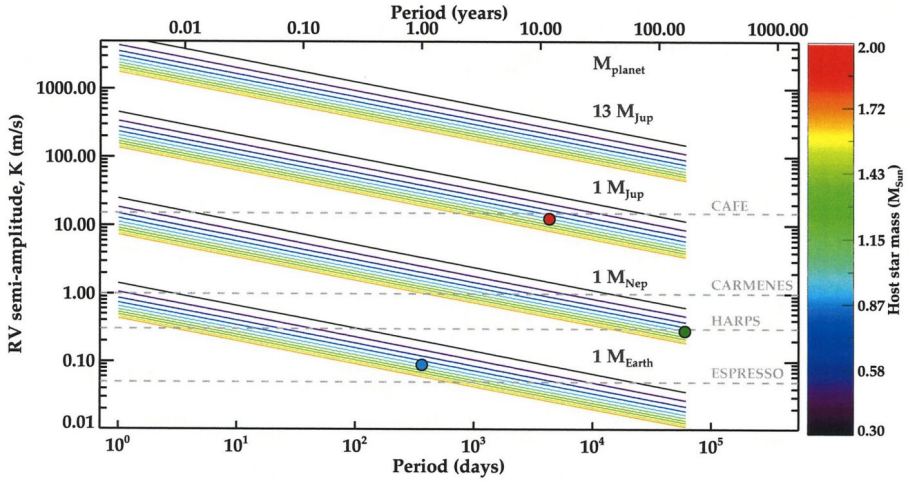

Figure 1.2: The radial velocity amplitude of a star hosting a planet with different masses and at different orbital separation. The diverse line colors represent the parent star mass. The three colored dots represent the Solar system's planets Jupiter, Neptune and the Earth (red, green and blue respectively). Figure credit: Lillo-Box (2015).

mospheric noise are properly taken into account, there is always an intrinsic noise that is not possible to remove. The source of this 'ultimate' noise has an astrophysical origin and is mainly due to the activity of the host star. The star's activity can introduce both periodic and stochastic signals that may completely cover the small periodic planet signal or, in some cases, be mistaken as due to a fictitious planet (e.g. Robertson et al. 2014). Several ways to remove this noise have been developed, among them: pre-whitening (e.g. Anderson et al. 2014), local trend fitting (LTF, e.g. Hatzes 2013) or floating chunk offset (FCO, e.g. Hatzes 2014). In particular the latter can be used just for planets with much shorter period with respect to the stellar rotation period, and in general all of these methods have to be carefully used and, when possible, the results should be checked using independently more of them on the same data-set. Anyhow, in all the cases where the stellar activity is significant, good data sampling is essential.

The first planet found with RV was the notorious Pegasi 51 b (Mayor & Queloz 1995), which opened the season of extrasolar-planet hunting (see Figure 1.3 for an example of RV measurement). Up to now the number of planets detected via RV has exceeded 500. These planets, as expected from the detection bias, are mainly massive. The periods of these planets span from very short ones (e.g. HD 86081 b, Johnson et al. 2006) to more than 14000 days (e.g. 47 Uma d, Gregory & Fischer 2010), with a pile up at very short periods ($1 \lesssim P \lesssim 10$) and an apparent decline at longer period due, most likely, to detection bias (Perryman 2014). The RV method provides the measure of the eccentricity of the planetary orbit: the planets, unlike what thought when just the Solar System's ones were known, show a wide variety of eccentricity going from perfectly circular orbits as HD 103197 b (Mordasini et al. 2011) to very eccentric ones as HD 4113 b (Tamuz et al. 2008). In particular, there seems to be a correlation between the eccentricity and the semi-major axis. Planets closer to their host star tend to have circular orbits, while planets farther away are more prone to be eccentric.

Before the transit technique took over in recent years, the RV method was the most efficient way to find planets. Although the number of planets discovered per year might has decreased, the character-

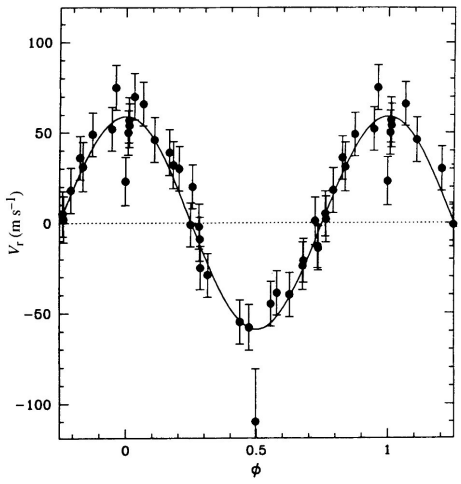

Figure 1.3: The radial velocity curve that brought to the discovery by Mayor & Queloz (1995) of the hot Jupiter Pegasi 51 b.

istics of the planets announced are starting to stand out from the crowd moving towards planets with smaller masses and/or with longer periods, as the HD 20794 system discovered by Pepe et al. (2011) hosting three super Earths, or the Jupiter analog HIP 11915 b found by Bedell et al. (2015).

After the first planetary system was found, several large surveys aiming to detect more exoplanets started. The most used instruments for large surveys are: HARPS installed at the 3.6 m ESO telescope (Pepe et al. 2004), CORALIE mounted on the Euler/Swiss telescope (Queloz et al. 2000), the Hamilton Spectrograph at the Lick Observatory (Fischer et al. 2014b) and FLAMES at the ESO VLT (Loeillet et al. 2006).

Nowadays there are several spectrographs actively used for finding exoplanets. Especially notable, are the HARPS and HARPS-N spectrographs (Mayor et al. 2003; Cosentino et al. 2012), with which it is possible to reach a precision of about 1 $m\,s^{-1}$ in RV measurements.
Among the several spectrographs that will soon be available there is CARMENES an optical-near infrared spectrograph built with the purpose to look for terrestrial planets around cool stars (Quirrenbach et al. 2014), and ESPRESSO to be mounted on the ESO VLT, with a nominal precision in RV measurement of few $cm\,s^{-1}$ (Pepe et al. 2010).

1.1.2 Microlensing

The main idea behind the concept of gravitational lensing is the fact that the gravitational field of a massive body (which can range from a galaxy cluster to a sub stellar-object) deflects the light coming from an aligned background source, allowing an observer to detect the otherwise occulted object a multiple images (in a cosmological context) or the magnification of the source (in a Galactic context). In order to explain this phenomenon, it is necessary to invoke general relativity concepts introduced by Einstein at the beginning of the past century. If the light of a generic source passes at close distance

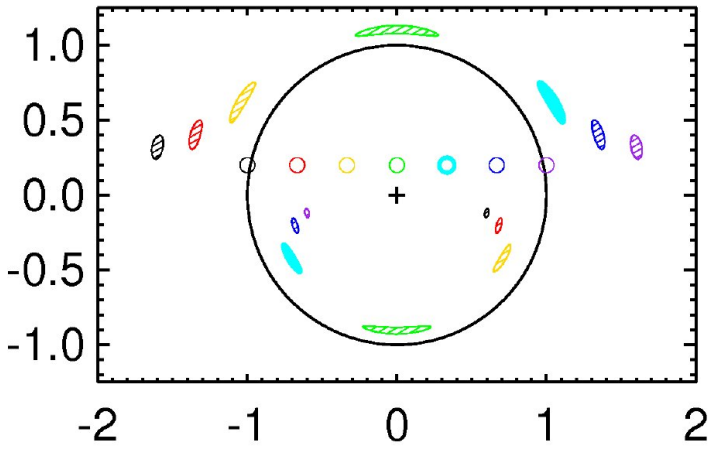

Figure 1.4: The different situations an observer can see by staring at a source (circles) moving behind a lensing object (black cross). The color of the small circles represent the different positions of the source and the colored filled voids are the relative lensed images. The black circle represent the Einstein ring. Figure from Fischer et al. (2014a).

r from an object with mass M, its path is bent by an angle of

$$\epsilon = \frac{4GM}{rc^2}, \tag{1.4}$$

where c is the light speed and G the gravitational constant. The source, according to the mutual position with the lens, will appear to the observer as a ring, if the alignment is perfect, or more commonly as two or more distorted images (see Figure 1.4).

Already in 1936, under the request of the Czech engineer R.W. Mandl, Einstein predicted and modeled the possibility to detect microlensing events, i.e. gravitational lensing events where both source and lens are of stellar or sub-stellar nature. In these cases, the angular separation of the two lensed images is too small to be resolved, resulting in a magnification of the source up to a factor of 1000 (Einstein 1936). At that time the idea of detecting such an event was considered ridiculous, as the probability to observe it was very small (1/100 000, with 100 000 being also the total number of stars observable with the available instruments at that time). It was only in the mid eighties that Paczynski (1986) proposed the first experiment modeling the expected light curve of an object magnified by a microlensing event.

Microlensing (ML) started as an observational field looking for the presence of dark matter within our galaxy and the Magellanic Clouds. In recent times it has become a powerful method to detect and characterize stellar and sub-stellar objects. The first ML event ever observed was monitored simultaneously by the MACHO and EROS collaborations in the Large Magellanic Cloud (Alcock et al. 1993; Aubourg et al. 1993).

An important parameter to describe a ML event is the Einstein radius, which describes how the light of a source perfectly aligned with the lens and the observer is bent due to the gravitational effect. The angular Einstein radius is defined as:

$$\theta_E = \sqrt{\frac{4GM}{c^2}\,\pi_{rel}}, \qquad \text{with} \quad \pi_{rel} = \frac{D_S - D_L}{D_S D_L} \tag{1.5}$$

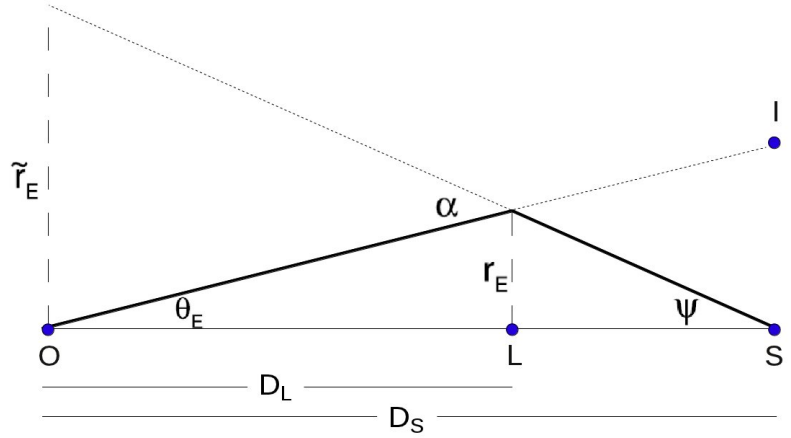

Figure 1.5: Schematized geometry of a microlensing event

the trigonometric parallax between lens and source and M the lens mass (see the geometry of the system in Figure 1.5).
In a ML event the main observable is the magnification of the source' light due to its relative motion with respect to the lensing object. Since the two different images are not resolvable (the angular separation is of the order of 10^{-3}arcsec), only the total magnification is observable, and depends on the projected separation between the source and the lens in Einstein radii, u:

$$A(u) = \frac{u^2 + 2}{u\sqrt{u^2 + 4}} \tag{1.6}$$

If the source and the lens are close to each other:

$$A(u) \sim \frac{1}{u}\left(1 + \frac{3}{8}u^2\right) \qquad \text{(if } u \ll 1\text{)} \tag{1.7}$$

the magnification can be considerable, up to 1000 times the luminosity of the source. On the other hand, if the relative distance is large the magnification is small and the effects can be seen only inside the Einstein ring:

$$A(u) \sim 1 + \frac{2}{(u^2 + 2)^2} \qquad \text{(if } u \gg 1\text{)} \tag{1.8}$$

At the Einstein radius the magnification is:

$$A(u = 1) = \frac{3}{\sqrt{5}} \simeq 1.34. \tag{1.9}$$

In the case that source and lens perfectly overlap ($u = 0$), the magnification is infinite. This point of infinite magnification is called *caustic*. However, this is only a theoretical concept that assumes both the source and the lens to be point-like. In reality, the finite dimension of the source cause the magnification, albeit of large magnitude, to be finite.

Unlike strong lensing, ML has a shorter duration perceivable on a human time scale. The typical duration of a ML event in the Galaxy has a time span ranging from weeks to months, and depends on the relative motion between source and lens. For this reason the source magnification is not constant

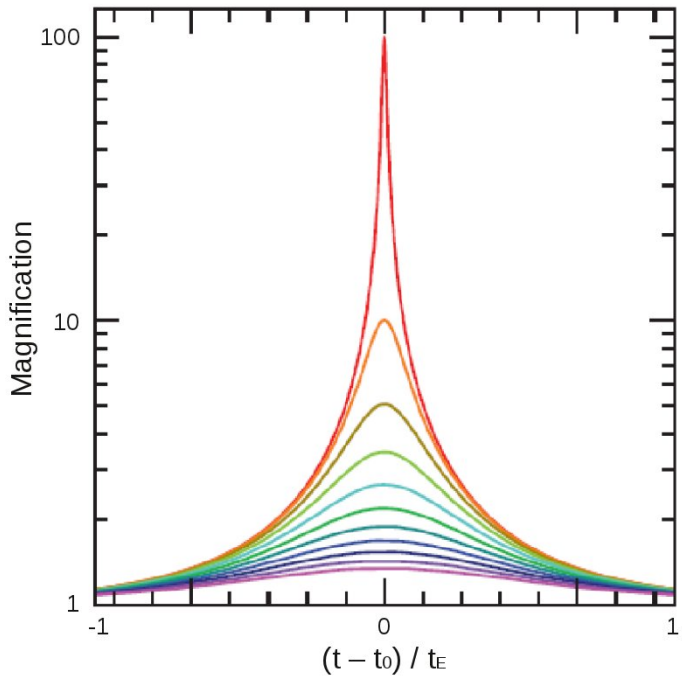

Figure 1.6: Typical shape of a Paczynski light curve of a microlensing event. The different colors refers to different projected separations u between lens and source, ranging from u =0.01 (red) to u =1 (purple). Figure credit: A. Gould (from the lectures at the *Advanced school on exoplanetary science*)

but varies in times resulting in a typical light curve shape called Paczynski curve (see Figure 1.6).

Since the origin of the source magnification is the lens gravity, the light curve shape does not depend on the wavelength used to observe. It is therefore possible to distinguish between a ML event and variable sources such as novae, supernovae, variable star, etc., by comparing the intensity variation in different bands.

In the case of a lens composed of multiple objects, such as a binary or planetary system, the lens-source system becomes more complicated. The caustic is not a point, coinciding with the position of the lensing object anymore but takes various and complex shapes according to the geometrical configuration of the lensing system. This implies a deviation from the traditional Paczynski curve that can either be the rise of multiple peaks of different intensity or, in particular cases, the presence of a dimple.

The first person hypotizing the possibility to observe a planet around a lens was Liebes (1964), but only Mao & Paczynski (1991) and later Gould & Loeb (1992) really took in consideration the probability of detecting planetary objects via ML and calculated the caustic for a double lens modeling the possible light curve shape.

The first planet ever detected with ML was OGLE-2003-BLG-235/MOA-2003-BLG53L b, discovered by Bond et al. (2004). It was a Jupiter-like planet orbiting around a main sequence star at a separation of $\sim$ 3 au (Figure 1.7). For a typical sun-like star the characteristic size of the Einstein ring is $\sim$ 4 au, therefore the maximum probability to detect a ML planetary event occurs when the planet is roughly at that separation from its host star; in the case of a M-dwarf the Einstein ring is smaller. ML

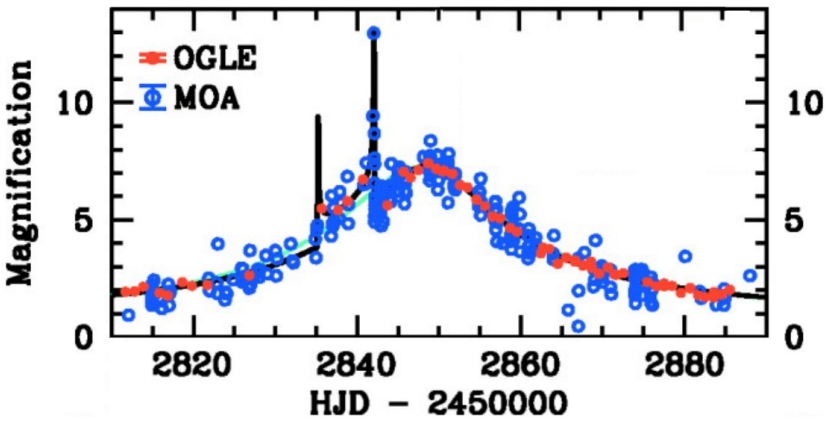

Figure 1.7: Light curve of the first planetary system found via microlensing by Bond et al. (2004): OGLE-2003-BLG-235/MOA-2003-BLG53Lb. The colors of the data-points refers to the different telescopes used to follow up the event, and the solid black line represent the best fit obtained by using a binary system lens model where the smaller object is of planetary nature. The median errors in the OGLE and MOA points are indicated in the legend.

detections do not depend on the brightness of the lens, therefore they are very sensitive to M-dwarfs, as stars belonging to this class are more frequent.

Given a ML event's light-curve there are several different methods and approaches to determine the type of lens and obtain the planet's complete orbital solution: e.g. contour integration (Gould & Gaucherel 1997; Bozza 2010), or inverse ray shooting (Bennett 2010; Dong et al. 2006). In some cases, it is possible to try to predict the diverse magnification peaks in an ongoing event in order to optimize the observing strategy.

Nowadays there are several surveys dedicated to ML observations, mainly MOA (Bond et al. 2001), OGLE (Udalski et al. 1992) and Wise (Abe et al. 2004). The main idea behind their observational strategy is to observe with wide field of view cameras in order to be able to monitor a large number of stars in the galactic bulge and look for magnitude variations for those stars that have not already been labeled as variables. In order to have the proper photometric coverage of a ML event necessary to spot anomalies, several collaborations such as MiNDSTEp, roboNet or MicroFUN, have created a telescope network spread around the world that can follow up an event, providing a continuous coverage in time.

New instruments and dedicated surveys are in development e.g. WFIRST (Barry et al. 2011), or have just started producing interesting reults e.g. KMTNet (Kim et al. 2011; Hwang et al. 2015).

Thanks to the synergy of current (Spitzer, Zhu et al. 2015) and future satellites such as GAIA and WFIRST, it will be possible to properly measure all the parameters necessary to disentangle the degeneracies in the orbital solution of a multiple lens and also be able to look for three or more body lenses.

1.1.3 Direct imaging

The direct imaging (DI) technique is the only method that directly observes the light coming from planets. This requires great instrumental performance and careful treatment of the data obtained. The main difficulty in obtaining an image of a planet is given by the fact that the light of the planet is outshined by its host star's light.

As an example, if we could observe the Solar System from a distance of ∼10 pc, Jupiter, the brightest planet, would have an angular separation from the Sun of nearly 0.5 arcsec and would look roughly 10^{-6} times fainter than the Sun in the infrared.
This is why both high resolution and light gathering (todetect signals at low contrast) are essential.

In the following a brief and general description of a DI observation is presented. The finite size of a telescope acts as a perturber creating a diffraction pattern and the PSF (point spread function) of a point-like source, instead of being a point, is the square Fourier transform of the telescope aperture. In the ideal case, the PSF is describable as the Airy ring. However, it is necessary to take into account the Earth's atmosphere, that perturbs the incoming wavefront of the star, further distorting the PSF and creating a pattern of speckles.

The effect of the atmospheric turbulence is neither constant in time, nor creates same magnitude distortion at different colors. Specifically, its effect varies as a power law with wavelength, diminishing towards the redder ones (see upper panel in Figure 1.8). Also, the diffraction limit has a wavelength dependency that grows with the wavelength. Howbeit, the dependence on the wavelength of the diffraction pattern becomes lower when the telescope aperture is larger (see lower panel in Figure 1.8). To minimize both effects it is therefore advisable to perform DI observations by means of large telescopes equipped with good adaptive optics (AO) systems and operationg at long wavelengths, typically in the near infrared regime.

In order to observe smaller angular separation Θ, it is fundamental either to use a large-sized telescope or to combine interferometrically the light coming from more telescopes, as:

$$\Theta \propto \frac{\lambda}{D} \qquad \text{or} \qquad \Theta \propto \frac{\lambda}{2B} \tag{1.10}$$

where λ is the chosen wavelength, D is the telescope diameter and B is the separation between the telescopes.

To be able to observe directly the light coming from the planet, the key is to carefully conceal the overpowering starlight. Different techniques and observing strategies have been developed, and can be divided in three main categories. To the first class belong all the techniques that make use of coronographs. The second way to get rid of the star light is to use interferometric techniques combining the light of the planetary system to obtain a minimum that coincide with the position of the star. Another method to remove the overwhelming light of the parent star is polarimetry. The star light is usually unpolarized, conversely the reflected light of a planet has some degree of polarization. This is due to the fact that the starlight incident on the planetary atmosphere interacts and gets reflected by the molecules and atoms of the atmosphere. By observing a planetary system with different polarizations, it is possible to subtract the star component from the total light, leaving only the light reflected by the planet.

Even if the starlight can be suppressed by means of coronographs, to be able to detect a faint com-

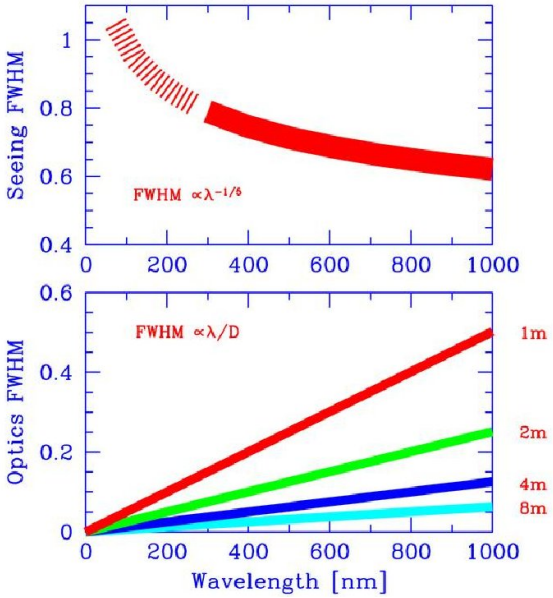

Figure 1.8: *Top panel*: the broadening of the PSF due to the atmospheric seeing according to the wavelength used to observe. *Lower panel*: FWHM of the diffraction pattern of a point-like source in function of the wavelength. The wavelength dependence is stronger for smaller telescopes (red line), while weakens for bigger telescopes (light blue line). Figure by R. Claudi (from the lectures at the *Advanced school on exoplanetary science*).

panion, it is still necessary to properly treat the speckle pattern. Several techniques, that require heavy post processing, are used and among them are the angular differential imaging (ADI, Marois et al. 2006) and spectral differential imaging (SDI, Racine et al. 1999). Both methods perform a posterior speckle subtraction counting on the fact that, unlike a possible planetary companion, the speckles positions and shapes do not vary when tilting the field of view and are wavelength dependent.

Given the intrinsic difficulties in detecting planets directly, the choice of the targets to be observed in looking for a planet falls on young stars in the solar neighborhood. Indeed, the light contrast between the young star and planet is lower as the newly formed planet did not have the time to cool down. Therefore, in addition to the reflected light from the star there is an extra component emitted directly by the planet itself. The selection of near stars is dictated by the angular resolution required.

The planets found via DI have complementary characteristics with respect to the ones found via RV or transit. Usually, the planets are young, massive and have long orbital periods. Worth noticing is the fact that with DI it is possible to detect and obtain information on the atmospheric composition of planets that lie outside the snow line. This is of particular interest in the context of planet formation and migration theories. Moreover, an advantage of the DI method is that, being able to resolve the planets, it is also possible to obtain direct spectral measurement and gain important information on the composition of their atmospheres. The DI method therefore provides a set of information that is diverse with respect to the other detection techniques: e.g. the luminosity of the planet, its spectrum and the architecture of planetary systems at young ages.

From a DI measurement is possible to measure the luminosity of a planet. If the age of the system is known, for instance due to its membership to a moving group of young stars, using planet evolu-

tionary models it is possible to infer the mass of the planet. However, these measurements are strictly model dependent and different initial assumptions can lead to very different results. An example for this is the assumption made on whether a Jupiter-like planet had a so called cold or hot start.

In brief, in the core accretion formation scenario it is possible to predict two different ways in which the material is accreted onto the planet. In the first case, *hot start*, all the gravitational potential of the accreted material is kept in the proto-planet, and only once the formation processes are concluded does the planet start to cool down. The second case, *cold start*, assumes that the inflowing material creates shocks that radiate away part of the gravitational energy. For a fixed age, according to which scenario one refers to, a planet can have different properties (see Figure 1.9), and obtain diverse values for the mass of the planet observed.

Since the beginning of this century, astronomers have started surveys looking for planets, with instruments such as NIRC2 mounted on the Keck telescope (Matthews & Soifer 1994) or NACO mounted on UT4 telescope of the ESO VLT in Paranal, Chile (Lenzen et al. 2003), but the throughput in terms of actual discovery has been pretty low and only upper limits on the occurrence of giant planets with large orbital radii were produced. Subsequent instruments have been developed such as the HiCIAO imager at the SUBARU telescope in Mauna Kea, Hawaii (Suzuki et al. 2010), or the Project 1640 making use of the IFS mounted on the 5 m Hale Telescope at the Palomar Observatory (Oppenheimer et al. 2013).

Only recently with the first light of two new powerful instruments built with the specific purpose to look for planets with DI, some of the very high technical requirement have been met, and there are great expectations for their results. The two instruments are GPI mounted on the 8 m Gemini South Telescope at the Las Campanas Observatory in Chile (Macintosh et al. 2012) and SPHERE, the European counterpart, installed on the VLT at Paranal (Beuzit et al. 2008).

Future projects for DI observations are being developed both for ground based telescopes, such as the Extremely Large Telescope, and for space (e.g. WFIRST or JWST).

The first planet discovered via DI is 2M1207 b (Chauvin et al. 2004), a $4\,M_{\rm Jup}$ planet orbiting at 46 au around a brown dwarf. Up to now, just a few tens of planets had been discovered via DI, but this number has recently started to increase and will continue following this positive trend thanks to the two new instruments mentioned above. To be noticed is the fact that most of the planetary systems found show, besides the planetary body, also a non negligible debris disk (e.g. β Pictoris or Fomalhaut, Lagrange et al. 2010; Kalas et al. 2005).

One of the latest great achievements in the DI field is the recent detection by the GPI consortium of a planetary companion (with a mass up to $13M_{\rm Jup}$ when hypothesizing a cold start, or $2M_{\rm Jup}$ considering a hot start) to the F type star 51 Eridani (Macintosh et al. 2015, see also Figure 1.10). The importance of this discovery is given by the extremely small angular separation the instrument was able to resolve: less that 0.5 as between the two objects.

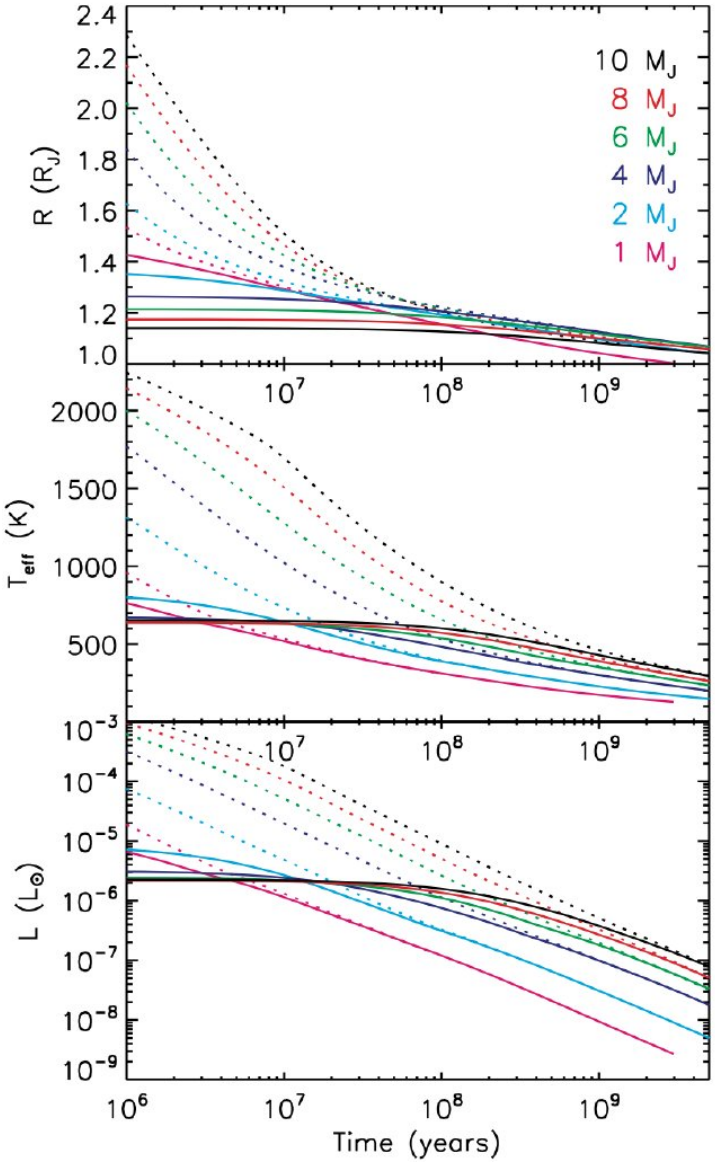

Figure 1.9: Figure by Marley et al. (2007) describing the change in radius, effective temperature and luminosity according to age. The relations are calculated for planets with different masses (from 1 to 10 M_{Jup}). The dotted lines represent the evolution under the assumption of a hot start, whilst solid lines are produced assuming a cold start.

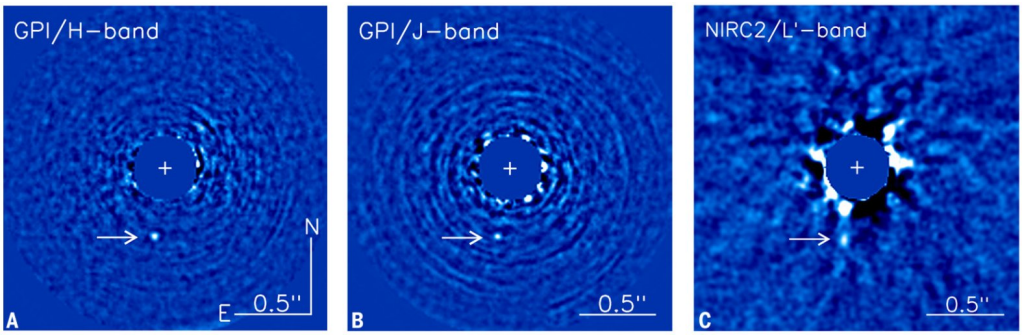

Figure 1.10: The 51 Eridani planetary system discovered by Macintosh et al. (2015). The planet, at the projected separation of 13 au, is indicated with an arrow. In panel A and B are reported the images obtained in H and J band respectively with GPI. In panel C is shown the image observed in L band with the NIRC2 camera mounted on the Keck telescope.

1.1.4 Transit method

When a planet passes in front of the disk of its host star, it blocks a small portion of the star light. Therefore, if one constantly observes the flux coming from that star a small drop in the intensity during the transit of the planet should be seen. As the planet is gravitationally bound to the star it has a close orbit around it, thus the short decrease of the light's intensity is periodic and can be repeatedly observed.

The possibility of observing the planetary eclipse of a star other than the Sun was already hypothesized by Struve (1952). Hence, as the first extrasolar planets were found via the Doppler technique, astronomers started to photometrically monitor those planetary systems looking for a periodic dimming. In 2000 two independent groups, Charbonneau et al. (2000) and Henry et al. (2000), reported the first observation of the transit of the planet HD 209458. After these observations several more Doppler planets were found to transit their star. Only three years later, Konacki et al. (2003) confirmed the discovery of the OGLE-TR-56 b planet by means of the transit method.

For a transit to be observed from the Earth it is necessary for the planetary orbit to be aligned edge-on with the line of sight. Therefore, only if the inclination is within a small interval around $i = 90°$ is the transit visible. As the inclination of the orbit is random, the probability to observe a planet transiting its parent star is very low. Moreover, it depends on the relative dimension between the star and the planet and the semi-major axis. Specifically, the probability that the line of sight lies in an interval di around a certain inclination angle i is given by

$$d(\text{Prob}) = \frac{\mathrm{d}\Omega}{4\pi} = \frac{2\pi \sin i \,\mathrm{d}i}{4\pi} = \frac{\mathrm{d}(\cos i)}{2}. \tag{1.11}$$

The condition for a transit to occur is (see Figure 1.11 for a visual description):

$$a \cos i \leq \mathrm{R}_\star + \mathrm{R}_\mathrm{p}, \tag{1.12}$$

where R_p and $\mathrm{R}_\star$ are the planetary and stellar radii. Therefore, combining the two Equations 1.11 and 1.12, and assuming $\mathrm{R}_\mathrm{p} \ll \mathrm{R}_\star$, the resultant probability for a transit to be observable is

$$\text{Prob} \approx \frac{\mathrm{R}_\star}{a} \approx 0.005 \left(\frac{\mathrm{R}_\star}{\mathrm{R}_\odot}\right)\left(\frac{1\text{au}}{a}\right). \tag{1.13}$$

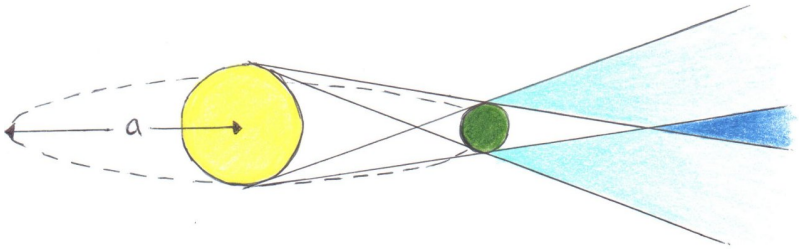

Figure 1.11: Sketch of a planetary system. For the planet to be seen in transit, the line of sight has to lie in the dark blue cone, while for a grazing transit is sufficient to lie in the light blue zone.

To give a couple of examples, for a typical hot Jupiter orbiting at 0.05 au from a Sun-like star, the transit probability is about 10%. If the same planet orbits farther away at 1 or 5 au, the probability drops dramatically to 0.5 and 0.1% respectively.

It is evident that, in order to catch the transit of a planet, it is necessary to monitor a large number of stars for a sufficiently long time.
For the aforementioned reason, in the early years of this century, several ground-based transiting survey were started: e.g. TrES (Alonso et al. 2004), HATNet (Bakos et al. 2004), SuperWASP (Pollacco et al. 2006), KELT (Pepper et al. 2007), and the more recent HATSouth (see Section 2.2) and QES (Alsubai et al. 2013). For an example on how a transiting survey handles the discovery process from the observations of the photometric data to the actual report of a newly confirmed planet, see Section 2.2.

As the dimming of the starlight due to the transit of the planet is very small (of the order of 1-2% for large close-in planet and fraction of percent for smaller and/or far away planets), the precision needed to detect such a signal is quite high. The best way to obtain precise photometry is to observe from space, where measurements are not affected by any atmospheric variation and contamination. In the recent years two satellites (CoRoT and *Kepler*, Barge et al. 2008, see Section 2.3) have been looking for transiting planets as primary goal of their mission. New surveys making use of more precise instruments are being developed and will soon start to discover and characterize new interesting planetary systems. Among them are the ground based NGTS (Chazelas et al. 2012) or SPECULOOS (Gillon et al. 2013) and the space missions TESS (Ricker et al. 2009), CHEOPS (Broeg et al. 2013) and PLATO (Catala & Plato Team 2006).

The transit method is particularly important because it is the only one providing a measurement of the dimension of the planet. Moreover, combined with the radial velocity measurements that provide the mass of the planet, it is possible to deduce the planetary mean density.

In the past years the main observing method to find planets was the radial velocity technique, however recently the planets found via transit have outnumbered those found with other methods. To date, more than 1200 planets are known to transit their star, some of which are in multiple systems, and the number is continuously growing.

This plethora of planets shows the most diverse characteristics, often showing properties that have no analogues in our Solar system. Despite the large variety of planets, some correlation within their properties can be found. For instance, there is a relation between the planet density and their mass (empirically derived laws describing the mass–density relation can be found in Bakos et al. 2015),

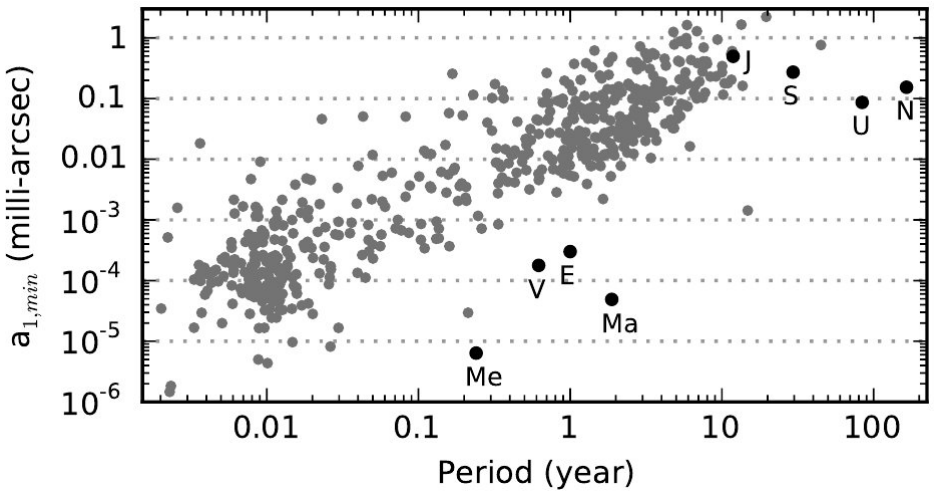

Figure 1.12: The minimum astrometric signature of the parent star as a function of the orbital period of the planet. In black, as a reference, the signature that the solar system's planets would cause on a solar-like star at 10 pc. Figure from Fischer et al. (2014a).

although between 0.05 and 1.5 M_{Jup} the scatter is considerable, with the presence of highly inflated planets.

As the transit method is the one used to detect and characterize all the planetary systems described in this thesis, further details on the used technique are presented in Section 1.2.

1.1.5 Other methods

There are also other methods to detect planetary systems that until now had a low efficiency but may be more productive in the future with new instruments recently becoming available.

Astrometry

Astrometry is the study of the position and motion of a star in the sky with respect to the position of other celestial objects in the background. This technique is based on the measurement of the parallax shift caused by the revolutionary motion of the Earth around the Sun. Astrometric measurement have been used already by the ancient Greeks to measure the position of the stars, and starting from the eighteen century were used to attempt measuring the distance and proper motion of celestial bodies. Only in the last decades, thanks to the development of instruments capable of reaching a precision of few milli-arcsecond, has it been possible to attempt the search for extrasolar planets with this technique.

When a star is circled by an undetected planet, it moves in an orbit around the common center of mass. By precisely measuring and modeling the star's position in time, it is possible to discover the perturbing planet (e.g. Black & Scargle 1982). In particular, the unknown planetary orbital quantities

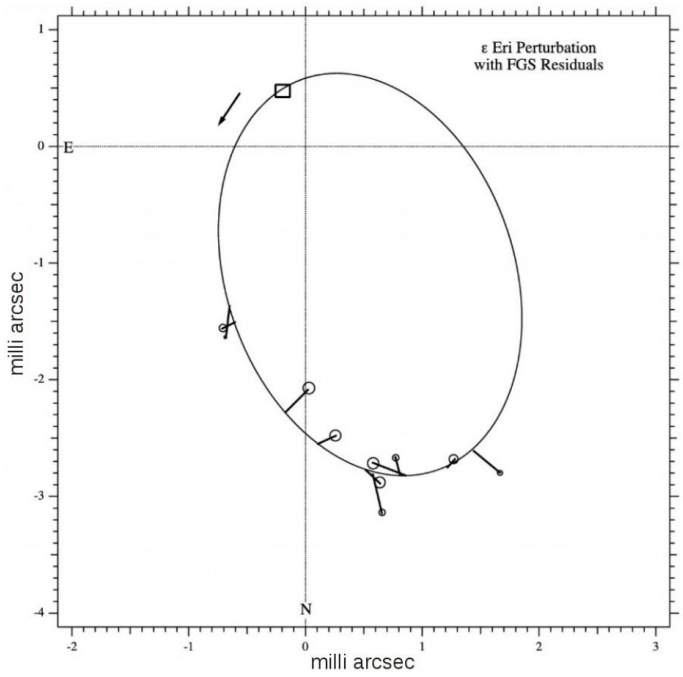

Figure 1.13: Perturbation orbit for ϵ Eri from the paper by Benedict et al. (2006). Residual vectors are plotted, connecting each normal-point residual to its predicted position at each epoch of observation. The direction of motion is indicated by the arrow.

such as inclination, eccentricity, period, etc., can be derived from observations by properly parametrizing the geometrical system in terms of astrometric signal measured along a chosen axis, that is directly dependent to the observable obtained from the parallax (Hilditch et al. 2001).

The astrometric signal to be detected scales directly with the amplitude of the angular semi-major axis a_1 defined as:

$$a_1 \propto \frac{\mathrm{M_p}}{d}\left(\frac{P}{\mathrm{M_\star}+\mathrm{M_p}}\right)^{\frac{2}{3}}. \tag{1.14}$$

Thus, the orbit apparent angular size decreases as the host star mass ($\mathrm{M_\star}$) and its distance from the Earth (d) increases, but increases for wider periods and larger planetary masses ($\mathrm{M_p}$).

Most of the first astrometric planetary discovery announcements turned out to be false detections, and just a very small number of massive planets/brown dwarfs has been confirmed to date (e.g. ϵ Eri Figure 1.13). This paucity is mainly due to the very high precision needed for the detection: from the relation in Eq. 1.14 we can deduce that a massive Jupiter-like planet around a solar-type star has an astrometric signature of the order of a fraction of an arc-second. An even greater accuracy of the order of $\sim 0.1 - 1\,\mu as$ is needed if the goal is to detect an Earth-like planet around a nearby star.

Figure 1.12 shows the astrometric precision needed to detect some of the known planet discovered with other techniques as a function of the planetary period. The value $a_{1,min}$ is a lower limit, as for planet where the orbital inclination was not known, $sin\, i = 1$ has been assumed.

To give an idea of the difficulties in obtaining proper planetary detection, one could look at the Hipparcos survey (Perryman 1989) that had an astrometric precision of $\sim 1\,mas$, and could have been able to detect just a handful of planets with very long periods. In cases of ground based observations,

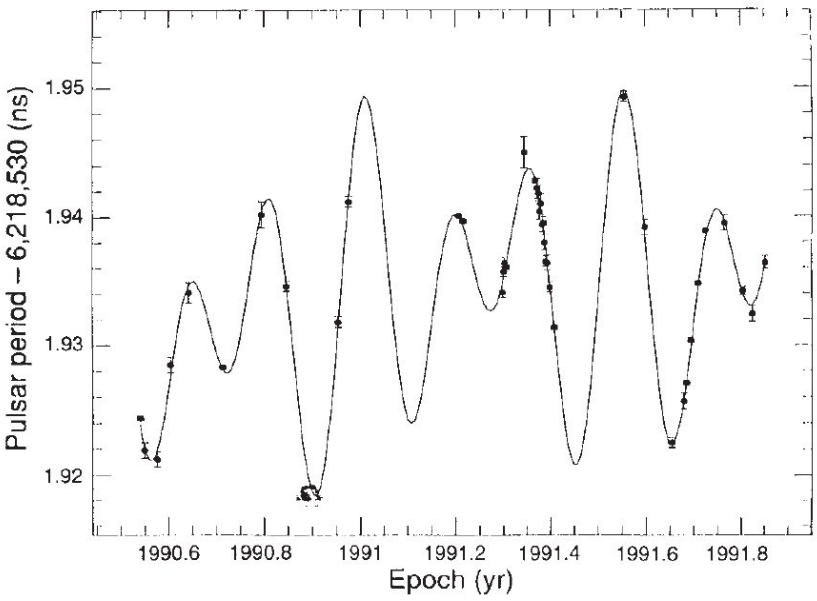

Figure 1.14: Period variation of the pulsar PRS1257+12. The solid lines represent the prediction of the variation in time pulse if two small sized planet are assumed circling around the pulsar. Figure from the discovery paper by Wolszczan & Frail (1992).

the main limitation is due to the atmospheric turbulence and the air-mass that the light coming from the target has to cross. The different and variable refraction index of the air column affects the position of the stars on the focal plane.

Unlike most of the other detecting methods, astrometry provides a measurement for all the orbital parameters, and if the stellar mass is determined independently, it gives the measure of the planetary mass unequivocally. Moreover, it is not affected by stellar activity and can therefore be used to properly obtain the census of planets around active or evolved stars.

For this reason there are great expectations for the new ESA mission GAIA, which started its operations in 2014. The GAIA satellite orbits around the Lagrangian point L2, and its primary goal is to build up an all-sky map by observing an average number of 70 times each stellar object in its 5 year time mission. For stars between 6 and 15 magnitude the expected astrometric precision for each point is of the order of $\sim 20-50\,\mu as$. Therefore, thousands of new exoplanets with periods $P \gtrsim 10\,yr$ could be found (as can also be seen by looking at Figure 1.12, Casertano et al. 2008; de Bruijne 2012).

Pulsar timing

The pulsar timing technique was the first method used to detect a planetary body external to our solar system. In particular, Wolszczan & Frail (1992) discovered the first exoplanets orbiting around a pulsar. A pulsar is a highly magnetized, fast rotating neutron star, whose magnetic axis is not aligned with the rotational axis. As a result, the electromagnetic emission of the star reaches the observer in periodic pulses.

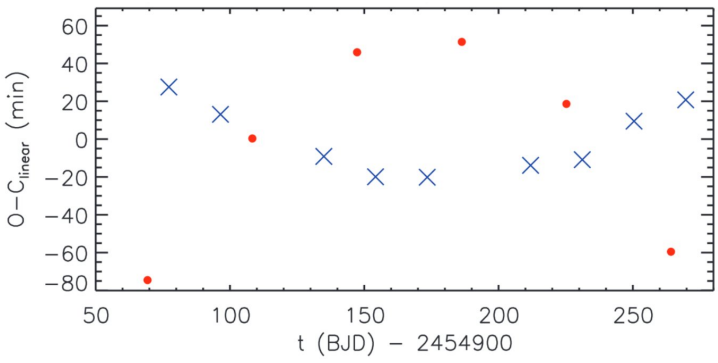

[b!]

Figure 1.15: The difference between the observed and calculated (O-C) values of the transit time for the planets Kepler-9 b (blue) and c (red). Figure by Holman et al. (2010).

The period of a pulsar, normally determined in the radio wavelength regime, can be measured with a very high precision up to 10^{-14} seconds (e.g. Kaspi et al. 1994). On a short time scale (within a year), the pulses due to the stellar rotation are extremely regular, and therefore it is possible to detect a small periodic variation from the expected pulse time due to a body gravitationally interacting with the pulsar (e.g. see Figure1.14).

With pulsar timing it is possible to precisely measure the masses of the planets, down to moon masses, and obtain a full orbital solution, making this technique the most sensitive to date. However, as for other methods, it is impossible to measure the dimension or have any information on the planetary bulk and atmosphere composition. The main limitation of this technique, and the cause of the very small number of planets found with it (19 to date[2]), is that the number of pulsars known is very limited.

Transit time variation

In a transiting system, the interval between the planet transits is constant. If a system has one or more planetary companions, which are not necessarily transiting the star, the interval is not constant anymore but shows periodical variations. Indeed, when three or more massive bodies are gravitationally bound they interact gravitationally, producing a time-variation whose amplitude depends on their mass. By measuring and modeling the transit time variations (TTV), it is possible to obtain information on the orbit and thus give a lower limit on the mass of the perturbing planet.

The development of instruments like *Kepler* (Borucki et al. 2010, for a description of the mission see also Section 2.3), capable of continuous and very precise photometry, allowed the employment of the TTV technique to detect planetary companions to already known planets. If the two or more planets detected via TTV are also transiting, the density of all the planets can be measured without the need of any RV measurement (Holman & Murray 2005).

The TTV method can detect planets with very small masses and is particularly sensitive to orbital configurations where the planets are in mean motion resonance. The first TTV measurement was made by Holman et al. (2010), who estimated the masses of the two transiting planets Kepler-9 b and

[2]For an updated number please see *exoplanet.eu*

c that seem to be in a 2:1 mean motion resonance (see Figure 1.15).
Thanks to TTV Nesvorný et al. (2013) found a non transiting companion to the Neptune-like planet KOI-142 b.

1.2 The transit method

As already introduced in the previous section, the transit method is nowadays the most efficient technique to detect exoplanets. Furthermore, it gives the opportunity to characterize the planet and its orbit, measuring, for instance, its density and the star's spin-orbit alignment. In some cases it is also possible to infer the atmospheric composition.

1.2.1 Geometry of a transit

The main observables of a planetary transit are its period, the dimming duration, and its depth. See Figure 1.16, where t_c is the mid-transit time, T the total duration of the transit, τ the interval between the first and second contact and δ the depth. Provided a few assumptions are made, from these quantities it is possible to derive several important quantities such as the dimensions of the parent star and the planet, the orbital inclination and the mean stellar density. In the case of circular orbit and neglecting the limb darkening effect (see Section 2.4 in the next chapter for a proper discussion on this effect), an analytical and unique description of all the photometric parameters can be found.

The four observables can be related to the physical quantities of system through three dimensionless equations that describe the geometry of the transit.

The transit depth is related to the amount of light that the planet covers, thus it depends on the size of the star and the planet:

$$\delta \simeq \left(\frac{\mathrm{R_p}}{\mathrm{R_\star}}\right)^2 . \tag{1.15}$$

As the stellar radius is bigger than the planetary one, the transit depth is just a small fraction of the total light of the system and a very good photometric precision is needed to detect it. For instance the transit depth due to the transit of Jupiter in front of the Sun would have a $\delta \approx 0.01$ mmag corresponding to roughly the 1% of the total flux.

The transit duration depends on the distance of the planet from the star and the stellar size. It can be expressed as:

$$T = \frac{P}{\pi} \sin^{-1}\left[\frac{\mathrm{R_\star}}{a \sin i} \sqrt{\left(1 + \frac{\mathrm{R_p}}{\mathrm{R_\star}}\right)^2 - b^2}\right], \tag{1.16}$$

$$t = \frac{P}{\pi} \sin^{-1}\left[\frac{\mathrm{R_\star}}{a \sin i} \sqrt{\left(1 - \frac{\mathrm{R_p}}{\mathrm{R_\star}}\right)^2 - b^2}\right], \tag{1.17}$$

where t is the time between the second and third contact, and b is the impact parameter, defined as the projected distance on the stellar disk of the planet from the center of the star: if the planet crosses the

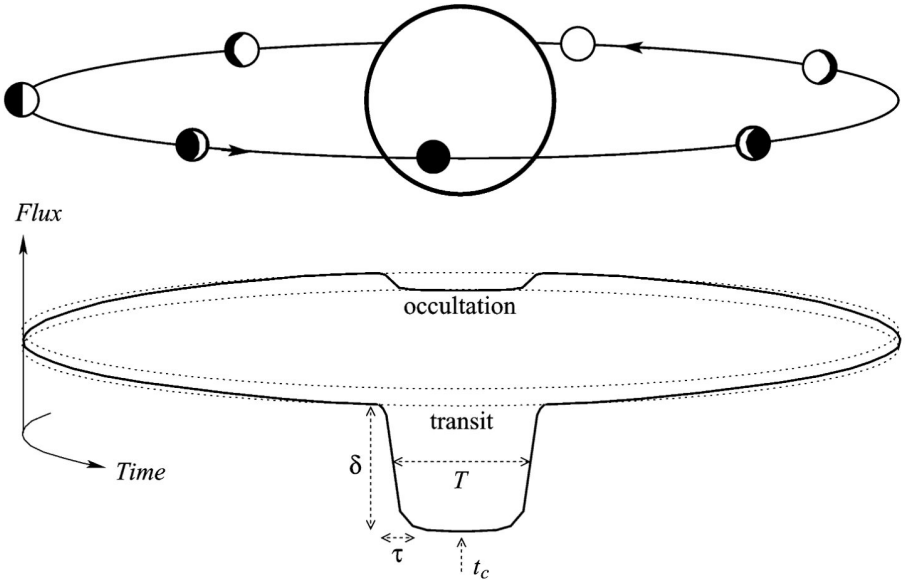

Figure 1.16: Schematic illustration of a transit. The figure shows the combined light of the parent star and the planet: during the transit part of the starlight is blocked by the planet. Subsequently, as the planet revolves around the star, it shows progressively the brighter day-side slightly increasing the total flux. Finally the flux diminishes again once the planet passes behind the star during the secondary eclipse. Figure by Winn (2009).

star in the middle $b = 0$, while when it just grazes the limb of the star $b = 1$.
Among the planets discovered until now, on average the transit duration is of the order of a couple of hours. The shortest transits last nearly 25 minutes (e.g. Kepler-42 d, Muirhead et al. 2012) and the longest up to ∼17 hours (e.g. Kepler-87 c, Ofir et al. 2014).

From this three equation describing the geometry and adding some more information, it is possible to derive some model-independent parameters:

$$\begin{aligned} &\text{Radius ratio} && \frac{\mathrm{R_p}}{\mathrm{R_\star}} \approx \sqrt{\delta} \\ &\text{Impact parameter} && b \approx 1 - \sqrt{\delta}\frac{T}{\tau} \\ &\text{Fractional stellar radius} && \frac{\mathrm{R_\star}}{a} \approx \frac{\pi}{P}\sqrt[4]{\frac{T^2\tau^2}{\delta}} \end{aligned} \tag{1.18}$$

Under the initial hypothesis of a circular orbit, combining the transit duration (Eq. 1.16) with the third Kepler law gives the relation for the stellar density:

$$\rho_\star \approx \frac{3P}{\pi^2 G}\left(\frac{\delta}{T^2\tau^2}\right)^{3/4}. \tag{1.19}$$

If the orbit is not circular, the stellar density parameter becomes degenerate with eccentricity.

Finally, if some RV measurements are available, one can derive directly the planetary surface gravity (Southworth et al. 2007):

$$g_\mathrm{p} = \frac{2\pi K}{P \sin i}\left(\frac{\mathrm{R_\star}}{\mathrm{R_p}}\right)^2\left(\frac{a}{\mathrm{R_\star}}\right)^2, \tag{1.20}$$

where K is the radial velocity semi-amplitude.
If astrometric measurements allow direct measurements of the radii of the closest stars to the Earth (Boyajian et al. 2012), it is possible to have a completely model-independent measurement of the bulk density of the planet:

$$\rho_{\rm p} = \frac{g\pi}{G\Theta}\left(\frac{\rm R_\star}{\rm R_p}\right), \tag{1.21}$$

where Θ is the angular diameter of the star.
myind For a comprehensive and complete description of the photometric parameter retrieval, refer to Seager & Mallén-Ornelas (2003) and Winn (2010).

1.2.2 Atmosphere of a transiting planet

Right after the first planets were found in the mid-nineties, the idea of detecting their atmosphere was a very remote possibility. However, while the number of exoplanets was growing the identification of some signature of planetary atmosphere seemed less and less inaccessible. Even before the first transiting planet was found in 2000, several theories started predicting the possible spectral feature and temperature-pressure profiles for highly irradiated planets (e.g. Seager & Sasselov 1998; Marley et al. 1999).

The discovery of transiting extrasolar planets opened the road to the study of the planets atmosphere. The particular geometrical configuration of a transiting planet allows indeed to have peculiar situations where either the starlight passes through the planet atmosphere (primary transit) or most of the disk facing towards the Earth is illuminated (seconday eclipse). Moreover, studying the luminosity changes of the star-planet light during an entire period can provide important information about the temperature gradient and redestribution between the planet day and night side (e.g. Knutson et al. 2012).

Primary transit

When a planet transits its host star, part of the light that enters in its atmosphere is not blocked but is partially refracted, diffused, absorbed or transmitted along our line of sight. The amount of transmitted light depends on the characteristics of the atmosphere, mainly the density and the composition. Indeed, according to the different molecules and atoms present in the atmosphere some wavelengths are absorbed while other pass through the atmosphere undisturbed. This translates to a different apparent size of the planet when observed in different wavelengths.

As described in the previous section, from the shape of a transit it is possible to measure the size of a planet. Therefore by measuring the transit depth at different wavelengths, one can measure the variation of radius of the planet and link it to its atmospheric composition. The resulting transmission spectrum probes the low pressure part of the atmosphere at the terminator.

The extent of the planetary radius variations with wavelength is diverse from planet to planet: it

depends on the planet properties and is proportional to the scale height. The scale height is defined as:

$$\mathrm{H} = \frac{k\,\mathrm{T}}{\mu\,g} \tag{1.22}$$

where k is the Boltzmann constant, T the planetary atmosphere temperature, μ the mean molecular weight and g the planet's surface gravity. This translates to a fractional variation of the transit depth equal to:

$$\delta \simeq \left(\frac{\mathrm{R_p} + 10\,\mathrm{H}}{\mathrm{R_\star}}\right)^2 - \left(\frac{\mathrm{R_p}}{\mathrm{R_\star}}\right)^2 \tag{1.23}$$

that is the ratio of the optically thin atmosphere to stellar areas. For a typical hot Jupiter the variation of the transit depth measured at wavelentgh with strong absorption features is of the order of 0.1% (Madhusudhan et al. 2014).

The atmosphere of a planet is a small portion of its dimensions, and the light that filters through the atmosphere of the planet and carries the information is diluted by the rest of the star light that is not blocked by the transit. Given the large radius and the presence of a hot atmosphere, it goes without saying that hot Jupiters are the preferential candidates when trying to perform transmission spectroscopic studies. A general criteria to select suitable targets for atmospheric studies is to choose those planets that have a large scale height, that is, planets with low surface gravity and/or high equilibrium temperature.

Studies aiming to characterize planetary atmospheres usually employes transmission spectroscopy as an observational technique, but other methods such as multi band photometry can also be used (see Section 2.4.1). The latter technique has been employed in the study of the four planetary systems presented in Chapters 6 and 7. To derive chemical aboundances and the temperature/pressure profiles of planetary atmospheres, the observed spectra are compared to atmosphere models (e.g. Burrows et al. 2007; Fortney et al. 2013) or retrieval techniques can be employed (e.g. Line et al. 2012; Benneke & Seager 2012).

Although great progress has been made in recent years, with the current instrumentation the ground-based detection of a molecular species in an exoplanet atmosphere is incredibly challenging. The situation is slightly better when trying to probe the atmosphere from space, using for instance, the Hubble telescope or Spitzer. The latter, notably, observe in the NIR-IR regime where the planet-star ratio is lower and the limb darkening effect is less important.

A couple examples of successful studies where a specific molecule or atom was found are HD 189733 b where water absorption features were detected (Birkby et al. 2013), or the presence of potassium in XO-2 b (Sing et al. 2011).

Besides instrumental issues, the detection of molecules or in general the interpretation of planetary radius-wavelength variations is complicated by the possible presence of clouds and hazes in the higher part of the atmosphere that cause degeneracy in the interpretation of the data. A clear example is given by GJ 1214 b (Kreidberg et al. 2014), which shows a featureless spectrum.

Secondary eclipse

While orbiting its host star, a transiting planet not only passes in front of it but also behind, being therefore invisible for a short period of time. During this time laps the light observed is coming just from the star. Therefore, by subtracting the stellar light measured during occultation from the combined star-planet light measured right before and after the secondary transit, it is possible to obtain only the light reflected and emitted from the dayside of the planet.

The study of the dayside atmosphere of an exoplanet started in 2005, when the Spitzer spacecraft became fully functional, and allowed to perform high precision photometry in the mid-inftared bands. In the mid-infrared regime the planet-star contrast is higher, and it is therefore more suitable to detect the planetary signature in the combined star-planet light.

From the light reflected by the planets around occultations it is possible to measure the temperature of their day-side (e.g. Deming et al. 2005; Charbonneau et al. 2005; Lanotte et al. 2014; Zhou et al. 2015). Moreover, retrieving information on the day-side of a planet and comparing them with the incident flux received or the stellar activity can pose some constraint on the planet albedo and on the presence of a thermal inversion (Schwartz & Cowan 2015; Knutson et al. 2010).

1.2.3 Rossiter-McLaughlin effect

As a star rotates, the spectral lines that are emitted from different parts of its surface are seen slightly shifted with respect to the others. The light emitted by the portion of the star that is moving toward the Earth is somewhat blue-shifted, and conversely those parts of the star that are moving away from us appears slightly red-shifted. Besides a few cases, the stellar disc is not resolvable and therefore the blue and redshift of some of the photons coming from the star is percievable as a symmetric broadening of the spectral lines.

During a transit, the planet blocks out different parts of the stellar disk at different times. When the planet covers the region where the blue-shifted photons originate, the profile of the spectral lines is deformed and their centroids move towards redder wavelengths. The same, with opposite direction, happens when the planet crosses the opposite part of the star's disk. This outcome is known as the Rossiter-McLaughlin effect, and was first used by Rossiter (1924) and McLaughlin (1924) to measure the mutual spin-orbit inclination in eclipsing binary systems.

By properly measuring this apparent shift in the centroid of the spectral lines, it is possible to understand the relative motion of the planet with respect to the stellar rotation axis. Depending on the projected inclination between the planetary orbit and the stellar spin, the RVs during the transit shows a small anomaly assuming different shapes (see a couple of examples of different configurations in Figure 1.17).

To date a measurement of the spin-orbit alignment is available for nearly a hundred transiting planets. Most of those planets show an alignment. However, there are also several cases where the planets circle their star in a retrograde orbit (e.g. HAT-P-14, Winn et al. 2011), or appear to have an inclination around 90° (e.g. HAT-P-32, Albrecht et al. 2012).

The study of the orbit inclination via Rossiter-McLaughlin effect is particularly important in the

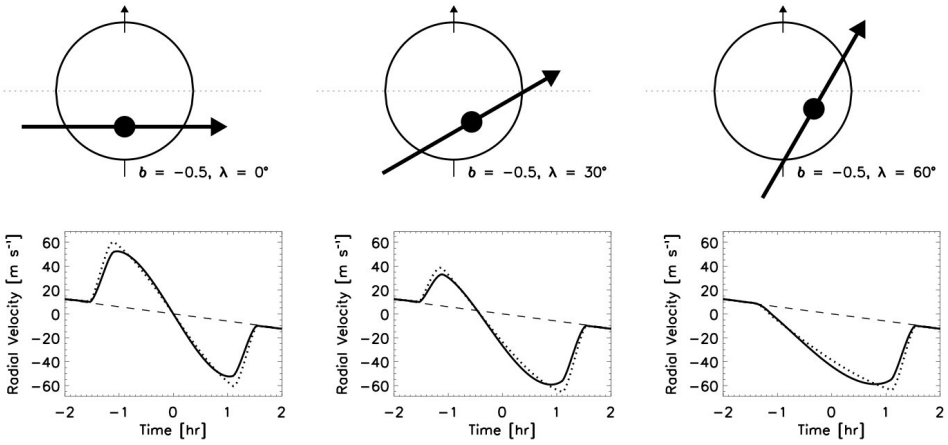

Figure 1.17: The figure form Gaudi & Winn (2007) shows three different examples of Rossiter-McLaughlin wave form according to the different spin-orbit inclinations. The dotted lines represent the curve without taking into account the limb darkening effect, while in the solid lines it is included.

context of planet migration and to disentangle the diverse dynamical theories that try to explain the position of very close-in and massive planets, the hot Jupiters, that could have hardly formed in situ.

1.2.4 False positive

Even if a light curve shows a typical transit shape, it is not necessarily true that it is due to the presence of a planet. There are indeed different false positive scenario that can mimic the transit shape. Here we briefly summarize the main cases. For a more comprehensive description and a false alarm probability study obtained from ground base transit survey, refer to Brown (2003), or to Désert et al. (2015) with probabilities obtained from the latest results of the *Kepler* satellite.

- *Grazing binaries*. If the two stars composing a binary system have a misaligned orbit with respect to our line of sight, they partially eclipse each other producing a transit that has a depth comparable to one due to a planetary sized companion (*a*) in Figure 1.18). The condition for this to happen is that the impact parameter b has to be within the difference and the sum of the two stellar radii: $R_1 - R_2 \leq b \leq R_1 + R_2$. However, it is possible to reveal the stellar identity of the transiting object by looking at the transit shape. Grazing binaries show typical V-shape curves. Moreover a high variation in the radial velocity and a spectral analysis can clearly rule out this kind of system as a false positive scenario.

- *Small stellar companion*. If the secondary star in a binary system is much smaller than the primary one, e.g. a M-dwarf or brown dwarf around an A, F or G-type star, or a main sequence star around a giant evolved one, the change in the observed flux during a transit can be of the order of $\sim 1\%$ (*c* in Figure 1.18). In this case the transit shape is identical to the planetary transit scenario, and spectroscopic measurements are needed in order to disentangle the enigma. Another way to the understand the nature of the system that requires only photometric measurements

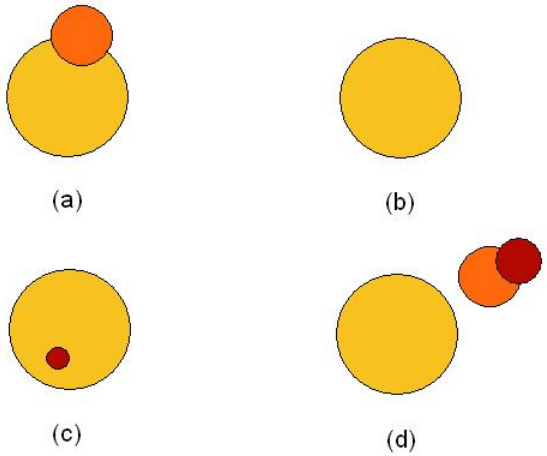

Figure 1.18: Scheme of common false positives: (a) grazing binaries, (b) statistical false positive or photometric variation, (c) binaries with a small companion, (d) binaries with a blended third star.

is to look for ellipsoidal variability (Stebbins 1920) by inspecting the out of transit part of the light curve.

- *Blend*. The light of transiting binary system can diluted by an unresolved third star. This third star can either be part of a hierarchical system to whom the binary system also belongs or just be a blending foreground or background star along the same line of sight (*d* in Figure 1.18). In this case the depth of transit light curve is diluted and comparable to a planetary transit one. As in the previous case, to disembroil the puzzle, it is possible to look for the typical V-shaped transit or for a large RV variation compatible with the transit period.

- *Statistical false positive*. A further misunderstanding can be given by photometric variability due to atmospheric variations, intrinsic variability of the star, or noise due to instrumental effects (*b* in Figure 1.18). In this case it is possible to rule out the planetary nature of the transit signal by looking at the transit shape and duration and verifying whether it is consistent with planetary sizes (Tingley & Sackett 2005).

1.3 Hot Jupiters

A hot Jupiter is an extrasolar planet with a mass similar or larger than Jupiter that orbits very close to its parent star. The proximity to the star is so that the planet is highly irradiated leading to very high effective temperature, hence the *hot* in the name.

Hot Jupiters (HJ) are gaseous planets with a massive atmosphere, but it is still not clear whether or not they harbor inner rocky cores. HJs revolve in very small orbits around their stars, having semi-major axis ranging from $\lesssim 0.01$ au (e.g. EPIC 201637175 b, Sanchis-Ojeda et al. 2015) up to nearly Mercury's orbit. Their periods are thus very short, normally below 10 days, reaching down to fraction

of a day (e.g. WASP-19 b, Hebb et al. 2010). Given their short average distance from the host star, most of the HJs are expected to be tidally locked to their host stars.

The overall occurrence of giant planets in planetary systems is between 5 and 20% depending on the stellar type and metallicity (Chabrier et al. 2014). There is a wide diversity in terms of composition and density; however there seem to be some general trends. Up to now, just a handful of HJs have been found to orbit around M-dwarfs, and the occurrence around metal poor stars is generally lower than for solar or super-solar metallicity (Johnson et al. 2010). Furthermore, a correlation is also found between the stellar metallicity and the planetary metal content (Guillot et al. 2006). A better probe for the metallicity of the planets may be their own masses: more massive planets are found to be less enriched than the lighter ones (showing the same trend seen in the gaseous planets in our Solar system, Miller & Fortney 2011).

HJs are a valuable exoplanet class. Despite their rareness with respect to small planets, they are relatively easy to detect and characterize. However, as just mentioned, their properties have a wide spread and are therefore a good benchmark to test planetary formation and evolution theories. To be valid a proposed theory should be able to explain the extreme cases given by these massive and close-in planets.

Giant planets are indeed an extremely important class of exoplanets when studying the formation and evolution of planetary systems. Among several reasons, one is that they shape the architecture of the planetary systems they are in. This is due to the fact that they form relatively fast and have large masses, making them responsible for the excitation of small bodies and the delivery of volatiles towards the inner parts of the planetary system. Another reason is given by the fact that, having accreted a non negligible fraction of the gas present in the disk during formation, studying their atmospheres can give constraint on the composition of the initial disk (Helled et al. 2014).

1.3.1 Jupiter-like planet formation

Planets are thought to form during the same processes that give birth to their parent star. A proto-planetary disk is formed from the initially spherical gravitational collapse of a cold molecular cloud due to the initial non zero angular momentum. The matter with the lowest angular momentum forms a central body called protostar, which contains a large fraction of the mass of the cloud, while the circumstellar disk retains most of the angular momentum. Planet formation occurs using the material of the circumstellar disk where the dust grains coaugulate, forming pebbles and larger sized rocky clumps called planetesimals. A schematic illustration of the phases of star-planet formation is shown in Figure 1.19.

For the purpose of this thesis, a brief introduction on the widely accepted star formation theory is sufficient. To a reader interested on the early stages of disk formation the following review on the topic is suggested: Li et al. (2014).

The various theories of planet formation that aim to explain the birth of hot Jupiter-like gaseous planets can be divided, to first order, in two different categories: the so called '*gravitational instability models*' and the '*core accretion models*'. Even though there is still no incontrovertible proof to completely rule out theories belonging to the first group, nowadays the latter are preferred. Nonethe-

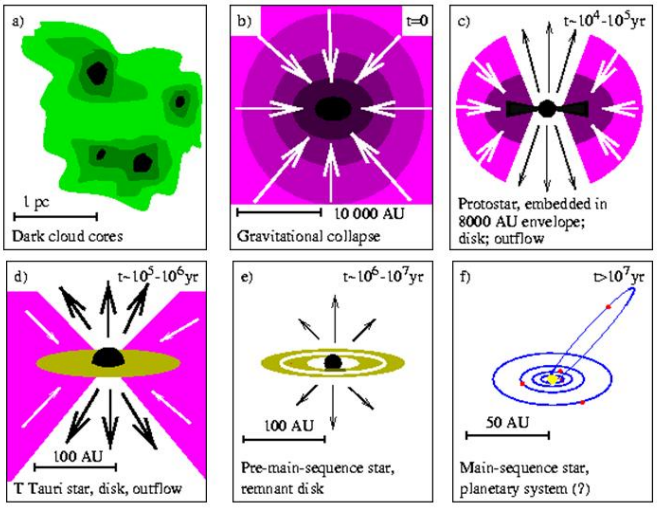

Figure 1.19: A schematic representation of the phases of star and planet formation. Illustration by Hogerheijde (1998).

less it may also be possible that both the methods contribute to the formation of the diverse types of planets that are observed.

Gravitational instability

The first scenario explains the formation of giant planets due to gravitational instabilities within the proto-planetary disk.

The planets are thought to form from the fragmentation of the disk in one or more local clumps due to a local gravitational instability. A well established criterion to determine if a disk is stable or not is the *Toomre criterion* (Toomre 1964):

$$Q = \frac{c_s \Omega}{\pi G \sigma_s}, \tag{1.24}$$

where c_s is the sound speed, Ω is the angular velocity at a certain distance and σ_s is the surface density of the disk. If Q >1 the disk is stable, otherwise if Q <1 it is unstable.

The main characteristic of this fragmentation scenario is that planets form relatively fast (in about 1000 yr) in the outer part of the disk. This is mainly due to the fact that the Toomre criterion is more likely to be satisfied at large radii, where the temperature and therefore also the sound speed are lower.

Another important quantity it is necessary to take into account for a fragment to form is the cooling time, which has to be efficient enough not to impede the collapse.

Given the formation of fragments, the disk instability scenario can be divided in three steps (Decampli & Cameron 1979). The first is the pre-collapse evolutionary stage: the fragment is cold, very extended, with a radius around an au large and composed mainly by molecular hydrogen.
After a certain time, ranging from 10^3 to 10^6 yr depending on several different physical phenomena and initial condition, the molecular hydrogen starts to dissociate, resulting in a collapse of the fragment. Finally, there is a long term evolution where the planet formed contracts and may migrate either

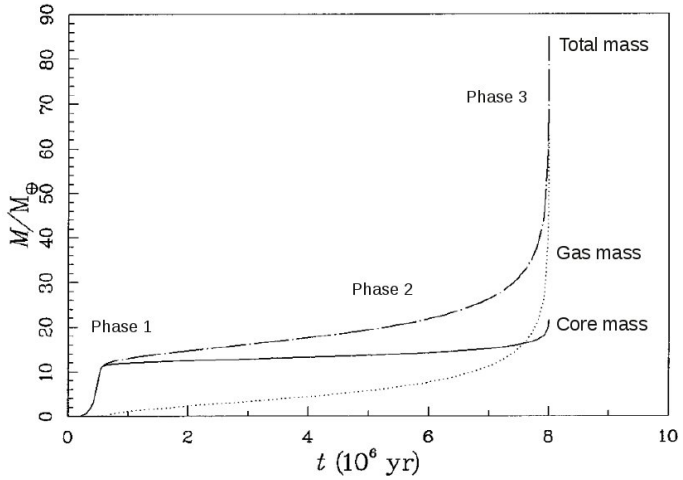

Figure 1.20: The figure from Pollack et al. (1996) describes the accretion rate of a proto-planet as a function of time. The dotted line refers to the gaseous component, the solid line to the accretion of the rocky component, while the dashed one is the total accretion rate of both solid and gas.

inward or outward.

The disk instability formation efficiency depends on several parameters, such as opacities, but there is still no agreement on how, and to what extent, they influence the processes (Meru & Bate 2010; Mayer et al. 2007).

The planets formed via disk instability have a wide range in metallicity, going from sub to super-stellar. The metal content of planets can be explained mainly in three different ways: proto-planetary clumps tend to form in the spiral arms of the disk, where the density is higher and dust grains are more concentrated and therefore more easily accreted (Boley & Durisen 2010). Another way to enrich the planets is to accrete planetesimals that are captured mostly in the pre-collapse phase when the fragment has a large extension. Furthermore, if a planet migrates inward, it may lose part of the external envelope composed mainly of H and He, resulting in a metal rich planet (Nayakshin 2010).

The presence of a rocky core in the inner part of a giant planet is not necessarily a symptom of a diverse formation mechanism. Indeed the planetesimal that are inside or captured by the fragment, can sediment and coagulate in the central part of the proto-planet giving birth to a rocky core (Helled & Schubert 2009).

Core accretion

The core accretion formation processes can be divided in three main steps: initially a rocky core is formed through planetesimal coagulation, secondly this core starts to accrete gas while still accumulating solids, and eventually it will accrete only gas in a runaway process.

The core accretion model assumes that planetesimals already exist in the proto-planetary disk, but does not consider how they form. In the first phase, the planetesimals and the dust grains coagulate and start to create an initial rocky core that keeps growing accreting other solid material. The core

accretion rate is given by:

$$\frac{\mathrm{d}\,\mathrm{M_{solid}}}{\mathrm{d}\,\mathrm{t}} = \dot{\mathrm{M}}_{\mathrm{core}} = \pi\,\mathrm{R}^2\,\Omega\,\sigma_{\mathrm{s}}\,\mathrm{F_g}, \tag{1.25}$$

where $\pi\,\mathrm{R}^2$ is the cross section, and describes the capture value of the proto-planet, which changes and grows as the planetesimals and the gas are accreted and accumulated. Ω is the orbital frequency, σ_{s} is the surface density and $\mathrm{F_g}$ is the gravitational enhancement factor. σ_{s} is a crucial parameter as the larger the density is, the faster the proto-planet accretes.

As the core grows, it starts to retain a gaseous envelope. The growth of the atmosphere is initially slow, till it reaches a turning point. When the mass of the envelope becomes comparable to that of the core $\mathrm{M_{core}} \sim \mathrm{M_{env}}$, it begins a fast contraction. The runaway phase is reached and the gas accretion rate raises abruptly (see Figure 1.20).

The gas accretion goes on till the gas is present in the disk, or until the planet creates a gap around itself, eventually running out of available material to incorporate (Lissauer et al. 2009).

The basic core accretion model, as presented for instance in Pollack et al. (1996), predicts a very long timescale to create a gas giant and a final mass of the rocky core of about $10\,\mathrm{M_\oplus}$. There are however different mechanism that can speed up the process, such as type II migration and disk interactions (Alibert et al. 2005) or opacity reduction due to the coagulation and settlement of dust grains (Movshovitz et al. 2010). If the latter scenario is assumed, the final rocky core mass is not fixed and may as well be very small depending on the place where it is formed.

The final properties of the planet formed via core accretion can be very diverse, and depend on the different initial conditions, for instance the values assumed for σ_s or the position in the disk where they formed. Although the first core accretion models were inclined towards metal rich planets, nowadays theories do not favor any enrichment a priori but several different possibilities, including sub-stellar metallicity, are possible. Moreover, the core accretion models do not predict a specific mass for the inner rocky core and even if it is initially massive, it can be eroded in time and result in a final core-less giant planet.

Chapter 2

Observations and Instruments

In the context of finding new planetary systems and enlarging our knowledge of their populations, presented here are two surveys that use the transit method to detect planets: the ground based HAT-South survey and the space based *Kepler* mission (Section 2.2 and 2.3 respectively).

The instruments, data processing and results of the HATSouth survey are introduced. In particular, the discovery of HATS-15 b and HATS-16 b, among the more than a dozen of planets found by the survey, will be presented in the next chapter of this thesis.

The *Kepler* spacecraft has produced, and still does, thousands of planetary candidates. We describe the mission and an ongoing project started with the aim to confirm a selected sample of its candidates. The instruments and goals are taken into consideration, and the main results of the project are presented. Amid the confirmed planets, of particular relevance for this work is Kepler-432 b whose confirmation is described in Chapter 4.

Another aim of this thesis work is to provide improved and reliable measurements of planetary sizes and masses, and gain some information on the planetary system characteristics. The goal is to create a set of planetary systems that have been self-consistently reduced and analysed, which can be used as a benchmark for population synthesis study or to test planet formation theories. In the last section of this chapter, an ongoing project aimed at characterizing already confirmed planetary systems through an extensive photometric follow-up campaign is described. The instruments and techniques to perform the observations of the transiting planets are presented, as well as a brief description of the reduction and analysis of these data. Within this project lay three of the works described in the following part of the thesis. In particular the characterization of six planetary systems: HAT-P-16, HAT-P-23, WASP-21, WASP-45, WASP-46, and WASP-48.

2.1 From a light curve to the planet

In this section are summarized the steps that lead to the discovery of a new planetary system starting from the collection of the photometric data, their reduction and analysis and the final confirmation of the candidate through follow up observations.

The quest for planets via the transit method starts with the continuous acquisition of photometric frames during a time lapse of the order of a few to several months. The photometric frames are usually collected with small wide field telescopes in order to gather the light of the largest number of stars as

possible. Before scientific information are extracted from the observed frames, the images are calibrated. Bias and dark images are subtracted from the science ones in order to account for the read-out noise and possible bad pixels of the CCD. Flat-fields are also applied to correct for the different pixel response and to eliminate the signature of possible impurities present along the light path.

Once the scientific images are properly calibrated the photometry of each star is usually extracted via aperture- or PSF- (point spread function) photometry. In every image the number of photons collected from a specific region of the CCD delimited by a ring or by a gaussian-like shape is counted. The light curve of each star is then the variation of the photon count with time. The light curves so obtained are however subject to trends due to instrumental effects or, in case of ground based surveys, to atmospheric variations. It is therefore important to properly take into account these effects and detrend the data. Different algorithms can be used for this purpose, such as SysRem (Collier Cameron et al. 2006), the Trend Filtering Algorithm (TFA; Kovács et al. 2005), or a procedure for filtering high-frequency modes (Barge et al. 2008).

Once the light curves are properly extracted and detrended, they are searched for a periodic signal that could be due to a transiting planet. In this first phase the transit dip due to a planet passing in front of its host star is generally modeled as a simple square box. If a periodic signal consistent with a planet is found, the light curve is phase folded according to that period and is then properly modeled to obtain a first estimate of the planet's properties and orbit ephemeris. If the spectral class of the star is already known, it is possible to give a first estimate of the planet's size by assuming a mass-radius relation for the star. Otherwise a solar-like radius might be assumed leaving the proper measurement to further studies.

To confirm the planetary nature of the transiting object, and constrain the system's orbital and physical parameters, follow-up observations are required. If the spectral type of the star in not known, low resolution spectroscopy can provide the necessary information, discerning also between a main sequence star or an evolved one. As mentioned in Section 1.2.4, there are several astrophysical scenarios that can mimic the transit of a planet. Follow-ups with different techniques can provide information on this regard: photometry, spectroscopy or high resolution imaging (for some examples see Sections 2.2.1 and 2.3.2).

Several high-resolution spectra are required to obtain the radial velocity (RV) of the parent star. From the RV variations with the orbital phase it is possible to measure the planet mass and the eccentricity. In the cases where the initial light curve is not of high precision (as it is usually the case for ground based survey) subsequent photometric follow up can provide the proper and precise measurement of the ephemeris and of the photometric properties of the system (e.g. planet and star size, and inclination of the system with respect to the observer's sight). High resolution imaging is particularly useful in ruling out false positive scenarios by checking that the transit photometric signal in not diluted by a previously unresolved foreground/background star along the same line of sight.

All the required information are gathered in this way, and it is then possible to announce the discovery of a new extrasolar planet.

Figure 2.1: Position of the three sites of the HATSouth facilities: the Las Campanas observatory (LCO), the High Energy Spectroscopic System site (HESS) and the Siding Spring Observatory (SSO). Figure from Bakos et al. (2013).

2.2 *HATSouth*

As mentioned in the previous Chapter (Section 1.1.4), the probability of a planet to transit its host star is tiny, and depends on the orbital inclination of the planetary system with respect to our line of sight. To identify a large number of transiting exoplanets, it is therefore necessary to monitor a substantial number of stars using a large scale survey. In this section, I will describe the HATSouth survey, thanks to which we were able to discover the two massive hot Jupiters HATS-15 and HATS-16 presented in Chapter 3.

The main scientific goal of the HATSouth network is to discover and characterize a large number of extrasolar planets using the transit detection method. In particular, given the capabilities of the survey, we are looking for detecting planets with long periods, greater than 10 days, and reach out to small planetary radii of the order of Neptune/Super-Earth size. The survey is operated by the combined effort of four institutes: Princeton University (PU), the Australian National University (ANU), the Pontificia Universidad Católica de Chile (PUC) and the Max Planck Institute for Astronomy (MPIA).

HATSouth is a network of six identical, fully automated wide field telescopes, and is the first ground base survey capable of continuous 24h coverage. This is made possible thanks to the location of its facilities, that are spread among three different sites of the Southern hemisphere nearly 120° apart from each other. Specifically, one station is located in Namibia at the HESS (High Energy Spectroscopic System) site, one in Australia at the Siding Spring Observatory (SSO) and the last one in Chile at the Las Campanas observatory (LCO). Figure 2.1 shows the exact location of the facilities.

Every site hosts two units, and each one is composed of four identical telescope tubes fixed on the same heavy equatorial fork mount. Each telescope is a Takahashi hyperbolic astrograph with a diameter of 18 cm, capable of a field of view (FOV) of roughly $4° \times 4°$. The four telescopes on the same mount have a different FOV that overlap along the edges resulting in a combined mosaic of $8.2° \times 8.2°$ in total. Each tube is equipped with an Apogee U16M 4000×4000 CCD detector that has a resolution of 3.7 arcsec per pixel, and a Sloan-*r* filter. The range in luminosity covered by the HAT-

South facilities ranges from 8 to 17 magnitude in the visible band. However the peak of sensitivity of the survey is around 13-14 magnitude: this makes it possible to monitor fainter stars (like M-dwarfs) that are not detected by the other ground-based surveys.

The observations are carried out with a cadence of 4 minutes for an average observing time of 10 hour per night per site (considering a monitoring period of two years). The observations are fully automated: the units are capable to self-operate by starting the CCD cooling roughly an hour before the sunset, opening the dome, start the calibration, autofocus and perform astrometric measurements to stabilize the position of the sources on the detector. Thanks to the continuous on-site monitoring of the weather conditions, the operations automatically stop in case of bad weather. For further information on the instrumentation and technical details of the survey, I refer to the description drawn by Bakos et al. (2013)[1].

Since the beginning of the operation in 2010, more than 60 fields have been monitored for a period that lasted an average time of 3 months (up to 6 months for some selected fields). So far we have collected more than 2.7 million[2] science frames. Each observed raw frame is properly calibrated via dark and bias subtraction and flat-fielding. Difference in the hardware and observing conditions are also properly taken into account by the reduction pipeline. The light curves of the stars in the field are then obtained performing aperture photometry (Bakos et al. 2010). After the light curves are being detrended thanks to a TFA (Kovács et al. 2005), planetary-like periodic signals are searched for with a Box-fitting Least Squares algorithm (BLS; Kovács et al. 2002). The light curves that we extract from the frames observed in each site have a very good precision. To give an example, for a V $\sim$12 mag target, the rms (root mean square) is lower than 1%; while for a fainter one of about V $\sim$14 mag the average rms is lower than 2% (e.g. HATS-1 and HATS-8 in Figure 2.2).
Thanks to several improvements, both in the hardware and in the software, the candidate rate is increasing year by year reaching now a total number of more than 1200 candidates.

2.2.1 Follow-ups

Photometric follow-ups

To confirm our candidates, we carry out extensive photometric and spectroscopic follow-up observations. These allow us to determine if the mass and radius of the observed objects are in the planetary regime, and to discard all the possible sources of false positive.

High-precision photometric follow-ups are important in determining the precise orbital parameters of the exoplanetary system (orbital inclination and the ephemeris) and in measuring important properties such as the planetary radius and the stellar density. Photometric follow-ups are also important to discard some false positive scenario by looking at the light curve shape. Moreover, by comparing transit observations obtained at diverse bandpasses, it is possible to check whether the transit depths are consistent with a planetary body. Indeed, a significant difference among the values measured at different wavelengths would indicate that the transiting object has a stellar nature (eclipsing binary).

[1] G.A. Bakos is the Principal Investigator of the HATSouth survey
[2] As of 15 July 2015

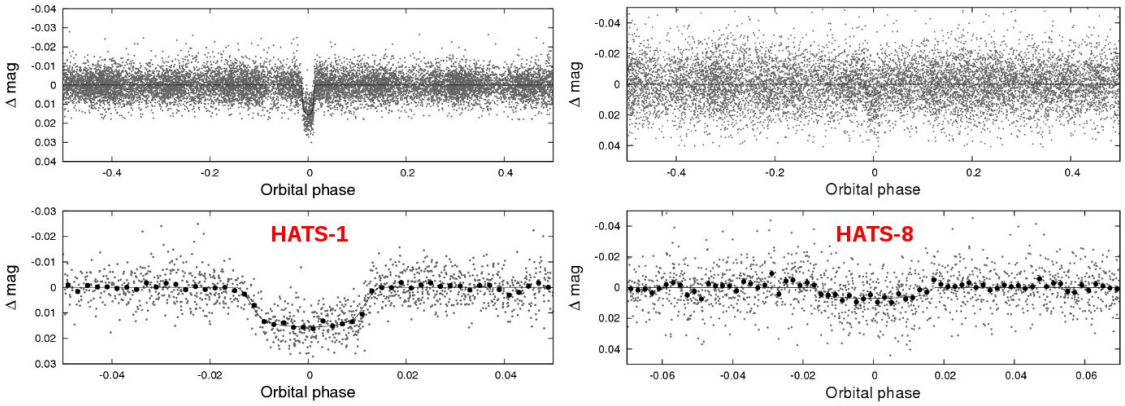

Figure 2.2: Examples of typical light curves from the HATSouth facilities. *Left:* targets with magnitude around V = 12 mag (e.g. HATS-1, Penev et al. 2013) have a rms lower than 1%. *Right:* fainter targets with V = 14 mag (e.g. HATS-8; Bayliss et al. (2015)) have a rms around 2%. In both the upper panels is presented the unbinned light curve phase folded with the planetary period (3.45 and 3.58 days for HATS-1 and HATS-8 respectively). In the lower panels is shown a zoom at the phase around the transit; dark filled points represent the binned light curve.

To perform these observations, we use an array of small- and medium-size class of telescopes, which are located at different sites in the southern hemisphere (see Table 2.1, right column, for an overview of the different telescopes and instruments used). Of particular note, is the GROND instrument, a seven-channel multi-band imager (see Section 2 in Chapter 7 for a brief description of the instrument). GROND allows to simultaneously monitor transit events in different bands, providing information about the planetary atmosphere or starspot characteristics in case of anomalies (small bumps) in the transit light curves (e.g. HATS-2, Mohler-Fischer et al. 2013). Another follow-up telescope worth of mention is the PEST 0.3m, operated by an amateur astronomer in western Australia. Although the precision of the telescope is not high (average rms of 1%), it is very efficient in obtaining good measurement of the ephemeris of the candidates that can then be used to plan high-precision photometric and spectroscopic follow-up.

Spectroscopic follow-ups

As far as it concerns the spectroscopic follow-up, we can divide them into two steps: reconnaissance and high-precision radial velocity. The first are obtained through low resolution spectrograph such as WiFeS and DuPont, and provide a first spectral classification of the star. With these spectra we are also able to rule out some possible false positive scenario including spectroscopic or grazing binary systems.

After this first stage, the candidates that have not been discarded as false positive undergo high precision spectroscopic measurements, which provide the necessary information to constraint the masses and the orbital parameters of the system (see Table 2.1, left column, for a list of the different spectrographs used).

Table 2.1: Telescopes and instruments used for the spectroscopic and photometric follow-ups of the HATSouth candidates

Spectroscopic observations			Photometric observations		
Keck 10m	HIRES	Mauna Kea	MPG 2.2m	GROND	La Silla
Subaru 8.2m	HDS	Mauna Kea	FTS 2.0m		SSO
Magellan 6.5m	PFS	LCO	Danish 1.5m	DEFOSC	La Silla
AAT 3.9m	CYCLOPS	SSO	Swope 1.0m		LCO
ESO 3.6m	HARPS	La Silla	LCOGT 1.0m		LCO
NOT 2.56m	FIES	La Palma	CTIO 0.9m		CTIO
ANU 2.3m	WiFeS	SSO	Perth 0.6m		Perth
MPG 2.2m	FEROS	La Silla	PEST 0.3m		Perth
Euler 1.2m	Coralie	La Silla			

2.2.2 The FEROS spectrograph

Among the instruments used by the HATSouth collaboration to perform the RV follow-up, the FEROS spectrograph is very efficient. This instrument was used to obtain most of the RV measurements that brought confirmation of the two planets HATS-15 b and HATS-16 b presented in Chapter 3.

FEROS (Fiber-fed Extended Range Optical Spectrograph) is an echelle spectrograph mounted on the 2.2 m MPG[3] Telescope at the ESO[4] La Silla observatory (Kaufer & Pasquini 1998; Stahl et al. 1999). The instrument is equipped with a 2000×2000 thinned CCD with a resoultion of 15 μm per pixel and is capable of a wide wavelength coverage in the optical regime, which goes from 3700 Å to 8600 Å. The high average resolution of $R = 48\,000 \pm 4\,000$ is achieved by means of an image slicer. FEROS can count on a very good stability thanks to its instrumental design, which does not include remotely movable parts, and its location in an environmental chamber that maintains constant temperature, humidity and barometric pressure.

Simultaneously to the science observations, it is possible with a second fibre to obtain a second spectrum to properly calibrate the science one. For the HATSouth observations the wavelength calibration are done using a ThAr lamp.

For the last two years, the reduction of the data and the analysis of the spectra, with the aim to obtain precise RV measurements, is performed utilizing a new pipeline especially developed for the echelle spectrographs of the La Silla observatory (FEROS and CORALIE) by colleagues of the HATS collaboration (Jordán et al. 2014; Brahm et al. 2015). The pipeline has already proved to have optimal performances, allowing to reach a precision in RV of few m s^{-1} for the brighter targets and a precision of 20-30 m s^{-1} for faint ones (V $\sim$14 mag). For a brief description of the pipeline, see Section 2.1 Chapter 7.

In the recent months we adopted a very efficient strategy to follow-up the HATS candidates: the observations taken during the night are reduced straightaway during the subsequent day allowing us to exclude from the target list false-positive candidates, which show double peaked cross-correlation

[3]Max Planck Gesellschaft
[4]European Southern Observatory

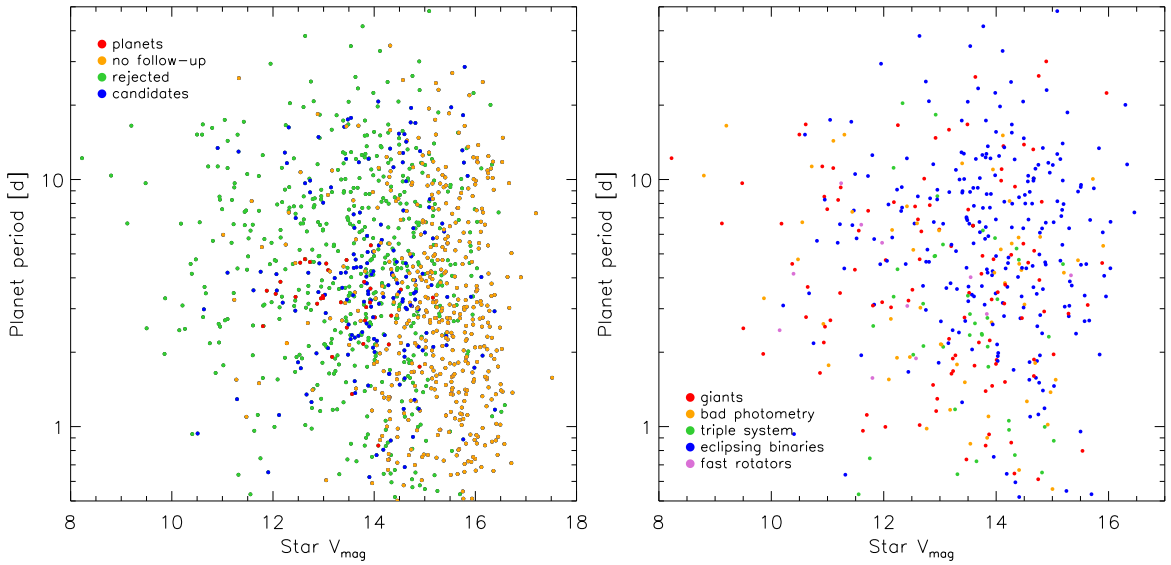

Figure 2.3: HATSouth candidates in a period–visible magnitude diagram. *Left*: the different colors represent the confirmed planets (red), those that have already been rejected as false positive (green),candidates that have not been followed up yet (yellow) and candidates in need of more observations to be properly confirmed (blue). *Right*: Only the rejected candidates are shown in this panel divided according to the false positive type. Specifically there are evolved star (red), candidates with bad photometric data (yellow), triple systems (green), eclipsing binaries (blue) and fast rotators (pink).

function (CCF) or have a RV variation of the order of few km/s. Moreover, we can properly determine the best observing time for each candidate, in order to recover an appropriate phase coverage. With this strategy, in a single observational run (lasting an average time of 10-12 days), we are able to confirm a hot-Jupiter planet with a period $\lesssim$ 5. Since the beginning of the follow-up observations, more than 200 candidates have been followed up at least once with FEROS. Roughly half of the candidates are still under analysis, as they need few more observations to properly constrain their properties. Instead, the other half have been discarded either because, within the experimental uncertainties, no periodic signal in the RV was measured or because of a clear sign of the presence of a stellar companion in the system.

2.2.3 The HATS planets

Starting from 2010, the number of the planetary candidates which were found by the HATSouth survey, have seen a constant increase (at the time this thesis being written, the number has already exceeded one thousand units). Nearly 60% of the candidates have already been followed up at least once, and, among them, roughly 30% of them have survived, as they were not rejected as a false positive (see left panel in Figure 2.3). By looking at the left panel in Figure 2.3 one may acknowledge that, thanks to the good sensitivity of the HATSouth instruments, the candidates have a large spread in the magnitude of the possible host star; furthermore, as a result of the 24-h coverage, with just $\sim$3

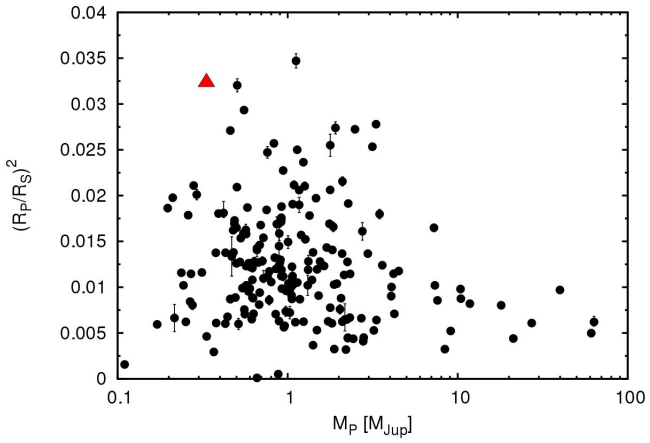

Figure 2.4: Transit depth–planetary mass diagram of the known transiting planets. The HATS-6 system is highlighted with a red triangle (Hartman et al. 2015).

months of observations, we obtain planetary candidates with orbital periods up to 30-40 days.
The HATSouth collaboration has discovered 16 planet so far. Their characteristics span a large region in parameter space, ranging from small planets down to $\sim 38\,M_\oplus$ (HATS-8 b Bakos et al. 2015) to massive ones of three times Jupiter's mass (HATS-16 b see Chapter 3). Among them, taking into account the irradiation received from the host star, some planets such as HATS-5 b (Zhou et al. 2014) are somewhat inflated, while others are compact (e.g. HATS-9 b, Brahm et al. 2015).

Among out candidates, two planets are particularly interesting and deserve mention: HATS-7 and HATS-8 (Bakos et al. 2015; Bayliss et al. 2015). These planets are two super-Neptunes orbiting a K and a G star respectively, and are, together with few more other planets, among the smallest planets detected from ground based surveys. Thanks to the good sensitivity in the fainter regime with respect to other ground-based surveys, and good photometric precision, we detected several candidates around M dwarf stars. An example is given by HATS-6: a planetary system composed of a Saturn-like planet orbiting around an M1 dwarf in roughly 3 days (Hartman et al. 2015). Giant planets like HATS-6, which orbits around an M dwarf, have deeper transits with respect to their analogues orbiting bigger stars, as shown in Figure 2.4. Given the high radii ratio, this planet is a very good candidate for further follow-up and transmission spectroscopy to study the planetary atmosphere. The HATSouth survey, being able to detect several M dwarfs, can therefore provide good targets to be followed up with new instruments that are, or will soon be, available both on the ground, such as Espresso or CARMENES (Pepe et al. 2010; Quirrenbach et al. 2014), or in space e.g. MIRI or NIRSpec (on the James Webb Space Telescope, Wright et al. 2003; Bagnasco et al. 2007).

2.3 *Kepler*

Kepler is a space-based mission, conceived within the search for extrasolar planets framework. Its primary goal is to detect a large number of transiting exoplanets, particularly the small sized ones around solar-like stars, in order to determine the frequency of Earth like planets and characterize the

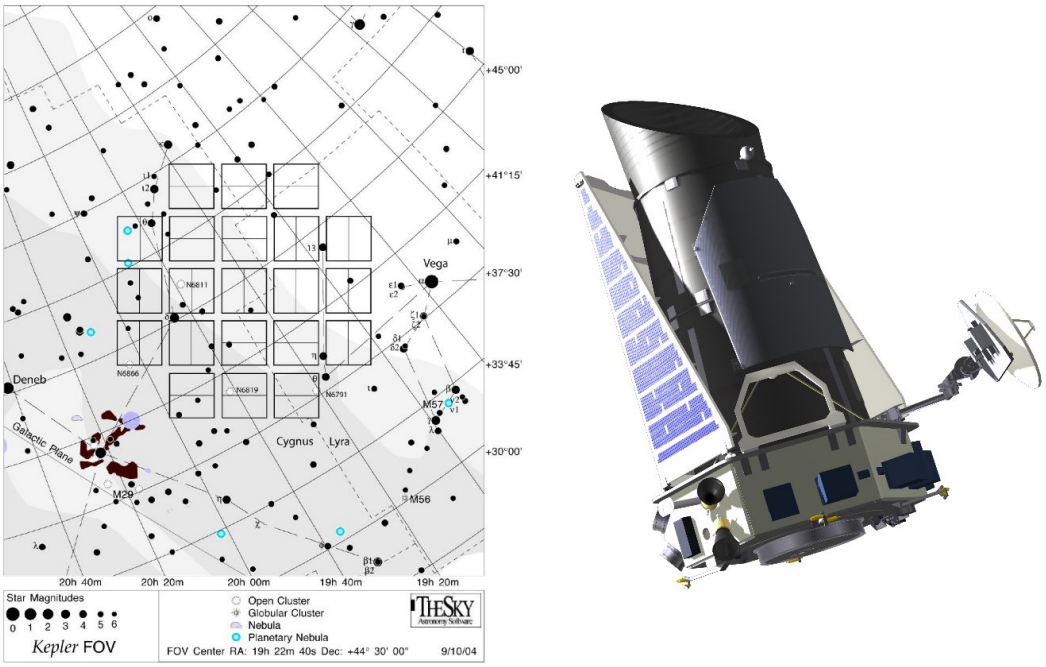

Figure 2.5: *Left*: *Kepler*'s field of view, near the Cygnus constellation and slightly above the galactic plane. *Right*: cartoon image of the *Kepler* satellites. Image credit NASA/JPL.

distribution of exoplanets in terms of their properties, such as radii, period and masses. The satellite was launched on March 2009 and after reaching an Earth-trailing heliocentric orbit, it continuously monitored the same portion of the sky, in the Cygnus-Lyra region (the field of view is centered at RA=$19^h22^m40^s$ and Dec=+44°30′00″, see Figure 2.5), for almost four year before a mechanical failure occurred.

Kepler is a photometer coupled to a Schmidt telescope, equipped with a 1.4 m primary mirror, and has a FOV of 105° × 105°. The only instrument installed on the spacecraft is an array of 42 back-side illuminated CCDs, each composed by 2200 × 1024 27 μm pixels (Borucki et al. 2004).
The observing strategy consists of taking images slightly out of focus (the point-like sources are defocused to reach ∼10 arcsec) with an integration time of nearly 30 minutes. For a sub-set of targets, a shorter integration time is used, in order to provide the necessary frequency to allow asterosysmic studies to be carried out.

Given the immense amount of data produced by the satellites, only the photometry of a sample of specifically selected stars is transmitted and stored on Earth (roughly 3-5%, Borucki et al. 2008). The sample consist of a total number of 100.000 main sequence stars, whose magnitude in the visible stands in the range of V = 9–16 mag. One of the primary goals of the mission is to produce a statistically significant number of planetary systems and study the variety of their architectures. This allows to understand how common is the Solar system in the Galaxy. Therefore, the selected stars belong to the spectral classes M, K, G and F. The massive stars were excluded because the possible transit of a terrestrial-like planet would have been too shallow to be detectable, considering Keplers nominal precision. Before the launch of the satellite, all the stars in the Kepler FOV with V $\lesssim$ 14 mag were

photometrically observed in different bands, thus providing the Kepler Input Catalog (KIC, Brown et al. 2011), from which the final targets were selected.

In spring 2013, after the failure of two reaction wheels, the spacecraft could not maintain for long terms its pointing stability anymore, which was fundamental for obtaining the ultra-high-precise photometry that yielded thousands of planetary candidates. However, considering the great successes in terms of planet discoveries achieved in the previous years, a new program (named *K*2), with a new observing strategy, was undertaken. Even though the main goal of the *K*2 program is still pointed towards finding new planetary systems with the transit technique, several other side projects, from microlensing to extragalactic science (Gould & Horne 2013; Edelson et al. 2015), have been included and will be performed in the coming months. The pointing stability of the *Kepler* space telescope can be reestablished thanks to the solar wind, but this limits the observations towards the ecliptic-plane directions only. With this new strategy, *Kepler* is currently observing selected fields along the ecliptic plane for roughly 80 days, providing almost the same performances reached in the previous mission (Howell et al. 2014). After only six months from the release of the data of the first field, numerous interesting planetary discoveries have been already announced, e.g. Crossfield et al. (2015b); Sanchis-Ojeda et al. (2015); Armstrong et al. (2015).

2.3.1 Confirmation of the candidates

A first skimming of the thousands of candidates produced by the satellite is done right after the data are reduced, through an automatic pipeline written by the *Kepler* team. In brief, the position of the photo-centroid is measured both inside and outside the transit region: a displacement in its position is symptomatic of the presence of an eclipsing binary close to the line of sight of a brighter foreground star (Batalha et al. 2010). The same pipeline separately measure the transit depth of the even and odd transit signals, and compare them looking for a significant difference, a signature of an eclipsing binary system with a period of double of the one of the supposed planet (Jenkins et al. 2010).

The candidates that pass the first automatic tests are officially considered as planetary candidates and are inserted in the *Kepler Object of Interest* catalog[5] and are denominated with a KOI prefix.

In order to unequivocally prove the planetary nature of the KOI's candidates, further observations and analysis are indispensable. One of the best ways to confirm a planet, and obtain almost all the properties of the new planetary system, is to perform systematic spectroscopic observations of the host star and, by measuring its RV, obtain the mass of the planet. Another very powerful method to confirm planets and measure their mass is the TTV technique (see Section 1.1.5), but it can only be used for multi-planetary systems.

Many of the smaller *Kepler* planetary candidates are orbiting around faint stars and exhibit very shallow transits. It is therefore very arduous and expensive in terms of highly competitive telescope time to confirm them via spectroscopic and photometric follow up. Statistical validation, in this case, can be a powerful tool to prove the planetary nature of small, and supposedly rocky candidates and reach out to Earth or even Mercury-sized objects. Examples of validation techniques that employ

[5]The catalog can be found at: http://exoplanetarchive.ipac.caltech.edu/cgi-bin/TblView/nph-tblView?app=ExoTbls&config=cumulative

Bayesian methods and require high-spatial resolution observations are PASTIS or BLENDER (Díaz et al. 2014; Torres et al. 2011). A recent and interesting example of the employment of these validation techniques is given by Kepler-452 b, the so called older cousin of the Earth', which was validated by Jenkins et al. (2015).

2.3.2 MPIA-CAB follow-up campaign

In this context lies the project of the MPIA-CAB[6] collaboration, that aims to confirm a sample of specifically selected *Kepler* candidates, following them up by means of the Calar Alto Observatory (Spain) facilities, mainly using the AstraLux lucky imaging camera and CAFE spectrograph.

Candidate selection

Among the more than four thousands candidates identified by the *Kepler* spacecraft, we selected a suitable set of targets according to the capabilities of the two instruments used:

- A first criterion in the selection was the magnitude of the targets according to the AstraLux specifics. The instrument is able to detect sources up to $K_\mathrm{p} \sim 20$ mag, therefore in order to reach a magnitude contrast of at least 4-5 magnitudes (necessary to rule out diluted eclipsing binary), we set a maximum limit of $K_\mathrm{p} \lesssim 16$ mag.
- The CAFE spectrograph has a RV precision of the order of 20 m/s. Therefore we selected our target sample to have an expected RV amplitude greater than $2-3$ times this limit. Thus those planets that presented a deeper transit signal were prioritized with respect to the others.
- Moreover, in order to obtain the precision necessary in the RV and taking into account the CAFE's capabilities, we set the upper magnitude limit to $\mathrm{Kep_{mag}} \lesssim 14$.
- Our initial sample also included a set of candidates with expected small sizes that were not meant to be followed up with the CAFE spectrograph but just with the AstraLux camera with the purpose of providing upper limits on the false positive alarm and be then validated with other methods (e.g. the planetary system Kepler-37, Barclay et al. 2013).

The final sample of selected *Kepler* candidates is composed of 233 planetary systems hosting 392 bona-fide planets.

AstraLux

A possible cause of a false positive, is the presence of a background star along the line of sight that dilutes the light of a binary system mimicking a planetary transit. This scenario is likely to occur due

[6]Max Plank Institute for Astronomy - Centro de AstroBiología

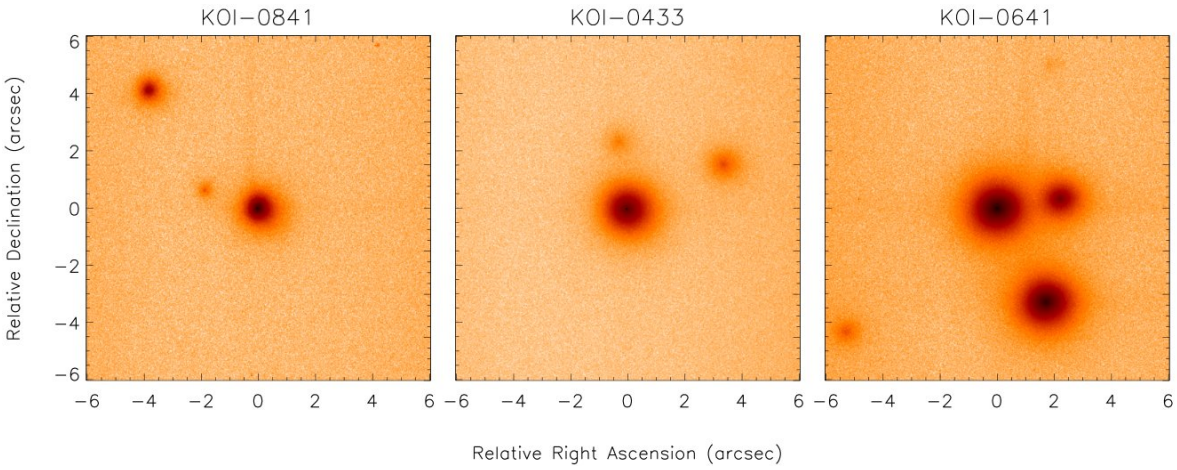

Figure 2.6: High-resolution images of three of the KOIs observed with AstraLux. The images have a FOV of $12'' \times 12''$ and the *Kepler* candidate is shown at the center of the image, while the companions are from 0–3 arcsec to 3–6 arcsec farther away. In the images north is up and east is left. Figure from Lillo-Box et al. (2012).

to the observing strategy used by *Kepler*: in order to obtain the required precision in photometry, the light of each star is spread over several pixels. This may cause the overlap on the same pixels of the light of two different sources lying very close on the sky.

We investigated this possible scenario by obtaining high resolution images of the candidates in our sample. To pursue this goal we used AstraLux, a Lucky Imaging camera mounted on the 2.2m telescope at the Calar Alto observatory in Spain. For a complete description of the instrument, please, refer to Hormuth et al. (2008).

The initial sample of 233 *Kepler* planetary system candidates were observed during the visibility window of the *Kepler* field (from May to September) from 2011 to 2013. The reduction was performed with the pipeline provided for the instrument by Hormuth (2007), and using the 10% selection rate for the frames. The images are then searched for the presence of a possible close-by source to our targets using a semi automated pipeline appositely written for this instrument (by J. Lillo-Box), and in the case of a positive outcome, the relative magnitude is measured with the IDL's *aper* routine.
Of the initial sample we found that nearly 33% of the candidates have a companion at less than 6 arcsec, and almost half of them show a companion closer than 3 arcsec (see Figure 2.6 for examples of candidates with close companion). Within the range of sensitivity of the instrument we found that 155 candidates seem to be isolated.

In a scenario where a faint companion is found close-in to the transiting system, it is necessary to quantify the effective contribution of its light in the total light budget. Indeed, if the star is faint enough, or its spectral class is particularly different with respect to the planetary candidate's host star, the dilution of the transit light curve can be negligible, and the planetary system can still be considered as a candidate. Following Lillo-Box et al. (2014a), it is possible to calculate the correction is necessary to apply to the measure of the planetary radius R_p obtained from the transit depth, in order to have its real size:

$$R_p^{true} = R_p^{obs} \left(1 + 10^{-\Delta m/2.5}\right)^{1/2} \tag{2.1}$$

where Δm is the contrast between the host and the blended star.

2.3.3 CAFE

Those candidates that did not show any evidence of a bright close-in companion, were then considered for high-resolution RV follow-up to confirm their planetary nature. Among the 155 isolated candidates, we selected a sub-sample of targets that presented characteristics suitable for a spectroscopic follow-up with the the Calar Alto Fiber-fed Echelle spectrograph (CAFE). CAFE, as with AstraLux is mounted on the 2.2 m telescope in Calar Alto. The spectrograph was built as a replacement of the FOCES spectrograph, with the specific purpose to perform precise radial velocity measurements of stellar objects (Aceituno et al. 2013).

It is a single-fiber fed echelle spectrograph working in the optical range with a wavelength coverage between 3900 and 9500 Å and an average resolution of R=63000. The spectrograph is equipped with a 2048 × 2048 back-illuminated CCD with a pixel dimension of 13.5 μm. The stability in the RV measurement is reached thanks to the location of the instrument in a temperature controlled room and a system of pneumatic stabilizers on the optical bench.

The spectra observed with CAFE are extracted thanks to a pipeline provided by the observatory appositely written for the instrument (based on the R3D pipeline by Sánchez 2006). The RV measurements were performed using different pipelines; for a brief description please refer to Lillo-Box et al. (2014b) or Chapter 4.

2.3.4 Results

From an initial set of 233 selected candidates, thanks to the high-spatial resolution AstraLux observations, we were able to discard many false-positive objects. We then proceeded to the radial velocity campaign with CAFE with a reduced sample of 155 candidates. After further reducing our target sample according to CAFE's capabilities, we started to follow-up the remaining candidates.

Up to now, our collaboration has confirmed five candidates (see Figure 2.7) and identified several other to be false positive such as fast rotators or eclipsing binary (Lillo-Box et al. 2015a).

Kepler-91 b (Lillo-Box et al. 2014c,b) and Kepler-432 b (see Chapter 4) are two hot Jupiters circling around evolved stars at shorter distancees with respect to the rest of the planetary population around giants and sub-giants stars. Kepler-447 b (Lillo-Box et al. 2015b) is a hot-Jupiter with an extremely grazing transit and is the planet with the greatest impact parameter found to date (b∼1.1). Another interesting study performed by the collaboration concerns the confirmation of KOI-0372 b, a giant planet on a 125.6 days slightly eccentric orbit, and the detection of a second planet in the same system on an even wider orbit (Mancini et al. 2015b).

Most of the targets in the remaining sample of unconfirmed planets show long periods up to ∼1500 days (e.g. KOI-1032), and require a longer time to obtain all the necessary RV measurement to properly constrain the orbit and mass of the planets.

Interestingly, given the capabilities of the instruments used, our initial sample was mainly targeting Jupiter-sized planets. However, the characteristics of the planets we have confirmed up to now are surprisingly interesting and not at all as common as one may have thought from the beginning. Most of them indeed lie in diverse region of the parameters space that are not well populated, making our

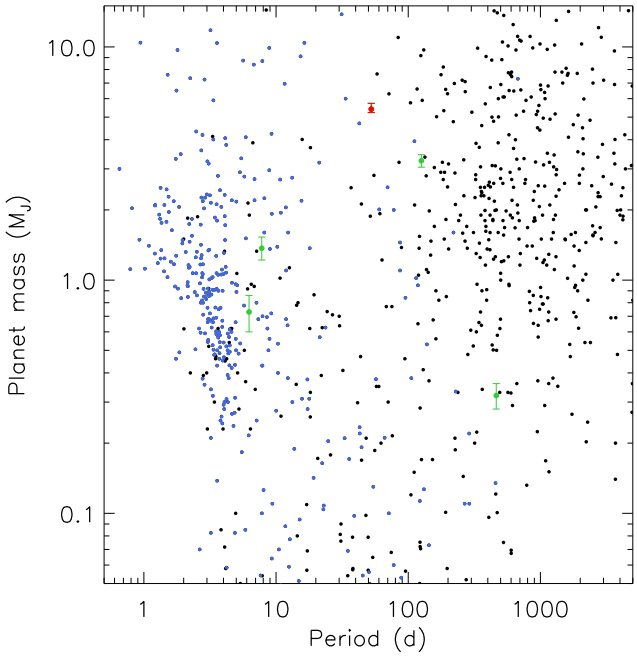

Figure 2.7: Planetary mass–semi major axis of the known planets (from exoplanet.eu). In green color are highlighted the planets confirmed by the MPIA-CAB collaboration, and in red is shown Kepler-432-b presented in Chapter 4.

sample extremely exiting.

2.4 Photometric follow-up of known planets

The increasing number of detected planets allows one to perform statistical studies on the planetary population that are meant to verify the different planetary formation and migration theories that are proposed nowadays (e.g. Mordasini et al. 2009). To perform a proper comparison within the planetary population, it is of primary importance that the characteristics and properties of each system are measured in a homogenoeus way. Boldly comparing quantities measured with different methods can indeed introduce systematics that might create unreal features and falsate the outcome of statistical studies.

Since 2008 we have been carrying out a large program of photometric follow-ups of known transiting planets started by Southworth (2008) to homogeneously describe as many planetary systems as possible. The observations are all performed with small-medium class telescopes located in both hemispheres (mainly with facilities located at the Calar Alto observatory for the northern hemisphere's targets and in the ESO La Silla Observatory for the southern ones).

Deffocussing technique

The main purpose of the project is to accurately measure the photometric properties of the selected targets. To reach this goal a very high photometric precision of the observed light curve is needed. Indeed the signature due to the planet we want to study and characterize is of the order, or even smaller than 1%, of the photometric signal detected. Such good precision can be reached by means of the defocussing technique, which is nowadays one of the most used methods to perform photometric observations of planetary transits (e.g. Gillon et al. 2009; Southworth et al. 2009).

This technique consists of using the telescope out of focus, spreading the light coming from the target on more pixels of the CCD.The PSF of a point-like source is typically Gaussian in shape. However, when the telescope is defocussed, the PSF tends towards an annulus, typically with a radius of between 30 and 100 pixels. The great advantage of using the telescope out of focus is that long exposure times can be used without incurring in the saturation of the bright targets. Long exposures help in reducing the atmospheric scintillation noise and, given the larger number of total photons collected, the Poisson noise is sensibly reduced. A larger area on which the photons are collect, suppresses other sources of noise such as the presence of bad pixels on the CCD, flat fielding, seeing variations and small tracking errors.

The time scale of a transit event is of the order of a few hours, and the ingress and egress phases are of the order of some tenths of minutes. In order to properly constrain the shape of the transit, it is necessary to have a large enough sample of data-points. This implies that, for each single planetary-transit observation, we establish a right balance between the defocussing and the exposure time to achieve a good cadence of experimental points.

Data reduction and analysis

All the photometric data obtained are reduced in the same way regardless of the different instruments and facilities used for observations. The images are calibrated via bias subtraction and flat fielding. The calibration images (bias and sky or dome flats) are usually obtained during each night of observations in order to account for instrumental defects such as the different pixel response of the CCD used or the presence of dust particles on the optical instrumentation.

Since the goal is the precise measurement of the flux variation of the host star, it is not necessary to obtain the light curve in absolute magnitude, but it is sufficient to obtain differential photometry combining the target and some comparison star's light curve. Obtaining differential photometry is indeed essential to get rid of the flux variation due to atmospheric changes, which can be several orders of magnitude bigger than the transit signal.

With a pipeline making use of the IDL's aperture photometry function (based on Stetson 1987 photometry package), the photometry of the target and a set of properly chosen comparison stars is extracted from the calibrated science images. The comparison stars are chosen among the stars present in the FOV according to their magnitude and their variability. In particular, the comparison star's magnitude should be as similar as possible to the target's one, and they should not present photometric variability. The photometry of each star is checked for clear photometric variations during the transit's

observations time, and those stars that present trends are rejected from the comparison star's bucket.

All the light curves are fitted with the JKTEBOP[7] code. The program was developed by J. Southworth in Fortran 77 language, and is based on the the EBOP (Etzel 1981) code created for the study of binary stars light curves.

The light curves are modeled with several free parameters to be adjusted and using most recent literature values as an initial guess. The photometric parameters measured from each light curve are the orbital period and inclination (P and i), the transit midpoint T_0, the reduced planetary and stellar radii r_b and $r_\star$ (where the fractional radii are defined as the absolute radii divided by the orbital semi-major axis). The JKTEBOP code allows a robust estimation of the uncertainties of the photometric parameters through a careful error propagation and by performing Bootstrapping or Monte Carlo simulations.

Limb darkening

When observing the transit of a planet in front of its parent star's disk, an important effect which is necessary to take into account, is the limb darkening (LD). The LD describes the diminishing intensity and brightness in the disk of a star when observed from its center to its edge. It is mainly due to two different effects: as the distance from the center increases the projected density of the star diminishes, but so does the temperature. Therefore, when the line of sight is directed towards the center of the disk, it is pointing to a deeper and hotter portion of the stellar atmosphere, while when pointing to the limb, it is looking into the outer and cooler layers of the atmosphere.

The LD effect depends strongly on wavelength and is stronger at higher frequencies, hence the reddening visible towards the star limb (e.g. in the Sun). Since the LD varies with wavelength, this means that given a perfectly spherical object, with a defined rim, the resulting transit's depth and shape would slightly vary according to the wavelength used to perform the observations.

The LD affects the shape of a transit light curve by rounding the bottom and the 'shoulders' of the curve softening the otherwise sharp edges. An example of a transit event simultaneously observed at different wavelengths is depicted in Figure 2.8. As described in Section 1.2.2, if a planet has an atmosphere, during the transit some starlight will pass through it, and according to the atmospheric composition, the transit depth varies slightly according to the bandpass used to observe it. A proper treatment and description of the LD is therefore necessary to disentangle the two phenomena and be able to probe the planetary composition.

Nowadays, it is still not clear how to properly describe the LD effect, and several parametric laws, trying to model it have been proposed so far. A first and most simple LD law is a linear one:

$$\frac{I(\mu)}{I(1)} = 1 - u(1-\mu) \tag{2.2}$$

where $\mu = cos\theta$, and θ being the angle of incidence of the line of sight on the stellar surface. $I(\mu)$ and $I(1)$ are respectively the flux per unit area received at angle θ and from the center of the stellar disk, and u is the linear coefficient. A linear description, however, does not properly describe the shape of a transit when the data are precise enough. Other laws admitting two coefficients have been therefore

[7] JKTEBOP is available at http:// www.astro.keele.ac.uk/jkt/codes/jktebop.html

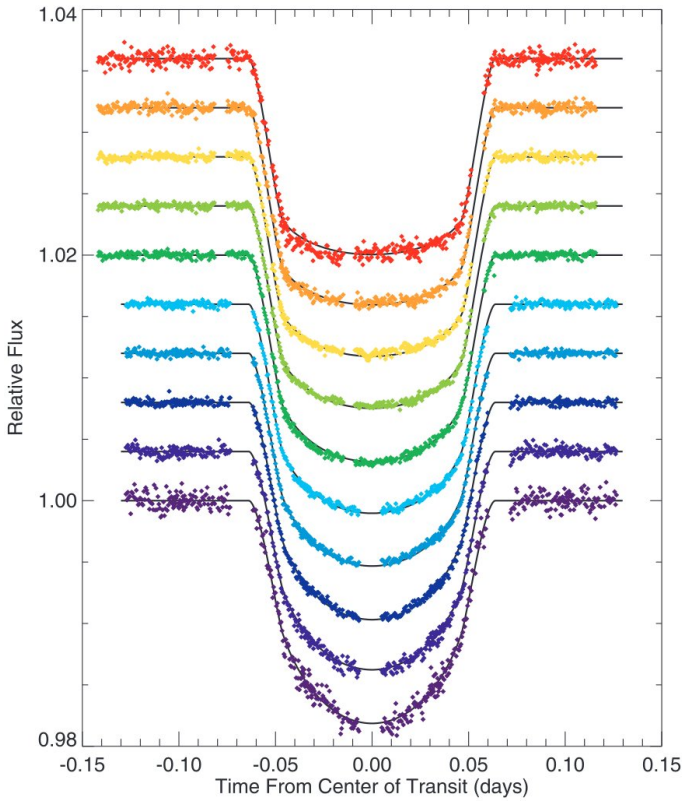

Figure 2.8: Light curves of a planetary transit of HD 209458 b observed with the STIS instrument mounted on the Hubble Space Telescope by (Knutson et al. 2007). The spectra obtained have been divided into 10 bins relative to equally spaced band-passes and treated separately to obtain the light curves shown in different colors. The spectral dependence of LD results in a changing light curve profile with wavelength.

proposed, such as the quadratic one:

$$\frac{I(\mu)}{I(1)} = 1 - c_1(1-\mu) - c_2(1-\mu)^2 \tag{2.3}$$

or the logarithmic and the square-root ones:

$$\frac{I(\mu)}{I(1)} = 1 - c_1(1-\mu) - c_2\mu\ln\mu \tag{2.4}$$

and

$$\frac{I(\mu)}{I(1)} = 1 - c_1(1-\mu) - c_2(1-\sqrt{\mu}) \tag{2.5}$$

where c_1 and c_2 are the linear and non linear coefficients for the laws. Other more complex laws have been proposed requiring more than two coefficients. However, given the numerous free parameters and the fact that often the coefficients are correlated to each others, a simpler 2-coefficient law is preferable. In general all the LD coefficients depend not only on the wavelength but also on the spectral type of the star and its characteristics, such as the effective temperature, the surface gravity, the chemical composition and the microturbolence velocity. Moreover, according to the different stellar atmosphere model used, the relative coefficients of these laws vary (the description of the limb darkening was based on Southworth 2006 Chapter 1, and references therein).

The strategy we usually adopt, unless there are contraindications for a specific case (e.g. see Chapter 7), is to describe the LD with a quadratic law fitting for the coefficient of the linear term while perturbing the quadratic one.

2.4.1 Multi-site and multi-band observations

It is not so rare that the planetary-transit light curves show anomalies and deviations from the expected transit shape. These irregularities may have different origins that span anywhere from instrumental failure, to odd atmospheric variations or astronomical variability. Diverse effects may give rise to the same anomalous shape, and a single transit light curve is usually not enough to unravel the enigma.

A possible solution to investigate the cause of these anomalies, is to observe the same transit event concurrently with two independent telescopes. In this way, if the same irregularity is present in both the light curves it is possible to rule out the atmosphere and instrumental systematics as sources of the deviation (see Figure 2.9 for an example of simultaneous light curves showing an asymmetry).

The two telescopes used for these simultaneous observations should be far enough from each other so that the atmospheric conditions are independent, but close enough so that the same transit event could be observed from both the facilities. A couple of examples of two facilities suitable for these kind of observations are the pair composed by the Loiano observatory in Italy and the Calar Alto observatory in Spain for the northern hemisphere, or the ESO La Silla and Paranal observatories in Chile in the southern hemisphere.

There are several possibilities to explain the presence of an anomaly, once its astrophysical nature has been established: stellar pulsations, stellar activity and presence of star-spots (e.g. Collier Cameron et al. 2010; Tregloan-Reed et al. 2015), or even the exotic possibility of the detection of

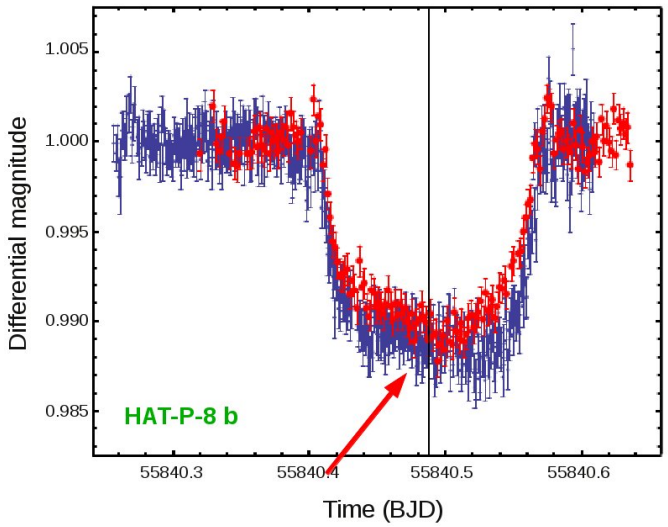

Figure 2.9: Transit event of HAT-P-8 observed on October 5th 2011 simultaneously from two different facilities (Mancini et al. 2013). Blue dots refers to the data obtained in Gunn-*i* filter filter at the Cassini telescope, whereas the red ones have been observed through a Johnson-*R* filter with the CAHA 1.23 m telescope. The red arrow and the vertical line are added to guide the eye in spotting the anomaly.

an exomoon (Kipping et al. 2009). The detection of a signal due to the presence of star spots on the parent star surface is of particular interest since from their study it is possible to measure the spin-orbit alignment or the stellar rotation (e.g. Sanchis-Ojeda & Winn 2011; Tregloan-Reed et al. 2013; Mancini et al. 2014).

Another useful method to obtain extra information from photometric observations of a planetary transit is to perform the observations using multi-imager instruments that allow one to obtain simultaneous light curves of the same transit in different bands. This observing strategy can be used as an alternative to transmission spectroscopy when looking for variation in the planetary radius with wavelength (see Section 1.2.2).

Two instruments particularly efficient in producing simultaneous multi-band observations are GROND and BUSCA, conveniently located in the southern and northern hemispheres respectively. GROND (Gamma Ray Optical Near-infrared Detector, Greiner et al. 2008) is a seven-channel imager mounted on the MPG 2.2 m telescope at the La Silla Observatory. Thanks to a set of dichroics, it allows one to obtain the same image in four optical passbands (g', r', i', z') and three near-infrared ones (J, H, and K).

BUSCA (Bonn University Simultaneous Camera, Reif et al. 1999) is an imager mounted on the 2.2 m Calar Alto telescope, and allows one to simultaneously perform observations in four different optical bands. The filters can be chosen from a set of standard ones. In particular both broad-band and narrow-band filters are available and are normally used according to the brightness of the target, for faint and bright targets respectively.

Chapter 3

Looking for planets: HATS-15 & HATS-16

In this chapter we present the discovery of two planetary systems found within the HATSouth collaboration. HATS-15 and HATS-16 are two massive planets orbiting around two old main sequence star. This papaer has been submitted to PASP and is currently under review.

Che fai tu, luna, in ciel?
dimmi, che fai,
Silenziosa luna?
Sorgi la sera, e vai
Contemplando i deserti; indi ti posi.

Canto notturno di un pastore errante dell'asia, G. Pascoli

DRAFT VERSION 0 SEPTEMBER 9, 2015
Preprint typeset using LaTeX style emulateapj v. 2/16/10

HATS-15b AND HATS-16b: TWO MASSIVE PLANETS TRANSITING OLD G DWARF STARS

CICERI, S.[1], MANCINI, L.[1], HENNING, T.[1], BAKOS, G.[2], PENEV, K.[2], BRAHM, R.[3,4], ZHOU, G.[5], HARTMAN, J. D.[2], BAYLISS, D.[6], JORDÁN, A.[3,4], CSUBRY, Z.[2], DE VAL-BORRO, M.[2], BHATTI, W.[2], RABUS, M.[3,1], ESPINOZA, N.[3,4], SUC, V.[3], SCHMIDT, B.[5], NOYES, R.[7], HOWARD, A. W.[8], FULTON, B. J.[8], ISAACSON, H.[9], MARCY, G. W.[9], BUTLER, R. P.[10], ARRIAGADA, P.[10], CRANE, J.[10], SHECTMAN, S.[10], THOMPSON, I.[10], TAN, T. G.,[11], LÁZÁR, J.[12], PAPP, I.[12], SARI, P.[12]

Draft version 0 September 9, 2015

ABSTRACT

We report the discovery of HATS-15 b and HATS-16 b, two massive transiting extrasolar planets orbiting evolved (~ 10 Gyr) main-sequence stars. The planet HATS-15 b, which is hosted by a G9 V star ($V = 14.8$ mag), is a hot Jupiter with mass of $2.17 \pm 0.15\,M_{\rm J}$ and radius of $1.105 \pm 0.0.040\,R_{\rm J}$, and completes its orbit in nearly 1.7 days. HATS-16 b is a very massive hot Jupiter with mass of $3.27 \pm 0.19\,M_{\rm J}$ and radius of $1.30 \pm 0.15\,R_{\rm J}$; it orbits around its G3 V parent star ($V = 13.8$ mag) in ~ 2.7 days. HATS-16 is slightly active and shows a periodic photometric modulation, implying a rotational period of 12 days which is unexpectedly short given its isochronal age. This fast rotation might be the result of the tidal interaction between the star and its planet.

Subject headings: planetary systems — stars: individual (HATS-15, HATS-16, GSC 7516-00867) – techniques: spectroscopic, photometric

1. INTRODUCTION

Before the *Kepler* mission (Borucki et al. 2010), most of the exoplanets discovered with the transit method by the ground-based surveys (e.g. WASP and HATNet, Pollacco et al. 2006; Bakos et al. 2004) were hot Jupiters (i.e. those planets in the Jupiter-mass regime that circle very close-in their host star). This is essentially due to the relative ease with which this kind of exoplanet can be detected: indeed both the radial velocity (RV) and transit detection techniques are biased towards finding massive planets at short periods. Nowadays, with an increased sample of more than 1800 planets, we realize that the hot-Jupiter occurrence is just a tiny fraction, $\lesssim 1\%$ for solar-like stars, compared to the larger number of smaller (Neptunian and rocky) planets (e.g. Mayor et al. 2011; Howard et al. 2012; Dong & Zhu 2013; Fressin et al. 2013).

However, hot-Jupiters are still of interest to astrophysicists because many of their properties are not well understood. In particular, it is not clear what are the physical mechanisms that cause them to migrate from their formation region down to $\sim 10^{-2}$ AU from the parent stars; it is also very puzzling that many of the known hot Jupiters have a radius larger than what predicted by standard models of structure of gaseous giant planets; hot Jupiters with masses $> 2\,M_{\rm J}$ are, on the other hand, more an exception than a rule (e.g. Jiang et al. 2007). In this work, we present two new hot-Jupiters transiting planets, HATS-15b and HATS-16b, belonging to the class of massive gas planets.

The HATS-15 and HATS-16 planetary systems have been discovered within the HATSouth ground-based survey (e.g. Bakos et al. 2013; Penev et al. 2013). HATSouth is a network of six completely automated units (named HS-1 to HS-6), which are stationed in pairs at three different sites in the southern hemisphere: Las Campanas Observatory in Chile (LCO), the High Energy Spectroscopic System (HESS) site in Namibia and the Siding Spring Observatory (SSO) in Australia. The main part of each station is the mount on which four 18 cm astrographs and four CCD cameras are lodged. The mutual distance of the three sites, nearly 120° from each other, permits operations of at least one station at any time, allowing a continuous 24–hour monitoring of a stellar field.

Operating since 2010, the HATSouth survey has dis-

[1] Max Planck Institute for Astronomy, Königstuhl 17, 69117, Heidelberg, Germany
[2] Department of Astrophysical Sciences, Princeton University, Princeton, NJ 08544, USA
[3] Instituto de Astrofísica, Pontificia Universidad Católica de Chile, Av. Vicuña Mackenna 4860, 7820436 Macul, Santiago, Chile
[4] Millennium Institute of Astrophysics, Av. Vicuña Mackenna 4860, 7820436 Macul, Santiago, Chile
[5] The Australian National University, Canberra, Australia
[6] Observatoire Astronomique de l'Université de Genève, 51 ch. des Maillettes, 1290 Versoix, Switzerland
[7] Harvard-Smithsonian Center for Astrophysics, Cambridge, MA 02138 USA
[8] Institute for Astronomy, University of Hawaii at Manoa,Honolulu, HI, USA
[9] Department of Astronomy, University of California, Berkeley, CA 94720-3411, USA
[10] Carnegie Institution of Washington Department of Terrestrial Magnetism, NW Washington, DC 20015-1305, USA
[11] Perth Exoplanet Survey Telescope, Perth, Australia
[12] Hungarian Astronomical Association, Budapest, Hungary
The HATSouth network is operated by a collaboration consisting of Princeton University (PU), the Max Planck Institute für Astronomie (MPIA), the Australian National University (ANU), and the Pontificia Universidad Católica de Chile (PUC). The station at Las Campanas Observatory (LCO) of the Carnegie Institute is operated by PU in conjunction with PUC, the station at the High Energy Spectroscopic Survey (H.E.S.S.) site is operated in conjunction with MPIA, and the station at Siding Spring Observatory (SSO) is operated jointly with ANU. Based in part on observations performed at the ESO La Silla Observatory in Chile, with the Coralie and FEROS spectrographs mounted on the Euler-Swiss and MPG 2.2 m telescopes respectively. This paper includes data gathered with the 6.5 m Magellan Telescopes located as Las Campanas Observatory, Chile. Based in part on data collected at Keck Telescope. Observations obtained with facilities of the Las Cumbres Observatory Global Telescope are used in this paper.

covered 16 exoplanets[2] so far, including the two presented in this paper. These planets span a range in masses that goes from super-Neptune (HATS-7 b and HATS-8 b, Bakos et al. 2015; Bayliss et al. 2015) to super-Jupiters (e.g. HATS-11 b and HATS-16 b, Rabus et al. 2015, this work).

The paper is organized as follows: in Section 2 we describe the observations and data reduction that allowed us to discover and confirm the planetary nature of HATS-15b and HATS-16b. In Section 3 we outline the diverse steps of our analysis that brought us to discard the false positive scenarios and determine the stellar and planetary parameters of the two systems. Finally in Section 4, we discuss and summarize our findings.

2. OBSERVATIONS

2.1. *Photometric detection*

HATS-15 is a $V = 14.77$ mag star, located in the Capricornus constellation, while HATS-16 (aka GSC 7516-00867) is a $V = 13.83$ mag star in the Sculptor constellation. Both the stars have been identified as planetary host candidates based on roughly six months of continuous photometric observations. Specifically, HATS-15 was in the field-of-view (FOV) of two different HATS-fields (G581 and G582), and was therefore observed from September 2009 to September 2010 with all the units in the three sites. HATS-16 was observed from June 2013 to December 2013 with the HS-2, HS-4 and HS-6 units (located at LCO, HESS and SSO respectively). The target was simultaneously observed with two different cameras in each site, as it was lying in the overlapping region of the FOV of two cameras. Table 1 shows the details of the photometric observations, displaying the total number of photometric measurements, the observing cadence and other information.

The light curves of the two stars were obtained through aperture photometry from the properly calibrated (bias and dark subtracted and flat fielded) science frames following Bakos et al. (2013) and Penev et al. (2013). The light curves were detrended, using the TFA algorithm (Trend Filtering Algorithm; see Kovács et al. 2005), and then searched for a periodical signal by fitting them with a box-shaped transit model (Box Least Square; Kovács et al. 2002). We found that the HATS-15 photometry shows a periodic dip every 1.75 days, while in the HATS-16 light curve we detected a transit signal with a periodicity of 2.69 days. The phase-folded light curves of both the planets are shown in Fig. 1, and the data are provided in Table 2.

2.2. *Spectroscopic Observations*

In order to confirm the planetary nature of the two candidates and obtain the complete set of their orbital and physical parameters, systematic spectroscopic observations of the two systems are mandatory. Our observations can be divided in two different steps: first we observed our targets with low resolution spectrographs, or at high resolution but low S/N, to obtain an initial characterization of the star and exclude some of the most probable false positive scenarios; subsequently, we obtained several high-resolution high S/N spectra to measure the radial velocity of the two stars.

For both the stars we obtained 4 spectra with the Wide-Field Spectrograph (WiFeS) mounted on the 2.3 m ANU telescope located at SSO. WiFeS is an image-slicing integral-field spectrograph (Dopita et al. 2007). According to the different slits used, it can achieve an average resolution up to $R = \lambda/\Delta\lambda \sim 7000$ over a wavelength rage of 3300–9200 Å. The spectra were extracted and reduced following Bayliss et al. (2013). One of the spectra, was observed with a resolution of $R = 3000$ for obtaining a first spectral classification of each star and verifying that they are not giants. By analyzing the spectra, we found that HATS-15 is a G9 dwarf ($T_{\rm eff,*} = 5000 \pm 300$ K and $\log g_\star = 3.5 \pm 0.3$) while HATS-16 is a G3 dwarf ($T_{\rm eff,*} = 6300 \pm 300$ K and $\log g_\star = 4.6 \pm 0.3$). The other three spectra where obtained with a higher resolution ($R = 7000$) to look for a possible periodic RV signal higher than $5\,{\rm km\,s^{-1}}$, which is the signature of an eclipsing binary that is the most probable false positive scenario. In both the cases, we did not find evidence of any RV variation higher than $0.5\,{\rm km\,s^{-1}}$ for HATS-15 and $2\,{\rm km\,s^{-1}}$ for HATS-16. Moreover, none of the two systems show a composed spectrum, allowing us to exclude the spectroscopic binary scenario.

Another reconnaissance spectrum for HATS-15 was observed with the du Pont telescope on August 21, 2013. The 2.5 m du Pont telescope is located at LCO, and is equipped with an echelle spectrograph capable to cover the optical range between 3700 and 7000 Å, achieving a maximum resolution of $R \sim 45000$. We used a a $1'' \times 4''$ slit that allowed a resolution of $R \sim 40000$. The spectrum was reduced with an automated pipeline written for this instrument and similar to the one used for Coralie and FEROS (Brahm et al. 2015).

The reconnaissance spectroscopy observations pointed towards a planetary system scenario for both the systems. Therefore, we started a campaign to get high precision RV measurements, in order to determine the mass of the companions, and verify that the periodical signals in RV were consistent with the photometric ones.

Between June and November 2012 we obtained three high resolution spectra of HATS-15 with Coralie. The spectrograph Coralie is fed from the 1.2 m Swiss-Euler telescope, which is located at the ESO Observatory in La Silla, Chile. The instrument is a fiber-fed spectrograph with a resolution of $R \sim 60000$ and a wavelength coverage between 3850 and 6900 Å (Queloz et al. 2001). During each science exposure, a simultaneous ThAr spectra was taken, to be able to operate a proper wavelength calibration. The spectra extraction was performed from the images calibrated with bias and flats obtained during the twilight following Marsh (1989). The RV of each spectrum was then measured by cross-correlation with a binary mask accurately chosen according to the spectral class of the target (for a complete description of the reduction pipeline see Jordán et al. 2014).

The bulk of the RV measurements, which allowed us to verify the planetary nature of both the candidates, was performed by utilizing the Fiber-fed Extended Range Optical Spectrograph (FEROS). It is an echelle spectrograph mounted on the MPG 2.2 m telescope, which is also situated at the La Silla Observatory. The instru-

[2] For a complete list with reference of all the HATSouth planets, see *http://hatsouth.org/*

Table 1
Summary of photometric observations

Instrument/Field[a]	Date(s)	# Images	Cadence[b] (sec)	Filter	Precision[c] (mmag)
HATS-15					
HS-1.3/G581	2009 Aug–2010 Sep	6802	288	r	19.1
HS-3.3/G581	2009 Sep–2010 Sep	8617	292	r	17.9
HS-5.3/G581	2009 Nov–2010 Sep	586	292	r	18.6
HS-2.2/G582	2009 Sep–2010 Sep	4450	284	r	19.9
HS-4.2/G582	2009 Sep–2010 Sep	7834	288	r	20.0
HS-6.2/G582	2010 Aug–2010 Sep	207	290	r	21.7
FTS 2 m/Spectral	2011 Sep 23	87	82	i	2.1
PEST 0.3 m	2013 May 21	143	130	$R_{\rm C}$	12.5
MPG 2.2 m/GROND	2013 Jun 15	71	224	g	1.1
MPG 2.2 m/GROND	2013 Jun 15	65	224	r	0.8
MPG 2.2 m/GROND	2013 Jun 15	70	224	i	1.2
MPG 2.2 m/GROND	2013 Jun 15	72	224	z	1.5
HATS-16					
HS-2.1/G588	2013 Jun–2013 Oct	3888	279	r	12.9
HS-4.1/G588	2013 Jun–2013 Dec	4683	291	r	13.5
HS-6.1/G588	2013 Jun–2013 Dec	3618	296	r	13.2
HS-2.2/G588	2013 Jun–2013 Oct	1929	281	r	12.2
HS-4.2/G588	2013 Jun–2013 Dec	3732	291	r	11.9
HS-6.2/G588	2013 Jun–2013 Dec	3678	296	r	11.8
DK 1.54 m/DFOSC	2014 Oct 06	170	116	R	2.1

[a] For HATSouth data we list the HATSouth unit, CCD and field name from which the observations are taken. HS-1 and -2 are located at Las Campanas Observatory in Chile, HS-3 and -4 are located at the H.E.S.S. site in Namibia, and HS-5 and -6 are located at Siding Spring Observatory in Australia. Each unit has 4 ccds. Each field corresponds to one of 838 fixed pointings used to cover the full 4π celestial sphere. All data from a given HATSouth field and CCD number are reduced together, while detrending through External Parameter Decorrelation (EPD) is done independently for each unique unit+CCD+field combination.
[b] The median time between consecutive images rounded to the nearest second. Due to factors such as weather, the day–night cycle, guiding and focus corrections the cadence is only approximately uniform over short timescales.
[c] The RMS of the residuals from the best-fit model.

Table 2
Light curve data for HATS-15 and HATS-16.

Object[a]	BJD[b] (2,400,000+)	Mag[c]	$\sigma_{\rm Mag}$	Mag(orig)[d]	Filter	Instrument
HATS-15	55435.70436	−0.02268	0.01260	···	r	HS
HATS-15	55374.54242	−0.00238	0.02157	···	r	HS
HATS-15	55386.77495	0.01740	0.01000	···	r	HS
HATS-15	55096.69186	0.02154	0.01436	···	r	HS
HATS-15	55416.48228	0.00679	0.00988	···	r	HS
HATS-15	55124.65174	−0.04501	0.01408	···	r	HS
HATS-15	55110.67192	−0.00283	0.02212	···	r	HS
HATS-15	55367.55285	0.02756	0.00964	···	r	HS
HATS-15	55381.53294	0.00608	0.01109	···	r	HS
HATS-15	55409.49282	−0.00161	0.01282	···	r	HS

Note. — This table is available in a machine-readable form in the on-line journal. A portion is shown here for guidance regarding its form and content.
[a] Either HATS-15, or HATS-16.
[b] Barycentric Julian Date is computed directly from the UTC time without correction for leap seconds.
[c] The out-of-transit level has been subtracted. For observations made with the HATSouth instruments (identified by "HS" in the "Instrument" column) these magnitudes have been corrected for trends using the EPD and TFA procedures applied *prior* to fitting the transit model. This procedure may lead to an artificial dilution in the transit depths. For HATS-15 the transit depth is 93% and 100% that of the true depth for the G581.3 and G582.2 observations, respectively. For HATS-16 it is 88% and 87% that of the true depth for the G588.1 and G588.2 observations, respectively. For observations made with follow-up instruments (anything other than "HS" in the "Instrument" column), the magnitudes have been corrected for a quadratic trend in time fit simultaneously with the transit. For HATS-16 an additional correction has been made for trends correlated with variations in the FWHM of the PSF.
[d] Raw magnitude values without correction for the quadratic trend in time, or for trends correlated with the seeing. These are only reported for the follow-up observations.

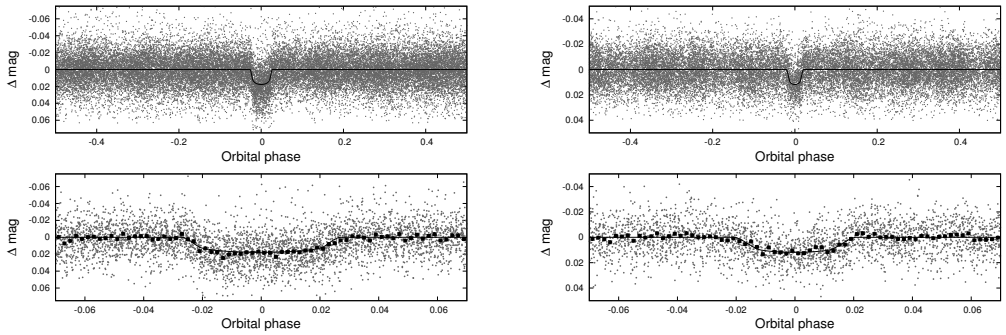

Figure 1. HATSouth photometry for HATS-15 (left) and HATS-16 (right). The top panel of each system shows the relative full light curve phase-folded and unbinned; the superimposed solid lines are the model fits to the light curves. The bottom panels show the light curve zoomed-in on the transit. The dark filled circles represent the light curves binned in phase with a bin size of 0.002.

ment is capable of a wide wavelength coverage from 3700 to 8600 Å and has an average resolution of $R \sim$48000 (Kaufer & Pasquini 1998). For HATS-15 we observed 13 spectra between September 2011 and May 2013, whereas 12 spectra were obtained for HATS-16 between June and October 2014. The data were reduced and RVs were measured, using the same pipeline written for Coralie and adapted for FEROS (Brahm et al. 2015).

Moreover, we obtained four observations of HATS-16 with HIRES in September 2014. HIRES (HIgh Resolution Echelle Spectrometer) is an echelle spectrograph mounted in the Nasmyth focus of the Keck-I telescope located on the mountain of Mauna Kea in Hawaii, USA. HIRES has a resolution up to 84000 and can cover wavelengths between 3000 and 11000 Å (Vogt et al. 1994). The observations were made using the standard high-precision RV setup for faint targets. We used the C2 decker obtaining a resolution of $R \sim 55000$. Unlike the previous two instruments used for high-resolution spectroscopy, the wavelength calibration was not conducted with the simultaneous observation of a ThAr spectrum, but with an Iodine absorption cell (Marcy & Butler 1992). The radial velocity extraction was performed using a theoretical synthetic template drawn from the Coelho (2014) grid as described by Fulton et al. (2015). This method provides greater precision measurements for faint stars than the traditional technique of obtaining an additional iodine-free observation to be used as a template (e.g., Bayliss et al. 2015).

The high resolution RV measurements of both the systems showed a periodicity consistent with the one measured form the photometric observations. A periodic signal, presented both in the light curve and in the RV, might not be necessarily due to the presence of a planetary companion, but can be produced by a blended eclipsing binary. To exclude this false positive scenario we measured the bisector span (BS) for both the systems finding no hint of a periodicity consistent with the orbital period; for the BS measurements we followed a procedure similar to that of Torres et al. (2007), appropriately adapted to each instrument. The spectroscopic observations are summarized in Table 3, and phased high-precision RV and BS measurements are shown for each system in Figure 2.

Finally, four further high–resolution spectra of HATS-15 were obtained in August-September 2014 with the Planet Finder Spectrograph (PFS). PFS is an echelle spectrograph mounted on the 6.5 m Magellan Clay Telescope at Las Campanas Observatory in Chile. The maximum wavelength coverage PSF is capable of span the optical region from 3880 to 6680 Å, and can be used in different modes, yielding a maximum resolution of $R \sim 190000$ (Crane et al. 2010). For our observations, we used a $0.5'' \times 2.5''$ slit having a resolving power of 76000. These spectra were used to determine the spectroscopic parameters for HATS-15 using the ZASPE program (see Section 3), while for HATS-16 the parameters have been measured by applying the same program to a combination of the FEROS spectra.

2.3. *Photometric follow-up observations*

Both the HATS-15 and HATS-16 planetary systems have been photometrically followed-up to properly constrain their orbital ephemeris and obtain a precise measure of the photometric parameters, which allow to directly estimate the mean density of the parent stars and, at the end, the radii of the planets. The photometric follow-up observations are summarized in Table 1 and the corresponding data are reported in Table 2 for both the systems.

We observed two partial transits and a complete one of HATS-15. Specifically, the first half transit was obtained with the Faulkes Telescope South (FTS) on September the 23$^{\rm th}$ 2011, and consisted in the out-of-transit data, ingress and partial transit observation. The FTS is a 2.0 m telescope, located at SSO, and is part of the Las Cumbres Observatory Global Telescope (LCOGT) network. The telescope is equipped with a 4000×4000 pixels camera with a pixel size of $0.15''$. The observations were performed with an i-band filter and with the telescope out of focus, as no close-in background star was detected. The data reduction was performed using an automated aperture photometry pipeline utilising Sextractor (Bertin & Arnouts 1996). In brief the science images are first calibrated via bias subtraction and flat-fielding, then the light curves are extracted via fix-aperture photometry.

The second-half transit was observed with the 30 cm PEST telescope on May the 21$^{\rm st}$ 2013, and covered almost the whole transit excluding egress. The SBIG ST-8XME camera mounted on this telescope has a FOV of $31' \times 21'$, with a resolution of 1.2 arcsec per pixel. A $R_{\rm C}$ filter was used to take in-focus images with a cadence of 130 s. The light curve was extracted from the calibrated images (dark subtracted and flat-fielded) with aperture photometry. For a more exhaustive overview on the instrument's characteristics and the data reduction description see Zhou et al. (2014).

A complete transit of HATS-15b was observed simultaneously in four different optical bands (g', r', i', z', similar to Sloan filters) using the multiband imager instrument GROND (Gamma Ray Optical Near-infrared Detector; Greiner et al. 2008). The observations, performed on June the 15$^{\rm th}$ 2013, were obtained with the telescope slightly out of focus to increase the photometric precision. After de-biasing and flat-fielding the science frames, the photometry was extracted with a pipeline based on DAOPHOT that make use of the APER IDL function (for the GROND observing strategy and subsequent data reduction refer to Penev et al. 2013; Mohler-Fischer et al. 2013). The light curves for all the HATS-15 follow-up transits are shown in Figure 3.

We obtained a transit of HATS-16 with the DFOSC camera on October the 6$^{\rm th}$ 2014. The DFOSC (Danish Faint Object Spectrograph and Camera) instrument is mounted on the 1.54 m Danish Telescope, at the La Silla Observatory. The CCD has a resolution of 0.39 arcsec per pixel and a FOV $13.7' \times 13.7'$. The telescope was defocused and a Bessel R filter was used. After properly calibrating the images, aperture photometry was done following Deeg & Doyle (2001) to obtain the light curve. See Rabus et al. (2015) for a complete description of the instrument and reduction pipeline. The light curve for HATS-16 is shown in Figure 4.

3. ANALYSIS

3.1. *Properties of the parent star*

Table 3
Summary of spectroscopy observations

Instrument	UT Date(s)	# Spec.	Res. $\Delta\lambda/\lambda/1000$	S/N Range[a]	$\gamma_{\rm RV}$[b] ($\rm km\,s^{-1}$)	RV Precision[c] ($\rm m\,s^{-1}$)
HATS-15						
Reconnaissance						
ANU 2.3 m/WiFeS	2011 Jul 26–28	3	7	13–22	-54.7	4000
ANU 2.3 m/WiFeS	2011 Jul 27	1	3	95	...	...
du Pont 2.5 m/Echelle	2013 Aug 21	1	40	36	-53.8	500
High resolution radial velocity						
MPG 2.2 m/FEROS	2011 Sep–2013 May	13	48	16–49	-54.145	81
Euler 1.2 m/Coralie	2012 Jun–Nov	3	60	12–13	-54.270	246
Magellan 6.5 m/PFS	2014 Sep	4	76	40	...	...
HATS-16						
Reconnaissance						
ANU 2.3 m/WiFeS	2014 Jun 3–5	3	7	21–82	28.7	4000
ANU 2.3 m/WiFeS	2014 Jun 4	1	3	101	...	...
Euler 1.2 m/Coralie	2014 Jun 20	1	60	14	31.625	100
High resolution radial velocity						
MPG 2.2 m/FEROS	2014 Jun–Oct	12	48	35–57	31.594	54
Keck 10 m/HIRES	2014 Jun 20	4	55	...	...	20

[a] S/N per resolution element near 5180 Å.
[b] For the Coralie and FEROS observations of HATS-15, and for the FEROS observations of HATS-16, this is the zero-point RV from the best-fit orbit. For the WiFeS and du Pont Echelle, and for the single Coralie observation of HATS-16 it is the mean value. We do not provide this quantity for the lower resolution WiFeS observations which were only used to measure stellar atmospheric parameters, or for the PFS observations of HATS-15 which were obtained without the I_2 cell and were used to determine the atmospheric parameters of the star.
[c] For High-precision RV observations included in the orbit determination this is the scatter in the RV residuals from the best-fit orbit (which may include astrophysical jitter), for other instruments this is either an estimate of the precision (not including jitter), or the measured standard deviation. We do not provide this quantity for low-resolution observations from the ANU 2.3 m/WiFeS, or for the PFS observations of HATS-15.

For achieving a precise determination of the physical properties of a new exoplanet, it is crucial to properly characterize its host star, especially its mass and radius. We obtained those quantities, and the other set of parameters describing the HATS-15 and HATS-16 stars, by properly combining the spectroscopic and photometric data.

The atmospheric parameters, including the effective temperature $T_{\rm eff}$, surface gravity $\log g$, metallicity [Fe/H] and the projected rotational velocity $v \sin i$, were measured by analyzing the high resolution spectra obtained with PFS for HATS-15 and FEROS for HATS-16. The analysis was performed using the Zonal Atmospherical Stellar Parameter Estimator (ZASPE) code (see Brahm et al. 2015). In brief, the atmospheric parameters are calculated iteratively, selecting a specific region of the spectra (between 5000 Å and 6000 Å) and fitting the median-combined observed spectra with a grid of synthetic ones (Husser et al. 2013). For HATS-15 we found: $T_{\rm eff} = 5296 \pm 76$, $\log g = 4.60 \pm 0.12$, [Fe/H]$= 0.090 \pm 0.040$ and $v \sin i = 4.36 \pm 0.24$; while for HATS-16: $T_{\rm eff} = 5840 \pm 120$, $\log g = 4.50 \pm 0.19$, [Fe/H]$= -0.010 \pm 0.070$ and $v \sin i = 6.01 \pm 0.50$.

The fundamental stellar parameters were obtained combining the spectroscopic and photometric quantities with the Yonsei-Yale stellar evolutionary models (Y2 hereafter; Yi et al. 2001). In particular, for the analysis with the isochrones, we used the stellar density $\rho_\star$ obtained from the photometry instead of $\log g$ from the spectra, as it provides a more precise and more accurate constraint on the stellar properties (following Sozzetti et al. 2007). Assuming a nil eccentricity of the planetary orbit, the stellar density can be directly measured from the transit light curve as described in Seager & Mallén-Ornelas (2003).

For both the systems we performed a second time the analysis: first we re-derived the spectroscopic quantities with ZASPE, this time fixing the values of the $\log g$ to the ones retrieved from the stellar evolution models. Then we obtained the stellar properties once more modeling the data with the Y2 isochrones. We found that HATS-15 has a mass $M_\star = 0.871 \pm 0.023\,M_\odot$, radius $R_\star = 0.922 \pm 0.027\,R_\odot$ and an age of $11.0^{+1.4}_{-2.0}$ Gyr; while HATS-16 has $M_\star = 0.970 \pm 0.035\,M_\odot$, $R_\star = 1.238^{+0.097}_{-0.127}\,R_\odot$ and age$=9.5 \pm 1.8$ Gyr. The final values adopted in the subsequent analysis to derive the planetary parameters are presented in Table 4, while in Figure 5 the two stars are shown in a $T_{\rm eff\star}$–$\rho_\star$ diagram (similar to a Hertzsprung-Russell diagram).

To measure the distance of the two planetary systems we compared the magnitude observed with each filter with a set of predicted ones. The predicted magnitudes were determined using the Y2 isochrones and assuming an extinction law with $R_{\rm V} = 3.1$ from Cardelli et al. (1989). Using the NASA/IPAC Extragalactic Database (NED[3]) we checked that the value for the extinction were

[3] The NASA/IPAC Extragalactic Database (NED) is operated

Table 4
Stellar parameters for HATS-15 and HATS-16

Parameter	**HATS-15** Value	**HATS-16** Value	Source
Astrometric properties and cross-identifications			
2MASS-ID	2MASS 20442207-1926150	2MASS 23541409-3000467	
GSC-ID	—	GSC 7516-00867	
R.A. (J2000)	$20^{\rm h}44^{\rm m}22.20$s	$23^{\rm h}54^{\rm m}14.04$s	2MASS
Dec. (J2000)	$-19°26'15.0''$	$-30°00'46.8''$	2MASS
$\mu_{\rm R.A.}$ (mas yr^{-1})	19.6 ± 2.5	21.7 ± 1.3	UCAC4
$\mu_{\rm Dec.}$ (mas yr^{-1})	3.7 ± 2.4	-2.6 ± 1.2	UCAC4
Spectroscopic properties			
$T_{\rm eff\star}$ (K)	5311 ± 77	5738 ± 79	ZASPE[a]
[Fe/H]	0.000 ± 0.050	-0.100 ± 0.050	ZASPE
$v \sin i$ (km s^{-1}) ...	4.18 ± 0.50	6.17 ± 0.22	ZASPE
$v_{\rm mac}$ (km s^{-1})	3.3	4.0	Assumed[b]
$v_{\rm mic}$ (m s^{-1})	0.85	1.06	Assumed[c]
$\gamma_{\rm RV}$ (km s^{-1})	-54.145 ± 0.020	31.594 ± 0.023	FEROS[d]
Photometric properties			
B (mag)	15.797 ± 0.030	14.477 ± 0.060	APASS[e]
V (mag)	14.774 ± 0.010	13.834 ± 0.020	APASS[e]
g (mag)	15.323 ± 0.010	14.086 ± 0.020	APASS[e]
r (mag)	14.592 ± 0.010	13.645 ± 0.010	APASS[e]
i (mag)	14.320 ± 0.010	13.496 ± 0.030	APASS[e]
J (mag)	13.261 ± 0.027	12.652 ± 0.024	2MASS
H (mag)	12.806 ± 0.024	12.335 ± 0.025	2MASS
K_s (mag)	12.724 ± 0.032	12.280 ± 0.021	2MASS
Derived properties			
$M_\star$ ($M_\odot$)	0.871 ± 0.023	0.970 ± 0.035	YY+$\rho_\star$+ZASPE [f]
$R_\star$ ($R_\odot$)	0.922 ± 0.027	$1.238^{+0.097}_{-0.127}$	YY+$\rho_\star$+ZASPE
$\log g_\star$ (cgs)	4.449 ± 0.022	4.239 ± 0.079	YY+$\rho_\star$+ZASPE
$\rho_\star$ (g cm^{-3})	1.57 ± 0.12	$0.72^{+0.26}_{-0.13}$	YY+$\rho_\star$+ZASPE [g]
$L_\star$ ($L_\odot$)	0.625 ± 0.057	1.49 ± 0.29	YY+$\rho_\star$+ZASPE
M_V (mag)	5.43 ± 0.11	4.41 ± 0.23	YY+$\rho_\star$+ZASPE
M_K (mag,ESO) ..	3.556 ± 0.071	2.85 ± 0.21	YY+$\rho_\star$+ZASPE
Age (Gyr)	$11.0^{+1.4}_{-2.0}$	9.5 ± 1.8	YY+$\rho_\star$+ZASPE
A_V (mag)	0.151 ± 0.063	0.000 ± 0.021	YY+$\rho_\star$+ZASPE
Distance (pc)	689 ± 23	774 ± 74	YY+$\rho_\star$+ZASPE
$P_{\rm rot\star}$ (d)	···	12.350 ± 0.024	HATS light curves

Note. — For HATS-15b the fixed-circular-orbit model has a Bayesian evidence that is ~ 2 times larger than the evidence for the eccentric-orbit model, while for HATS-16b the fixed-circular-orbit model has a Bayesian evidence that is ~ 6 times larger than the evidence for the eccentric-orbit model. We therefore assume a fixed circular orbit in generating the parameters listed here.

[a] ZASPE = Zonal Atmospherical Stellar Parameter Estimator routine for the analysis of high-resolution spectra (Brahm et al. 2015), applied to the PFS and FEROS spectra of HATS-15 and HATS-16 respectively. These parameters rely primarily on ZASPE, but have a small dependence also on the iterative analysis incorporating the isochrone search and global modeling of the data.

[b] The macro-turbulence values are obtained using the relations presented in Valenti & Fischer (2005)

[c] The micro-turbulence values are computed interpolating the results reported in the SWEET-Cat catalogue (Santos et al. 2013) for the relative $T_{\rm eff}$ and $\log g$.

[d] The error on $\gamma_{\rm RV}$ is determined from the orbital fit to the FEROS RV measurements, and does not include the systematic uncertainty in transforming the velocities from FEROS to the IAU standard system. The velocities have not been corrected for gravitational redshifts.

[e] From APASS DR6 for HATS-15, HATS-16 as listed in the UCAC 4 catalog (Zacharias et al. 2012).

[f] YY+$\rho_\star$+ZASPE = Based on the YY isochrones (Yi et al. 2001), $\rho_\star$ as a luminosity indicator, and the ZASPE results.

[g] In the case of $\rho_\star$ the parameter is primarily determined from the global fit to the light curves and RV data. The value shown here also has a slight dependence on the stellar models and ZASPE parameters due to restricting the posterior distribution to combinations of $\rho_\star$+$T_{\rm eff\star}$+[Fe/H] that match to a YY stellar model.

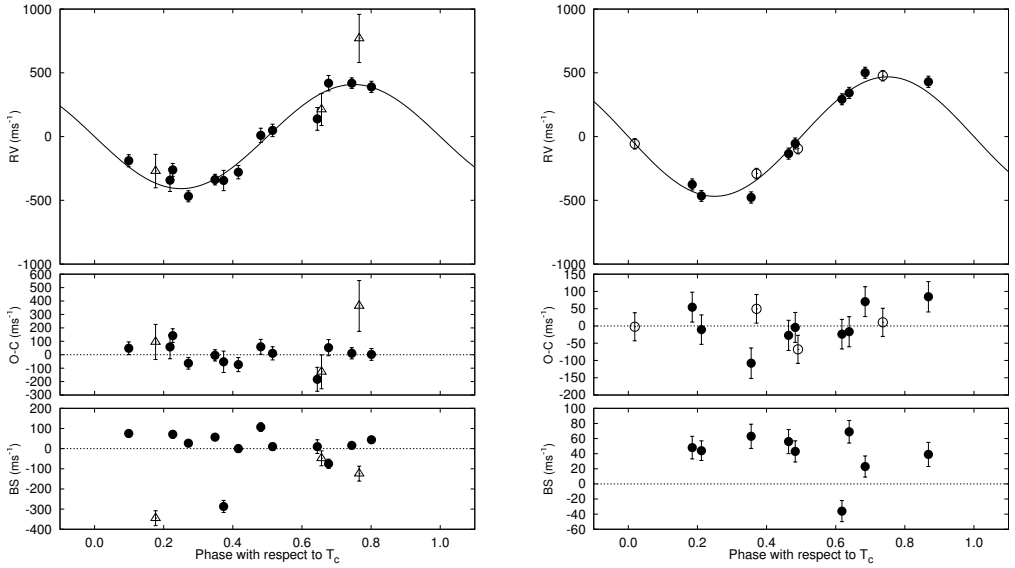

Figure 2. Phased high-precision RV measurements for HATS-15 (left), and HATS-16 (right) from FEROS (filled circles), Coralie (open triangles), and HIRES (open circles). The top panel shows the phased measurements together with our best-fit circular-orbit model (see Table 5) for each system. Zero-phase corresponds to the time of mid-transit and the center-of-mass velocity has been subtracted. The second panel shows the velocity $O-C$ residuals from the best fit. The error bars include the jitter terms listed in Table 5 added in quadrature to the formal errors for each instrument. The third panel shows the bisector spans (BS). Note the different vertical scales of the panels.

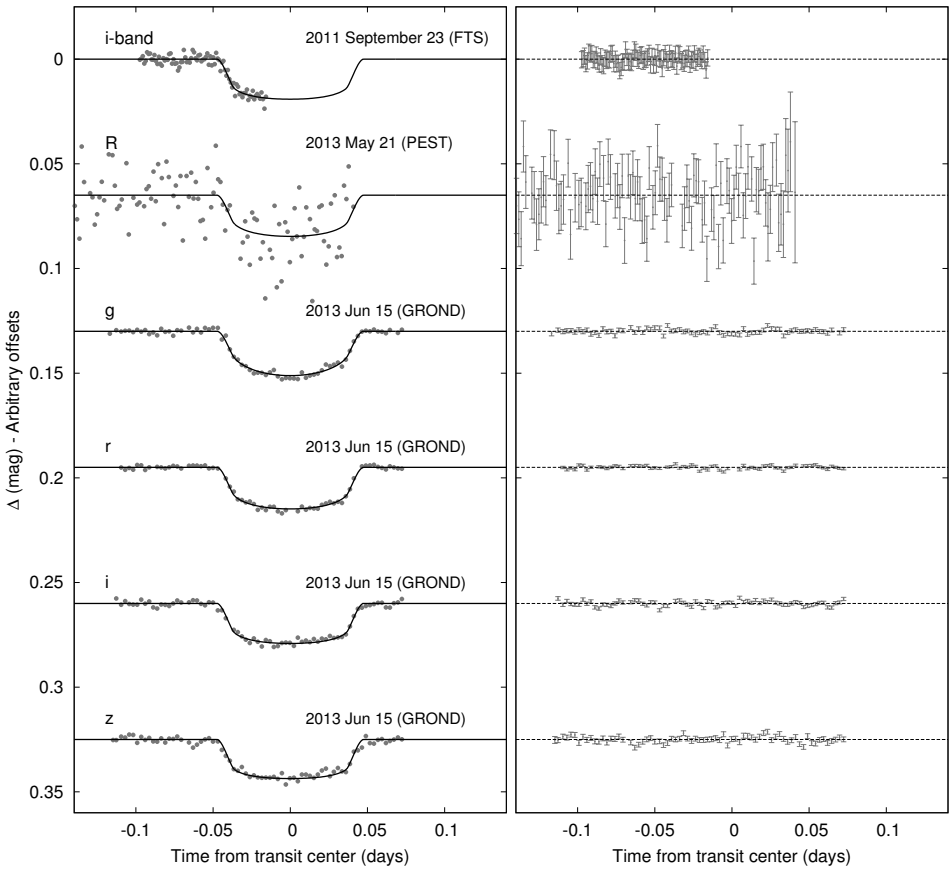

Figure 3. Left: Unbinned transit light curves for HATS-15. The light curves have been corrected for quadratic trends in time fitted simultaneously with the transit model. The dates of the events, filters and instruments used are indicated. Light curves following the first are displaced vertically for clarity. Our best fit from the global modeling described in Section 3.5 is shown by the solid lines. Right: residuals from the fits are displayed in the same order as the left curves. The error bars represent the photon and background shot noise, plus the readout noise.

consistent with the expected reddening at the Galactic position of both the systems. We found that, within the error bars the A_V are consistent with those predicted from the extinction map by Schlegel et al. (1998) and Schlafly & Finkbeiner (2011). HATS-15 is 690 ± 23 pc distant from the Sun, and HATS-16 is slightly farther away at 774 ± 74 pc.

3.2. *Rotational modulation*

We inspected the entire light curves obtained from the HATS survey of both HATS-15 and HATS-16, in order to look for possible periodic modulations, caused by the presence of star spots on the surface of the host stars.

Already with a quick look at the light curves, it is possible to identify a periodicity around 12-13 days for HATS-16, while no perceivable modulation is visible in the HATS-15 photometry. In order to quantify the variability and check for possible false alarm, we used GLS, a FORTRAN based routine by Zechmeister & Kürster (2009), to calculate the generalized Lomb-Scargle periodogram. In brief the data are fitted with a sinusoidal function at different frequencies starting from a provided minimum of 0.0056 [1/d] (that is related to the time range over which the photometric data were acquired) to a maximum frequency of 22.33, with about 79000 steps. A window function is also provided, giving information on the possible false periodicity created by the data sampling. We found a peak in the frequencies corresponding to a period of $P = 12.350 \pm 0.024$ days and an amplitude of 2.91 ± 0.47 mmag, with an extremely low false alarm probability (FAP, Cumming 2004).

As a sanity check, we obtained the periodogram in several different ways always obtaining consistent values of the period. In particular, we calculated the periodogram both for the un-binned and binned data (using several bin sizes) and using also another program (Systemic2, by Meschiari et al. 2009) besides GLS. If the modulation is due to the activity of the star, then the amplitude of the periodic signal may vary in time with the spot coverage, while the period remains constant. We checked for this effect by dividing our data-set into three segments and calculating a periodogram for each one. The three

Table 5
Orbital and planetary parameters for HATS-15b and HATS-16b

Parameter	**HATS-15 b** Value	**HATS-16 b** Value
Light curve parameters		
P (days)	$1.74748753 \pm 0.00000094$	2.686502 ± 0.000011
T_c (BJD) [a]	$2456387.21161 \pm 0.00015$	$2456824.79069 \pm 0.00076$
T_{12} (days) [a]	0.09457 ± 0.00074	0.1092 ± 0.0032
$T_{12} = T_{34}$ (days) [a]	0.01144 ± 0.00069	0.0211 ± 0.0044
$a/R_\star$	6.33 ± 0.16	$6.50^{+0.70}_{-0.43}$
$\zeta/R_\star$ [b]	$23.991^{+0.118}_{-0.081}$	22.27 ± 0.49
$R_p/R_\star$	0.1229 ± 0.0012	0.1075 ± 0.0037
b^2	$0.100^{+0.044}_{-0.054}$	$0.536^{+0.065}_{-0.125}$
$b \equiv a\cos i/R_\star$	$0.317^{+0.064}_{-0.101}$	$0.732^{+0.043}_{-0.091}$
i (deg)	$87.13^{+0.97}_{-0.67}$	$83.53^{+1.37}_{-0.86}$
Limb-darkening coefficients [c]		
c_1, g (linear term)	0.6795	...
c_2, g (quadratic term)	0.1376	...
c_1, r	0.4560	0.3526
c_2, r	0.2619	0.3264
c_1, i	0.3470	...
c_2, i	0.2834	...
c_1, z	0.2742	...
c_2, z	0.2937	...
c_1, R	0.4259	0.3289
c_2, R	0.2687	0.3276
RV parameters		
K ($\mathrm{m\,s^{-1}}$)	399 ± 26	485 ± 25
e [d]	< 0.126	< 0.000
Planetary parameters		
M_p (M_J)	2.17 ± 0.15	3.27 ± 0.19
R_p (R_J)	1.105 ± 0.040	1.30 ± 0.15
$C(M_p, R_p)$ [e]	0.18	0.10
ρ_p ($\mathrm{g\,cm^{-3}}$)	1.97 ± 0.24	$1.86^{+0.94}_{-0.48}$
$\log g_p$ (cgs)	3.641 ± 0.040	$3.685^{+0.117}_{-0.086}$
a (AU)	0.02712 ± 0.00023	0.03744 ± 0.00045
T_eq (K)	1505 ± 30	1592^{+61}_{-82}
Θ [f]	0.1211 ± 0.0088	$0.194^{+0.030}_{-0.021}$
$\log_{10}\langle F\rangle$ (cgs) [g]	9.064 ± 0.035	$9.161^{+0.065}_{-0.092}$

Note. — For HATS-15b the fixed-circular-orbit model has a Bayesian evidence that is ~ 2 times larger than the evidence for the eccentric-orbit model, while for HATS-16b the fixed-circular-orbit model has a Bayesian evidence that is ~ 6 times larger than the evidence for the eccentric-orbit model. We therefore assume a fixed-circular-orbit in generating the parameters listed here.

[a] Times are in Barycentric Julian Date calculated directly from UTC *without* correction for leap seconds. T_c: Reference epoch of mid transit that minimizes the correlation with the orbital period. T_{12}: total transit duration, time between first to last contact; $T_{12} = T_{34}$: ingress/egress time, time between first and second, or third and fourth contact.

[b] Reciprocal of the half duration of the transit used as a jump parameter in our MCMC analysis in place of $a/R_\star$. It is related to $a/R_\star$ by the expression $\zeta/R_\star = a/R_\star(2\pi(1 + e\sin\omega))/(P\sqrt{1-b^2}\sqrt{1-e^2})$ (Bakos et al. 2010).

[c] Values for a quadratic law, adopted from the tabulations by Claret (2004) according to the spectroscopic (ZASPE) parameters listed in Table 4.

[d] For fixed circular orbit models we list the 95% confidence upper limit on the eccentricity determined when $\sqrt{e}\cos\omega$ and $\sqrt{e}\sin\omega$ are allowed to vary in the fit.

[e] Correlation coefficient between the planetary mass M_p and radius R_p estimated from the posterior parameter distribution.

[f] The Safronov number is given by $\Theta = \frac{1}{2}(V_\mathrm{esc}/V_\mathrm{orb})^2 = (a/R_p)(M_p/M_\star)$ (see Hansen & Barman 2007).

[g] Incoming flux per unit surface area, averaged over the orbit.

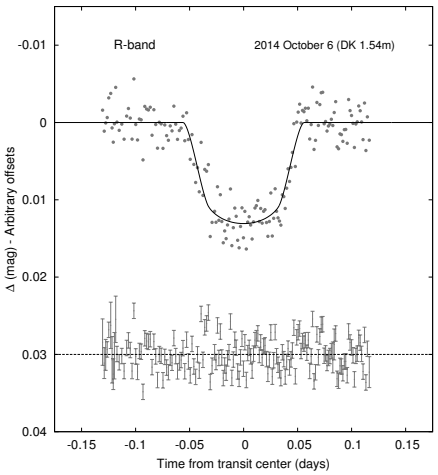

Figure 4. Similar to Figure 3; we show the follow-up light curve for HATS-16. In this case, variations in the light curve that are correlated with the FWHM of the PSF are corrected simultaneously to the fitting of the transit.

periods are consistent within the error bars, even if in the last dataset the significance of the first peak is lower, as the amplitude of the signal is smaller than that in the first two cases. We assume the variability is due to the apparent spot coverage of the star changing as the star rotates and take the photometric period to be a measure of the stellar rotational period.

By comparing the rotational period found from the photometry to that inferred from the spectroscopic $v \sin i$ (assuming $\sin i = 1$ and propagating the errors we obtain $P = 10.148^{+0.874}_{-1.102}$ days), we find a slight inconsistency: the two periods are nearly 2σ away, and the latter is smaller than the first one. However, we stress that the measurement of the $v \sin i$ should be considered as an upper limit. It actually describes the broadening of the spectral lines that is caused by a multiplicity of other effects, which are difficult to take into account. Moreover, the rotational period found from photometry doesn't take into account the possibility to have differential rotation. As the latitude of the spot group causing the photometric signal is unknown, the mean period might be larger (if the spots lie around the equator) or smaller (if the spots have a high latitude).

The periodogram, and the phase folded HATSouth photometry with the period of $P = 12.35$ d are shown in Figure 6.

3.3. *Age of the systems*

To determine the age of the two planetary systems, we used different methods. A first determination for both the systems was done by modeling the stellar parameters with the Y2 evolutionary model, which was already used in 3.1. We found an age of $11.0^{+1.4}_{-2.0}$ Gyr and 9.5 ± 1.8 Gyr for HATS-15 and HATS-16, respectively, which suggest that both the systems are old.

Since the rotation of a star is expected to slow down during its lifetime (e.g. Soderblom 1983), it is therefore possible to correlate the stellar period to its age through the gyrochronology. According to Barnes (2007) the errors in the age estimation via gyrochronology for G and K stars are about 28%. Following the relations in Barnes (2007), and using the improved coefficients values from Angus et al. (2015), we calculated the gyrochronology age of HATS-16 from the rotational period, finding that is younger than 1 Gyr. Using gyrochronology we also calculated the lower limit for the age of HATS-15 using the period obtained from $v \sin i$ and assuming $i = 90$ deg. However the lower limit we found of $\gtrsim 0.5$ Gyr does not give any useful constraint.

As expected from the rotational modulation (Figure 6), the HATS-16 star is slightly active and shows a cromospheric emission in the core of the Ca H & K absorption lines. We quantified this activity by calculating the activity indices from the ratio of the emission in the line cores, obtaining $S = 0.2524$ and $\log R'_{\rm H\,K} = -4.644$. Then, using the age-activity relation presented in Mamajek & Hillenbrand (2008), we estimated that the expected age of the star is 1.47 Gyr, compatible with the age based on gyrochronology, but substantially younger than the isochrone-based age.

A further way to constrain the age of a star is to measure its peculiar velocity in the Galactic frame and compare it with those of other stars in our Galaxy, whose age are well determined. Knowing the position of the planetary systems and their kinematics (radial velocity and proper motion measurements from Table 4), one may convert them to peculiar velocities U, V, W that describe the motion of a star in galactic coordinates. Specifically, U represents the radial component of the velocity, V is the circular component, and W is the vertical component with respect to the Milky Way disk. To compute the peculiar velocity of HATS-15 and HATS-16, we used a web-based calculator[4] provided by D. Rodriguez. We then corrected our velocity values for the peculiar motion of the Sun ($U_\odot = 7.01 \pm 0.20\,{\rm km\,s^{-1}}$, $V_\odot = 10.13 \pm 0.12\,{\rm km\,s^{-1}}$ and $W_\odot = 4.95 \pm 0.09\,{\rm km\,s^{-1}}$, Huang et al. 2015). The results obtained for both the planets are $U = -75.89\,{\rm km\,s^{-1}}$, $V = 6.18\,{\rm km\,s^{-1}}$ and $W = -12.03\,{\rm km\,s^{-1}}$ for HATS-15 and $U = -41.72\,{\rm km\,s^{-1}}$, $V = -30.85\,{\rm km\,s^{-1}}$ and $W = -43.00\,{\rm km\,s^{-1}}$ for HATS-16. For a very young star on a circular orbit, U and W should be close to 0 ${\rm km\,s^{-1}}$; stars with ages around 1 Gyr can have a higher dispersion in velocities, with an average value of the order of $10 - 12\,{\rm km\,s^{-1}}$; finally, at an age around 10 Gyr, the velocities are expected to be of the order of $25 - 35\,{\rm km\,s^{-1}}$ (Binney et al. 2000). This increase in velocity dispersion with age can be explained taking into account the fact that stars, initially formed in the galactic plane (where molecular clouds and star forming region are mainly located), interact with the galactic environment and gain vertical and radial velocity component in the galactic reference frame (Nordström et al. 2004, and reference therein). The peculiar velocities of our two stars, compared with the average velocities for the stars in our Galaxy, point towards an old age, which is in good agreement with the ones that we found from the isochrone fitting.

3.4. *Excluding blend scenarios*

[4] The calculator can be found at http://www.das.uchile.cl/drodrigu/UVWCalc.html

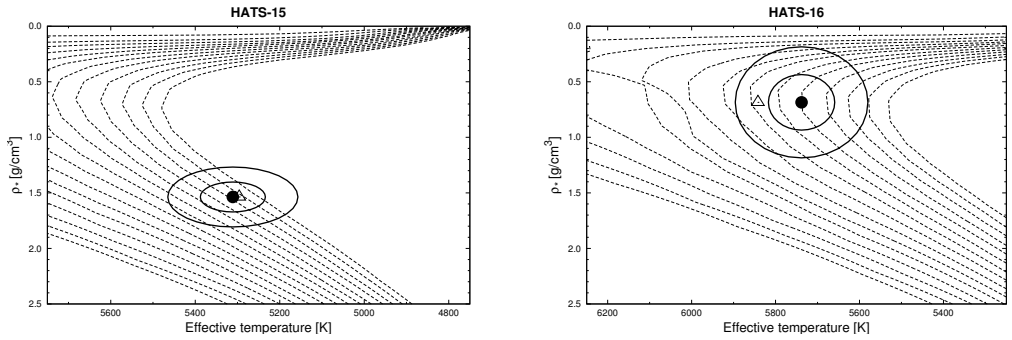

Figure 5. Model isochrones from Yi et al. (2001) for the measured metallicities of HATS-15 (left) and HATS-16 (right). We show models for ages of 0.2 Gyr and 1.0 to 14.0 Gyr in 1.0 Gyr increments (ages increasing from left to right). The adopted values of $T_{\rm eff\star}$ and $\rho_\star$ are shown together with their 1σ and 2σ confidence ellipsoids. The initial values of $T_{\rm eff\star}$ and $\rho_\star$ from the first ZASPE and light curve analysis are represented with a triangle.

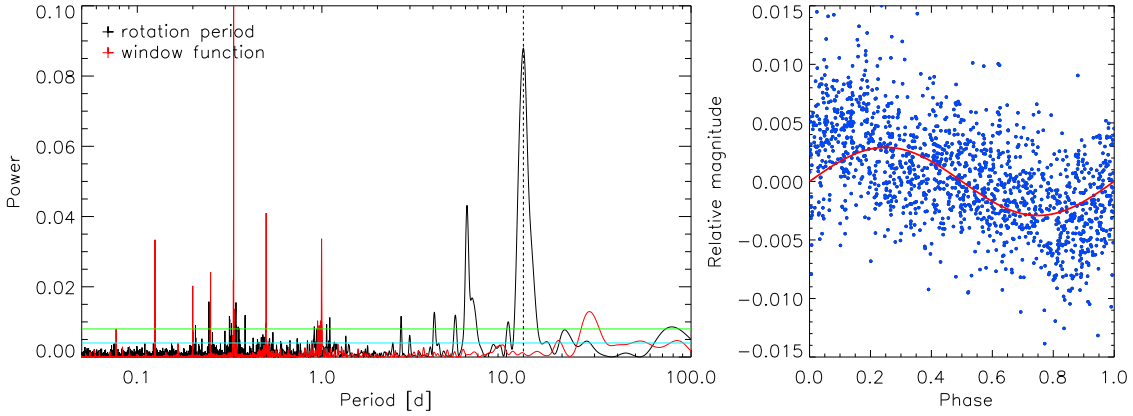

Figure 6. *Left:* periodogram for the HATSouth photometric data of HATS-16 obtained during the ∼6 months of observations. The horizontal lower (light blue) and upper (green) lines represent the false alarm probability FAP= 0.001 and 0.0001 respectively. In the same panel the window function is displayed with red lines. *Right:* HATSouth photometric data phase folded and binned in 0.001 phase bins for the period. The red solid line represent the best fit obtained.

One of the most common false positive scenarios for candidates produced by transiting surveys are blends. We attempt to exclude the possibility that our two planetary systems are not hosting planets, but instead are diluted eclipsing binaries, following Hartman et al. (2012).

We modeled the available photometric data for each object as a blend between an eclipsing binary star system and a third star along the line of sight. The physical properties of the stars were constrained using the Padova isochrones (Bertelli et al. 2008), while we also required that the brightest of the three stars in the blend had atmospheric parameters consistent with those measured with ZASPE.

We found that for both HATS-15 and HATS-16, a model consisting of a single star with a transiting planet provides a lower χ^2 fit to the available photometric data than any of the blended stellar eclipsing binary models tested. Based solely on the photometry, for HATS-15 we ruled out blend models with $\sim 1\sigma$ confidence, while for HATS-16 we rule them out with $\sim 2\sigma$ confidence. Moreover, we found that for both systems any blend model that could plausibly fit the photometry (i.e., which cannot be rejected with greater than 5σ confidence) would have been easily identified as a composite system based on the spectroscopic observations. Indeed, we simulated the cross-correlation functions for these possible blend systems, finding that in all the cases, at some of the observed phases, a double peak should have been seen, and that all of the blend scenarios which could plausibly fit the photometry of either system would have produced large RV and BS variations (greater than $1\,{\rm km\,s^{-1}}$), which is in conflict with the observations. We conclude, therefore, that both HATS-15 and HATS-16 are transiting planet systems, and that neither object is a blended stellar eclipsing binary system.

Albeit we can rule out the possibility that the two systems are not blended by an eclipsing binary, we cannot rule out the possibility that one of the two systems is a transiting planet system, whose photometry is diluted by the light coming from an unresolved stellar component. For HATS-15 we find that a system consisting of a $0.84\,M_\odot$ star with a transiting planet and a $0.65\,M_\odot$ binary companion provides a slightly better fit to the photometric data ($\sim 1.5\sigma$) than the best-fit single-star-

with-planet model. The secondary-to-primary V-band light ratio of this binary system is 14%, which would be marginally detectable in the observed CCFs unless the system were near conjunction. We also find that a binary star companion of any mass, up to that of the transiting planet host, provides a fit to the photometric data which cannot be distinguished from the best-fit single-star-with-planet model. For HATS-16 we find that binary star systems with a secondary mass between $0.65\,M_\odot$ and $0.8\,M_\odot$ can be ruled out at 3σ confidence based on the photometry. This is driven by the broad-band photometric colors which are consistent with the measured effective temperature of the primary star assuming no reddening. Binary companions close in mass to the primary yield similar photometric colors and are not ruled out, while binary companions below $0.65\,M_\odot$ are too faint to significantly affect the photometric colors. Higher spatial resolution imaging and/or continued RV monitoring would be needed to search for binary star companions to either system. For the remainder of the paper we assume that each of the two systems is an isolated star with a close-in transiting planet.

3.5. *Global modeling of the data*

In order to measure the physical properties of the two planets, we modeled all the photometric and spectroscopic data in our possession following the same approach as in Pál et al. (2008); Bakos et al. (2010); Hartman et al. (2012).

As far as it concerns the light curves, both the HATSouth and the follow-up ones, the fit was performed using the transit models from Mandel & Agol (2002), employing a quadratic law to describe the limb darkening effect, and fixing the coefficients to those from Claret (2004). In the case of the HATSouth photometry, in modelling the transit depth, we included an extra parameter describing the possible dilution caused by the blending of neighboring stars, and the over-correction by the trend-filtering method. To correct for systematic errors in the photometry of the follow-up light curves, a quadratic trend was included in the model of each transit event. The RV data were fitted with Keplerian orbits, allowing the zero-point and the RV jitter for each instrument to vary independently as a free parameter.

To determine the posterior distribution of the parameters and obtain the relative uncertainties we used a Differential Evolution Markov Chain Monte Carlo (DEMCMC ter Braak 2006; Eastman et al. 2013).

We fitted both fixed circular orbits and free-eccentricity models to the data, and for both systems found that the data are consistent with a circular orbit. As for both systems the fixed circular orbit model had a higher Bayesian evidence, we adopted the parameters assuming no eccentricity for either object.

The parameters obtained from this analysis for each system are listed in Table 5. In brief we found that HATS-15b has a mass of $M = 2.17 \pm 0.15\,M_{\rm J}$ and a radius of $R = 1.105 \pm 0.040\,R_{\rm J}$, resulting in a bulk density of $\rho = 1.48 \pm 0.18\,\rho_{\rm J}$. For HATS-16b, we found that it is more massive, $M = 3.27 \pm 0.19\,M_{\rm J}$, and larger, $R = 1.30 \pm 0.15\,R_{\rm J}$, which imply a slightly lower density, $\rho = 1.39^{+0.71}_{-36}\,\rho_{\rm J}$.

4. DISCUSSION AND CONCLUSION

We have presented the discovery of HATS-15b and HATS-16b, two massive hot Jupiters orbiting around old dwarf stars. By carefully analyzing the photometric and spectroscopic data, we can exclude false positive scenarios, confirming the planetary nature of the transiting bodies. We found that HATS-15 is a planetary system, ~ 690 pc far away from our Sun, that hosts a $2.17 \pm 0.15\,M_{\rm J}$ hot Jupiter, which orbits around a G9 V star in ~ 1.75 days. HATS-16b is a massive $3.27 \pm 0.19\,M_{\rm J}$ hot Jupiter ~ 770 pc away from us, and is orbiting a G3 V star in ~ 2.69 days. Fig. 7 shows the locations of the two new planets in the period–mass diagram, together with the other known transiting exoplanets.

In § 3.3, we have presented several methods to estimate the stellar ages. In the case of HATS-15, the two different methods that we used (Y2 isochrones fitting and stellar kinematics) gave consistent values; we therefore adopted the value found from the modeling with the Y2, which dates the star to be $11.0^{+1.4}_{-2.0}$ Gyr old.

Concerning HATS-16, instead, we found a strong discrepancy between the age measured with Y2 and stellar kinematics, compared with the one obtained with gyrochronology and stellar activity. However, we believe that the age obtained from the stellar evolutionary models (9.5 ± 1.8 Gyr) is more reliable than the very young age found based on its activity. Indeed, an old age is more compatible with the slightly low density of the star, compared to what is expected for a young star with its effective temperature and metallicity. Moreover, the short rotation period (12.4 d) of HATS-16, may be explained in a planet-star interaction context, in which the star has been tidally spun up by the planet (e.g. Pont 2009; Husnoo et al. 2012). Given the mass of the planet, its distance from the star, and assuming a stellar tidal quality factor (i.e. the efficiency of tidal dissipation in the star) Q_*=10^6, obtained from a rough estimation of the orbital evolution timescale (following Penev & Sasselov 2011), we calculated that just few Gyr are necessary for spinning up the star to its current rotation (here we have assumed that all the angular momentum is dumped in the convective zone, and that only a few percent change in the orbital period is needed).

Considering the entire population of known gas planets, most of the planets in the high-mass regime are found to orbit their star at a large distance, and just few tens are hot Jupiters (see Fig. 7). The rareness of massive giants with $M \gtrsim 2\,M_{\rm J}$ and $P \lesssim 5$ d cannot be explained by observational biases, since the two more efficient detection methods (transit and RV) are more prone to find massive planets in short orbits than in larger ones [5]

The reason of this paucity should be related to different channels that were undertaken by these planets during their formation and migration history. Alternatively, they are simply rarer than the lighter hot Jupiters, as it happens between planets and brown dwarfs. Actually, the existence of the brown-dwarf desert (i.e. companions

[5] In some cases, massive close-in giant planets may spin-up their parent star, causing higher values of its $v \sin i$ than expected, as in the present case of HATS-16 ($v \sin i = 6.17$). Then, a possible planetary candidate identified by a transiting or RV survey may be discarded, and not be further followed up, because of its fast rotating host star (Pont 2009). For this reason, planet-candidate rejections based on $v \sin i$ should be relaxed in order to do not miss possible massive hot Jupiters.

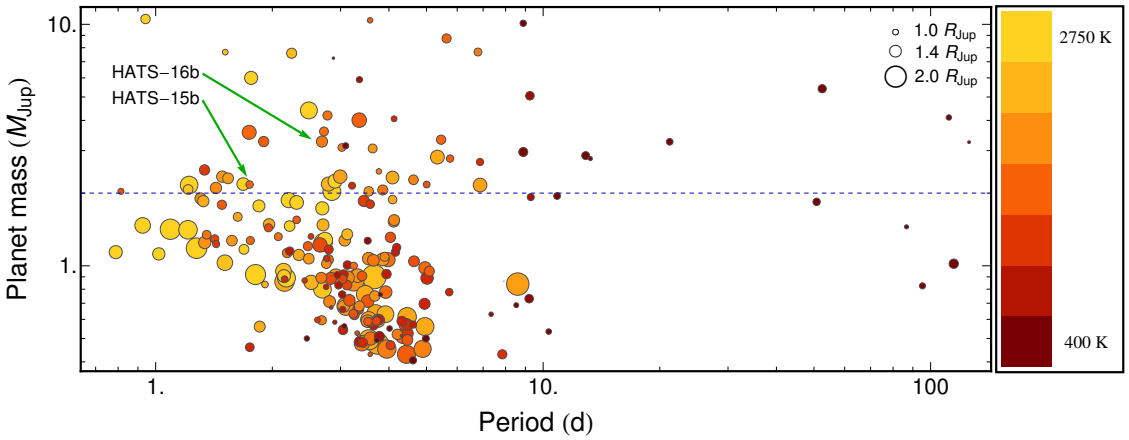

Figure 7. Mass–period diagram of transiting exoplanets in the mass range $0.4\,M_J < M_p < 10\,M_J$. The planets are represented by circles, whose size is proportional to planet radius. Color indicates equilibrium temperature. The dashed line demarcates the high-mass regime ($M_p > 2\,M_J$). The error bars have been suppressed for clarity. Data taken from the Transiting Extrasolar Planet Catalogue (TEPCat), which is available at http://www.astro.keele.ac.uk/jkt/tepcat/.

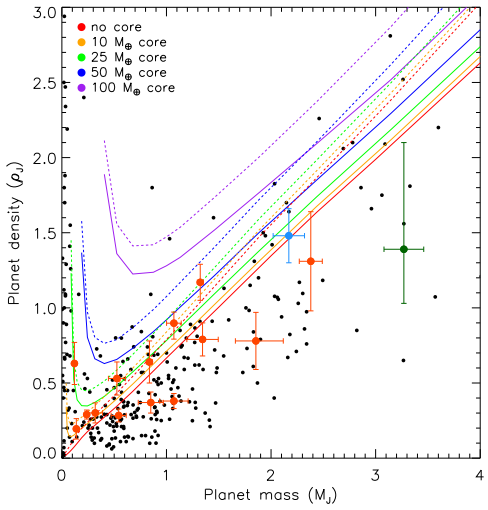

Figure 8. The HATSouth planets (highlighted in orange) are presented in the mass–density diagram of the known transiting planets. The planets described in this paper are shown in light blue (HATS-15) and dark green (HATS-16). The superimposed lines represent the expected radius of the planet having an inner core of 0, 10, 25, 50 and 100 Earth masses, and calculated for 10 Gyr old planets at 0.02 au, solid lines, and 0.045 au, dashed lines (Fortney et al. 2007).

in the mass range $10-100\,M_J$ are ~ 1 order-of-magnitude rarer compared to less massive objects, e.g., Winn & Fabrycky 2014 and references therein) is by now well ascertained. Finding and characterizing new hot Jupiters is the only key to clarify the causes of the rareness of massive hot Jupiters and the ongoing ground-based surveys, as well as the upcoming (TESS, Ricker et al. 2009) and future (PLATO, Catala & Plato Team 2006) space missions, are essential for this purpose.

Using the planetary mass–density relations for planets with $M_p \gtrsim 0.4\,M_J$ presented in Bakos et al. (2015), we find that both the planets fall within the predicted range, in particular HATS-15b shows an average density among the planets with the same mass, while HATS-16b lies close to the lower limit of the relation. In addition, comparing the mass and radius of the two planets with the predictions of Fortney et al. (2007), we give some constraints on the presence of an inner heavy core. According to the distance from its parent star, the age of the system and for a fixed planetary mass, the expected radius of the planet is computed in the cases of different internal core masses. We found that HATS-16b is well described by a core-less model, whereas in the case of HATS-15b we expect that it has a very light core. Indeed, we can exclude the case of a massive core as our measurement is only consistent with models predicting a core-mass lower than $50\,M_\oplus$ (see Fig. 8).

Comparing HATS-16 b with known planets in the same mass range, we found that the majority of the planets are located far away from their host star having periods greater than 200 days. The eccentricity distribution for those planets seems to be more flat than for the confirmed planets with smaller masses, where there is a slight preference for circular orbits. Howbeit, this can be easily explained taking into account the fact most of those planets have very short periods and therefore are more prone to suffer from circularizations and tidal locking mechanism that result in circular orbits.

In the mass–period parameter space the twin systems to HATS-16 are Kepler-43 (Bonomo et al. 2012) and WASP-10 (Christian et al. 2009). The first system doesn't show any hint of stellar activity or planet-star interaction, however this might not be surprising given the young age of the system. In the latter case the planet has an eccentric orbit that, assuming a $Q_* \sim 10^5$ or $\sim 10^6$, should have disappeared because of circularizations due to tidal interaction, but still persist indicating some other form of interaction e.g. the presence of an external massive body belonging to the same system.

Although having a mass twice that of Jupiter, HATS-

15 b lies in a more populated region of the parameter space than HATS-16 b. There are indeed both long period and short period planets in its mass range that share their average properties with all the other planets. HATS-15 b finds its twin planet in WASP-87A b (Anderson et al. 2014). The main difference between the two planetary systems is that while HATS-15 is a single star, WASP-87 is composed by two stars: the mid-F type host star and a mid-G companion. More over given the different spectral class of the host star HATS-15 b has a less inflated radius than its twin and is therefore denser.

Development of the HATSouth project was funded by NSF MRI grant NSF/AST-0723074, operations have been supported by NASA grants NNX09AB29G and NNX12AH91H, and follow-up observations receive partial support from grant NSF/AST-1108686. A.J. acknowledges support from FONDECYT project 1130857, BASAL CATA PFB-06, and project IC120009 "Millennium Institute of Astrophysics (MAS)" of the Millenium Science Initiative, Chilean Ministry of Economy. R.B. and N.E. are supported by CONICYT-PCHA/Doctorado Nacional. R.B. and N.E. acknowledge additional support from project IC120009 "Millenium Institute of Astrophysics (MAS)" of the Millennium Science Initiative, Chilean Ministry of Economy. V.S. acknowledges support form BASAL CATA PFB-06. M.R. acknowledges support from FONDECYT postdoctoral fellowship 3120097. This work is based on observations made with Telescopes at the ESO La Silla Observatory. This paper also uses observations obtained with facilities of the Las Cumbres Observatory Global Telescope. Work at the Australian National University is supported by ARC Laureate Fellowship Grant FL0992131. We acknowledge the use of the AAVSO Photometric All-Sky Survey (APASS), funded by the Robert Martin Ayers Sciences Fund, and the SIMBAD database, operated at CDS, Strasbourg, France. The imaging system GROND has been built by the high-energy group of MPE in collaboration with the LSW Tautenburg and ESO.

We thank F. Rodler, W. Brandner, M. Wöllert and J. Schliederfor useful comments and advices. We thank Helmut Steinle and Jochen Greiner for supporting the GROND observations presented in this manuscript. We are grateful to P.Sackett for her help in the early phase of the HATSouth project.

REFERENCES

????
08. 1
Anderson, D. R., Brown, D. J. A., Collier Cameron, A., et al. 2014, ArXiv e-prints, 1410.3449
Angus, R., Aigrain, S., Foreman-Mackey, D., & McQuillan, A. 2015, MNRAS, 450, 1787
Bakos, G., Noyes, R. W., Kovács, G., et al. 2004, PASP, 116, 266
Bakos, G. Á., Torres, G., Pál, A., et al. 2010, ApJ, 710, 1724
Bakos, G. Á., Csubry, Z., Penev, K., et al. 2013, PASP, 125, 154
Bakos, G. Á., Penev, K., Bayliss, D., et al. 2015, ArXiv e-prints, 1507.01024
Barnes, S. A. 2007, ApJ, 669, 1167
Bayliss, D., Zhou, G., Penev, K., et al. 2013, AJ, 146, 113
Bayliss, D., Hartman, J. D., Bakos, G. Á., et al. 2015, ArXiv e-prints, 1506.01334
Bertelli, G., Girardi, L., Marigo, P., & Nasi, E. 2008, A&A, 484, 815
Bertin, E., & Arnouts, S. 1996, A&AS, 117, 393
Binney, J., Dehnen, W., & Bertelli, G. 2000, MNRAS, 318, 658
Bonomo, A. S., Hébrard, G., Santerne, A., et al. 2012, A&A, 538, A96
Borucki, W. J., Koch, D., Basri, G., et al. 2010, Science, 327, 977
Brahm, R., et al. 2015, in prep.
Cardelli, J. A., Clayton, G. C., & Mathis, J. S. 1989, ApJ, 345, 245
Catala, C., & Plato Team. 2006, in ESA Special Publication, Vol. 1306, ESA Special Publication, ed. M. Fridlund, A. Baglin, J. Lochard, & L. Conroy, 497
Christian, D. J., Gibson, N. P., Simpson, E. K., et al. 2009, MNRAS, 392, 1585
Claret, A. 2004, A&A, 428, 1001
Coelho, P. R. T. 2014, MNRAS, 440, 1027
Crane, J. D., Shectman, S. A., Butler, R. P., et al. 2010, in Society of Photo-Optical Instrumentation Engineers (SPIE) Conference Series, Vol. 7735, Society of Photo-Optical Instrumentation Engineers (SPIE) Conference Series
Cumming, A. 2004, MNRAS, 354, 1165
Deeg, H. J., & Doyle, L. R. 2001, in Third Workshop on Photometry, ed. W. J. Borucki & L. E. Lasher, 85
Dong, S., & Zhu, Z. 2013, ApJ, 778, 53
Dopita, M., Hart, J., McGregor, P., et al. 2007, Ap&SS, 310, 255
Eastman, J., Gaudi, B. S., & Agol, E. 2013, PASP, 125, 83
Fortney, J. J., Marley, M. S., & Barnes, J. W. 2007, ApJ, 659, 1661
Fressin, F., Torres, G., Charbonneau, D., et al. 2013, ApJ, 766, 81
Fulton, B. J., Collins, K. A., Gaudi, B. S., et al. 2015, ArXiv e-prints, 1505.06738
Greiner, J., Bornemann, W., Clemens, C., et al. 2008, PASP, 120, 405
Hansen, B. M. S., & Barman, T. 2007, ApJ, 671, 861
Hartman, J. D., Bakos, G. Á., Béky, B., et al. 2012, AJ, 144, 139
Howard, A. W., Marcy, G. W., Bryson, S. T., et al. 2012, ApJS, 201, 15
Huang, Y., Liu, X.-W., Yuan, H.-B., et al. 2015, MNRAS, 449, 162
Husnoo, N., Pont, F., Mazeh, T., et al. 2012, MNRAS, 422, 3151
Husser, T.-O., Wende-von Berg, S., Dreizler, S., et al. 2013, A&A, 553, A6
Jiang, I.-G., Yeh, L.-C., Chang, Y.-C., & Hung, W.-L. 2007, AJ, 134, 2061
Jordán, A., Brahm, R., Bakos, G. Á., et al. 2014, AJ, 148, 29
Kaufer, A., & Pasquini, L. 1998, in Society of Photo-Optical Instrumentation Engineers (SPIE) Conference Series, Vol. 3355, Optical Astronomical Instrumentation, ed. S. D'Odorico, 844–854
Kovács, G., Bakos, G., & Noyes, R. W. 2005, MNRAS, 356, 557
Kovács, G., Zucker, S., & Mazeh, T. 2002, A&A, 391, 369
Mamajek, E. E., & Hillenbrand, L. A. 2008, ApJ, 687, 1264
Mandel, K., & Agol, E. 2002, ApJ, 580, L171
Marcy, G. W., & Butler, R. P. 1992, PASP, 104, 270
Marsh, T. R. 1989, PASP, 101, 1032
Mayor, M., Marmier, M., Lovis, C., et al. 2011, ArXiv e-prints, 1109.2497
Meschiari, S., Wolf, A. S., Rivera, E., et al. 2009, PASP, 121, 1016
Mohler-Fischer, M., Mancini, L., Hartman, J. D., et al. 2013, A&A, 558, A55
Nordström, B., Mayor, M., Andersen, J., et al. 2004, A&A, 418, 989
Pál, A., Bakos, G. Á., Torres, G., et al. 2008, ApJ, 680, 1450
Penev, K., & Sasselov, D. 2011, ApJ, 731, 67
Penev, K., Bakos, G. Á., Bayliss, D., et al. 2013, AJ, 145, 5
Pollacco, D. L., Skillen, I., Collier Cameron, A., et al. 2006, PASP, 118, 1407
Pont, F. 2009, MNRAS, 396, 1789
Queloz, D., Mayor, M., Udry, S., et al. 2001, The Messenger, 105, 1
Rabus, M., et al. 2015, in prep.
Ricker, G. R., Latham, D. W., Vanderspek, R. K., et al. 2009, in Bulletin of the American Astronomical Society, Vol. 41
Santos, N. C., Sousa, S. G., Mortier, A., et al. 2013, A&A, 556, A150
Schlafly, E. F., & Finkbeiner, D. P. 2011, ApJ, 737, 103

Schlegel, D. J., Finkbeiner, D. P., & Davis, M. 1998, ApJ, 500, 525
Seager, S., & Mallén-Ornelas, G. 2003, ApJ, 585, 1038
Soderblom, D. R. 1983, ApJS, 53, 1
Sozzetti, A., Torres, G., Charbonneau, D., et al. 2007, ApJ, 664, 1190
ter Braak, C. J. F. 2006, Statistics and Computing, 16, 239
Torres, G., Bakos, G. Á., Kovács, G., et al. 2007, ApJ, 666, L121
Valenti, J. A., & Fischer, D. A. 2005, ApJS, 159, 141
Vogt, S. S., Allen, S. L., Bigelow, B. C., et al. 1994, in Society of Photo-Optical Instrumentation Engineers (SPIE) Conference Series, Vol. 2198, Instrumentation in Astronomy VIII, ed. D. L. Crawford & E. R. Craine, 362
Winn, J. N., & Fabrycky, D. C. 2014, ArXiv e-prints, 1410.4199
Yi, S., Demarque, P., Kim, Y.-C., et al. 2001, ApJS, 136, 417
Zacharias, N., Finch, C. T., Girard, T. M., et al. 2012, VizieR Online Data Catalog, 1322, 0
Zechmeister, M., & Kürster, M. 2009, A&A, 496, 577
Zhou, G., Bayliss, D., Hartman, J. D., et al. 2014, MNRAS, 437, 2831

Table 6
Relative radial velocities and bisector spans for HATS-15 and HATS-16.

BJD (2,456,000+)	RV[a] ($m\,s^{-1}$)	σ_{RV}[b] ($m\,s^{-1}$)	BS ($m\,s^{-1}$)	σ_{BS} ($m\,s^{-1}$)	Phase	Instrument
HATS-15						
−188.27661	418.77	54.00	−75.0	23.0	0.677	FEROS
−186.41173	418.77	32.00	16.0	15.0	0.744	FEROS
−185.23774	−279.23	45.00	0.0	19.0	0.416	FEROS
81.70953	−270.39	131.00	−345.0	37.0	0.176	Coralie
82.73890	769.61	189.00	−124.0	37.0	0.766	Coralie
146.71065	−344.23	75.00	−287.0	30.0	0.373	FEROS
162.62586	9.77	49.00	107.0	21.0	0.481	FEROS
167.63696	−337.23	32.00	57.0	15.0	0.348	FEROS
172.74493	−468.23	34.00	27.0	15.0	0.271	FEROS
241.56988	212.61	126.00	−48.0	37.0	0.657	Coralie
400.84394	389.77	35.00	44.0	16.0	0.801	FEROS
404.85903	−189.23	39.00	75.0	17.0	0.099	FEROS
406.82914	−261.23	43.00	71.0	19.0	0.226	FEROS
424.80863	48.77	41.00	10.0	18.0	0.515	FEROS
426.78243	138.77	85.00	10.0	34.0	0.644	FEROS
427.78530	−342.23	84.00	···	···	0.218	FEROS
HATS-16						
841.86396	−477.43	18.00	63.0	16.0	0.355	FEROS
844.89323	−54.43	16.00	43.0	14.0	0.483	FEROS
846.85037	−465.43	14.00	44.0	13.0	0.211	FEROS
852.89702[c]	−435.43	19.0	−215	16.0	0.462	FEROS
853.84870[c]	439.57	23.0	−363	19.0	0.816	FEROS
854.90341[c]	−482.43	19.0	−429	16.0	0.208	FEROS
858.68871	292.57	15.00	−36.0	14.0	0.618	FEROS
858.86912	500.57	16.00	23.0	14.0	0.685	FEROS
866.80486	342.57	17.00	69.0	15.0	0.639	FEROS
871.70647	−133.43	17.00	56.0	16.0	0.464	FEROS
908.12221	−57.08	5.94	···	···	0.019	HIRES
909.06821	−290.30	9.17	···	···	0.371	HIRES
910.05021	477.26	6.37	···	···	0.736	HIRES
912.07720	−94.72	6.24	···	···	0.491	HIRES
932.74739	−375.43	16.00	48.0	15.0	0.185	FEROS
942.64274	429.57	18.00	39.0	16.0	0.868	FEROS

[a] The zero-point of these velocities is arbitrary. An overall offset γ_{rel} fitted independently to the velocities from each instrument has been subtracted.
[b] Internal errors excluding the component of astrophysical jitter considered in Section 3.5.
[c] These observations were excluded from the analysis because the extracted spectra had significant contamination from scattered moonlight leading to large systematic errors in the measured RVs and BSs.

Chapter 4

Confirmation of a new planet: Kepler-432 b

In this chapter we present the confirmation of the planetary nature of Kepler-432 b, pubblished in A&A in 2015: Ciceri et al. (2015a)

Odi et amo, quare id faciam fortasse requiris
nescio, sed fieri sentio, et excrucio

Carmen LXXXV, Catullo

A&A 573, L5 (2015)
DOI: 10.1051/0004-6361/201425145

Astronomy & Astrophysics

L E

Kepler-432 b: a massive planet in a highly eccentric orbit transiting a red giant⋆

S. Ciceri[1], J. Lillo-Box[2], J. Southworth[3], L. Mancini[1], Th. Henning[1], and D. Barrado[3]

[1] Max Planck Institute for Astronomy, Königstuhl 17, 69117, Heidelberg, Germany
e-mail: ciceri@mpia.de
[2] Departamento de Astrofísica, Centro de Astrobiología (CSIC-INTA), 28691 Villanueva de la Cañada, Madrid, Spain
[3] Astrophysics Group, Keele University, Staffordshire, ST5 5BG, UK

Received 10 October 2014 / Accepted 28 November 2014

ABSTRACT

We report the first disclosure of the planetary nature of Kepler-432 b (aka *Kepler* object of interest KOI-1299.01). We accurately constrained its mass and eccentricity by high-precision radial velocity measurements obtained with the CAFE spectrograph at the CAHA 2.2-m telescope. By simultaneously fitting these new data and *Kepler* photometry, we found that Kepler-432 b is a dense transiting exoplanet with a mass of $M_p = 4.87 \pm 0.48\,M_{Jup}$ and radius of $R_p = 1.120 \pm 0.036\,R_{Jup}$. The planet revolves every 52.5 d around a K giant star that ascends the red giant branch, and it moves on a highly eccentric orbit with $e = 0.535 \pm 0.030$. By analysing two near-IR high-resolution images, we found that a star is located at 1.1″ from Kepler-432, but it is too faint to cause significant effects on the transit depth. Together with Kepler-56 and Kepler-91, Kepler-432 occupies an almost-desert region of parameter space, which is important for constraining the evolutionary processes of planetary systems.

Key words. planetary systems – stars: fundamental parameters – stars: individual: Kepler-432

1. Introduction

Since its first data release (Borucki et al. 2011a), the *Kepler* spacecraft has been the most productive planet-hunting mission. It has allowed the discovery of over 4000 exoplanet candidates to date, with a very low false positive frequency at least for small planets (e.g. Marcy et al. 2014; Fabrycky et al. 2014). The false-positive rate is higher (∼70%) for *Kepler*'s giant stars (Sliski & Kipping 2014).

One of the best ways to unequivocally prove the planetary nature of a transiting object is to obtain radial velocity (RV) measurements of the parent star, which also allows precise constraints on the mass of the planet. Unfortunately, the host stars of most of the *Kepler* candidates are too faint or their RV variation is too small to determine the mass of the planets with current spectroscopic facilities. Nevertheless, considerable effort is made to observationally characterize many interesting *Kepler* candidates (e.g. Hébrard et al. 2013; Howard et al. 2013; Pepe et al. 2013) and develop new instruments with higher resolution and better performance (see Pepe et al. 2014 for a comprehensive review).

Thanks to the extremely high photometric precision of the *Kepler* telescope, other methods such as transit-timing variation (e.g. Holman et al. 2010; Steffen et al. 2013; Xie 2013) and orbital brightness modulation (e.g. Charpinet et al. 2012; Quintana et al. 2013; Faigler et al. 2013) have been adopted to confirm the planetary nature of candidate objects. Using the latter method, Huber et al. (2013a) detected two planets in the Kepler-56 system, while Lillo-Box et al. (2014a) confirmed the hot-Jupiter Kepler-91 b, whose planetary nature was also recently supported by an independent study based on multi-epoch high-resolution spectroscopy (Lillo-Box et al. 2014c). Kepler-56 b,c and Kepler-91 b were found to be the first transiting planets orbiting giant stars.

Up to now, more than 50 exoplanets have been detected around evolved giants with Doppler spectroscopy, and their general characteristics are different from those found orbiting main sequence (MS) stars. According to the study of Jones et al. (2014), they are more massive, prefer low-eccentricity orbits, and have orbital semi-major axes of more than 0.5 au with an overabundance of between 0.5 and 0.9 au. Furthermore, the correlation between stellar metallicity and the number of planets seems to be reversed compared with MS stars, even though there is still an open debate on this matter (see discussion in Jones et al. 2014). In this context, the discovery of more exoplanets around evolved stars is vital to enlarge the sample and better characterize the statistical properties of these planetary systems. The cases in which the parent stars are K or G giants, which are known to evolve from F- and A-type MS stars, are also very interesting for planet formation and evolution theories and help to form a better demographic picture of planets around early-type stars.

Here we describe the confirmation via RV measurements of the transiting planet Kepler-432 b (aka KOI-1299.01), which we show to be a massive gas giant moving on a very eccentric orbit around an evolved K giant that is ascending the red giant branch. Both Kepler-432 b and Kepler-91 b are on tight orbits and present physical characteristics that deviate from the systems detected so far by the RV method.

⋆ RV data (Table A.1) are only available at the CDS via anonymous ftp to cdsarc.u-strasbg.fr (130.79.128.5) or via http://cdsarc.u-strasbg.fr/viz-bin/qcat?J/A+A/573/L5

A&A 573, L5 (2015)

Table 1. Photometric and physical properties of the host star and transit signal from previous studies.

Parameter	Value	Reference
R (mag)	12.135	NASA Archive
K_p (mag)	12.183	NASA Archive
Depth (ppm)	914	NASA Archive
Duration (h)	14.7951	NASA Archive
$R_\star$ ($R_\odot$)	4.160 ± 0.120	Huber et al. (2013b)
$M_\star$ ($M_\odot$)	1.353 ± 0.101	Huber et al. (2013b)
$\rho_\star$ (g cm^{-3})	0.02650 ± 0.00049	Huber et al. (2013b)

Notes. The data taken from the NASA Exoplanet Archive are available on http://exoplanetarchive.ipac.caltech.edu.

Table 2. Measured properties of sytem Kepler-432.

Parameter	Value
$T_{\rm eff}$ (K)	4850 ± 100
log g (cgs)	3.0 ± 0.5
T_0 (BJD/TDB)	2 455 477.02906 ± 0.0014
P (d)	52.50097 ± 0.00021
$K_\star$ (km s^{-1})	0.256 ± 0.021
V_γ (km s^{-1})	–35.73 ± 0.014
$e \cos \omega$	0.256 ± 0.071
$e \sin \omega$	0.469 ± 0.038
e	0.535 ± 0.030
ω (degrees)	61.3 ± 7.9
$r_\star$	0.06374 ± 0.00039
r_p	0.001763 ± 0.000022
i (degrees)	88.9 ± 1.3
M_p ($M_{\rm Jup}$)	4.87 ± 0.48
R_p ($R_{\rm Jup}$)	1.120 ± 0.036
g_p (m s^{-2})	96 ± 11
ρ_p ($\rho_{\rm Jup}$)	3.46 ± 0.48
a (au)	0.3034 ± 0.0089

2. Observations and data analysis

Kepler-432 was continuously monitored by *Kepler* from May 2009 to May 2013, being observed in all the 17 quarters in long-cadence mode and during 8 quarters in short-cadence mode. It was recognized as a *Kepler* object of interest by Borucki et al. (2011b) after it showed a periodic dimming in the light curve every 52.5 d. A subsequent study of *Kepler* candidates by Huber et al. (2013b), making use of the asteroseismology technique, refined some parameters of this system. These were updated by Burke et al. (2014). We summarise relevant parameters in Table 1.

2.1. CAFE data

In 2012 we started a programme to confirm a subset of *Kepler* candidates via spectroscopic follow-up observations. For this purpose, we used the Calar Alto Fiber Echelle (CAFE) spectrograph mounted on the 2.2 m Calar Alto telescope. CAFE is an echelle spectrograph capable of achieving an average resolution of $R = 63\,000 \pm 4000$ in the optical regime. The nominal precision in measuring RVs of stellar objects, tested on known exoplanet host stars (Aceituno et al. 2013; Lillo-Box et al. 2014a), is a few tens of m s^{-1}, sufficient to detect a signal caused by a close-in Jupiter-like planet.

We obtained 28 spectra of Kepler-432 during 16 nights of observations carried out in the 2013 and 2014 seasons, during the best visibility time of the *Kepler* field. The exposure time was 1800 s for most spectra, but increased to 2700 s for six spectra to compensate for the presence of thin clouds and veils. Each spectrum was extracted from the raw data using the pipeline provided by the Calar Alto observatory based on the extant R3D pipeline developed by Sanchez et al. (2006). In brief, each order of a spectrum is extracted from the flat-fielded and debiased science image thanks to a continuum image that traces the orders along the pixels. Each spectrum is calibrated in wavelength using the lines of a ThAr spectrum taken after the science frame.

RV measurements were obtained by cross-correlating each observed spectrum with a synthetic spectrum created from the stellar parameters found in the literature. In particular, the cross-correlation was made order by order, and the final RV measurement was the median value of all those obtained (Müller et al. 2013). The RV values estimated are listed in Table A.1 together with their relative uncertainties. Finally, to better characterize Kepler-432, we combined several CAFE spectra of the star to obtain one with a high signal-to-noise ratio, from which, following the methodology described in Fossati et al. (2010), we inferred the effective temperature of the star $T_{\rm eff}$ and its surface gravity log g, see Table 2. We first fitted the RV data by using the package Systemic Console 2 (Meschiari et al. 2009). To obtain the uncertainties relative to the fitted parameters, we performed bootstrapping and MCMC simulations and adopted the higher values of the uncertainties found with the two methods. The different orbital solutions obtained from the bootstrapping simulations show a clear preference for an eccentric orbit.

As a sanity check, we obtained a Lomb-Scargle periodogram of the RVs without considering the transit times from the photometry. Among the first three peaks we found $P = 51.95$ d (with a false-positive probability of 0.0136), a value similar to that obtained from the *Kepler* photometry.

2.2. Excluding false-positive scenarios

To rule out the possibility that Kepler-432 is a blended stellar binary system that mimics the observable properties of a transiting planet system, we analysed two high-resolution images of Kepler-432 in J and K bands that were obtained with the NIRC2 imager mounted on the Keck II telescope, used in adaptive optics mode[1]. In these images, there is a clear detection of a nearby star at 1.1 arcsec, which is much fainter than Kepler-432 A, with $\Delta_J = 5.68 \pm 0.04$ mag and $\Delta_K = 5.19 \pm 0.01$ mag. We translated these differences into K_p-band magnitudes by using the formulae from Howell et al. (2012), obtaining that the component B is 6.68 ± 0.17 mag fainter than Kepler-432 A in the *Kepler* band. Finally, using the relations from Lillo-Box et al. (2014b), we estimated the dilution effect of this faint star on the depth of the transit events, finding a correction of 0.01 $R_\oplus$ for the radius of the eclipsing object. This correction is much smaller than the uncertainty in our measurement of the radius of Kepler-432 b. Another possibility that we have to consider is that the B component might be an eclipsing binary. However, since we detected an RV signal of a planetary-mass object with the same periodicity as the transit signal and the companion is very faint, this scenario is very unlikely. Instead, the most probable scenario is that the planet is orbiting component A and that B only acts as

[1] The images were published by David Ciardi on the Community Follow-up Observing Program (CFOP), https://cfop.ipac.caltech.edu/home/

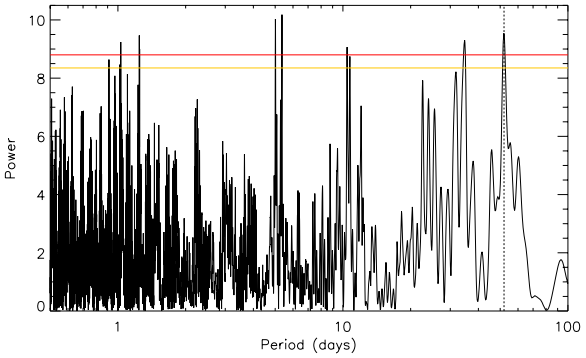

Fig. 1. Lomb–Scargle periodogram obtained from the CAFE RV measurements for Kepler-432. The dashed line highlights the orbital period of Kepler-432 b. The red and orange lines represent the 5% and 10% false-alarm probability.

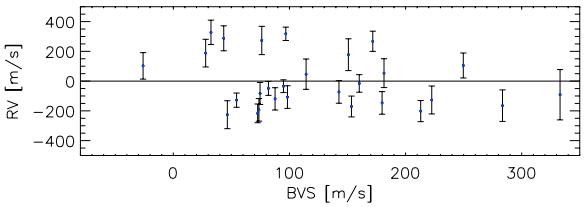

Fig. 2. Radial velocity (RV) versus bisector velocity span (BVS) for Kepler-432.

a diluting source, having very weak implications on the planet (and orbital) properties derived from the light curve.

Another possible source of false positives is stellar activity, which could mimic the presence of a planetary body in the RV signal. To rule out this possibility as well, we determined the bisector velocity span (BVS) from the same spectra from which we obtained the RV measurements. The BVS values are plotted in Fig. 2 together with the best-fitting line, which is consistent with a horizontal line. This means that we did not find any significant correlation between RV and BVS.

3. Physical properties of the system

To determine the physical parameters of the system, we simultaneously modelled the *Kepler* photometry and the CAFE RVs using the code (see Southworth 2013 and references therein). The parameters of the fit were chosen to be the fractional radii of the two objects ($r_\star = \frac{R_\star}{a}$ and $r_\mathrm{p} = \frac{R_\mathrm{p}}{a}$ where a is the orbital semi-major axis), orbital inclination i, orbital period P_orb, reference transit midpoint T_0, velocity amplitude $K_\star$, systemic velocity V_γ of the star, the eccentricity (e), and argument of periastron (ω) expressed using the combinations $e\cos\omega$ and $e\sin\omega$.

The *Kepler* long- and short-cadence data were each converted from flux to magnitude units. Data with more than two transit durations from a transit midpoint (approximately 95% of the data points for both cadences) were rejected to aid computational efficiency. Each transit was rectified to zero differential magnitude by subtracting a linear or quadratic polynomial trend versus time, fitted to the out-of-transit data points. The short-cadence data were additionally treated by iteratively rejecting 3σ outliers, totalling 1.2% of the data points. Error bars for the data

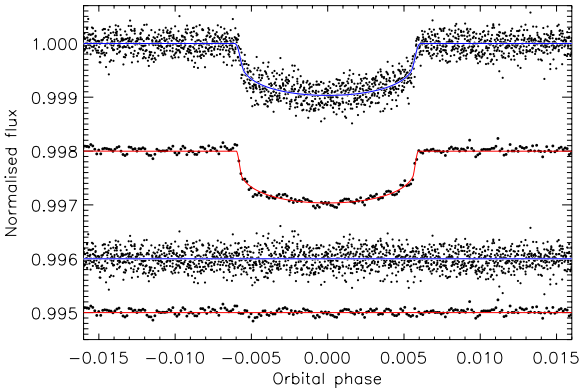

Fig. 3. *Kepler* long-cadence (top light curve) and short-cadence (bottom light curve) data around transit. The best fits are shown using solid lines. The residuals of the fits are shown offset towards the base of the figure. We phase-binned the short-cadence data by a factor of 100 to make this plot clearer.

for each cadence were assigned to force a reduced chi-squared of $\chi^2_\nu = 1.0$. The radial velocity error bars were scaled by $\sqrt{1.8}$ to achieve the same goal.

The very low ratio of the radii means that the transit is shallow and the partial phases (ingress and egress) are short. Their length is poorly determined by the data, leading to i and $r_\star$ being highly correlated. The solution is indeterminate without outside constraints. Fortunately, the asteroseismic density from Huber et al. (2013b) can be used to rescue the situation: under the assumption that $M_\star \gg M_\mathrm{p}$, the density is directly related to $r_\star$ (Seager & Mallén-Ornelas 2003). We therefore fixed $r_\star$ at the value for the known density (Table 1) and fitted for i. Limb darkening was specified using the quadratic law, whose coefficients were fixed at the theoretical values given by Sing (2010). We also assumed that, neglecting the detected B component, no other light came from the planet or from any additional object along the same sightline. The low sampling rate of the long-cadence data was dealt with as in Southworth (2011).

The best fits are shown in Figs. 3 and 4; the scatters around the best fits were 0.19 mmag and 0.42 mmag for the long- and short-cadence. To determine error estimates, we ran Monte Carlo and residual-permutation (Southworth 2008) simulations and adopted the larger of the two error bars for each parameter. We also needed to account for the uncertainty in $r_\star$. We did this by calculating solutions with $r_\star$ fixed at its asteroseismic value ± its error bar to determine the effect on each parameter, and added this in quadrature to the uncertainty from the Monte Carlo and residual-permutation simulations.

The result of this process was values for $r_\star$, r_p, i, P_orb, T_0, $K_\star$, V_γ and e. Independent results were calculated for both cadences and found to be consistent. We adopted those from the short-cadence data because they yield parameter values with a better precision. The final physical properties of the system were then calculated using standard formulae, and the uncertainties were propagated with a Monte Carlo approach. These results are collected in Table 2.

4. Results and conclusions

We confirmed the planetary nature of Kepler-432 b, a planet with a mass of 4.87 ± 0.48 M_Jup and a radius of 1.120 ± 0.036 R_Jup,

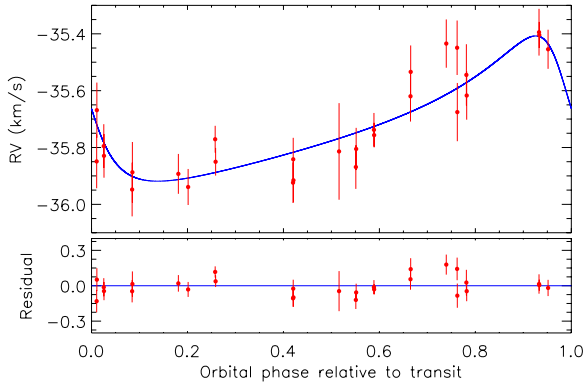

Fig. 4. *Upper panel*: phased RVs for Kepler-432 red points) and the best fit from (blue line). *Lower panel*: residuals of RVs versus best fit.

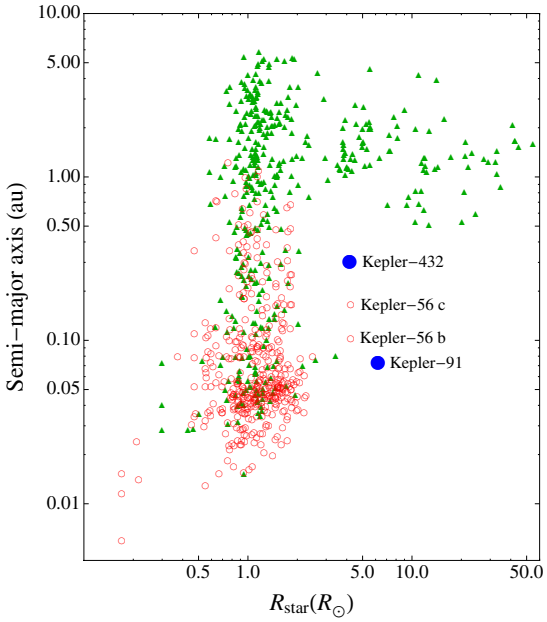

Fig. 5. Stellar radii and semi-major axis of the orbits of known planetary systems. Green triangles denote systems found by the RV method, while red circles are for those found by transit method. Blue points highlight the positions of Kepler-432 and Kepler-91.

orbiting a K giant that is ascending the red giant branch. The planet has an eccentric orbit ($e = 0.535 \pm 0.030$) with a period of 52.50097 ± 0.00021 d. After Kepler-56 b,c and Kepler-91 b, Kepler-432 b becomes the fourth known transiting planet orbiting an evolved star. These planets have quite different characteristics from those detected by the RV method, and cover regions of parameter spaces that were considered to be deserts until now, see Fig. 5. They are also important indicators of the formation processes and evolutionary scenarios for planets around early-type stars.

Mazeh et al. (2013) found no significant transit-time variations for Kepler-432, and our RV data do not show any hint of a trend caused by a longer-period companion. More RVs and a longer time-span are necessary to constrain the possible presence of a third body that might be responsible for the location and eccentricity of Kepler-432 b.

Since Kepler-432 A is still evolving and expanding, this planetary system is also very interesting from a dynamical point of view. Currently, the planet reaches the minimum distance of $7.29 \pm 0.52\, R_\star$ at periastron, while at apastron is $24.08 \pm 0.85\, R_\star$ away. However, at the end of the red giant branch, the star will have a radius of $\sim 8\, R_\odot$ and, if we exclude a possible orbital decay due to angular momentum transfer mechanism, the distance of the planet from the star at periastron will be $\sim 3.8\, R_\star$. This means that the planet will not be devoured by its parent star, but will instead accompany it towards a more distant common fate.

The present Letter was contemporaneously submitted with that by Ortiz et al. (2015), who also confirm the planetary nature of Kepler-432 b.

Acknowledgements. Based on observations obtained with the CAHA 2.2 m Telescope and the publicly available data obtained with the NASA space satellite *Kepler*. The Keck images used in this work were taken by David Ciardi. S.C. thanks D. Gandolfi, M. I. Jones, L. Fossati, and M. Ortiz for useful discussion.

References

Aceituno, J., Sãnchez, S. F., Grupp, F., et al. 2013, A&A, 552, A31
Borucki, W. J., Koch, D., Basri, G., et al. 2011a, ApJ, 728, 20
Borucki, W. J., Koch, D., Basri, G., et al. 2011b, ApJ, 736, 19
Burke, C. J., Bryson, S. T., Mullally, F., et al. 2014, ApJ, 210, 19
Charpinet, S., Fontaine, G., Brassard, P., et al. 2012, Nature, 480, 496
Fabrycky, D. C., Lissauer, J. J., et al. 2014, ApJ, 790, 146
Faigler, S., Tal-Or, L., Mazeh, T., et al. 2013, ApJ, 771, 26
Fossati, L., Bagnulo, S., Elmasli, A., et al. 2011, ApJ, 720, 872
Hébrard, G., Almenara, J.-M., Santerne, A., et al. 2013, A&A, 554, A114
Holman, M. J., Fabrycky, D. C., Ragozzine, D., et al. 2010, Science, 330, 51
Howard, A., Sanchis-Ojeda, R., Marcy, G. W., et al. 2013, Nature, 503, 381
Howell, S. B., Rowe, J. F., Bryson, S. T., et al. 2012, ApJ, 746, 123
Huber, D., Carter, J. A., Barbieri, M., et al. 2013a, Science, 342, 331
Huber, D., Chaplin, W. J., Christensen-Dalsgaard, J., et al. 2013b, ApJ, 767, 127
Jones, M. I., Jenkins, J. S., Bluhm, P., et al. 2014, A&A, 566, A113
Lillo-Box, J., Barrado, D., Moya, A., et al. 2014a, A&A, 562, A109
Lillo-Box, J., Barrado, D., & Bouy, H. 2014b, A&A, 566, A103
Lillo-Box, J., Barrado, D., Henning, Th., et al. 2014c, A&A, 568, L1
Marcy, G. W., Isaacson, H., Howard, A. W., et al. 2014, ApJS, 210, 20
Mazeh, T., Nachmani, G., Holczer, T., et al. 2013, ApJ, 208 16
Meschiari, S., Wolf, A. S., Rivera, E., et al. 2009, PASP, 121, 1016
Müller, A., Roccatagliata, V., Henning, Th., et al. 2013, A&A, 556, A3
Ortiz, M., Gandolfi, D., & Reffert, S. 2015, A&A, 573, L6
Pepe, F., Cameron, A. C., Latham, D. W., et al. 2013, Nature, 503, 377
Pepe, F., Ehrenreich, D., Meyer, M. R. 2014, Nature, 513, 358
Quintana, E. V., Rowe, J. F., Barclay, T., et al. 2013, ApJ, 767, 137
Sánchez, S. F. 2006, Astron. Nachr., 327, 850
Seager, S., & Mallén-Ornelas, G. 2003, ApJ, 585, 1038
Sing, D. 2010, A&A, 510, A21
Sliski, D. H., & Kipping, D. M. 2014, ApJ, 788, 148
Southworth, J. 2008, MNRAS, 386, 1644
Southworth, J. 2011, MNRAS, 417, 2166
Southworth, J. 2013, A&A, 557, A119
Steffen, J. H., Fabrycky, D. C., Agol, E., et al. 2013, MNRAS, 428, 1077
Xie, J.-W. 2013, ApJS, 208, 22

Appendix A: Radial velocity measurements

Table 4.1: BVS and RV measurements of Kepler-432.

Date of observation (BJD-2450000)	BVS [$m\,s^{-1}$]	RV [$km\,s^{-1}$]	err_{RV} [$km\,s^{-1}$]
6418.5145	32.43	-35.394	0.061
6418.5390	96.87	-35.404	0.034
6426.4901	46.53	-35.948	0.070
6426.5199	283.46	-35.887	0.079
6431.5465	153.41	-35.893	0.052
6432.6174	72.63	-35.939	0.047
6435.5761	81.90	-35.771	0.035
6435.6233	54.48	-35.850	0.036
6496.6430	73.72	-35.915	0.057
6501.6327	333.03	-35.814	0.126
6505.4502	160.12	-35.738	0.044
6505.4721	94.86	-35.757	0.032
6513.3674	43.42	-35.434	0.063
6514.5522	76.16	-35.449	0.071
6514.5742	114.34	-35.676	0.076
6515.5659	150.76	-35.545	0.080
6515.6022	249.71	-35.617	0.063
6524.5087	171.76	-35.454	0.051
6811.6033	213.03	-35.924	0.053
6811.6253	87.62	-35.842	0.056
6818.4792	179.78	-35.869	0.057
6818.5115	74.71	-35.805	0.055
6824.4574	-26.04	-35.620	0.066
6824.4794	27.84	-35.534	0.069
6842.6148	222.54	-35.849	0.070
6842.6368	181.43	-35.669	0.072
6843.3949	142.63	-35.795	0.057

Chapter 5

Multi-site observations of HAT-P-16 & WASP-21

In this chapter we present the characterization of the two planetary systems HAT-P-16 and WASP-21, pubblished in A&A in 2013 Ciceri et al. (2013)

I glitrende solskinn
Et landskap som våkner
Vi seiler inn mot havnen
Hjem til deg i dine armer
En historie å fortelle
Ankomst ankomst gi meg havn
Ankomst ankomst åpne din favn

Ankomst, Leaves' Eyes

A&A 557, A30 (2013)
DOI: 10.1051/0004-6361/201321669

Astronomy & Astrophysics

Simultaneous follow-up of planetary transits: revised physical properties for the planetary systems HAT-P-16 and WASP-21⋆

S. Ciceri[1], L. Mancini[1], J. Southworth[2], N. Nikolov[1,3], V. Bozza[4,5], I. Bruni[6], S. Calchi Novati[4,7], G. D'Ago[4], and Th. Henning[1]

[1] Max Planck Institute for Astronomy, Königstuhl 17, 69117 Heidelberg, Germany
e-mail: ciceri@mpia.de
[2] Astrophysics Group, Keele University, Staffordshire, ST5 5BG, UK
[3] Astrophysics Group, University of Exeter, Stocker Road, EX4 4QL, Exeter, UK
[4] Department of Physics, University of Salerno, via Ponte Don Melillo, 84084 Fisciano (SA), Italy
[5] Istituto Nazionale di Fisica Nucleare, Sezione di Napoli, Napoli, Italy
[6] INAF – Osservatorio Astronomico di Bologna, via Ranzani 1, 40127 Bologna, Italy
[7] Istituto Internazionale per gli Alti Studi Scientifici (IIASS), Vietri Sul Mare (SA), Italy

Received 8 April 2013 / Accepted 19 July 2013

ABSTRACT

Context. By now, more than 300 planets transiting their host star have been found, and much effort is being put into measuring the properties of each system. Light curves of planetary transits often contain deviations from a simple transit shape, and it is generally difficult to differentiate between anomalies of astrophysical nature (e.g. starspots) and correlated noise due to instrumental or atmospheric effects. Our solution is to observe transit events simultaneously with two telescopes located at different observatories.
Aims. Using this observational strategy, we look for anomalies in the light curves of two transiting planetary systems and accurately estimate their physical parameters.
Methods. We present the first photometric follow-up of the transiting planet HAT-P-16 b, and new photometric observations of WASP-21 b, obtained simultaneously with two medium-class telescopes located in different countries, using the telescope defocusing technique. We modeled these and other published data in order to estimate the physical parameters of the two planetary systems.
Results. The simultaneous observations did not highlight particular features in the light curves, which is consistent with the low activity levels of the two stars. For HAT-P-16, we calculated a new ephemeris and found that the planet is 1.3σ colder and smaller ($R_b = 1.190 \pm 0.037\ R_{Jup}$) than the initial estimates, suggesting the presence of a massive core. Our physical parameters for this system point toward a younger age than previously thought. The results obtained for WASP-21 reveal lower values for the mass and the density of the planet (by 1.0 and 1.4σ respectively) with respect to those found in the discovery paper, in agreement with a subsequent study. We found no evidence of any transit timing variations in either system.

Key words. planetary systems – stars: fundamental parameters – techniques: polarimetric – stars: individual: HAT-P-16 – stars: individual: WASP-21

1. Introduction

Since the discovery of the first planet orbiting a main sequence star (Mayor & Queloz 1995), more than 900 extrasolar planets have been found using different techniques. It is therefore possible to analyze these planets from a statistical viewpoint, and compare the predictions of theoretical models (e.g. Fortney et al. 2007; Liu et al. 2011; Mordasini et al. 2012a,b) to the available data (e.g. Gould et al. 2010; Mayor et al. 2011; Howard et al. 2012; Cassan et al. 2012; Fressin et al. 2013). Such comparisons are fundamental to confirm or discard different theories of planet formation and evolution.

Whilst it is important to enlarge the number of detected planets, it is also vital to accurately measure the main physical properties of each planetary system used in statistical analysis. In this context, the transiting extrasolar planets (TEPs) are extraordinary sources of information. The particular geometry of these systems enables measurement of the complete set of their physical properties (e.g. Charbonneau et al. 2000; Henry et al. 2000). From the light curve obtained during transit events, it is possible to measure the inclination of the orbit with respect to the line of sight and the size of the system's components. Combining these results with spectroscopic measurements, we can obtain a precise value of the mass of the planet (rather than just a lower limit as for extrasolar planets detected by radial velocity measurements; Marcy & Butler 1998).

TEPs are also the only extrasolar planets for which we can investigate the atmospheric composition, both with spectroscopy during transit and occultation (e.g. Charbonneau et al. 2002; Deming et al. 2005; Knutson et al. 2007; Swain et al. 2008; Borucki et al. 2009), and by multi-band photometric observations with the aim of detecting variation of the planet's radius as a function of wavelength (Southworth et al. 2012b; Mancini et al. 2013a,b,c; Nikolov et al. 2013). Moreover, the presence of an additional body orbiting the host star can be inferred based on transit timing variation studies (e.g. Holman et al. 2010; Steffen et al. 2013; Maciejewski et al. 2013), which require a large sample of accurate mid-transit times.

Anomalies in the light curves of planetary transits can arise from several phenomena affecting the parent stars, such as gravity darkening (Barnes 2009; Szabó et al. 2011), stellar pulsation

⋆ Reduced light curves are only available at the CDS via anonymous ftp to cdsarc.u-strasbg.fr (130.79.128.5) or via http://cdsarc.u-strasbg.fr/viz-bin/qcat?J/A+A/557/A30

A&A 557, A30 (2013)

(Collier Cameron et al. 2010), starspots (e.g. Sanchis-Ojeda et al. 2011; Tregloan-Reed et al. 2013) and even the presence of exomoons (Kipping et al. 2009). High-quality photometric observations are therefore not only important to accurately determine the physical parameters of TEP systems, but can yield further astrophysical information. However, even if we use the telescope-defocusing method, which allows a much better photometric precision than traditional in-focus photometry (e.g. Tregloan-Reed & Southworth 2013), it is generally a hard task to distinguish transit anomalies due to astrophysical effects from those caused by random or systematic noise attributable to instrumental or atmospheric effects.

One solution is to monitor the same transit event simultaneously from two telescopes located at different sites. If data from both the telescopes contain the same anomaly, we can discard the possibility that it is caused by instrumental effects or effects due to Earth's atmosphere. We successfully implemented this observational strategy to follow up several planetary transits by using the *Cassini* 1.5 m telescope at the INAF/Astronomical Observatory of Bologna in Loiano (Italy) and the CA 1.23 m telescope at the German-Spanish Astronomical Center at Calar Alto (Spain). These two telescopes are sufficiently distant from each other that their observations are completely independent in terms of instrumental effects and atmospheric conditions, but close enough that they can contemporaneously observe the same transit event. Additionally, the new data should provide a better estimation of the photometric parameters. We tested this approach in 2011, when we observed a transit of HAT-P-8 simultaneously with the two telescopes. We did indeed notice an asymmetry into the light curve, and its presence in both datasets confirms the reality of the signal (Mancini et al. 2013a). Here we present the results of this simultaneous-observation approach applied to two planetary systems, HAT-P-16 and WASP-21, both of which host a close-in gaseous TEP.

1.1. Case history

HAT-P-16 b was detected by Buchhave et al. (2010), who found it to be a be a 4.2 $M_{\rm Jup}$ hot Jupiter on a slightly eccentric 2.8 day orbit ($e = 0.036$) around a $V = 10.8$ mag, F-type star. With a radius of 1.3 $R_{\rm Jup}$ the planet is nearly twice as dense as Jupiter. The Rossiter-McLaughlin effect has been detected by Moutou et al. (2011) who found a projected spin-orbit angle of $\lambda = -10° \pm 16°$, which is consistent with a prograde, aligned orbit.

The WASP-21 system hosts a hot Saturn-like planet with a mass of 0.3 $M_{\rm Jup}$ and radius of 1.1 $R_{\rm Jup}$ (Bouchy et al. 2010). The planet moves on a circular orbit with a period of ~4.32 days around a $V = 11.58$ mag, G-type star. The parent star has a mass and radius similar to the Sun, but also one of the lowest metallicities known ($[\frac{\rm Fe}{\rm H}] = -0.46$) for a TEP host star. The physical parameters of this system were revised by Barros et al. (2011),who found that the WASP-21 A star is evolving off the main sequence and, depending on the assumptions made in the analysis used, has a lower density than found in the discovery paper. The revised planetary properties pointed to a lower mass and slightly larger radius. The low density implies the planet is coreless and has a H/He composition.

In this work we present simultaneous transit observations of these two planetary systems from two telescopes. In Sect. 2 we show the first follow-up observations of HAT-P-16 and new photometric data for WASP-21. We used these new light curves to revise the physical parameters of these two TEP systems. The details of the light curve analysis are described in Sect. 3, whereas our estimations of the physical parameters are reported in Sect. 4. The results of our work are summarized in Sect. 5.

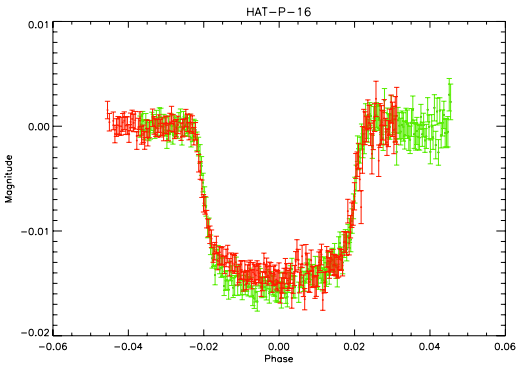

Fig. 1. Observations of the October 2012 transit of HAT-P-16. The green points show the data from the CA 1.23 m telescope, and the red points the data from the *Cassini* telescope.

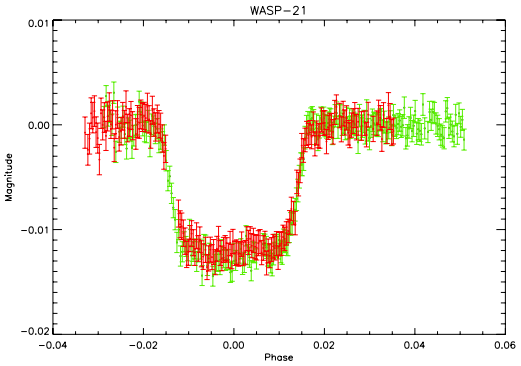

Fig. 2. Observations of the September 2012 transit of WASP-21. The green points show the data from the CA 1.23 m telescope, and the red points the data from the *Cassini* telescope.

2. Observations and data reduction

For both planetary systems, we observed one transit event simultaneously with two telescopes (Figs. 1 and 2). These observations were carried out between September and October 2012 from the Loiano and Calar Alto observatories. An additional transit of HAT-P-16 was observed on October 29th 2010 from Loiano during the PLAN microlensing campaign toward M31 (Calchi Novati et al. 2009, 2010). Another transit of HAT-P-16 was observed in Calar Alto on August 22th 2011. In total we present six new light curves, five of them being from defocused 1.2–1.5 m telescopes (see Table 1). With the telescope-defocusing technique we can use larger exposure times (~50−120 s) which allows us to collect many more photons over a large number of pixels, thus reducing the Poisson and scintillation noise and minimizing systematic noise due to flat-fielding errors, seeing variations and image motion (Southworth et al. 2009a,b). This is particularly useful for planetary transits, because the variation in flux of the star due to the planet passing in front of it is small, generally 2% or less.

Table 1. Observing log for the two TEP systems.

Telescope	Date of first obs	Start time (UT)	End time (UT)	N_{obs}	T_{exp} (s)	T_{obs} (s)	Filter	Airmass	Moon illum.	Aperture radii (px)	Scatter (mmag)
HAT-P-16:											
Cassini	2010 10 29	21:19	03:01	261	50–60	70	Johnson *I*	1.00 → 2.16	56%	17, 38, 58	1.01
CA 1.23 m	2011 08 22	23:08	04:36	537	11–15	39	Cousins *R*	1.00 → 1.33	39%	15, 40, 60	1.85
Cassini	2012 10 03	23:28	04:41	197	70–80	92	Johnson *I*	1.01 → 2.15	86%	18, 50, 70	0.96
CA 1.23 m	2012 10 04	00:02	05:31	216	70–80	90	Cousins *I*	1.00 → 2.04	86%	24, 38, 60	0.88
WASP-21:											
Cassini	2012 09 11	19:06	02:10	177	120	135	Gunn *i*	1.72 → 1.11	18%	17, 28, 46	0.88
CA 1.23 m	2012 09 11	19:28	03:48	218	100–130	135	Cousins *I*	1.63 → 1.08	18%	22, 40, 65	0.86

Notes. N_{obs} is the number of observations, T_{exp} is the exposure time, T_{obs} is the observational cadence, and "Moon illum." is the fractional illumination of the Moon at the midpoint of the transit.

2.1. 1.52 m Cassini Telescope

One transit event of WASP-21 and two of HAT-P-16 were observed with the *Cassini* telescope. This 152 cm telescope is located at the Loiano Observatory near Bologna (Italy), and was already successfully used to follow up several planetary transits (e.g. Harpsøe et al. 2012; Southworth et al. 2012a). It has an German-type equatorial mount with a Ritchey-Chrétien configuration. It is equipped with the Bologna Faint Object Spectrograph and Camera (BFOSC), whose CCD has 1300 × 1340 pixels and a plate scale of 0.58″ pixel^{-1}, resulting in a a field of view of 13′ × 12.6′. For all observations, the CCD was windowed to decrease the readout time and the telescope was defocused and autoguided. For the WASP-21 transit we used a Gunn-*i* filter, while the HAT-P-16 ones were observed through a Johnson-*I* filter.

The science images were bias subtracted and flat-fielded. Master bias and flat-field images were created combining multiple suitably scaled bias and flat images. The bias and the flat-field frames were collected during the same nights as the observations. In particular the flat-field frames were taken on the sky immediately after sunset. Light curves were extracted using an aperture-photometry routine based on the `DAOPHOT` photometry package (Stetson 1987) and IDL's `astrolib/APER` routine. We tried different values for the circular apertures in order to find the most precise photometry, i.e. the light curve with the smallest scatter in the out-of-transit region. We noticed that changes in the aperture size do not have a significant effect on the shape of the light curves but do cause small differences in the scatter of the datapoints. The apertures used for each transit are reported in Table 1. For fixed aperture size we also tried different numbers of comparison stars to obtain differential photometry. The final comparison stars were chosen according to their brightness and the scatter in the resulting light curve.

2.2. 1.23 m Calar Alto Telescope

We observed two transits of HAT-P-16 and one of WASP-21 with the 1.23 m telescope at Calar Alto. Mounted in the Cassergrain focus of this telescope is the new DLR-MKIII camera, which has 4000 × 4000 pixels, a plate scale of 0.32″ pixel^{-1} and a field of view of 21.5′ × 21.5′. This instrumental equipment was already successfully used to observe planetary transits (e.g. Mancini et al. 2013a; Maciejewski et al. 2013). For the two transits observed in 2012 we used a Cousins-*I* filter, the telescope was autoguided and defocused, and the CCD was windowed (Table 1). For the transit observed on August the 22th 2011 a different camera with a smaller field of view (the SITE#2b CCD, with a plate scale of 0.51 arcsec per pixel) was used with a Cousins-*R* filter, and the telescope was autoguided but not defocused. The observations were reduced in the same way as those from the *Cassini* Telescope.

3. Light curve analysis

To measure the photometric parameters of the systems, all the light curves were fitted individually following much of the methodology of the *Homogeneous Studies* project (Southworth 2012, and references within). The fits were performed using the code (Southworth 2008), which models the two components of the planetary system as biaxial spheroids. The main parameters fitted by the code are the orbital inclination i, the time of transit midpoint T_0, the sum of the reduced radii ("reduced" radius is the ratio between the true radius of the object and the semi-major axis a of the orbit) $r_A + r_b$, and the ratio of the radii $k = r_b/r_A$.

An important effect to consider when fitting transit light curves is limb darkening (LD). We used the quadratic LD law and obtained theoretical coefficients from interpolation in the tables of Claret & Hauschildt (2003). We tried two different strategies: (i) fitting the linear LD coefficient and fixing the quadratic coefficient to the theoretical value; (ii) fixing both LD coefficients to the theoretical values. From the two analysis we kept the results with greatest internal consistency.

For WASP-21 we adopted a circular orbit, following the findings of Barros et al. (2011) and Pont et al. (2011). By contrast, HAT-P-16 has a well-established orbital eccentricity, e, and longitude of periastron, ω. We adopted the constraints $e\cos\omega = -0.030 \pm 0.003$ and $e\sin\omega = -0.021 \pm 0.006$ (Buchhave et al. 2010) to include the effects of an eccentric orbit in the light curve fits.

In order to take into account the red noise and compensate for the underestimated errorbars produced by the algorithm, we performed a two-step inflation of the errorbars, as used in several published studies (e.g. Gibson et al. 2008; Winn et al. 2008, 2009; Nikolov et al. 2012; Mancini et al. 2013a,b). It consists of running the fitting code once for each light curve and then rescaling the errorbars of each dataset to give a reduced χ^2 of $\chi^2_\nu = 1$. The errorbars are then further inflated through the β approach (Pont et al. 2006; Gillon et al. 2006; Winn et al. 2007). We then ran once more on these error-rescaled datasets, obtaining the final values of the parameters, which are reported in Tables 2 and 3. The light curves and best-fitting models are shown in Fig. 3 for HAT-P-16, and Fig. 4 for WASP-21. The residuals of each fit are plotted at the bottom of the figures.

A&A 557, A30 (2013)

Table 2. Photometric properties of the HAT-P-16 system derived by fitting the light curves with .

Source	$r_A + r_b$	k	i	r_A	r_b
Cassini (transit #1)	0.1416 ± 0.0040	0.1062 ± 0.0008	88.45 ± 0.96	0.1280 ± 0.0035	0.01359 ± 0.00043
Cassini (transit #2)	0.1549 ± 0.0068	0.1085 ± 0.0009	86.72 ± 0.85	0.1398 ± 0.0060	0.01516 ± 0.00078
CA 1.23 m (transit #1)	0.1407 ± 0.0011	0.1032 ± 0.0005	89.96 ± 0.34	0.1275 ± 0.0010	0.01316 ± 0.00012
CA 1.23 m (transit #2)	0.1485 ± 0.0054	0.1116 ± 0.0011	87.28 ± 0.79	0.1335 ± 0.0048	0.01491 ± 0.00065
Final results	**0.1441 ± 0.0025**	**0.1067 ± 0.0014**	**87.74 ± 0.59**	**0.1303 ± 0.0022**	**0.01377 ± 0.00038**
Buchhave et al. (2010)	0.1542	0.1071 ± 0.0014	86.6 ± 0.7	0.1392	0.0149

Notes. The final parameters are given in bold and are compared with those found by Buchhave et al. (2010).

Table 3. Photometric properties of the WASP-21 system derived by fitting the light curves with .

Source	$r_A + r_b$	k	i	r_A	r_b
Cassini	0.1166 ± 0.0084	0.0998 ± 0.0016	87.18 ± 1.00	0.1050 ± 0.0075	0.01048 ± 0.00091
CA 1.23 m	0.1182 ± 0.0057	0.1037 ± 0.0010	86.83 ± 0.57	0.1071 ± 0.0050	0.01110 ± 0.00062
Barros et al. (2011)	0.1166 ± 0.0042	0.1086 ± 0.0009	87.01 ± 0.44	0.1052 ± 0.0037	0.01142 ± 0.00049
Final results	**0.1169 ± 0.0031**	**0.1055 ± 0.0023**	**86.97 ± 0.33**	**0.1057 ± 0.0028**	**0.01117 ± 0.00035**
Bouchy et al. (2010)	0.1046	$0.10820^{+0.00037}_{-0.00035}$	$88.75^{+0.84}_{-0.70}$	0.0948	0.00983
Barros et al. (2011)	0.1149	$0.10705^{+0.00082}_{-0.00086}$	87.34 ± 0.29	0.1038	0.01112
Southworth (2012)	0.1186 ± 0.0042	0.1095 ± 0.0014	86.77 ± 0.45	0.1069 ± 0.0037	0.01170 ± 0.00054

Notes. The light curves from Barros et al. (2011) were combined in phase and then analyzed. The final parameters are given in bold and are compared with those found by other authors.

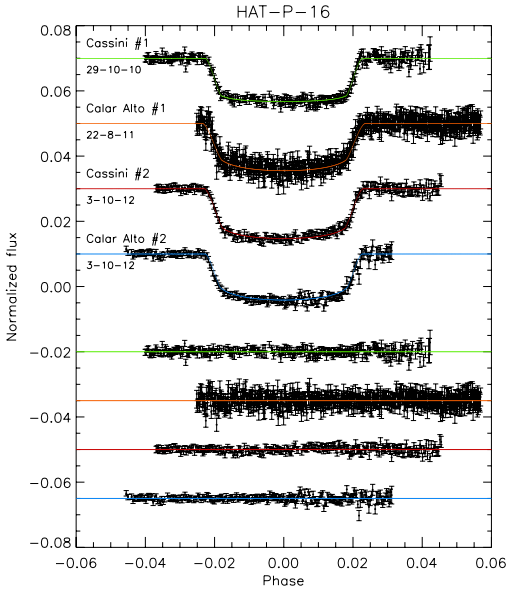

Fig. 3. Light curves of HAT-P-16 compared with the best fits. The dates and instruments used for each transit event are indicated. Residuals from the fits are displayed at the bottom, in the same order as the top curves.

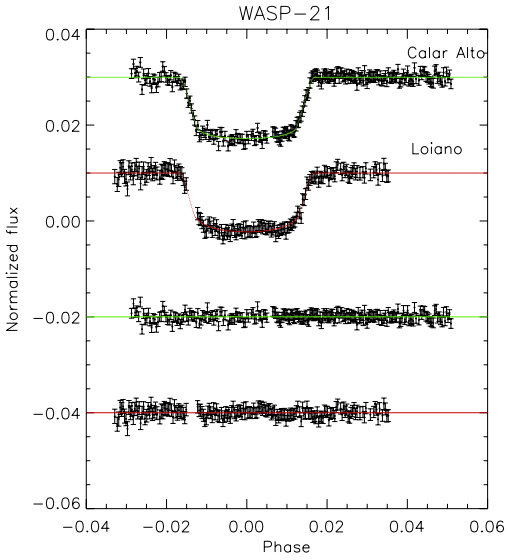

Fig. 4. Light curves of WASP-21 compared with the best fits. The instruments used for each transit event are indicated. Residuals from the fits are displayed at the bottom, in the same order as the top curves.

In the case of WASP-21, we also considered the three light curves obtained by Barros et al. (2011). These do not cover complete transits, so we converted them to orbital phase before analyzing them in the same manner as described above (see Table 3).

3.1. New orbital ephemerides

During our analysis, we estimated the central transit time of each of our light curves. We enlarged the sample by considering other mid-transit times available in the literature or on websites such as the TRansiting ExoplanetS and CAndidates (TRESCA) archive, which essentially contain light curves obtained by amateur astronomers. We selected only the light curves with a data quality index higher than 3 (see Tables 4 and 5). Armed with these times of minimum light, we made a linear fit of all the collected mid-transit times as a function of their epoch. We obtained the following ephemeris for HAT-P-16:

$$T_0 = \mathrm{BJD(TDB)}\ 2\,455\,027.59281\,(40) + 2.7759712\,(15)\,E,$$

Table 4. Transit mid-times of HAT-P-16 and their residuals.

Time of minimum BJD(TDB)−2 400 000	Epoch	Residual (JD)	Reference
55 027.59293 ± 0.00031	0	0.000117	Buchhave et al. (2010)
55 085.88780 ± 0.00049	21	–0.000409	Buchhave et al. (2010)
55 135.853622 ± 0.000504	39	–0.002069	Buchhave et al. (2010)
55 388.46897 ± 0.00123	130	–0.000101	Trnka (TRESCA)
55 463.42067 ± 0.00049	157	–0.000985	Vrašták (TRESCA)
55 463.4193 ± 0.0008	157	0.000375	Világi, Gajdoš (TRESCA)
55 471.7491 ± 0.0007	160	0.000902	Shadick (TRESCA)
55 477.30172 ± 0.00149	162	0.001569	Vrašták (TRESCA)
55 482.85087 ± 0.00066	164	–0.001223	Shadick (TRESCA)
55 485.6291 ± 0.0005	165	0.001065	Sanchez (TRESCA)
55 499.50837 ± 0.00019	170	0.000453	This work (Loiano 152 cm)
55 796.53707 ± 0.00034	277	0.000230	This work (Calar Alto 123 cm)
55 829.84931 ± 0.00059	289	0.000812	Shadic (TRESCA)
55 835.40206 ± 0.00091	291	–0.001041	Sauer (TRESCA)
55 835.3994 ± 0.0014	291	0.001619	Trnka (TRESCA)
55 843.72852 ± 0.00081	294	0.000165	Shadic (TRESCA)
55 904.79696 ± 0.00065	316	–0.002761	Shadic (TRESCA)
55 935.3302 ± 0.0012	327	–0.005204	Garcia (TRESCA)
55 968.64736 ± 0.00106	339	0.000301	Shadic (TRESCA)
56 201.83115 ± 0.00103	423	0.002512	Shadic (TRESCA)
56 204.604209 ± 0.000318	424	–0.000404	This work (Calar Alto 123 cm)
56 204.604513 ± 0.000296	424	–0.000100	This work (Loiano 152 cm)

Table 5. Transit mid-times of WASP-21 and their residuals.

Time of minimum BJD(TDB)−2 400 000	Epoch	Residual (JD)	Reference
54 743.0419 ± 0.0022	0	0.001310	Bouchy et al. (2010)
54 743.0283 ± 0.0062	0	–0.012210	Barros et al. (2011)
55 084.51951 ± 0.00032	79	-0.000004	Barros et al. (2011)
55 438.9709 ± 0.0011	161	0.004859	Evans (TRESCA)
55 525.4130 ± 0.0024	181	–0.003433	Barros et al. (2011)
55 797.73268 ± 0.00097	244	–0.002409	Shadic (TRESCA)
56 169.4727 ± 0.0015	330	0.001008	Gajdoš (TRESCA)
56 182.43915 ± 0.00036	333	–0.000100	This work (Calar Alto 123 cm)
56 182.43986 ± 0.00079	333	0.000616	This work (Loiano 152 cm)
56 260.24459 ± 0.00044	351	0.000002	Ivanov, Sokov (TRESCA)

and for WASP-21:

$$T_0 = \mathrm{BJD(TDB)}\ 2\,454\,743.04054\,(71) + 4.3225186\,(30)\,E.$$

The numbers in brackets are the uncertainties to be referred at the last two digits of the number they follow, and E is the number of the cycles after the reference epoch. The quality of the fit is relatively poor ($\chi^2_\nu = 3.68$ and 3.24), implying that the uncertainties in the individual timings are underestimated. We have increased our quoted uncertainties to reflect this.

The central times of the transits are also useful to check for the presence of additional bodies. If another planetary object is a member of the system, it should gravitationally interact with the known planet, causing a periodical variation in T_0. Other phenomena can cause timing variations, for example starspots (Barros et al. 2013). We plot the residuals of the linear fits to the times of minimum light in Figs. 5 and 6. In both cases we do not find any clear evidence of periodic variations in the transit timings.

3.2. Final photometric parameters

Each light curve was modeled separately, yielding its own set of best-fitting parameter values. To assign uncertainties to these values we executed 10 000 Monte Carlo simulations and took the central 68% of the distribution of simulation parameter values to represent 1σ uncertainties. We also calculated uncertainties using a residual-permutation algorithm (Southworth 2008), which is sensitive to correlated noise in light curves. We then took the larger of the Monte Carlo or residual-permutation errorbar for each parameter.

The individual results for each light curve of one TEP were then combined into a single set of final photometric parameters. We did this by taking the weighted mean for each parameter, and increasing the errorbar in those cases where the χ^2_ν of the weighted mean was greater than unity. The final parameters are given in Tables 2 and 3. We found that the agreement between different light curves was good for WASP-21 and acceptable for HAT-P-16. The exception is k for WASP-21, which has $\chi^2_\nu = 14.2$. This value is large, but is not excessive when compared to the results for many of the TEPs analyzed within the Homogeneous Studies project (Southworth 2012). A likely source of the discrepancy is spot activity on the host star.

4. Physical properties of HAT-P-16 and WASP-21

We have measured the main parameters of the two planetary systems, to give a comprehensive picture of their physical

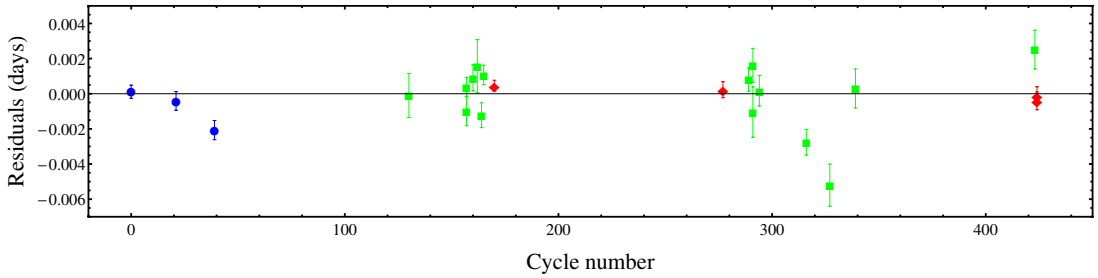

Fig. 5. Residuals of the timing of mid-transit of HAT-P-16 versus a linear ephemeris. The different colors blue, green and red stands for data found in literature, data obtained from the TRESCA catalog and our data, respectively.

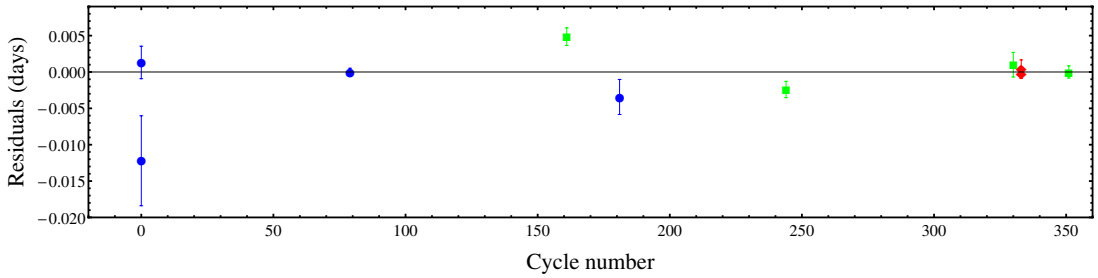

Fig. 6. Residuals of the timing of mid-transit of WASP-21 versus a linear ephemeris. The different colors blue, green and red stands for data found in literature, data obtained from the TRESCA catalog and our data, respectively.

Table 6. Spectroscopic properties of the host stars in HAT-P-16 and WASP-21 adopted from the literature and used in the determination of the physical properties of the systems.

Source	HAT-P-16	Ref.	WASP-21	Ref.
$T_{\rm eff}$ (K)	6140 ± 72	1	5800 ± 100	3
$\left[\frac{\rm Fe}{\rm H}\right]$	0.12 ± 0.08	1	-0.46 ± 0.11	3
$K_{\rm A}$ (m s^{-1})	531.1 ± 2.8	2	116.7 ± 2.2	3
e	0.036 ± 0.004	2	0	3

Notes. (1) Torres et al. (2012); (2) Buchhave et al. (2010); (3) Bouchy et al. (2010).

characteristics. To perform this step, we used standard theoretical models, the photometric parameters derived in the previous section, and the best spectroscopic parameters available in the literature (summarized in Table 6).

Physical properties were calculated following the approach developed by Southworth (2009). In short, we began with an initial estimate of the stellar mass and iteratively adjusted it to find the best agreement between the calculated stellar radius and observed $T_{\rm eff}$ versus those predicted by stellar models for this mass. This process was performed for a grid of stellar ages between the zero-age and terminal-age main sequence in order to find the overall best fit.

We ran the analysis using each of five different sets of theoretical stellar models (see Southworth 2010) in order to determine the variation in results arising from stellar theory, and also propagated the errorbars of the input parameters using a perturbation analysis. This yielded a set of physical properties for each system, a model-based age estimate, and separate statistical and systematic errorbars. These results are shown in Tables 7 and 8.

5. Summary and conclusions

We obtained simultaneous observations of planetary transits in the HAT-P-16 and WASP-21 TEP systems, with the purpose of improving our knowledge of the physical properties of these two systems. The simultaneous observations were performed at two different sites with two medium-class telescopes operating in defocusing mode, achieving observational scatters $\lesssim$1 mmag per point in four of the six light curves. Our observational strategy was aimed at detecting anomalies in the light curves, which might be attributable to astrophysical phenomena (e.g. star spots), but we did not find any clear evidence of these. Small anomalies are detectable by eye in the residuals of the light curve versus the best fits. Each deviation is present in only one light curve, so can safely be attributed to systematic effects arising from the telescope and instrument, or more likely variations in Earth's atmosphere.

We used the new photometric data to revise the ephemerides and physical parameters of the systems. We found the following results:

HAT-P-16

- We obtained improved estimates of the radius of the star and the planet. The value found for the stellar radius is consistent with the one reported in the discovery paper (Buchhave et al. 2010), while the planetary radius is smaller by more than 1σ. The planet has a larger density and surface gravity than previously thought.
- The planet is colder, and the system is less evolved than previously thought.
- Comparing our result obtained for the planetary radius with the theoretical values predicted by Fortney et al. (2007) for a planet at $a = 0.045$ AU, we found that the hot Jupiter size is consistent within 1σ with the 25 $M_{\rm Earth}$ core model of a H/He planet of nearly 0.3 Gyr. However since the predictions

Table 7. Physical properties of the HAT-P-16 system obtained in this work and compared with the discovery paper.

	This work (final)	Buchhave et al. (2010)
M_A ($M_\odot$)	$1.216 \pm 0.042 \pm 0.036$	1.218 ± 0.039
R_A ($R_\odot$)	$1.158 \pm 0.023 \pm 0.011$	1.237 ± 0.054
$\log g_A$ (cgs)	$4.396 \pm 0.016 \pm 0.004$	4.34 ± 0.03
ρ_A ($\rho_\odot$)	0.784 ± 0.040	–
M_b (M_{jup})	$4.193 \pm 0.098 \pm 0.083$	4.193 ± 0.094
R_b (R_{jup})	$1.190 \pm 0.035 \pm 0.012$	1.289 ± 0.066
g_b (ms^{-2})	73.4 ± 4.1	63.1 ± 5.8
ρ_b (ρ_{jup})	$2.33 \pm 0.20 \pm 0.02$	1.95 ± 0.28
T_{eq} (K)	1567 ± 22	1626 ± 40
Θ	$0.2391 \pm 0.0073 \pm 0.0024$	0.220 ± 0.011
a (AU)	$0.04130 \pm 0.00047 \pm 0.00041$	0.0413 ± 0.0004
Age (Gyr)	$0.5^{+0.4\,+0.5}_{-0.5\,-0.5}$	2.0 ± 0.8

Notes. The first errorbar given in our results gives the statistical uncertainty and the second refers to the systematic uncertainty.

Table 8. Physical properties of the WASP-21 system obtained in this work and compared with those found in literature.

	This work (final)	Bouchy et al. (2010)	Barros et al. (2011)	Southworth (2012)
M_A ($M_\odot$)	$0.890 \pm 0.071 \pm 0.035$	1.01 ± 0.03	0.86 ± 0.04	$0.98 \pm 0.12 \pm 0.07$
R_A ($R_\odot$)	$1.136 \pm 0.049 \pm 0.015$	1.06 ± 0.04	$1.097^{+0.035}_{-0.022}$	$1.186 \pm 0.081 \pm 0.028$
$\log g_A$ (cgs)	$4.277 \pm 0.025 \pm 0.006$	4.39 ± 0.03	4.29 ± 0.02	$4.281 \pm 0.031 \pm 0.010$
ρ_A ($\rho_\odot$)	0.607 ± 0.048	0.84 ± 0.09	0.65 ± 0.05	0.587 ± 0.061
M_b (M_{jup})	$0.276 \pm 0.018 \pm 0.007$	0.300 ± 0.011	0.27 ± 0.01	$0.295 \pm 0.027 \pm 0.014$
R_b (R_{jup})	$1.162 \pm 0.052 \pm 0.015$	1.07 ± 0.06	$1.143^{+0.045}_{-0.030}$	$1.263 \pm 0.085 \pm 0.029$
g_b (ms^{-2})	5.07 ± 0.35	–	5.13 ± 0.23	4.58 ± 0.45
ρ_b (ρ_{jup})	$0.165 \pm 0.018 \pm 0.002$	0.24 ± 0.05	$0.181^{+0.015}_{-0.020}$	$0.137 \pm 0.021 \pm 0.003$
T_{eq} (K)	1333 ± 28	–	–	1340 ± 32
Θ	$0.0267 \pm 0.0015 \pm 0.0004$	–	–	$0.0245 \pm 0.0019 \pm 0.0006$
a (AU)	$0.0499 \pm 0.0013 \pm 0.0007$	$0.052^{+0.00041}_{-0.00044}$	0.0494 ± 0.0009	$0.0516 \pm 0.0020 \pm 0.0012$
Age (Gyr)	–	12 ± 5	12 ± 2	–

Notes. The first error given in our, and Southworth's results is referred to the statistical errors whereas the second refers to the systematic uncertainties.

by Fortney et al. (2007) were made for G-type star and HAT-P-16 is an F-type star, we also compared our results with the predictions for $a = 0.02$ AU. In this case the model that best fits our result (within 2σ) is the prediction for a gaseous planet with a 100 M_{Earth} core. Both cases suggest that HAT-P-16 is likely a heavy-element rich planet.

WASP-21

- We found that the planetary radius is greater than that measured in the discovery paper (Bouchy et al. 2010), in agreement with the studies by Barros et al. (2011) and Southworth (2012).
- We compared our result with the prediction made by Fortney et al. (2007), for a similar case: our results are consistent within 3σ with a core-less model for a H/He-dominated planet. This discrepancy may be due to the unavailability of theoretical predictions of a planet with the exact characteristics of those we measure for WASP-21 b. Indeed, the lower metallicity of the host star implies that the planet is composed of lighter elements and therefore has a bigger radius. Another possible explanation is proposed by Fortney et al. (2007, and references therein): a planet which was formerly more massive, but has experienced mass loss and became a Neptune-like planet, may have a radius that significantly exceeds 1 R_{jup}.

Acknowledgements. Based on observations collected at the Centro Astronómico Hispano Alemán (CAHA) at Calar Alto, Spain, operated jointly by the Max-Planck Institut für Astronomie and the Instituto de Astrofísica de Andalucía (CSIC), and on observations obtained with the 1.52 m *Cassini* telescope at the OAB Observatory in Loiano, Italy. J.S. acknowledges financial support from STFC in the form of an Advanced Fellowship. We thank Ulli Thiele and Roberto Gualandi for their technical assistance at the CA 1.23 m telescope and *Cassini* telescope, respectively. The following internet-based resources were used in research for this paper: the ESO Digitized Sky Survey; the NASA Astrophysics Data System; the SIMBAD data base operated at CDS, Strasbourg, France; and the arXiv scientific paper preprint service operated by Cornell University. L.M. thanks the Departamento de Astronomía y Astrofísica of the Pontificia Universidad Católica de Chile for kind hospitality.

References

Barnes, J. W. 2009, ApJ, 705, 683
Barros, S. C. C., Pollacco, D. L., Gibson, N. P., et al. 2011, MNRAS, 416, 2593
Barros, S. C. C., Boué, G., Gibson, N. P., et al. 2013, MNRAS, 430, 3032
Bouchy, F., Hebb, L., Skillen, I., et al. 2010, A&A, 519, A98
Borucki, W. J., Koch, D., Jenkins, J., et al. 2009, Science, 325, 709
Buchhave, L. A., Bakos, G. A., Hartman, J. D., et al. 2010, ApJ, 720, 1118
Calchi Novati, S., Bozza, V., De Paolis, F., et al. 2009, ApJ, 695, 442
Calchi Novati, S., Dall'Ora, M., Gould, A., et al. 2010, ApJ, 717, 987
Cassan, A., Kubas, D., Beaulieu, J.-P., et al. 2012, Nature, 481, 167
Charbonneau, D., Brown, T. M., Latham, D. W., & Mayor, M. 2000, ApJ, 529, L45
Charbonneau, D., Brown, T. M., Noyes, R. W., & Gilliland, R. L. 2002, ApJ, 568, 377
Claret, A., & Hauschildt, P. H. 2003, A&A, 412, 241
Collier Cameron, A., Guenther, E., Smalley, B., & Mcdonald, I. 2010, MNRAS, 407, 507
Deming, D., Seager, S., Richardson, L. J., & Harrington, J. 2005, Nature, 434, 740
Fortney, J. J., Marley, M., & Barnes, J. W. 2007, ApJ, 659, 1661
Fressin, F., Torres, G., Charbonneau, D., et al. 2013, ApJ, 766, 81

Gibson, N. P., Pollacco, D., Simpson, E. K., et al. 2008, A&A, 492, 603
Gillon, M., Pont, F., Moutou, C., Bouchy, F., et al. 2006, A&A, 459, 249
Gould, A., Dong, S., Gaudi, B. S., et al. 2010, ApJ, 720, 1073
Harpsøe, K., Hardis, S., Hinse, T., et al. 2012, A&A, 549, A10
Henry, G. W., Marcy, G. W., Butler, R. P., & Vogt, S. S. 2000, ApJ, 529, L41
Holman, M. J., Fabrycky, D. C., Ragozzine, D., et al. 2010, Science, 330, 51
Howard, A. W., Marcy, G. W., Bryson, S. T., et al. 2012, ApJS, 201, 15
Kipping, D. M., Fossey, S. J., & Campanella, G. 2009, MNRAS, 400, 398
Knutson, H. A., Charbonneau, D., Allen, L. E., et al. 2007, Nature, 447, 183
Liu, H., Zhou, J.-L., & Wang, S. 2011, ApJ, 732, 66
Maciejewski, G., Dimitrov, D., Seeliger, M., et al. 2013, A&A, 551, A108
Mancini, L., Southworth, J., Ciceri, S., et al. 2013a, A&A, 551, A11
Mancini, L., Nikolov, N., & Southworth, J., 2013b, MNRAS, 430, 2932
Mancini, L., Ciceri, S., & Chen, G., 2013c, MNRAS, submitted [arXiv:1306.6384]
Marcy, G. W., & Butler, R. P. 1998, ARA&A, 6, 57
Mayor, M., & Queloz, D. 1995, Nature, 378, 355
Mayor, M., Marmier, M., Lovi, C., et al. 2011, A&A, submitted [arXiv:1109.2497]
Mordasini, C., Alibert, Y., Klahr, H., & Henning, T. 2012a, A&A, 547, A111
Mordasini, C., Alibert, Y., Georgy, C., et al. 2012b, A&A, 547, A112
Moutou, C., Díaz, R. F., Udry, S., & Hébrard, G. 2011, A&A, 533, A113
Nikolov, N., Henning, Th., Koppenhoefer, J., et al. 2012, A&A, 539, A159
Nikolov, N., Chen, G., Fortney, J., et al. 2013, A&A, 553, A26
Pont, F., Zucker, S., & Queloz, D. 2006, MNRAS, 373, 231
Pont, F., Husnoo, N., Mazeh, T., & Fabrycky, D. 2011, MNRAS, 414, 1278
Sanchis-Ojeda, R., Winn, J. N., Holman, M. J., et al. 2011, ApJ, 733, 127
Southworth, J. 2008, MNRAS, 386, 1644
Southworth, J. 2009, MNRAS, 394, 272
Southworth, J. 2010, MNRAS, 408, 1689
Southworth, J. 2012, MNRAS, 426, 1291
Southworth, J., Hinse, T. C., Jørgensen, U. G., et al. 2009a, MNRAS, 396, 1023
Southworth, J., Hinse, T. C., Burgdorf, M. J., et al. 2009b, MNRAS, 399, 287
Southworth, J., Bruni, I., Mancini, L., & Gregorio, J. 2012a, MNRAS, 420, 2580
Southworth, J., Mancini, L., Maxted, P. F. L., et al. 2012b, MNRAS, 422, 3099
Steffen, J. H., Fabrycky, D. C., Agol, E., et al. 2013, MNRAS, 428, 1077
Stetson, P. B. 1987, PASP, 99, 191
Swain, M. R., Vasisht, G., & Tinetti, G. 2008, Nature, 452, 329
Szabó, Gy. M., Szabó, R., Benkõ, J. M., et al. 2011, ApJ, 736, L4
Torres, G., Fischer, D. A., Sozzetti, A., et al. 2012, ApJ, 757, 161
Tregloan-Reed, J., & Southworth, J. 2013, MNRAS, 431, 966
Tregloan-Reed, J., Southworth, J., & Tappert, C. 2013, MNRAS, 428, 3671
Winn, J. N., Holman, M. J., Bakos, G. Á., et al. 2007, AJ, 134, 1707
Winn, J. N., Holman, M. J., Torres, G., et al. 2008, ApJ, 683, 1076
Winn, J. N., Holman, M. J., Carter, J. A., et al. 2009, AJ, 137, 3826

Chapter 6

Multiband observations of HAT-P-23 & WASP-48

In this chapter we present the characterization of the two planetary systems HAT-P-23 and WASP-48, pubblished in A&A in 2015: Ciceri et al. (2015b)

Twinkle, twinkle, little star,
How I wonder what you are!
Up above the world so high,
Like a diamond in the sky.

The Star, Jane Taylor

A&A 577, A54 (2015)
DOI: 10.1051/0004-6361/201425449

Astronomy & Astrophysics

Physical properties of the HAT-P-23 and WASP-48 planetary systems from multi-colour photometry⋆

S. Ciceri[1], L. Mancini[1], J. Southworth[2], I. Bruni[3], N. Nikolov[4], G. D'Ago[5,6], T. Schröder[1], V. Bozza[5,6], J. Tregloan-Reed[7], and Th. Henning[1]

[1] Max-Planck Institute for Astronomy, Königstuhl 17, 69117 Heidelberg, Germany
e-mail: ciceri@mpia.de
[2] Astrophysics Group, Keele University, Staffordshire, ST5 5BG, UK
[3] INAF–Osservatorio Astronomico di Bologna, via Ranzani 1, 40127 Bologna, Italy
[4] Astrophysics Group, University of Exeter, Stocker Road, EX4 4QL, Exeter, UK
[5] Department of Physics, University of Salerno, via Ponte Don Melillo, 84084 Fisciano (SA), Italy
[6] Istituto Nazionale di Fisica Nucleare, Sezione di Napoli, 80126 Napoli, Italy
[7] NASA Ames Research Center, Moffett Field, CA 94035, USA

Received 2 December 2014 / Accepted 2 March 2015

ABSTRACT

Context. Accurate and repeated photometric follow-up observations of planetary transit events are important to precisely characterize the physical properties of exoplanets. A good knowledge of the main characteristics of the exoplanets is fundamental in order to trace their origin and evolution. Multi-band photometric observations play an important role in this process.
Aims. By using new photometric data, we computed precise estimates of the physical properties of two transiting planetary systems at equilibrium temperatures of ∼2000 K.
Methods. We present new broadband, multi-colour photometric observations obtained using three small class telescopes and the telescope-defocussing technique. In particular we obtained 11 and 10 light curves covering 8 and 7 transits of HAT-P-23 and WASP-48, respectively. For each of the two targets, one transit event was simultaneously observed through four optical filters. One transit of WASP-48 b was monitored with two telescopes from the same observatory. The physical parameters of the systems were obtained by fitting the transit light curves with and from published spectroscopic measurements.
Results. We have revised the physical parameters of the two planetary systems, finding a smaller radius for both HAT-P-23 b and WASP-48 b, $R_b = 1.224 \pm 0.037\,R_{Jup}$ and $R_b = 1.396 \pm 0.051\,R_{Jup}$, respectively, than those measured in the discovery papers ($R_b = 1.368 \pm 0.090\,R_{Jup}$ and $R_b = 1.67 \pm 0.10\,R_{Jup}$). The density of the two planets are higher than those previously published ($\rho_b \sim 1.1$ and $\sim 0.3\,\rho_{jup}$ for HAT-P-23 and WASP-48, respectively) hence the two hot Jupiters are no longer located in a parameter space region of highly inflated planets. An analysis of the variation of the planet's measured radius as a function of optical wavelength reveals flat transmission spectra within the experimental uncertainties. We also confirm the presence of the eclipsing contact binary NSVS-3071474 in the same field of view of WASP-48, for which we refine the value of the period to be 0.459 d.

Key words. planetary systems – stars: fundamental parameters – techniques: photometric – stars: individual: HAT-P-23 – stars: individual: WASP-48

1. Introduction

Among the almost 2000 extrasolar planets known to exist, those that transit their parent stars are of particular interest. In contrast to the exoplanets detected with other techniques, most of the physical and orbital parameters of transiting extrasolar planet (TEP) systems are measurable to within a few percent points using standard astronomical methods (e.g. Seager & Mallén-Ornelas 2003; Sozzetti et al. 2007; Southworth et al. 2007; Torres et al. 2008; Southworth 2008). Obtaining estimations of the planets' masses and sizes can give some hints and direction in discriminating between gaseous and rocky structure, and we can therefore infer their formation and evolution history. In particular, precise measurements of planetary sizes can provide strong constraints for those theoretical models that try to explain the inflation mechanisms for highly irradiated gaseous planets. After the discovery of a group of inflated planets (e.g. WASP-17b, TrES-4b and HAT-P-32, Anderson et al. 2011; Sozzetti et al. 2015; Seeliger et al. 2014), several theories invoking tidal friction, enhanced atmospheric opacities, turbulent mixing, ohmic dissipation, windshocks, or more exotic mechanisms have been proposed to account for the slow cooling rate of these planets, resulting in an unexpectedly large radius (see e.g. Baraffe et al. 2014; Spiegel & Burrows 2013; Ginzburg & Sari 2015, and references therein). Deducing their chemical composition is also possible by looking for elemental and molecular signatures in transmission spectra observed during transit events (Seager & Sasselov 2000; Brown 2001).

In this context, we are carrying out a large program to study these TEP systems and to robustly determine their physical properties via photometric monitoring of transit events in different passbands. We are utilising an array of 1−2 m class telescopes, located in both of Earth's hemispheres, and single- or multi-channel imaging instruments. In some cases, a two-site observational strategy was adopted for simultaneous follow-up

⋆ The photometric light curves are only available at the CDS via anonymous ftp to cdsarc.u-strasbg.fr (130.79.128.5) or via http://cdsarc.u-strasbg.fr/viz-bin/qcat?J/A+A/577/A54

A&A 577, A54 (2015)

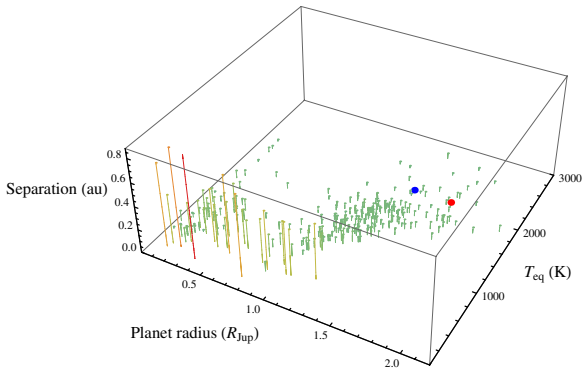

Fig. 1. 3D plot of the known transiting exoplanets. The quantities on the axes are the planetary radius and the temperature, and their semi-major axes. The positions of HAT-P-23 b and WASP-48 b are highlighted by a blue and red point, respectively. Data taken from the TEPcat catalogue.

of transit events (e.g. Ciceri et al. 2013; Mancini et al. 2013a, 2014a). We have so far refined the measured parameters of several TEP systems (e.g. Southworth et al. 2011; Mancini et al. 2013a, 2014c), studied starspot crossing events (Mancini et al. 2013c, 2014b), and probed opacity-induced variations of measured planetary radius with wavelength (e.g. Southworth et al. 2012b; Mancini et al. 2013b,c, 2014b; Nikolov et al. 2013).

In this work, we focus our attention on the HAT-P-23 and WASP-48 systems, both hosting a star with effective temperature $T_{\rm eff} \sim 6000$ K and a close-in gas-giant transiting planet with a high equilibrium temperature of $T_{\rm eq} \sim 2000$ K. We report these characteristics in Fig. 1, together with those of the other known TEPs (data taken from TEPCat[1]). The other main properties of the two TEP systems are summarized in the next two subsections. Observations of 15 new transit events of the two planets, performed at two different observatories, are presented in Sect. 2 together with the reduction of the corresponding photometric data. The analysis of the light curves, described in Sect. 3, is followed by the revision of the physical parameters of the two planetary systems in Sect. 4. We also present new light curves of the eclipsing binary NSVS 3071474, which is located close to WASP-48. Our conclusions are presented in Sect. 5.

1.1. HAT-P-23

The HAT-P-23 system, discovered by Bakos et al. (2011), is composed of a G0 dwarf star (mass 1.13 $M_{\odot}$, radius 1.20 $R_{\odot}$, and metallicity +0.13) and a hot Jupiter (mass 2.09 $M_{\rm Jup}$ and radius 1.37 $R_{\rm Jup}$) revolving around its parent star on a circular orbit with a period of $P = 1.2$ d. Using the SOPHIE spectrograph, Moutou et al. (2011) measured the projected spin-orbit angle through observation of the Rossiter-McLaughlin (R-M) effect. Their finding of $\lambda = 15° \pm 22°$ suggests an aligned and prograde planetary orbit. A reanalysis of the main parameters of the system was performed by Ramón-Fox & Sada (2013). Recently, O'Rourke et al. (2014) reported accurate photometry of planet occultations observed at 3.6 μm and 4.5 μm with the *Spitzer* space telescope and at H and $K_{\rm S}$ bands with the Hale Telescope. They found the emission spectrum to be consistent with a planetary atmosphere having a low efficiency of energy transport from its day-side to night-side, no thermal inversion and a lack of strongly absorbing substances, similar to the case of WASP-19 b (Mancini et al. 2013c).

1.2. WASP-48

WASP-48 is a TEP system composed of a slightly evolved F-type star (mass 1.19 $M_{\odot}$, radius 1.75 $R_{\odot}$, and metallicity −0.12) and an inflated hot Jupiter (mass 0.98 $M_{\rm Jup}$, radius 1.67 $R_{\rm Jup}$, and an orbital period of $P = 2.1$ d; Enoch et al. 2011). The lithium abundance and the absence of Ca II H and K emission suggests that the host star is old and evolving off the main sequence. However, by measuring the age from the rotation period, the star seems to be much younger (Enoch et al. 2011). This discrepancy can be explained if tidal forces between the planet and the parent star have spun up the latter, making it difficult to obtain a reasonable value for the age based on gyrochronology (e.g. Pont 2009). The emission spectrum of WASP-48 b was also investigated by O'Rourke et al. (2014) through IR observations of the planet occultations with the *Spitzer* and the Hale telescopes. The nature of the atmosphere of WASP-48 b was found to be very similar (moderate energy recirculation, no temperature inversion, absence of strong absorbers) to that of HAT-P-23 b.

2. Observations and data reduction

In this section we present photometric observations of eight transits of HAT-P-23 b and seven of WASP-48 b. For both systems, one transit was observed with a multi-band imaging camera. One transit of WASP-48 was simultaneously monitored with two telescopes from the same observatory. The details of the observations are summarized in Table 1.

2.1. Calar Alto 1.23 m telescope

Seven transits of HAT-P-23 b and four of WASP-48 b were remotely observed using the Zeiss 1.23 m telescope at the Calar Alto Observatory in Spain. The telescope has an equatorial mount and is equipped with a DLR-MKIII camera positioned at its Cassegrain focus. The CCD, which was used unbinned, has 4096×4096 pixels and a field of view (FOV) of $21.5' \times 21.5'$ leading to a resolution of $0.32''$ pixel^{-1}. The telescope was autoguided and defocussed for all science observations. This observing mode consists of using the telescope out of focus to spread the light of the stars in the FOV on many more pixels of the CCD than normal in-focus observations. In this way it is possible to use longer exposures, greatly increasing the signal-to-noise ratio (S/N) and reducing the uncertainties due to many sources of noise (Southworth et al. 2009). In our cases, the exposure times were fine-tuned at the beginning of each observation, together with the amount of defocussing, in order to properly optimize the S/N and have a maximum count per pixel for the target star between 25 000 to 35 000 ADUs. Once the defocussing amount was set, it was kept fixed for the entire monitoring of the transit (a typical PSF of the target covered a region with a diameter from 15 to 25 pixel). In some cases, it was necessary to modify the exposure time during the night to avoid the CCD saturation or to account for changes in counts caused by variation of the air mass of the target or weather conditions (e.g. dramatic variations of the external temperature or sudden appearance of cirrus and veils). The filter used to observe HAT-P-23 b was Cousins R; for WASP-48 b the first and last transits were observed through Cousins R and the other two transits through Cousins I (Table 1).

[1] TEPcat is the catalogue of the physical properties of transiting planetary systems (Southworth 2011) and is available at http://www.astro.keele.ac.uk/jkt/tepcat/

Table 1. Details of the observations presented in this work.

Telescope	Date of first obs.	Start time (UT)	End time (UT)	N_{obs}	T_{exp} (s)	T_{obs} (s)	Filter	Airmass	Moon illum.	Aperture radii (px)	Scatter (mmag)
HAT-P-23:											
CA 1.23 m	2011 Aug. 19	23:16	00:52	60	80	103	Cousins *R*	1.78 → 1.34	67%	13, 70, 90	1.41
CA 1.23 m	2012 Jul. 21	00:34	04:30	139	50 to 120	101	Cousins *R*	1.07 → 1.78	9%	14, 70, 90	0.69
CA 1.23 m	2012 Jul. 26	20:25	02:37	286	30 to 130	91	Cousins *R*	1.70 → 1.07	58%	23, 70, 90	1.22
CA 1.23 m	2013 Jun. 16	22:50	03:49	120	135	151	Cousins *R*	1.81 → 1.07	53%	23, 60, 90	0.95
CA 1.23 m	2013 Jul. 03	21:47	03:49	194	85 to 100	110	Cousins *R*	1.78 → 1.07	15%	16, 70, 90	0.77
CA 1.23 m	2013 Jul. 26	20:25	02:37	87	30 to 130	61	Cousins *R*	1.70 → 1.07	76%	23, 70, 90	1.59
CA 1.23 m	2013 Jul. 31	19:55	03:02	147	145 to 155	166	Cousins *R*	1.80 → 1.07	28%	25, 70, 90	1.19
CA 2.2 m	2013 Sep. 03	19:39	23:45	113	60 to 120	133	Thuan-Gunn *u*	1.21 → 1.07	2%	10, 25, 40	3.55
CA 2.2 m	2013 Sep. 03	19:39	23:45	117	60 to 120	133	Thuan-Gunn *g*	1.21 → 1.07	2%	23, 55, 70	0.92
CA 2.2 m	2013 Sep. 03	19:39	23:45	118	60 to 120	133	Thuan-Gunn *r*	1.21 → 1.07	2%	21, 45, 65	0.71
CA 2.2 m	2013 Sep. 03	19:39	23:45	116	60 to 120	133	Thuan-Gunn *z*	1.21 → 1.07	2%	17, 50, 70	1.49
WASP-48:											
Cassini	2011 May 23	22:04	01:02	91	52 to 90	92	Gunn *r*	1.30 → 1.04	57%	13, 70, 90	0.82
Cassini	2011 May 25	21:33	02:45	222	50 to 90	81	Gunn *r*	1.37 → 1.02	38%	13, 70, 90	0.81
CA 1.23 m	2011 Aug. 23	22:56	03:53	259	25 to 42	63	Cousins *R*	1.77 → 1.27	29%	11, 30, 45	1.90
CA 1.23 m	2012 Sep. 12	19:08	01:25	136	120 to 160	151	Cousins *I*	1.07 → 1.74	5%	20, 70, 90	1.01
CA 1.23 m	2013 Jul. 24	20:10	04:12	214	110 to 120	125	Cousins *I*	1.05 → 1.59	92%	22, 70, 90	0.61
CA 2.2 m	2011 Aug. 23	21:23	04:40	256	50 to 80	101	Strömgren *u*	1.07 → 2.36	29%	10, 16, 30	2.88
CA 2.2 m	2011 Aug. 23	21:23	04:40	246	50 to 80	101	Thuan-Gunn *g*	1.07 → 2.36	29%	25, 40, 80	1.19
CA 2.2 m	2011 Aug. 23	21:23	04:40	248	50 to 80	101	Thuan-Gunn *r*	1.07 → 2.36	29%	23, 33, 60	1.09
CA 2.2 m	2011 Aug. 23	21:23	04:40	134	50 to 80	101	Cousins *I*	1.07 → 2.36	29%	18, 28, 50	1.25
CA 1.23 m	2014 Jun. 02	20:34	03:40	184	115 to 134	126	Cousins *R*	2.12 → 1.05	25%	20, 80, 100	0.89

Notes. N_{obs} is the number of observations, T_{exp} is the exposure time, T_{obs} is the mean observational cadence, and "Moon illum." is the fractional illumination of the Moon.

2.2. Cassini 1.52 m telescope

Two transit light curves of WASP-48 were obtained on 2011 May 23 and 25 at the Astronomical Observatory of Bologna in Loiano, Italy. Observations were carried out with BFOSC (Bologna Faint Object Spectrograph and Camera) mounted at the Cassegrain focus of the 1.52 m *Cassini* telescope (see Table 1). The 1300×1340 pixels CCD has a FOV of $13' \times 12.6'$ resulting in a resolution of $0.58''$ pixel^{-1}. For both transits a Gunn-*r* filter was used and the telescope was autoguided and defocussed. During the acquisition of the science images, the CCD was windowed to decrease the readout time, thus achieving a higher temporal cadence.

2.3. Calar Alto 2.2 m telescope

One transit of each object was observed with the Bonn University Simultaneous Camera (BUSCA, Reif et al. 1999) mounted on the Calar Alto 2.2 m telescope. BUSCA can obtain photometry in four different passbands simultaneously, the incoming light being split by dichroics. Each of the four channels has a 4096×4096 pixel CCD, which were used with 2×2 binning to give a plate scale of $0.35''$ pixel^{-1}. The FOV of each channel depends on the filter in the light beam, which is $5.8'$ in diameter for the Thuan-Gunn and Strömgren filters and $12' \times 12'$ for the Cousins *I* filter. The telescope was autoguided and defocussed during both observing sequences.

Unfortunately, the BUSCA controller requires that the same exposure time be used in all four channels. The exposure times were therefore chosen to avoid saturation in the *r* band, for which the count rate was highest. This meant that the redder channels yielded better-quality data than the bluer channels, especially the *u* band.

2.4. Data reduction

Data reduction was performed using standard methods. Bias and flat-field images on the sky were collected before and during twilight, respectively, and median-combined to generate master bias and flat-field frames. These were used to calibrate the science images. Light curves were then obtained using aperture photometry algorithms from (Stetson 1987) as implemented in the [2]-based pipeline (see Southworth et al. 2014, and references therein), which uses subroutines from the NASA [3] library.

The sizes of the software apertures used for the aperture photometry are listed in Table 1, and were chosen to be those that gave the lowest out-of-transit (OOT) scatter. We noticed that changes in the aperture size of both the target region and the sky annulus do not affect the overall light-curve shape, but do cause a slight variation in the scatter of the data points. Once the aperture sizes were set, we extracted instrumental magnitudes for the target and possible comparison stars in the FOV. Pointing variations were corrected by cross-correlating each image against a reference frame. The light curves were then detrended by a second-order polynomial whilst optimising the weights of an ensemble of comparison stars. The choice of the comparison stars was carried out according to their brightness, by comparing the different OOT scatter and taking the combination that gave the lowest scatter.

[2] The acronym stands for Interactive Data Language and is a trademark of ITT Visual Information Solutions. For further details see: http://www.ittvis.com/ProductServices/IDL.aspx

[3] The subroutine library is distributed by NASA. For further details see: http://idlastro.gsfc.nasa.gov/

A&A 577, A54 (2015)

Table 2. Stellar atmospheric parameters used to calculate the limb darkening coefficients, and weighted-mean values of the linear coefficients obtained from the fit of the light curves.

Parameter	HAT-P-23 A	WASP-48 A
$T_{\rm eff}$ (K)	5905	6000
$\log g$ (cm s^{-2})	4.33	4.03
$[\frac{\rm Fe}{\rm H}]$	0.1	−0.1
$V_{\rm micro}$ (km s^{-1})	2.0	2.0
LD coeff R	0.317 ± 0.031	0.277 ± 0.075
LD coeff I	–	0.101 ± 0.067
LD coeff u	0.780 ± 0.511	1.09 ± 0.33
LD coeff g	0.239 ± 0.090	0.631 ± 0.164
LD coeff r	0.221 ± 0.066	0.229 ± 0.065
LD coeff z	0.179 ± 0.139	–

3. Light curve analysis

We separately analyzed each of the light curves observed using the [4] code (see Southworth 2008, and references therein). fits an observed light curve with a synthetic one, constructed according to the values of a set of initial parameters. Some of the input parameters are left free to vary until the best fit is reached. The main photometric parameters that we can measure with are the orbital inclination, i; the orbital period, P; the transit midpoint, T_0; and the sum and ratio of the fractional radii of the star and planet, $r_{\rm A} + r_{\rm b}$ and $k = r_{\rm b}/r_{\rm A}$. The fractional radii are defined as $r_{\rm A} = R_{\rm A}/a$ and $r_{\rm b} = R_{\rm b}/a$, where a is the orbital semi-major axis, and $R_{\rm A}$ and $R_{\rm b}$ are the absolute radii of the star and the planet, respectively.

We assumed circular orbits for both the planetary systems (Enoch et al. 2011; O'Rourke et al. 2014). The values of the planet-star mass ratio were fixed to those obtained using the estimated masses from the discovery papers. The limb darkening effect on the light curves was taken into account by modelling it using a quadratic law, and we checked that the difference in the results obtained using a linear or a logarithmic law is negligible.

The fits of the light curves were performed using theoretical values of the limb darkening coefficients (Claret 2000, 2004a) and by fitting the linear coefficients whilst fixing the quadratic coefficients but perturbing them during the error analysis simulations. The atmospheric parameters of the stars HAT-P-23 A and WASP-48 A, assumed for deriving the initial values of the limb-darkening coefficients, and the weighted-mean values of the limb-darkening coefficient obtained from the fit of the light curves are listed in Table 2.

Since the routine, which we used to perform aperture photometry on the calibrated science images, commonly underestimates the error bars, we enlarged them for each data set by multiplying the error bar for each photometric point by the square root of the χ^2_ν obtained through an initial fit of the corresponding light curve. We then further inflated the errors using the β approach (e.g. Pont et al. 2006; Gillon et al. 2006; Winn et al. 2007) to take into account the presence of systematic effects and correlated noise.

To assign the uncertainties to each parameter obtained from the fitting process, we generated 10 000 simulations with a Monte Carlo algorithm and also used a residual-permutation algorithm (Southworth 2008). Since none of the two techniques systematically gives lower uncertainties, we took the larger of the 1σ values obtained using the two algorithms. The best-fitting model and the residuals for each of the 21 light curves are shown in Figs. 2–5.

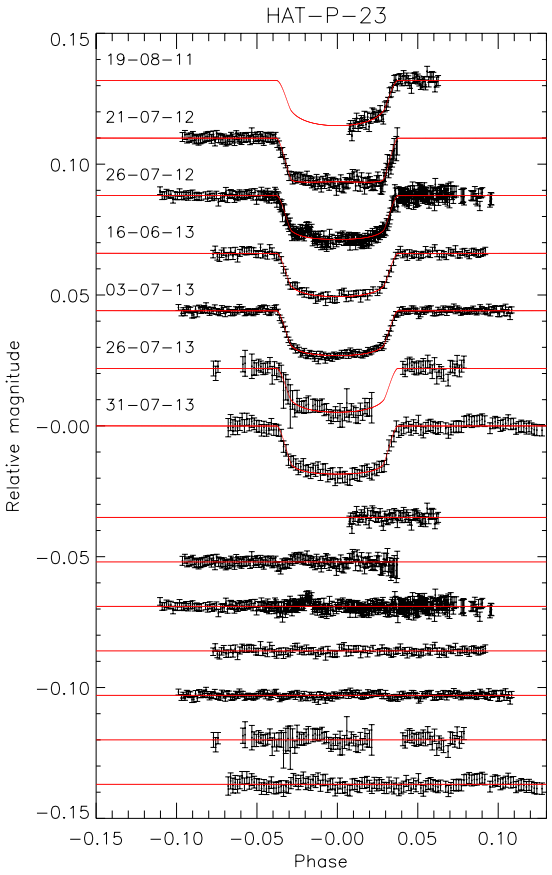

Fig. 2. Light curves of transits of HAT-P-23 b, observed with the Calar Alto 1.23 m telescope, compared with the best-fitting models given by . The date of each observation is given next to the corresponding light curve. The residuals from the fits are shown at the base of the figure in the same order as the light curves.

3.1. New orbital ephemeris

We refined the orbital periods of both planets by using our new photometric data and transit timings available in the literature or at the ETD[5] website.

We made a linear fit to the transit midpoints versus cycle numbers in order to improve the ephemeris. All the transits considered in the linear fit for the two planetary systems are listed in Tables 3 and 4. The new values for the ephemeris found from the fits are

$$T_0 = \text{BJD(TDB)}\ 2\,454\,852.26599\,(20) + 1.21288287\,(17)\,E,$$

and

$$T_0 = \text{BJD(TDB)}\ 2\,455\,364.55241\,(24) + 2.14363544\,(58)\,E.$$

[4] The source code of is available at http://www.astro.keele.ac.uk/jkt/codes/jktebop.html

[5] The Exoplanet Transit Database (ETD) website can be found at http://var2.astro.cz/ETD

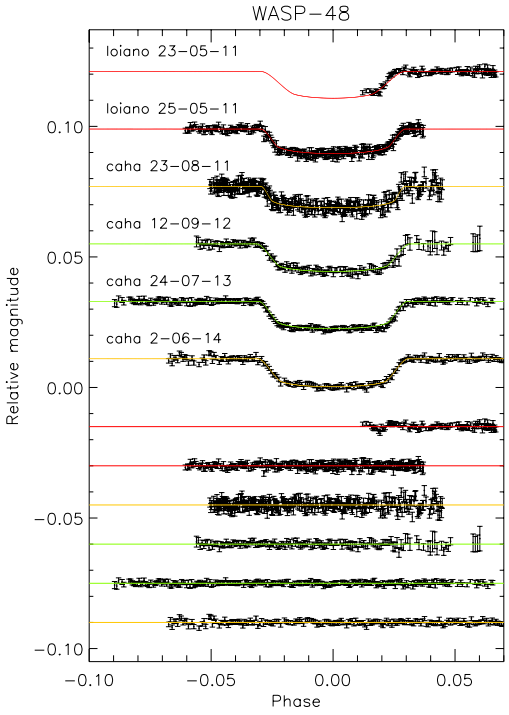

Fig. 3. Light curves of transits of WASP-48 b, observed with the *Cassini* 1.52-m ("loiano") and Calar Alto 1.23 m ("caha") telescopes, compared with the best-fitting curves given by . The date of each observation is given next to the corresponding light curve. The residuals from the fits are shown at the base of the figure in the same order as the light curves.

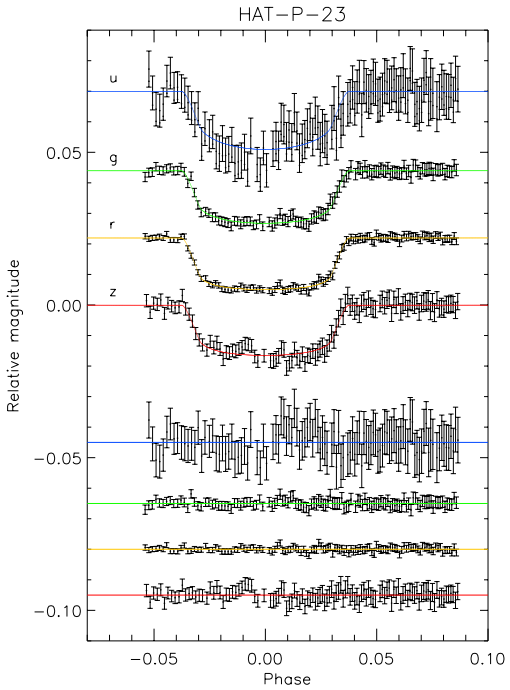

Fig. 4. A planetary transit event of HAT-P-23 b as observed with the BUSCA instrument mounted on the CAHA 2.2 m telescope. The light curves in the Thuan-Gunn *ugrz* are shown from top to bottom and are compared to the best fits. The residuals are plotted at the base of the figure.

for HAT-P-23 and WASP-48, respectively. The numbers in brackets are the errors relative to the last digit, and E represents the cycle number.

If a TEP system, known to be composed of a parent star and a planet, hosts other planets, the gravitational interaction between the planetary components results in a periodic delay and advance in the times of transit of the known planet. We checked for a possible third component in the HAT-P-23 and WASP-48 systems by looking to see whether there was a periodic variation in the transit times of the known planets.

The residuals from the linear fits are plotted in Figs. 6 and 7 as a function of cycle number and do not show any clear systematic deviation from the predicted transit times. However, the quality of the fits, $\chi^2_\nu = 3.26$ for HAT-P-23 and $\chi^2_\nu = 10.05$ for WASP-48, indicates that a linear ephemeris is not a good match to the observations in both the cases. Based on our experience with a similar situation in previous studies (e.g. Southworth et al. 2012a,b; Mancini et al. 2013a,c), we conservatively do not interpret the large χ^2_ν values as a sign of transit timing variations, but as an underestimation of the uncertainties in the various T_0 measurements.

3.2. Final photometric parameters

The final photometric parameters for the HAT-P-23 system were obtained taking into account only the complete transit light curves (i.e. discarding the two partial ones). This choice was

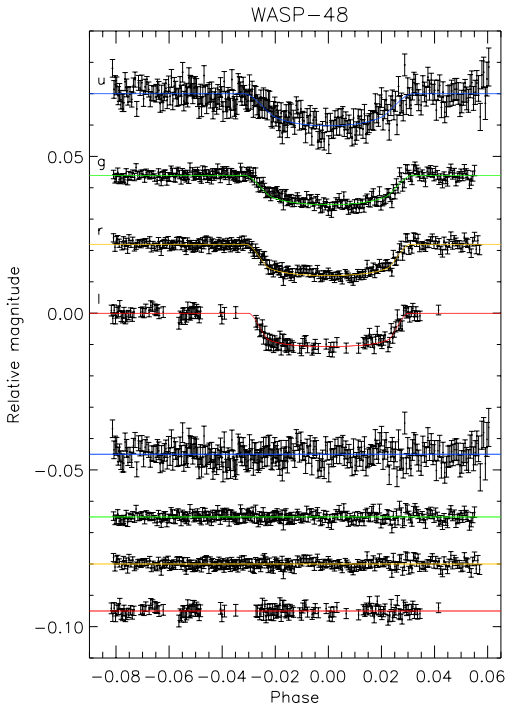

Fig. 5. As for Fig. 4 but for WASP-48 b. A Cousins I filter was used in the reddest arm of BUSCA, while a Strömgren u was used in the bluest arm.

A&A 577, A54 (2015)

Table 3. Times of transit midpoint of HAT-P-23 b and their residuals.

Time of minimum BJD(TDB) −2 400 000	Epoch	Residual (JD)	Reference
54 852.265383 ± 0.00018	0	–0.00061	(1)
55 434.453087 ± 0.00103	480	0.00331	(2)
55 451.430268 ± 0.00112	494	0.00013	(2)
55 736.460815 ± 0.00086	729	0.00321	(2)
55 749.802945 ± 0.00072	740	0.00362	(2)
55 753.439625 ± 0.00112	743	0.00166	(2)
55 776.484166 ± 0.00085	762	0.00142	(2)
55 783.762296 ± 0.00051	768	0.00226	(2)
55 812.871847 ± 0.00114	792	0.00262	(2)
55 838.341217 ± 0.00063	813	0.00145	(2)
56 129.433378 ± 0.00060	1053	0.00172	(2)
56 129.433908 ± 0.00068	1053	0.00225	(2)
56 129.432399 ± 0.00041	1053	0.00057	(3)
56 135.496648 ± 0.00157	1058	0.00263	(2)
56 135.495288 ± 0.00032	1058	0.00158	(3)
56 159.756359 ± 0.00085	1078	0.00202	(2)
56 186.438739 ± 0.00090	1100	–0.00075	(2)
56 460.547674 ± 0.00033	1326	0.00124	(3)
56 477.528543 ± 0.00025	1340	–0.00137	(3)
56 478.743946 ± 0.00091	1341	0.00074	(2)
56 500.574007 ± 0.00281	1359	–0.00079	(3)
56 505.425061 ± 0.00052	1363	–0.00101	(3)
56 539.383814 ± 0.00168	1391	–0.00050	(4) u
56 539.385859 ± 0.00036	1391	0.00019	(4) g
56 539.385926 ± 0.00021	1391	–0.00029	(4) r
56 539.385145 ± 0.00051	1391	–0.00226	(4) z
56 562.430097 ± 0.00122	1410	–0.00021	(2)
56 562.432087 ± 0.00098	1410	–0.00015	(2)
56 579.409838 ± 0.00114	1424	–0.00093	(2)

References. (1) Bakos et al. (2011); (2) TRESCA; (3) CA 1.23 m, this work; (4) CA 2.2 m, this work.

Table 4. Times of transit midpoint of WASP-48 b and their residuals.

Time of minimum BJD(TDB)−2 400 000	Epoch	Residual (JD)	Reference
55 364.55202 ± 0.00027	0	–0.00039	(1)
55 696.80915 ± 0.00131	155	–0.00675	(2)
55 696.81647 ± 0.00155	155	0.00056	(2)
55 750.41680 ± 0.00151	180	0.01000	(2)
55 782.56695 ± 0.00195	195	0.00562	(2)
55 797.56545 ± 0.00160	202	–0.00131	(2)
55 825.43480 ± 0.00152	215	0.00076	(2)
56 033.37084 ± 0.00162	312	0.00416	(2)
56 065.51850 ± 0.00187	327	–0.00270	(2)
56 168.42213 ± 0.00067	375	0.00642	(2)
56 391.34809 ± 0.00218	479	–0.00570	(2)
56 393.49772 ± 0.00087	480	0.00029	(2)
56 453.51930 ± 0.00181	508	0.00007	(2)
56 468.53007 ± 0.00110	515	0.00540	(2)
56 487.81919 ± 0.00060	524	0.00180	(2)
56 511.40314 ± 0.00252	535	0.00576	(2)
56 541.40894 ± 0.00103	549	0.00067	(2)
56 541.41054 ± 0.00139	549	0.00227	(2)
55 705.37900 ± 0.01013	159	–0.01145	(3)
55 707.53160 ± 0.00041	160	–0.00248	(3)
55 797.57056 ± 0.00063	202	0.00378	(4)
55 797.56621 ± 0.00162	202	–0.00056	(5) u
55 797.56614 ± 0.00063	202	–0.00063	(5) g
55 797.56473 ± 0.00053	202	–0.00204	(5) r
55 797.56569 ± 0.00050	202	–0.00108	(5) I
56 183.42469 ± 0.00062	382	0.00353	(4)
56 498.53535 ± 0.00025	529	–0.00021	(4)
56 811.50538 ± 0.00025	675	–0.00094	(4)

References. (1) Enoch et al. (2011); (2) TRESCA; (3) Loiano 1.52 m, this work; (4) CA 1.23 m, this work; (5) CA 2.2 m, this work.

made after noticing that the χ^2_ν, relative to the ratio of the radii of the planet and the star, decreases significantly (from 4.37 to 0.99) when rejecting them. Concerning WASP-48, we discarded the incomplete light curve and those with very high scatter (i.e. the light curve observed on 2011 Aug. 23 with the CA 1.23 m and with BUSCA in the u band). Even discarding three light curves, the χ^2_ν for the k parameter remained rather high (8.48). This discrepancy is discussed further in Sect. 4.1.

The final values were obtained as a weighted mean of all the transits taken into account. The relative errors, obtained from the weighted mean, are rescaled by multiplying them for the relative χ^2_ν.

The parameters of the fits to each of our light curves are given in Tables 5 and 6 for HAT-P-23 and WASP-48, respectively. These tables also show the final photometric parameters in bold font, and the results from the discovery papers for comparison.

4. Physical properties of HAT-P-23 and WASP-48

Following the methodology used by Southworth (2010), the main physical parameters of the TEP systems HAT-P-23 and WASP-48 were found from the photometric parameters deduced from the parameters available in the literature (see Table 7 for values and references), and by interpolating within the tabulated predictions of five sets of theoretical stellar models (Claret 2004b; Demarque et al. 2004; Pietrinferni et al. 2004; VandenBerg et al. 2006; Dotter et al. 2008). In brief, an initial estimate of the stellar mass was specified and the observed quantities were compared to the ones predicted by stellar models for this mass. The mass was then iteratively adjusted to find the best agreement between the observed and expected values.

Since the radius versus mass relation varies according to the age of the star, the interpolation was performed for different ages of the system, starting from 0.1 Gyr until the end of the main-sequence lifetime of the star, in steps of 10 Myr. The output set of physical parameters is the one that gives the best agreement between the predicted and the measured quantities. Separate sets of results were calculated using each of the five sets of theoretical model tabulations.

The final values found are shown in Table 8 for HAT-P-23 and Table 9 for WASP-48. Most quantities have two error bars, and in these cases the first is a statistical error obtained by propagating the uncertainties on the input measurements, and the second is a systematic error which is the scatter of the results from each of the five different sets of theoretical models (see Southworth 2009).

4.1. Radius versus wavelength variation

Photometric observations of planetary transit events through different filters allow us to measure the apparent radius of transiting planets in each passband, obtaining an insight of the composition

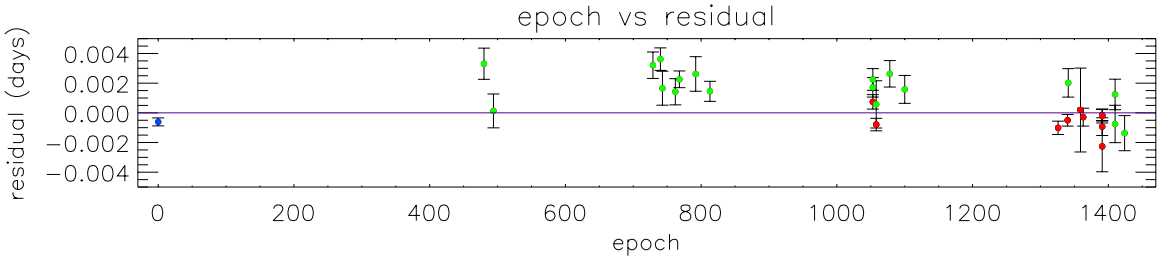

Fig. 6. Residuals of the timing of mid-transit of HAT-P-23 versus a linear ephemeris. The points indicate literature results (blue), data obtained from the TRESCA catalogue (red), and our data (green).

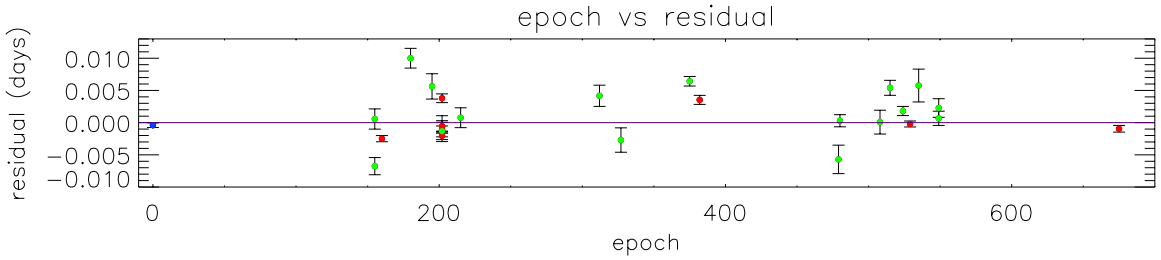

Fig. 7. Residuals of the timing of mid-transit of WASP-48 versus a linear ephemeris. The points indicate the value from the discovery paper (blue), data obtained from the TRESCA catalogue (red), and our data (green).

Table 5. Photometric properties of the HAT-P-23 system derived by fitting the light curves with .

Source	$r_A + r_b$	k	i	r_A	r_b
CA 1.23 m # 1*	0.26447 ± 0.02107	0.11350 ± 0.00267	89.72 ± 0.90	0.23751 ± 0.01893	0.02696 ± 0.00224
CA 1.23 m # 2*	0.28307 ± 0.01135	0.12220 ± 0.00103	82.01 ± 1.19	0.25225 ± 0.01002	0.03083 ± 0.00138
CA 1.23 m # 3	0.23870 ± 0.00861	0.11343 ± 0.00129	88.48 ± 2.23	0.21438 ± 0.00765	0.02432 ± 0.00102
CA 1.23 m # 4	0.24324 ± 0.00856	0.11196 ± 0.00180	87.05 ± 2.44	0.21875 ± 0.00745	0.02450 ± 0.00116
CA 1.23 m # 5	0.25716 ± 0.00625	0.11732 ± 0.00113	84.48 ± 0.92	0.23016 ± 0.00539	0.02700 ± 0.00086
CA 1.23 m # 6	0.25561 ± 0.01734	0.11175 ± 0.00498	86.56 ± 3.42	0.22992 ± 0.01533	0.02569 ± 0.00216
CA 1.23 m # 7	0.25067 ± 0.01582	0.12028 ± 0.00201	85.94 ± 3.22	0.22376 ± 0.01382	0.02691 ± 0.00205
CA 2.2 m *u*	0.28919 ± 0.03285	0.12114 ± 0.01224	81.87 ± 4.85	0.25794 ± 0.02940	0.03125 ± 0.00462
CA 2.2 m *g*	0.25315 ± 0.02248	0.11856 ± 0.00192	84.18 ± 3.71	0.22632 ± 0.01972	0.02683 ± 0.00278
CA 2.2 m *r*	0.24223 ± 0.00920	0.11668 ± 0.00121	86.30 ± 2.50	0.21692 ± 0.00819	0.02531 ± 0.00124
CA 2.2 m *z*	0.23377 ± 0.00981	0.11505 ± 0.00207	87.17 ± 2.64	0.20965 ± 0.00854	0.02412 ± 0.00131
Final results	**0.24539 ± 0.00499**	**0.11616 ± 0.00081**	**85.74 ± 0.95**	**0.21998 ± 0.00436**	**0.02541 ± 0.00065**
Bakos et al. (2011)	0.268 ± 0.014	0.1169 ± 0.0012	85.1 ± 1.5	0.240 ± 0.014	0.028 ± 0.014

Notes. The final parameters are given in bold and are compared with those of the discovery paper. (*) Light curve not taken into account for the final result.

Table 6. Photometric properties of the WASP-48 system derived by fitting the light curves with .

Source	$r_A + r_b$	k	i	r_A	r_b
Cassini # 1*	0.23478 ± 0.02433	0.08349 ± 0.00233	84.33 ± 2.50	0.21668 ± 0.02273	0.01809 ± 0.00184
Cassini # 2	0.22734 ± 0.01098	0.09028 ± 0.00081	82.34 ± 0.96	0.20852 ± 0.00995	0.01883 ± 0.00102
CA 1.23 m # 1*	0.18406 ± 0.00280	0.07810 ± 0.00131	89.90 ± 0.65	0.17072 ± 0.00270	0.01333 ± 0.00022
CA 1.23 m # 2	0.23268 ± 0.01670	0.09426 ± 0.00201	82.49 ± 1.70	0.21264 ± 0.01496	0.02004 ± 0.00179
CA 1.23 m # 3	0.23979 ± 0.00790	0.09648 ± 0.00046	81.56 ± 0.67	0.21870 ± 0.00715	0.02110 ± 0.00074
CA 2.2 m *u**	0.28972 ± 0.04443	0.09503 ± 0.01380	78.88 ± 3.66	0.26458 ± 0.03772	0.02515 ± 0.00678
CA 2.2 m *g*	0.20267 ± 0.01931	0.08247 ± 0.00407	85.24 ± 3.25	0.18723 ± 0.01750	0.01544 ± 0.00193
CA 2.2 m *r*	0.22335 ± 0.02172	0.08900 ± 0.00367	83.23 ± 2.25	0.20509 ± 0.01958	0.01825 ± 0.00230
CA 2.2 m *I*	0.21368 ± 0.01603	0.09392 ± 0.00145	83.98 ± 1.63	0.19533 ± 0.01449	0.01835 ± 0.00156
CA 1.23 m # 4	0.23689 ± 0.01140	0.09613 ± 0.00126	81.79 ± 1.04	0.21612 ± 0.01020	0.02078 ± 0.00123
Final results	**0.23276 ± 0.00578**	**0.09584 ± 0.00077**	**81.99 ± 0.54**	**0.21272 ± 0.00520**	**0.02010 ± 0.00059**
Enoch et al. (2011)	0.259 ± 0.013	0.098 ± 0.014	$80.09^{+0.88}_{-0.79}$	0.2364 ± 0.0125	0.0227 ± 0.0272

Notes. The final parameters are given in bold and are compared with those of the discovery paper. (*) Light curve not taken into account for the final result.

A&A 577, A54 (2015)

Table 7. Spectroscopic parameters of the stars HAT-P-23 A and WASP-48 A.

Source	HAT-P-23 A	Ref.	WASP-48 A	Ref.
$T_{\rm eff}$ (K)	5885 ± 72	1	6000 ± 150	4
$\left[\frac{\rm Fe}{\rm H}\right]$	0.13 ± 0.08	1	−0.12 ± 0.12	4
$K_{\rm A}$ (m s^{-1})	368.5 ± 17.6	2	$136.0^{+11.0}_{-11.1}$	4
e	0.0 fixed	3	0.0 fixed	4

References. (1) Torres et al. (2012); (2) Bakos et al. (2011); (3) O'Rourke et al. (2014); (4) Enoch et al. (2011).

Table 8. Physical properties for the HAT-P-23 system.

	This work (final)	Bakos et al. (2011)
$M_{\rm A}$ ($M_\odot$)	1.104 ± 0.043 ± 0.018	1.13 ± 0.04
$R_{\rm A}$ ($R_\odot$)	1.089 ± 0.027 ± 0.006	1.20 ± 0.07
$\log g_{\rm A}$ (cgs)	4.407 ± 0.018 ± 0.002	4.33 ± 0.06
$\rho_{\rm A}$ ($\rho_\odot$)	0.855 ± 0.051	–
$M_{\rm b}$ ($M_{\rm jup}$)	2.07 ± 0.12 ± 0.02	2.090 ± 0.111
$R_{\rm b}$ ($R_{\rm jup}$)	1.224 ± 0.036 ± 0.007	1.368 ± 0.090
$g_{\rm b}$ (m s^{-2})	34.3 ± 2.4	27.5 ± 3.2
$\rho_{\rm b}$ ($\rho_{\rm jup}$)	1.057 ± 0.097 ± 0.006	0.81 ± 0.15
$T_{\rm eq}$ (K)	1951 ± 30	2056 ± 66
Θ	0.0706 ± 0.0040 ± 0.0004	0.062 ± 0.004
a (AU)	0.02302 ± 0.00030 ± 0.00012	0.0232 ± 0.0002
Age (Gyr)	$2.1^{+3.4\,+1.1}_{-4.5\,-2.0}$	4.0 ± 1.0

Notes. The results obtained in this work are reported and compared with those of the discovery paper.

of their atmosphere (e.g. Southworth et al. 2012b; Copperwheat et al. 2013; Nikolov et al. 2013; Mancini et al. 2013c; Narita et al. 2013; Chen et al. 2014). We used our multi-band data to investigate possible variations of the radius of HAT-P-23 b and WASP-48 b in different optical passbands.

We phased all the light curves collected with the same telescope and filter combination and, following the strategy used by Southworth et al. (2012b), we re-fitted them and the BUSCA curves with all parameters fixed to the final values listed in Tables 8 and 9, with the exception of k. This approach allows the sources of uncertainty common to all data sets to be removed, maximizing the accuracy of estimations of the planet/star radius ratio as a function of wavelength. Because of the very large uncertainty, the values of k measured in the u band were ignored. The results in the other bands are shown in Fig. 8 for HAT-P-23 b and Fig. 9 for WASP-48 b. The vertical bars represent the relative errors in the measurements and the horizontal bars show the full width at half-maximum (FWHM) transmission of the passbands used. Transmission curves of the adopted filters are shown in the bottom panel.

For illustration, the results obtained for HAT-P-23 b are compared with three spectra calculated from 1D model atmospheres by Fortney et al. (2010) for a Jupiter-mass planet with a surface gravity of $g_{\rm b} = 25\,{\rm m\,s^{-2}}$, a base radius of 1.25 $R_{\rm Jup}$ at 10 bar, and $T_{\rm eq} = 2000$ K. The first model (red line) is run in an isothermal case taking into account chemical equilibrium and the presence of strong absorbers, such as TiO and VO. The second model (green line) is obtained omitting the presence of the strong absorbers. The last model (blue line) is obtained by artificially removing the strong absorbers, as in the previous case, but also increasing the H_2/He Rayleigh scattering by a factor of 100. The values of k for WASP-48 b were compared with another model from Fortney et al. (2010) similar to previous ones, but for a Jupiter-mass planet with a surface gravity of $g_{\rm b} = 10\,{\rm m\,s^{-2}}$ and without strong absorbers.

Table 9. Final results for the physical parameters of WASP-48 obtained in this work compared to those of the discovery paper.

	This work (final)	Enoch et al. (2011)
$M_{\rm A}$ ($M_\odot$)	1.062 ± 0.074 ± 0.014	1.19 ± 0.05
$R_{\rm A}$ ($R_\odot$)	1.519 ± 0.051 ± 0.007	1.75 ± 0.09
$\log g_{\rm A}$ (cgs)	4.101 ± 0.023 ± 0.002	4.03 ± 0.04
$\rho_{\rm A}$ ($\rho_\odot$)	0.303 ± 0.022	0.22 ± 0.03
$M_{\rm b}$ ($M_{\rm jup}$)	0.907 ± 0.085 ± 0.008	0.98 ± 0.09
$R_{\rm b}$ ($R_{\rm jup}$)	1.396 ± 0.051 ± 0.006	1.67 ± 0.10
$g_{\rm b}$ (m s^{-2})	11.5 ± 1.1	8.1 ± 1.1
$\rho_{\rm b}$ ($\rho_{\rm jup}$)	0.312 ± 0.037 ± 0.001	0.21 ± 0.04
$T_{\rm eq}$ (K)	1956 ± 54	2030 ± 70
Θ	0.0406 ± 0.0036 ± 0.0002	–
a (AU)	0.03320 ± 0.00077 ± 0.00015	0.03444 ± 0.00043
Age (Gyr)	$6.6^{+1.0\,+0.6}_{-4.9\,-2.8}$	$7.9^{+2.0}_{-1.6}$

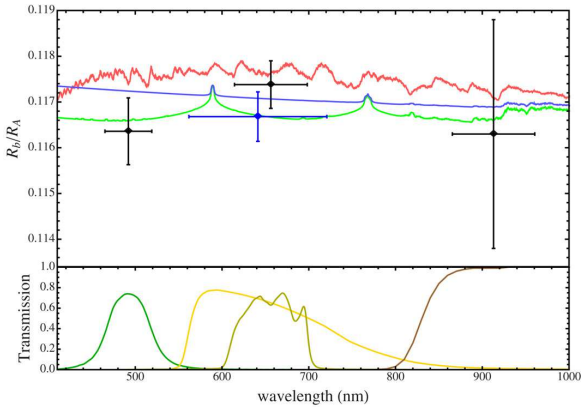

Fig. 8. Variation of the planetary radius of HAT-P-23 b, in terms of planet/star radius ratio, with wavelength. The black points are from the transit observed with BUSCA, while the blue point is the weighted-mean results coming from the seven transits observed in Cousins R with the CA 1.23 m telescope. The vertical bars represent the errors in the measurements and the horizontal bars show the FWHM transmission of the passbands used. The observational points are compared with three synthetic spectra for a Jupiter planet with a surface gravity of $g_{\rm b} = 25\,{\rm m\,s^{-2}}$ and $T_{\rm eq} = 2000$ K. The synthetic spectra in green and blue do not include TiO and VO opacity, while the spectrum in red does, based on equilibrium chemistry. With respect to the model identified with the green line, the blue one has H_2/He Rayleigh scattering increased by a factor of 100. An offset is applied to all three models to provide the best fit to our radius measurements. Transmission curves of the filters used are shown in the bottom panel.

The precision of the final results does not allow us to discriminate among the models. We can only note that, since there are no large variations in the planet's radius at shorter wavelengths within the experimental uncertainties, the atmospheres of the two planets should be quite transparent and not affected by large Rayleigh scattering. They are well suited to further investigation at the optical wavelengths with more precise instruments.

4.2. Eclipsing binary

The eclipsing binary candidate NSVS 3071474 is located at sky position RA(J2000) = 19 24 03.821 and Dec(J2000) = 55 27 33.33. It is sufficiently close to WASP-48 that it is present

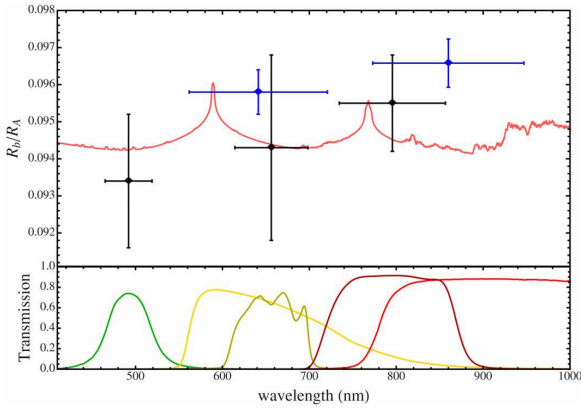

Fig. 9. Variation of the planetary radius of WASP-48 b, in terms of planet/star radius ratio, with wavelength. The black points are from the transit observed with BUSCA, while the blue points are the weighted-mean results coming from the two transits observed in Cousins R and the two in I with the CA 1.23 m telescope. The vertical bars represent the errors in the measurements and the horizontal bars show the FWHM transmission of the passbands used. The observational points are compared with a synthetic spectrum for a Jupiter planet with a surface gravity of $g_b = 10\,\mathrm{m\,s^{-2}}$ and $T_{eq} = 2000\,\mathrm{K}$, which does not include TiO and VO opacity. An offset is applied to all three models to provide the best fit to our radius measurements. Transmission curves of the filters used are shown in the *bottom panel*.

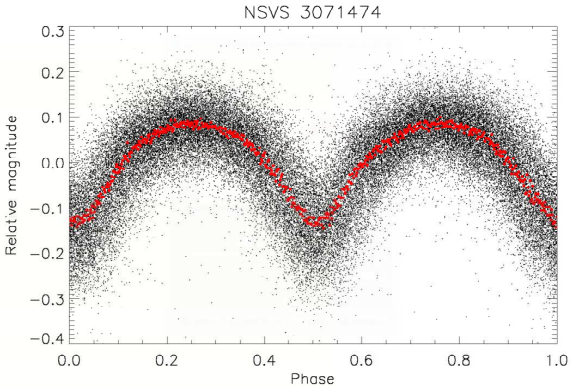

Fig. 10. Light curves of NSVS 3071474 (1SWASP J192403.81+552734.5) phased (black dots) and binned (red dots) observed by the WASP survey between 2008 and 2010.

in the FOV of some of the transits that we monitored. We have extracted light curves of this object and confirm the nature of the system to be that of a contact eclipsing binary.

We also obtained the light curve observed by the SuperWASP survey (Pollacco et al. 2006), where it is called 1SWASP J192403.81+552734.5. The phased and binned WASP data, and the light curves obtained from our frames are shown in Figs. 10 and 11, respectively.

By fitting both the WASP data, and our light curves with we obtained a measurement of the period of the eclipsing binary of 0.458998509 ± 0.000000011 days.

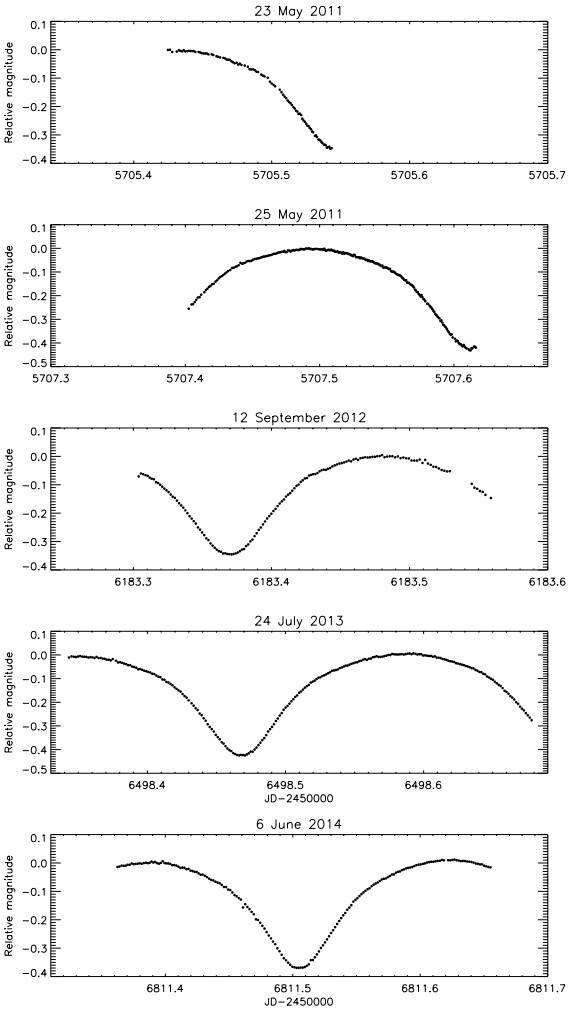

Fig. 11. Light curves of NSVS 3071474, the eclipsing binary close to WASP-48. The curves in the *top two panels* were observed with the 1.52 m *Cassini* telescope while the *bottom two* were observed with the 1.23 m Calar Alto telescope.

5. Discussion and conclusions

In this paper we presented refined parameters for the two TEP systems HAT-P-23 and WASP-48 obtained from new photometric data of transit events. We also presented simultaneous observations in different optical bands. Our principal results are as follows.

- We confirmed the mass value of HAT-P-23 b, but obtained a radius for it that is smaller by roughly 1.5σ. This TEP now occupies a more populated region of the mass-radius diagram and is no longer found to be one of the highly inflated transiting planets (see Fig. 12). The mean density is therefore higher than what was found in the discovery paper.
- We obtained improved estimates of the mass and radius of both the star and the planet of the WASP-48 planetary system. The values for the stellar and planetary radius are smaller than those found in the discovery paper by

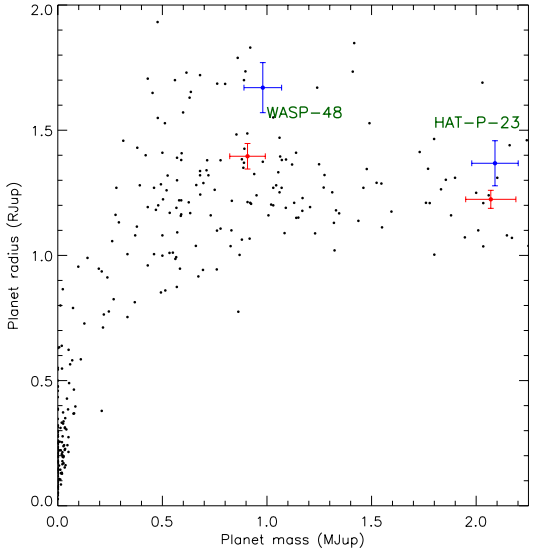

Fig. 12. Mass versus radius diagram of the transiting planets. The blue and red dots represent the values for HAT-P-23 and WASP-48 found in literature and obtained in this work, respectively.

roughly 2.2σ and 2.4σ, respectively. The masses are consistent with previous results.

- A study of the planet's radius variation as a function of optical wavelength, based on the data presented in this work, do not indicate any large variation for either planet, suggesting that their atmospheres are not affected by a large Rayleigh scattering. Further investigations of the transmission spectra of these two planets are needed to validate this statement.
- Finally, we also presented new light curves for the eclipsing binary NSVS 3071474, refining the measurement of the orbital period to be 0.458998509 (11) days.

Acknowledgements. Based on observations obtained with the 1.52 m *Cassini* telescope at the OAB Observatory in Loiano (Italy), and with the 1.23 m and 2.2 m telescopes at the Centro Astronómico Hispano Alemán (CAHA) at Calar Alto (Spain), jointly operated by the Max-Planck Institut für Astronomie and the Instituto de Astrofísica de Andalucía (CSIC). The reduced light curves presented in this work will be made available at the CDS (http://cdsweb.u-strasbg.fr/). Special thanks go to D. Pollacco and A. Cameron for allowing us to use both the public and the unpublished WASP data of the eclipsing binary NSVS 3071474. S.C. thanks M. Line, J. Fortney and his group for useful discussions and for the kind hospitality at UCSC. We acknowledge the use of the following internet-based resources: the ESO Digitized Sky Survey; the TEPCat catalog; the SIMBAD data base operated at CDS, Strasbourg, France; and the arXiv scientific paper preprint service operated by Cornell University.

References

Anderson, D. R., Smith, A. M. S., Lanotte, A. A., et al. 2010, MNRAS, 416, 2108
Bakos, G., Hartman, J., Torres, G., et al. 2011, ApJ, 742, 116
Baraffe, I., Chabrier, G., Fortney, J., & Sotin, C. 2014, Protostar and Planet VI Conf. Proc., 763
Brown, T. M. 2001, ApJ, 553, 1006
Ciceri, S., Mancini, L., Southworth, J., et al. 2013, A&A, 557, A30
Claret, A. 2000, A&A, 363, 1081
Claret, A. 2004a, A&A, 428, 1001
Claret, A. 2004b, A&A, 424, 919
Chen, G., van Boekel, R., Wang, H., et al. 2014, A&A, 563, A40
Copperwheat, C. M., Wheatley, P. J., Southworth, J., et al. 2013, MNRAS, 434, 661
Demarque, P., Woo, J.-H., Kim, Y.-C., & Yi, S. K. 2004, ApJS, 155, 667
Dotter, A., Chaboyer, B., Jevremović, D., et al. 2008, ApJS, 178, 89
Enoch, B., Anderson, D. R., Barros, S. C. C., et al. 2011, ApJ, 142, 86
Fortney, J. J., Shabram, M., Showman, A. P., et al. 2010, ApJ, 709, 1396
Gillon, M., Pont, F., Moutou, C., et al. 2006, A&A, 459, 249
Ginzburg, S., & Sari, R. 2015, ApJ, 803, 111
Mancini, L., Southworth, J., Ciceri, S., et al. 2013a, A&A, 551, A11
Mancini, L., Nikolov, N., Southworth, J., et al. 2013b, MNRAS, 430, 2932
Mancini, L., Ciceri, S., Chen, G., et al. 2013c, MNRAS, 436, 2
Mancini, L., Southworth, J., Ciceri, S., et al. 2014a, A&A, 562, A126
Mancini, L., Southworth, J., Ciceri, S., et al. 2014b, MNRAS, 443, 2391
Mancini, L., Southworth, J., Ciceri, S., et al. 2014c, A&A, 568, A127
Moutou, C., Díaz, R. F., Udry, S., & Hébrard, G. 2011, A&A, 533, A113
Narita, N., Fukui, A., Ikoma, M., et al. 2013, ApJ, 773, 144
Nikolov, N., Chen, G., Fortney, J. J., et al. 2013, A&A, 533, A26
O'Rourke, J. G., Knutson, H. A., Zhao, M., et al. 2014, ApJ, 781, 109
Pietrinferni, A., Cassisi, S., Salaris, M., & Castelli, F. 2004, ApJ, 612, 168
Pollacco, D. L., Skillen, I., Collier Cameron, A., et al. 2006, PASP, 118, 1407
Pont, F. 2009, MNRAS, 396, 1789
Pont, F., Zucker, S., & Queloz, D. 2006, MNRAS, 373, 231
Ramón-Fox, F. G., & Sada, P. V. 2013, Rev. Mex. Astron. Astrofís., 49, 71
Reif, K., Bagschik, K., de Boer, K. S., et al. 1999, Proc. SPIE, 3649, 109
Seager, S., & Mallén-Ornelas, G. 2003, ApJ, 585, 1038
Seager, S., & Sasselov, D. D. 2000, ApJ, 537, 916
Seeliger, M., Dimitrov, D., Kjurkchieva, D., et al. 2014, MNRAS, 441, 304
Southworth, J. 2008, MNRAS, 386, 1644
Southworth, J. 2009, MNRAS, 394, 272
Southworth, J. 2010, MNRAS, 408, 1689
Southworth, J. 2011, MNRAS, 417, 2166
Southworth, J., Wheatley, P. J., & Sams, G. 2007, MNRAS, 379, L11
Southworth, J., Hinse, T. C., Jørgensen, U. G., et al. 2009, MNRAS, 396, 1023
Southworth, J., Dominik, M., Jørgensen, U. G., et al. 2011, A&A, 527, A8
Southworth, J., Bruni, I., Mancini, L., & Gregorio, J. 2012a, MNRAS, 420, 2580
Southworth, J., Mancini, L., Maxted, P. F. L., et al. 2012b, MNRAS, 422, 3099
Southworth, J., Hinse, T. C., Burgdorfet, M., et al. 2014, MNRAS, 444, 776
Sozzetti, A., Torres, G., Charbonneau, D., et al. 2007, ApJ, 664, 1190
Sozzetti, A., Bonomo, A. S., Biazzo, K., et al. 2015, A&A, 575, L15
Spiegel, D. S., & Burrows, A. 2013, ApJ, 772, 76
Stetson, P. B. 1987, PASP, 99, 191
Torres, G., Winn, J. N., & Holman, M. W. 2008, ApJ, 677, 1324
Torres, G., Fischer, D. A., Sozzetti, A., et al. 2012, ApJ, 757, 161
VandenBerg, D. A., Bergbusch, P. A., & Dowler, P. D. 2006, ApJS, 162, 375
Winn, J. N., Holman, M. J., Bakos, G. Á., et al. 2007, AJ, 134, 1707

Chapter 7

Multiband observations of WASP-45& WASP-46

In this chapter we present the characterization of the two planetary systems WASP-45 and WASP-46, submitted to MNRAS

Sicelides Musae, paulo maiora canamus.
non omnis arbusta iuvant humilesque myricae;
si canimus silvas, silvae sint consule dignae.
Ultima Cumaei venit iam carminis aetas;
magnus ab integro saeclorum nascitur ordo.

Eclogae quartae, Vergilius

Physical properties of the planetary systems WASP-45 and WASP-46 from simultaneous multi-band photometry ⋆

S. Ciceri[1]†, L. Mancini [1,2], J. Southworth[3], M. Lendl[4,5], J. Tregloan-Reed[6,3], R. Brahm[7,8], G. Chen[9,10], G. D'Ago[11,12,22], M. Dominik[13], R. Figuera Jaimes[13,14], P. Galianni[13], K. Harpsøe[15], T. C. Hinse[16], U. G. Jørgensen[15], D. Juncher[15], H. Korhonen[15,17], C. Liebig[13], M. Rabus[1,7], A. S. Bonomo[2], K. Bott[18,19], Th. Henning[1], A. Jordán[7,8], A. Sozzetti[2], K. A. Alsubai[20], J. M. Andersen[15,21], D. Bajek[13], V. Bozza[12,22], D. M. Bramich[20], P. Browne[13], S. Calchi Novati[23,11,12⋆‡], Y. Damerdji[4], C. Diehl[24,25], A. Elyiv[4,26,27], E. Giannini[24], S-H. Gu[28,29], M. Hundertmark[15], N. Kains[30], M. Penny[31,15], A. Popovas[15], S. Rahvar[32], G. Scarpetta[11,12,22], R. W. Schmidt[24], J. Skottfelt[33,15], C. Snodgrass[34,35], J. Surdej[4], C. Vilela[3], X-B. Wang[28,29] and O. Wertz[4]

[1] *Max Planck Institute for Astronomy, Königstuhl 17, 69117 – Heidelberg, Germany*
[2] *INAF – Osservatorio Astrofisico di Torino, via Osservatorio 20, 10025 – Pino Torinese, Italy*
[3] *Astrophysics Group, Keele University, Staffordshire, ST5 5BG, UK*
[4] *Institut d'Astrophysique et de Géophysique, Université de Liège, Allée du 6 Août 17, Bât. B5C, Liège 1, 4000 Belgium*
[5] *Observatoire de Genève, Université de Genève, Chemin des maillettes 51, 1290 Sauverny, Switzerland*
[6] *NASA Ames Research Center, Moffett Field, CA 94035, USA*
[7] *Instituto de Astrofísica, Pontificia Universidad Católica de Chile, Av. Vicuña Mackenna 4860, 7820436 – Macul, Santiago, Chile*
[8] *Millennium Institute of Astrophysics, Av. Vicuña Mackenna 4860, 7820436 – Macul, Santiago, Chile*
[9] *Key Laboratory of Planetary Sciences, Purple Mountain Observatory, Chinese Academy of Sciences, Nanjing 210008, China*
[10] *Instituto de Astrofísica de Canarias, E-38205 La Laguna, Tenerife, Spain*
[11] *International Institute for Advanced Scientific Studies (IIASS), Via G. Pellegrino 19, 84019 – Vietri Sul Mare (SA), Italy*
[12] *Department of Physics "E. R. Caianiello", University of Salerno, Via Giovanni Paolo II 132, Fisciano (SA) – 84084*
[13] *SUPA, University of St Andrews, School of Physics & Astronomy, North Haugh, St Andrews, Fife KY16 9SS, UK*
[14] *European Southern Observatory, Karl-Schwarzschild Straße 2, 85748 – Garching bei München, Germany*
[15] *Niels Bohr Institute & Centre for Star and Planet Formation, University of Copenhagen, Øster Voldgade 5, 1350 – Copenhagen K, Denmark*
[16] *Korea Astronomy and Space Science Institute, 305-348 Daejeon, Republic of Korea*
[17] *Finnish Centre for Astronomy with ESO (FINCA), University of Turku, Väisäläntie 20, FI-21500 Piikkiö, Finland*
[18] *School of Physics, UNSW Australia, NSW 2052, Australia*
[19] *Australian Centre for Astrobiology, UNSW Australia, NSW 2052, Australia*
[20] *Qatar Environment and Energy Research Institute, Qatar Foundation, Tornado Tower, Floor 19, PO Box 5825, Doha, Qatar*
[21] *Department of Astronomy, Boston University, 725 Commonwealth Avenue, Boston, MA 02215, USA*
[22] *Istituto Nazionale di Fisica Nucleare, Sezione di Napoli, I-80126 Napoli, Italy*
[23] *NASA Exoplanet Science Institute, MS 100-22, California Institute of Technology, Pasadena CA 91125*
[24] *Astronomisches Rechen-Institut, Zentrum für Astronomie, Universität Heidelberg, Mnchhofstraße 12-14, D-69120 Heidelberg, Germany*
[25] *Hamburger Sternwarte, Universität Hamburg, Gojenbergsweg 112, D-21029 Hamburg, Germany*
[26] *Dipartimento di Fisica e Astronomia, Universit di Bologna, Viale Berti Pichat 6/2, I-40127 Bologna, Italy*
[27] *Main Astronomical Observatory, Academy of Sciences of Ukraine, vul. Akademika Zabolotnoho 27, UA-03680 Kyiv, Ukraine*
[28] *Yunnan Observatories, Chinese Academy of Sciences, Kunming 650011, China*
[29] *Key Laboratory for the Structure and Evolution of Celestial Objects, Chinese Academy of Sciences, Kunming 650011,China*
[30] *Space Telescope Science Institute, 3700 San Martin Drive, Baltimore, MD 21218, USA*
[31] *Department of Astronomy, Ohio State University, McPherson Laboratory, 140 West 18th Avenue, Columbus, OH 43210-1173, USA*
[32] *Department of Physics, Sharif University of Technology, PO Box 11155-9161 Tehran, Iran*
[33] *Centre for Electronic Imaging, Dept. of Physical Sciences, The Open University, Milton Keynes MK7 6AA, UK*
[34] *Planetary and Space Sciences, Department of Physical Sciences, The Open University, Milton Keynes, MK7 6AA, UK*
[35] *Max Planck Institute for Solar System Research, Justus-von-Liebig-Weg 3, D-37077 Göttingen, Germany*

2015 July 12

Mon. Not. R. Astron. Soc. **000**, 2–13 (2015) Printed 2 October 2015 (MN LATEX style file v2.2)

ABSTRACT

Accurate measurements of the physical characteristics of a large number of exoplanets are useful to strongly constrain theoretical models of planet formation and evolution, which lead to the large variety of exoplanets and planetary-system configurations that have been observed. We present a study of the planetary systems WASP-45 and WASP-46, both composed of a main-sequence star and a close-in hot Jupiter, based on 29 new high-quality light curves of transits events. In particular, one transit of WASP-45 b and four of WASP-46 b were simultaneously observed in four optical filters, while one transit of WASP-46 b was observed with the NTT obtaining a precision of 0.30 mmag with a cadence of roughly three minutes. We also obtained five new spectra of WASP-45 with the FEROS spectrograph. We improved by a factor of four the measurement of the radius of the planet WASP-45 b, and found that WASP-46 b is slightly less massive and smaller than previously reported. Both planets now have a more accurate measurement of the density ($0.959 \pm 0.077\,\rho_{\rm Jup}$ instead of $0.64 \pm 0.30\,\rho_{\rm Jup}$ for WASP-45 b, and $1.103 \pm 0.052\,\rho_{\rm Jup}$ instead of $0.94 \pm 0.11\,\rho_{\rm Jup}$ for WASP-46 b). We tentatively detected radius variations with wavelength for both planets, in particular in the case of WASP-45 b we found a slightly larger absorption in the redder bands than in the bluer ones. No hints for the presence of an additional planetary companion in the two systems were found either from the photometric or radial velocity measurements.

Key words: stars: fundamental parameters – stars: individual: WASP-45 – stars: individual: WASP-46 – planetary systems

1 INTRODUCTION

The possibility to obtain detailed information on extrasolar planets, using different techniques and methods, has revealed some unexpected properties that are still challenging astrophysicists. One of the very first was the discovery of Jupiter-like planets on very tight orbits, which are labelled hot Jupiters, and the corresponding inflation-mechanism problem (Baraffe et al. 2014, and references therein). To find the answers to this and other open questions, it is important to have a proper statistical sample of exoplanets, whose physical and orbital parameters are accurately measured.

One class of extrasolar planets, those which transit their host stars, has lately seen a large increase in the number of its known members. This achievement has been possible thanks to systematic transit-survey large programs, performed both from ground (HATNet: Bakos et al. 2004; TrES: Alonso et al. 2004; XO: McCullough et al. 2005; WASP: Pollacco et al. 2006; KELT: Pepper et al. 2007; MEarth: Charbonneau et al. 2009; QES: Alsubai et al. 2013; HATSouth: Bakos et al. 2013), and from space (CoRoT: Barge et al. 2008, *Kepler*: Borucki et al. 2011).

The great interest in transiting planets lies in the fact that it is possible to measure all their main orbital and physical parameters with standard astronomical techniques and instruments. From photometry we can estimate the period, the relative size of the planet and the orbital inclination, whilst precise spectroscopic measurements provide a lower limit for the mass of the planet (but knowing the inclination from photometry the precise mass can be calculated) and the eccentricity of its orbit. Unveiling the bulk density of the planets allows the imposition of constraints on, or differentiation between, the diverse formation and migration theories which have been advanced (see Kley & Nelson 2012; Baruteau et al. 2014 and references therein).

Furthermore, transiting planets allow astronomers to investigate their atmospheric composition, when observed in transit or occultation phases (e.g. Charbonneau et al. 2002; Richardson et al. 2003). However, is also important to stress that, besides instrumental limitations, the characterisation of planets' atmosphere is made difficult by the complexity of their nature. Retrieving the atmospheric chemical composition may be hindered by the presence of clouds, resulting in a featureless spectrum (e.g. GJ 1214 b, Kreidberg et al. 2014).

In this work, we focus on two transiting exoplanet systems: WASP-45 and WASP-46. Based on new photometric and spectroscopic data, we review their physical parameters and probe the atmospheres of their planets.

1.1 WASP-45

WASP-45 is a planetary system discovered within the SuperWASP survey by Anderson et al. (2012) (A12 hereafter). The light curve of WASP-45, shows a periodic dimming (every $P = 3.126$ days) due to the presence of a hot Jupiter (radius $1.16^{+0.28}_{-0.14}\,R_{\rm Jup}$ and mass $1.007 \pm 0.053\,M_{\rm Jup}$) that transits the stellar disc. The host (mass of $0.909 \pm 0.060\,M_{\odot}$ and radius of $0.945^{+0.087}_{-0.071}\,R_{\odot}$) is a K2 V star with a higher metallicity than the Sun ([Fe/H] $= +0.36 \pm 0.12$). The study of the Ca II H+K lines in the star's spectra revealed weak emission lines, which indicates a low chromospheric activity.

⋆ Based on data collected by the MiNDSTEp collaboration with the Danish 1.54 m telescope, and on data observed with the NTT (under program number 088.C-0204(A)), 2.2m and Euler-Swiss Telescope all located at the ESO La Silla Observatory.

† E-mail: ciceri@mpia.de
‡ Sagan visiting fellow

1.2 WASP-46

WASP-46 is a G6 V type star (mass $0.956 \pm 0.034\,M_{\odot}$, radius $0.917 \pm 0.028\,R_{\odot}$ and [Fe/H] $= -0.37 \pm 0.13$). A12 discovered a hot Jupiter (mass $2.101 \pm 0.073\,M_{\rm Jup}$ and radius $1.310 \pm 0.051\,R_{\rm Jup}$) that orbits the star every 1.430 days on a circular orbit. As in the case of WASP-45, weak emission visible in the Ca II H+K lines indicates a low stellar activity. Moreover, the WASP light curve shows a photometric modulation, which allowed the measurement of the rotation period of the star, and a gyrochronological age of the system of 1.4 Gyr. By observing the secondary eclipse of the planet, Chen et al. (2014) detected the emission from the day-side atmosphere finding brightness temperatures consistent with a low heat redistribution efficiency.

2 OBSERVATIONS AND DATA REDUCTION

A total of 29 light curves of 14 transit events of WASP-45 b and WASP-46 b, and five spectra of WASP-45 were obtained using four telescopes located at the ESO La Silla observatory, Chile. The details of the photometric observations are reported in Table 1.

The photometric observations were all performed with the telescopes in auto-guided mode and out of focus to minimise the sources of noise and increase the signal to noise ratio (S/N). By spreading the light of each single star on many more pixels of the CCD, it is then possible to utilise longer exposure times without incurring saturation. Atmospheric variations, change in seeing, or tracking imprecision lead to changes in the position and/or size of the point spread function (PSF) on the CCD and, according to the different response of each single pixel, spurious noise can be introduced in the signal. By obtaining a doughnut-shaped PSF that covers a circular region with a diameter from roughly 15 to 30 pixels, the small variations in position are averaged out and have a much lower effect on the photometric precision (Southworth et al. 2009).

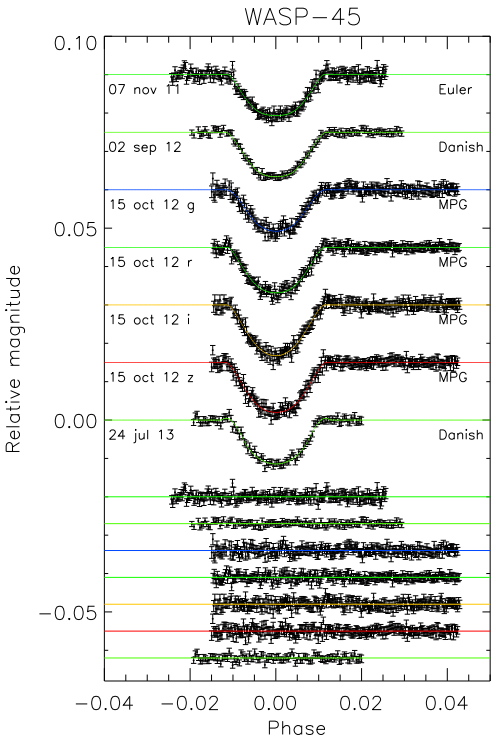

Figure 1. Phased light curves corresponding to four transits of WASP-45 b. The date and the telescope used for each transit event are indicated close to the corresponding light curve. Each light curve is shown with its best fit obtained with JKTEBOP. The residuals relative to each fit are displayed at the base of the figure in the same order as the light curves. The curves are shifted along the y axis for clarity.

1.2 m Euler-Swiss Telescope

The imager of the 1.2m Euler-Swiss telescope, EulerCam, is a 4000×4000 e2v CCD with a field of view (FOV) of $15.7' \times 15.7'$, yielding a resolution of 0.23 arcsec per pixel. Since its installation in 2010, EulerCam has been used intensively for photometric follow-up observations of planet candidates from the WASP survey (e.g. Hellier et al. 2011; Lendl et al. 2014), as well as for the atmospheric study of highly irradiated giant planets (Lendl et al. 2013). We observed one transit of WASP-45 b and two transits of WASP-46 b with EulerCam between June and September 2011 using a Gunn *r'* fiter.

3.58 m NTT

One transit of WASP-46 b was observed with the New Technology Telescope (NTT) on the 23 October 2011. The telescope has a primary mirror of 3.58 m and is equipped with an active optics system. The EFOSC2 instrument (ESO Faint Object Spectrograph and Camera 2), mounted on its Nasmyth B focus, was utilised. The field of view of its Loral/Lesser camera is $4.1' \times 4.1'$ with a resolution of 0.12 arcsec per pixel. During the observation of the whole transit, only a small region of the CCD, including the target and some reference stars, was read out in order to diminish the readout time and increase the sampling. The filter used was a Gunn *g* (ESO #782).

1.54 m Danish Telescope

Two transits of WASP-45 b and three of WASP-46 b were observed with the 1.54 m Danish Telescope, using the DFOSC (Danish Faint Object Spectrograph and Camera) instrument mounted at the Cassegrain focus. The instrument, now used exclusively for imaging, has a CCD with a FOV $13.7' \times 13.7'$ and a resolution of 0.39 arcsec per pixel. The CCD was windowed and a Bessell *R* filter was used for all the transits.

Table 1. Details of the transit observations presented in this work. $N_{\rm obs}$ is the number of observations, $T_{\rm exp}$ is the exposure time, $T_{\rm obs}$ is the observational cadence, and 'Moon illum.' is the fractional illumination of the Moon at the midpoint of the transit. The triplets of numbers in the *Aperture radii* column correspond to the inner radius of the circular aperture (star) and outer radii of the ring (sky) selected for the photometric measurements. [a] The aperture radii of the Euler-Swiss light curves are referred to the target aperture and are expressed in arcsec.

Telescope	Date of first obs	Start time (UT)	End time (UT)	$N_{\rm obs}$	$T_{\rm exp}$ (s)	$T_{\rm obs}$ (s)	Filter	Airmass	Moon illum.	Aperture radii (px)	Scatter (mmag)
WASP-45:											
Eul 1.2m	2011 Nov 07	02:12	05:57	197	50	69	Gunn r	1.00 → 1.51	89%	6.0 [a]	0.91
Dan 1.54m	2012 Sep 02	05:05	08:46	122	100	106	Bessel R	1.15 → 1.51	93%	17,60,75	0.55
MPG 2.2m	2012 Oct 15	23:40	03:58	238	40	65	Sloan g'	1.46 → 1.01	1%	23,70,85	0.85
MPG 2.2m	2012 Oct 15	23:40	03:58	240	40	65	Sloan r'	1.46 → 1.01	1%	23,55,70	0.65
MPG 2.2m	2012 Oct 15	23:40	03:58	238	40	65	Sloan i'	1.46 → 1.01	1%	21,45,65	0.83
MPG 2.2m	2012 Oct 15	23:40	03:58	241	40	65	Sloan z'	1.46 → 1.01	1%	17,50,70	0.75
Dan 1.54m	2013 Jul 24	07:47	10:43	100	100	106	Bessel R	1.15 → 1.34	97%	13,55,70	0.62
WASP-46:											
Eul 1.2m	2011 Jun 10	03:40	07:11	117	90	108	Gunn r	1.95 → 1.17	63%	5.2 [1]	1.26
Eul 1.2m	2011 Sep 01	02:47	06:37	72	170	180	Gunn r	1.12 → 1.36	14%	4.3 [1]	0.88
NTT 3.58m	2011 Oct 24	00:42	05:24	85	150	176	Gunn g	1.14 → 2.21	10%	52,80,100	0.30
MPG 2.2m	2012 Jul 03	04:19	10:29	116	115	145	Sloan g'	1.12 → 1.39	100%	20,65,80	0.56
MPG 2.2m	2012 Jul 03	04:19	10:29	121	115	145	Sloan r'	1.12 → 1.39	100%	22,65,80	0.64
MPG 2.2m	2012 Jul 03	04:19	10:29	120	115	145	Sloan i'	1.12 → 1.39	100%	22,65,80	0.56
MPG 2.2m	2012 Jul 03	04:19	10:29	119	115	145	Sloan z'	1.12 → 1.39	100%	23,65,80	0.62
Dan 1.54m	2012 Sep 24	04:24	08:03	97	120	131	Bessel R	1.14 → 1.95	66%	11,65,80	1.52
MPG 2.2m	2012 Oct 17	01:03	05:55	106	90	116	Sloan g'	1.13 → 2.27	4%	25,90,105	0.80
MPG 2.2m	2012 Oct 17	01:03	05:55	107	90	116	Sloan r'	1.13 → 2.27	4%	25,90,105	0.75
MPG 2.2m	2012 Oct 17	01:03	05:55	109	90	116	Sloan i'	1.13 → 2.27	4%	23,90,100	0.81
MPG 2.2m	2012 Oct 17	01:03	05:55	108	90	116	Sloan z'	1.13 → 2.27	4%	23,90,105	0.85
MPG 2.2m	2013 Apr 25	06:07	10:30	59	120 to 170	215	Sloan g'	2.18 → 1.15	100%	24,65,80	0.70
MPG 2.2m	2013 Apr 25	06:07	10:30	59	120 to 170	215	Sloan r'	2.18 → 1.15	100%	24,65,80	0.63
MPG 2.2m	2013 Apr 25	06:07	10:30	57	120 to 170	215	Sloan i'	2.18 → 1.15	100%	25,65,80	0.90
MPG 2.2m	2013 Apr 25	06:07	10:30	57	120 to 170	215	Sloan z'	2.18 → 1.15	100%	24,65,80	0.81
MPG 2.2m	2013 Jun 17	05:36	09:01	83	130 to 70	137	Sloan g'	1.28 → 1.12	55%	26,70,85	0.61
MPG 2.2m	2013 Jun 17	05:36	09:01	82	130 to 70	137	Sloan r'	1.28 → 1.12	55%	26,70,85	0.64
MPG 2.2m	2013 Jun 17	05:36	09:01	84	130 to 70	137	Sloan i'	1.28 → 1.12	55%	28,65,80	0.70
MPG 2.2m	2013 Jun 17	05:36	09:01	81	130 to 70	137	Sloan z'	1.28 → 1.12	55%	28,70,85	0.85
Dan 1.54m	2013 Aug 06	07:19	10:28	99	100	115	Bessel R	1.12 → 1.53	1%	11,65,80	0.68
Dan 1.54m	2013 Aug 28	04:06	08:39	132	100	125	Bessel R	1.15 → 1.43	42%	12,65,80	0.88

2.2 m MPG Telescope - GROND

The 2.2 m MPG Telescope holds in its Coudé-like focus the GROND (Gamma Ray Optical Near-infrared Detector) instrument (Greiner et al. 2008). GROND is a seven channel imager capable of performing simultaneous observations in four optical bands (g', r', i', z', similar to Sloan filters) and three near-infrared (NIR) bands (J, H, K). The light, split into different paths using dichroics, reaches two different sets of cameras. The optical cameras have 2048×2048 pixels with a resolution of 0.16 arcsec per pixel. The NIR cameras have a lower resolution 0.60 arcsec per pixel, but a larger FOV of $10' \times 10'$ (almost double the optical ones). The primary goal of GROND is the detection and follow-up of the optical/NIR counterpart of gamma ray bursts, but it has already proven to be a great instrument to perform multicolour, simultaneous, photometric observations of planetary-transit events (e.g. Mancini et al. 2013b; Southworth et al. 2015). With this instrument, we observed one transit event of the planet WASP-45 b and four of WASP-46 b.

The exposure time must be the same for each optical camera, and is also partially constrained by the NIR exposure time chosen. We therefore decided to fix the exposure time to that optimising the r'-band counts (generally higher than in the other bands) in order to avoid saturation.

2.2 m MPG Telescope - FEROS

The 2.2 m MPG telescope also hosts FEROS (Fibre-fed Extended Range Optical Spectrograph). This échelle spectrograph covers a wide wavelength range of 370 nm to 860 nm and has an average resolution of $R = 48\,000 \pm 4\,000$. The precision of the radial velocity (RV) measurements obtained with FEROS is good enough ($\geqslant 10\,{\rm m\,s^{-1}}$) for detecting and confirming Jupiter-size exoplanets (e.g. Penev et al. 2013; Jones et al. 2015). Simultaneously to the science observations, we always obtained a spectrum of a ThAr lamp in order to have a proper wavelength calibration. Five spectra of WASP-45 were obtained with FEROS.

2.1 Data reduction

For all photometric data, a suitable number of calibration frames, bias and (sky) flat-field images, were taken on the same day as the observations. Master bias and flat-field images were created by median-combining all the individual bias and flat-field images, and used to calibrate the scientific images.

With the exception of the EulerCam data, we then extracted the photometry from the calibrated images using a version of the aperture-photometry algorithm DAOPHOT (Stetson 1987) implemented in the DEFOT pipeline (Southworth et al. 2014). We measured the flux of the targets and

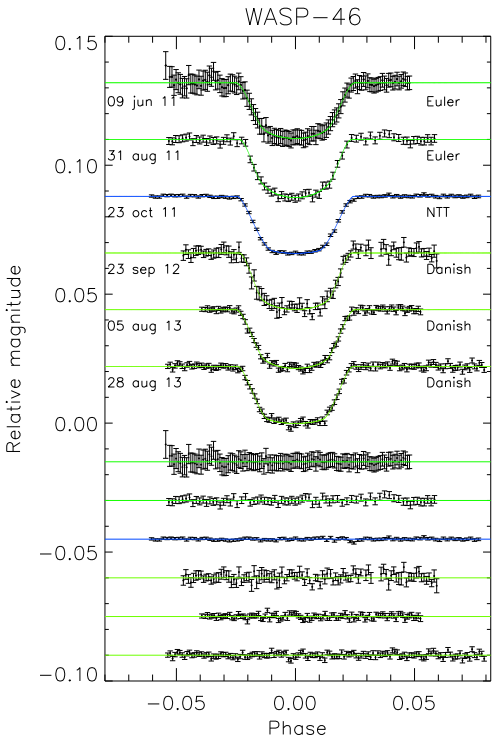

Figure 2. Phased light curves of the transits of WASP-46 b, observed with the Euler, NTT, and Danish telescopes, compared with the best-fitting curves given by JKTEBOP. The date and the telescope used for each transit event are indicated close to the corresponding light curve. The residuals relative to each fit are displayed at the base of the figure in the same order as the light curves.The curves are shifted along the y axis for clarity.

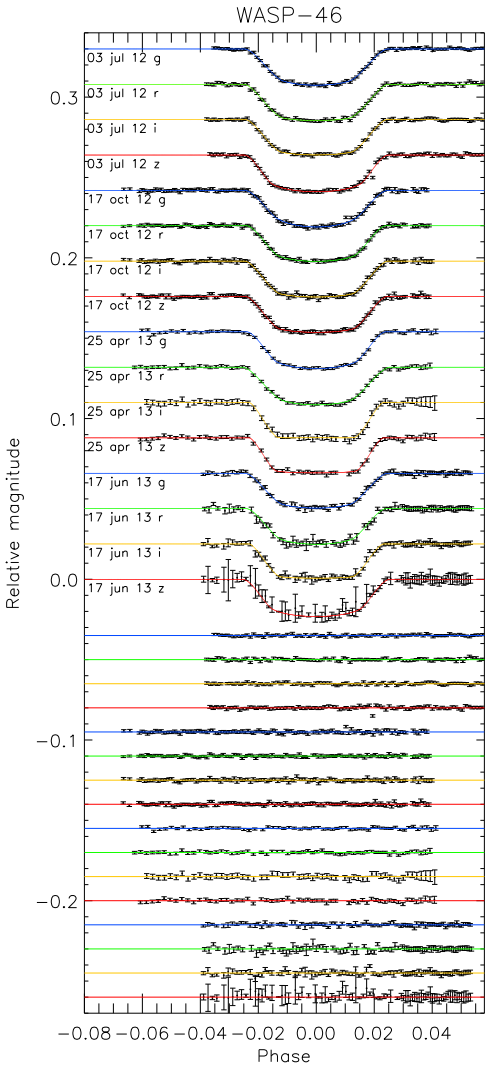

Figure 3. Phased light curves of four transits of WASP-46 observed with GROND. Each transit was observed simultaneously in four optical bands. As in Figs. 1 and 2 the light curves are compared with the best-fitting curves given by JKTEBOP, and the residuals from the fits are displayed at the bottom in the same order as the light curves.The curves are shifted along the y axis for clarity.

of several reference stars in the FOVs, selecting those of similar brightness to the target and not showing any significant brightness variation due to intrinsic variability or instrumental effects. For each dataset, we tried different aperture sizes for both the inner and outer rings, and the final ones that we selected (see Table 1) were those that gave the lowest scatter in the out-of-transit (OOT) region. Light curves were then obtained by performing differential photometry using the reference stars in order to correct for non-intrinsic variations of the flux of the target, which are caused by atmospheric or air-mass changes. Also in this case we tried different combinations of multiple comparison stars and chose those that gave the lowest scatter in the OOT region. We noticed that the different options gave consistent transit shapes but had a small effect on the scatter of the points in the light curves. Finally, each light curve was obtained by optimising the weights of the chosen comparison stars.

The EulerCam photomety was also extracted using relative aperture photometry with the extraction being performed for a number of target and sky apertures, of which the best was selected based on the final lightcurve RMS. The selection of the reference stars was done iteratively, optimizing the scatter of the full transit lightcurves based on preliminary fits of transit shapes to the data at each optimization step. For further details, please see Lendl et al. (2012).

To properly compare the different light curves and avoid underestimation of the uncertainties assigned to each photometric point, we inflated the errors by multiplying them by the $\sqrt{\chi^2_\nu}$ (defined as $\chi^2_\nu = \Sigma((x_i - x_{best})^2/\sigma^2)/$ DOF, where DOF is the number of degrees of freedom) obtained

Table 2. FEROS RV measurements of WASP-45.

Date of observation BJD-2400000	RV $\mathrm{km\,s^{-1}}$	$\mathrm{err_{RV}}$ $\mathrm{km\,s^{-1}}$
56939.69704138	4.368	0.010
56941.64378526	4.557	0.011
56942.69196252	4.382	0.010
57037.53926492	4.650	0.010
57049.54110894	4.502	0.010

from the first fit of each light curve. We then took into account the possible presence of correlated noise or systematic effects using the β approach (e.g. Gillon et al. 2006; Winn et al. 2007), with which we further enlarged the uncertainties.

The NIR light curves observed with GROND were reduced following Chen et al. (2014b), by carefully subtracting the dark from each image and flat-fielding them, and correcting for the read-out pattern. No sky subtraction was performed since no such calibration files were available. Unfortunately, the quality of the data was not good enough to proceed with a detailed analysis of the transits.

FEROS spectra reduction

The spectra obtained with FEROS were extracted using a new pipeline written for échelle spectrographs, adapted for this instrument and optimised for the subsequent RV measurements (Jordán et al. 2014; Brahm et al. 2015). In brief, first a master-bias and a master-flat were constructed as the median of the frames obtained during the afternoon routine calibrations. The master-bias was subtracted from the science frames in order to account for the CCD intrinsic inhomogeneities, while the master-flat was used to find and trace all 39 échelle orders. The spectra of the target and the calibration ThAr lamp were extracted following Marsh (1989). The science spectrum was then calibrated in wavelength using the ThAr spectrum, and a barycentric correction was applied. In order to measure the RV of the star, the spectrum was cross-correlated with a binary mask chosen according to the spectral class of the target. For each échelle order a cross correlation function (CCF) was found and the RV measured by fitting a combined one, which is obtained as a weighted sum of all the CCF, with a Gaussian. The uncertainties on the RVs were calculated using empirical scaling relations from the width of the CCF and the mean S/N measured around 570 nm. The RV measurements are reported in Table 2.

3 LIGHT CURVE ANALYSIS

The light curve shape of a transit (its depth and duration) directly depends on values that describe the planet and its host star (e.g. Seager & Mallén-Ornelas 2003). In particular, by fitting the transit shape it is possible to obtain the measurement of the stellar and planetary relative radii, $r_* = \frac{R_*}{a}$ and $r_b = \frac{R_b}{a}$ (where a is the semi-major axis of the orbit), the inclination of the planetary orbit with respect to the line of sight of the observer, i, and the time of the transit centre, T_0.

Table 3. Stellar atmospheric parameters used to calculate the LD coefficients used to model the light curves.

Parameter	WASP-45	WASP-46
$T_{\rm eff}(K)$	5100	5600
$\log g$ (cm $\mathrm{s^{-2}}$)	4.5	4.5
$[\frac{\rm Fe}{\rm H}]$	0.5	−0.3
$V_{\rm micro}$ ($\mathrm{km\,s^{-1}}$)	2.0	2.0

Using the JKTEBOP[1] code (version 34, Southworth 2013, and references therein), we separately fitted each light curve initially setting the fitted parameters to the values published in the discovery paper. The values for each parameter were then obtained through a Levenberg-Marquardt minimisation, while uncertainties were estimated by running Monte Carlo and residual-permutation algorithms (Southworth 2008). The coefficients of a second order polynomial were also fitted to account for instrumental and astrophysical trends possibly present in the light curves. In particular, Ndata-1 simulations for both the algorithms were run, and the larger of the two 1-σ values were adopted as the final uncertainties. The JKTEBOP code is capable of simultaneously fitting light curves and RVs, and therefore giving also an estimation of the semi-amplitude K and systemic velocity $\gamma_{\rm sys}$.

To properly constrain the planetary system's quantities we took into account the effect of the star's limb darkening (LD) while the planet is transiting the stellar disc. We applied a quadratic law to describe this effect, and used the LD coefficients provided by the stellar models of Claret (2000, 2004) once the stellar atmospheric parameters were supplied (Table 3). Each light curve was firstly fitted for the linear coefficient, while the quadratic one was perturbed during the Monte Carlo and residual-permutation algorithms in order to account for its uncertainty. Then we repeated the fitting process whilst keeping both the LD coefficients fixed.

Considering the discussion in A12, we fixed the eccentricity to zero for both the planetary systems. As an extra check, we used the Systemic Console 2 (Meschiari et al. 2009) to fit the RVs published in the discovery paper and those we observed with FEROS, obtaining a value consistent with $e = 0$ (from the fit we obtained $e = 0.041 \pm 0.043$ for WASP-45). All the light curves observed along with the best fit are shown in Fig.1 for WASP-45 and Figs. 2 and 3 for WASP-46.

3.1 New orbital ephemeris

From the fit of each light curve, we obtained, among the other properties, accurate values of the mid-transit times. By also taking into account the values found from the discovery paper A12 and those from the Exoplanet Transit Database (ETD)[2] website, we refined the ephemeris values. In particular for WASP-46 we used only those light curves from the ETD catalogue that had a data quality index better than 3 and whose light curve didn't show evident deviation

[1] The JKTEBOP source code can be downloaded at `http://www.astro.keele.ac.uk/jkt/codes/jktebop.html`

[2] The database can be found on `http://var2.astro.cz/ETD`

Table 4. Times of mid-transit point of WASP-45 b and their residuals. References: (1)A12; (2) ETD; (3) Euler, this work; (4) GROND, this work; (5) Danish, this work.

Time of minimum BJD(TDB)−2400000	Epoch	Residual (JD)	Reference
55441.27000 ± 0.00058	0	-0.00128	(1)
55782.01007 ± 0.00235	109	0.00310	(2)
55872.67006 ± 0.00030	138	-0.00011	(3)
56119.62852 ± 0.00081	217	0.00301	(2)
56172.77422 ± 0.00018	234	0.00094	(5)
56216.54008 ± 0.00029	248	0.00042	(4) g
56216.54153 ± 0.00021	248	-0.00103	(4) r
56216.54110 ± 0.00024	248	-0.00060	(4) i
56216.54001 ± 0.00025	248	0.00049	(4) z
56497.88958 ± 0.00026	338	-0.00044	(5)

Table 5. Times of mid-transit point of WASP-46 b and their residuals. References: (1) A12; (2) ETD; (3) Euler, this work; (4) NTT, this work; (5) GROND, this work; (6) Danish, this work.

Time of minimum BJD(TDB)−2400000	Epoch	Residual (JD)	Reference
55392.31628 ± 0.00020	0	-0.00032	(1)
55722.73197 ± 0.00013	231	0.00045	(3)
55757.06235 ± 0.00098	255	0.00201	(2)
55805.69409 ± 0.00020	289	0.00125	(3)
55858.61624 ± 0.00011	326	-0.00020	(4)
56108.92758 ± 0.00091	501	-0.00320	(2)
56111.79133 ± 0.00011	503	-0.00050	(5) g
56111.79141 ± 0.00013	503	-0.00019	(5) r
56111.79132 ± 0.00013	503	-0.00018	(5) i
56111.79102 ± 0.00013	503	-0.00010	(5) z
56130.38924 ± 0.00042	516	0.00295	(2)
56194.74962 ± 0.00027	561	-0.00322	(6)
56217.63904 ± 0.00013	577	0.00005	(5) g
56217.63892 ± 0.00011	577	0.00012	(5) r
56217.63883 ± 0.00010	577	0.00020	(5) i
56217.63877 ± 0.00012	577	0.00032	(5) z
56227.65622 ± 0.00062	584	0.00493	(2)
56407.87778 ± 0.00014	710	-0.00056	(5) g
56407.87730 ± 0.00033	710	-0.00051	(5) r
56407.87711 ± 0.00017	710	-0.00031	(5) i
56407.87705 ± 0.00021	710	0.00017	(5) z
56460.80084 ± 0.00016	747	-0.00038	(5) g
56460.80090 ± 0.00020	747	-0.00031	(5) r
56460.80147 ± 0.00028	747	-0.00030	(5) i
56460.80092 ± 0.00025	747	0.00025	(5) z
56510.86498 ± 0.00013	782	0.00090	(6)
56510.86827 ± 0.00067	782	0.00419	(2)
56520.88045 ± 0.00067	789	0.00379	(2)
56533.74905 ± 0.00013	798	-0.00092	(6)
56882.76628 ± 0.00065	1042	0.00661	(2)
56942.83897 ± 0.00083	1084	0.00386	(2)

from a transit shape that could affect the T_0 measurement.

The new values for the period and the reference time of mid-transit, T_0, were obtained performing a linear fit to all the mid-transit times versus their cycle number (see Tables 4 and 5). We obtained:

$$T_0 = \text{BJD(TDB)}\ 2\,455\,441.2687\,(10) + 3.1260960\,(49)\,E,$$

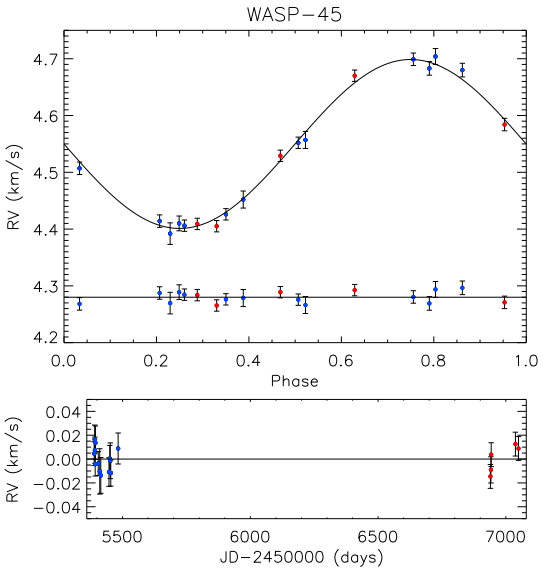

Figure 6. *Upper panel*: RV measurements with the best fit obtained from JKTEBOP; residuals are displayed at the bottom. *Lower panel*: residuals of the best fit displayed as a function of the days when the spectra were observed. In both the panels blue points refer to the data from the discovery paper A12, whilst the red ones are those observed with FEROS.

for WASP-45, and

$$T_0 = \text{BJD(TDB)}\ 2\,455\,392.31659\,(58) + 1.43036763\,(93)\,E.$$

for WASP-46, where the numbers in brackets represent the uncertainties on the last digit of the number they follow, and E is the number of orbits the planet has completed since the T_0 used as reference. The presence of an additional planetary companion in either of the two systems can be detected thanks to the gravitational effects that it would generate on the motion of the known bodies. Indeed, if another planet orbits the same star as WASP-45 b or WASP-46 b, it will affect their orbital motion, by periodically advancing and retarding the transit time (e.g. Holman & Murray 2005; Lissauer et al. 2011). Here, the fit has a $\chi^2_\nu = 9.5$ and 22.7 for WASP-45 and WASP-46, respectively, indicating that the linear ephemeris is a good match to the observations in both the cases. The plots of the residuals, displayed in Figs. 4 and 5, do not show any evidence for systematic deviations from the predicted transit times.

A signature of additional planetary or more massive bodies in one of the two systems can also be found by looking for a periodicity or a linear trend in the residual of the RV data, once the sinusoidal signal due to the known planet is removed (e.g. Butler et al. 1999; Marcy et al. 2001). Considering both the data from the discovery paper and the new ones presented in this work, we studied the distribution of the RV residuals in time for WASP-45 (shown in Fig. 6 along with the best fit), but did not find any particular trend.

This is not surprising given the low probability to find a close in companion to a hot Jupiter (e.g. Mustill et al. 2015; Ford 2014; Izidoro et al. 2015).

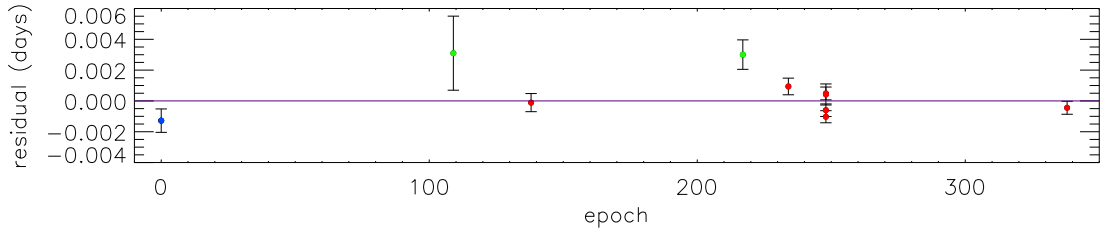

Figure 4. Plot of the residuals of the timing of mid-transit of WASP-45 versus a linear ephemeris. The different colours of the points refer to the value from the discovery paper (blue), values obtained from the ETD catalogue (green), and our data (red).

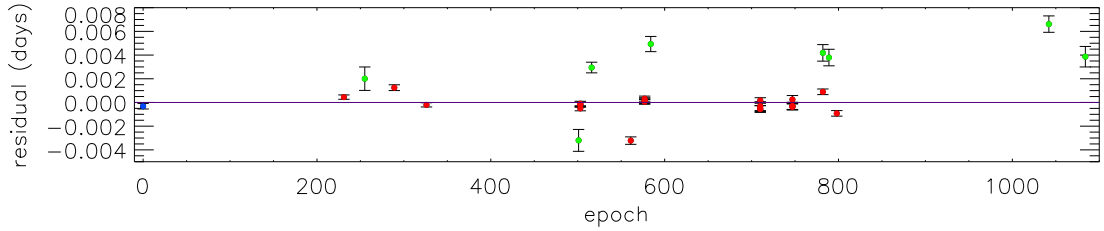

Figure 5. Plot of the residuals of the timing of mid-transit of WASP-46 versus a linear ephemeris. The different colours of the points refer to the value from the discovery paper (blue), values obtained from the ETD catalogue (green), and our data (red).

3.2 Final photometric parameters

For both the planets, each final photometric parameter was obtained as a weighted mean of the values extracted from the fit of all the individual light curves, using the relative errors as a weight. The final uncertainties, also obtained from the weighted mean, were subsequentely rescaled according to the $\sqrt{\chi^2_\nu}$ calculated for each quantity. The results together with their uncertainties and the relative χ^2_ν are shown in Table 6, in which they are compared with those from the discovery paper A12. The photometric parameters obtained from each single light curve are reported in Tables A1 and A2 in the Appendix.

For both planets, we decided to adopt the results obtained from the fit in which we fixed the LD coefficients for all light curves. This choice was dictated by the following reasoning. In near-grazing transits, only the region near the limb of the star is transited, so there is very little information on its LD (Howarth 2011; Müller et al. 2013). As the impact parameters of the systems are high ($b = 0.87$ for WASP-45 and $b = 0.71$ for WASP-46) and thus the transits are nearly-grazing, we decided to not fit for the LD coefficients in order to avoid biasing the results. However, we checked that the results, obtained either fixing or fitting for the LD coefficients, were compatible with each other. We assigned to the parameters of each light curve a 1-σ uncertainty, estimated by Monte Carlo simulations, because these values were systematically higher than those obtained with the residual-permutation algorithm.

4 PHYSICAL PROPERTIES OF WASP-45 AND WASP-46

Using the results obtained from the photometry (Table 6) and taking into account the spectroscopic results from the discovery paper, we redetermined the main physical parameters that characterise the two planetary systems. Following the methodology described in Southworth (2010), the missing information such as the age of the system and the planetary velocity semi-amplitude were iteratively interpolated using stellar evolutionary model predictions until the best fit to the photometric and spectroscopic parameters was reached. This was done for a sequence of ages separated by 0.1 Gyr and covering the full main sequence lifetimes of the stars. We independently repeated the interpolation using different stellar models (Girardi et al. 2000; Claret 2004; Demarque 2004; Pietrinferni et al. 2004; VandenBerg 2006; Dotter 2008); for a complete list see Southworth 2010), and the final values were obtained as a weighted mean. In the final results presented in Tables 7 and 8, the first uncertainty is a statistical one, which is derived by propagating the uncertainties of the input parameters, while the second is a systematic uncertainty, which takes into account the differences in the predictions coming from the different stellar models used. The final values for the ages of the two system are not well constrained. The uncertainty that most affects the precision on these measurements is the large errorbars on $T_{\rm eff}$ (from A12 $T_{\rm eff} = 5140 \pm 200$ and $T_{\rm eff} = 5620 \pm 160$ for WASP-45 and WASP-46 respectively). Moreover, we noticed that for metallicity different to solar, the discrepancies

Table 6. Photometric properties of the WASP-45 and WASP-46 systems derived by fitting the light curves with JKTEBOP, and taking the weighted mean of the single values obtained from each transit. The values from the discovery paper A12 are shown for comparison. k is the ratio of the planetary and stellar radii, i the orbital inclination, r_* and r_b the stellar and planetary relative radii respectively.

Parameter	WASP-45			WASP-46		
	Result	χ^2_ν	A12	Result	χ^2_ν	A12
$r_* + r_b$	0.1172 ± 0.0017	0.84	0.1217 ± 0.0098	0.1950 ± 0.0013	1.28	0.1992 ± 0.0059
k	0.1095 ± 0.0024	5.37	0.1234 ± 0.0246	0.14075 ± 0.00035	1.16	0.1468 ± 0.0017
i (deg.)	84.686 ± 0.098	1.03	$84.47^{+0.54}_{-0.79}$	82.80 ± 0.17	1.31	82.63 ± 0.38
r_*	0.1053 ± 0.0014	0.98	0.1084 ± 0.0094	0.1709 ± 0.0011	1.28	0.1742 ± 0.0057
r_b	0.01172 ± 0.00026	0.81	0.0134 ± 0.0024	0.02403 ± 0.00021	1.30	0.0250 ± 0.0010

Table 7. Final results for the physical parameters of WASP-45 obtained in this work compared to those of the discovery paper. The mass M, radius R, surface gravity g and mean density ρ for the star and the planet are displayed; as well as the equilibrium temperature of the planet, the Safronov number Θ, the semi major axis a and the age of the system. $^{(a)}$This is the gyrochronological age measured in A12. The same authors also obtained a value for the stellar age from lithium abundance measurements, finding that the star is at least a few Gyr old.

	This work	A12
M_* ($M_\odot$)	$0.904 \pm 0.066 \pm 0.010$	0.909 ± 0.060
R_* ($R_\odot$)	$0.917 \pm 0.024 \pm 0.003$	$0.945^{+0.087}_{-0.071}$
$\log g_*$ (cgs)	$4.470 \pm 0.014 \pm 0.002$	$4.445^{+0.065}_{-0.075}$
ρ_* ($\rho_\odot$)	1.174 ± 0.047	$1.08^{+0.27}_{-0.24}$
M_b (M_{jup})	$1.002 \pm 0.062 \pm 0.007$	1.007 ± 0.053
R_b (R_{jup})	$0.992 \pm 0.038 \pm 0.004$	$1.16^{+0.28}_{-0.14}$
g_b (ms^{-2})	25.2 ± 1.3	$17.0^{+4.9}_{-6.0}$
ρ_b (ρ_{jup})	$0.959 \pm 0.077 \pm 0.003$	0.64 ± 0.30
T_{eq} (K)	1170 ± 24	1198 ± 69
Θ	$0.0903 \pm 0.0044 \pm 0.0003$	–
a (AU)	$0.0405 \pm 0.0010 \pm 0.0001$	0.04054 ± 0.00090
Age (Gyr)	$7.2^{+5.8\,+6.8}_{-9.0\,-1.2}$	$1.4^{+2.0}_{-1.0}$ ^{a}

between the different stellar models increase and therefore the systematic errorbar on the age estimation swells.

5 RADIUS VS WAVELENGTH VARIATION

During a transit event, a fraction of the light coming from the host star passes through the atmosphere of the planet and, according to the atmospheric composition and opacity, it can be scattered or absorbed at specific wavelengths (Seager & Sasselov 2000). Similarly to transmission spectroscopy, by observing a planetary transit at different bands simultaneously, it is then possible to look for variations in the value of the planet's radius measured in each band, and thus probe the composition of its atmosphere (e.g. Southworth et al. 2012; Mancini et al. 2013a; Narita et al. 2013).

To pursue this goal, we phased and binned all the light curves observed with the same instrument and filter, and performed once again a fit with JKTEBOP. Following Southworth et al. (2012), we fixed all the parameters to the final values previously obtained (see Tables 7 and 8) and fitted just for the planetary and stellar radii ratio k. In this way, we removed sources of uncertainty common to all datasets, maximising the relative precision of the planet/star radius

Table 8. Final results for the physical parameters of WASP-46 obtained in this work compared to those of the discovery paper. See Table. 7 for the description of the parameters listed. This is the gyrochronological age measured in A12. $^{(a)}$The same authors also obtained a value for the stellar age from lithium abundance measurements, finding that the star is at least a few Gyr old.

	This work	A12
M_* ($M_\odot$)	$0.828 \pm 0.067 \pm 0.036$	0.956 ± 0.034
R_* ($R_\odot$)	$0.858 \pm 0.024 \pm 0.013$	0.917 ± 0.028
$\log g_*$ (cgs)	$4.489 \pm 0.013 \pm 0.006$	4.493 ± 0.023
ρ_* ($\rho_\odot$)	1.310 ± 0.025	1.24 ± 0.10
M_b (M_{jup})	$1.91 \pm 0.11 \pm 0.06$	2.101 ± 0.073
R_b (R_{jup})	$1.174 \pm 0.033 \pm 0.017$	1.310 ± 0.051
g_b (ms^{-2})	34.3 ± 1.1	$28.0^{+2.2}_{-2.0}$
ρ_b (ρ_{jup})	$1.103 \pm 0.050 \pm 0.016$	0.94 ± 0.11
T_{eq} (K)	1636 ± 44	1654 ± 50
Θ	$0.0916 \pm 0.0035 \pm 0.0014$	–
a (AU)	$0.02335 \pm 0.00063 \pm 0.00034$	0.02448 ± 0.00028
Age (Gyr)	$9.6^{+3.4\,+1.4}_{-4.2\,-3.5}$	$1.4^{+0.4}_{-0.6}$ $^{(a)}$

ratio measurements as a function of wavelength. In order to have a set of data as homogeneous as possible, we preferred to use the light curves obtained with the same reduction pipeline and, thus, we excluded the light curves from the Euler telescope from this analysis.

The values of k that we obtained at different passbands are reported in Table 9 and illustrated in Figs. 7 and 8 for WASP-45 and WASP-46, respectively. In these figures, for comparison, we also show the expected values of the planetary radius in function of wavelength, obtained from synthetic spectra constructed from model planetary atmospheres by Fortney et al. (2010), using different molecular compositions. The models were estimated for a Jupiter-mass planet with a surface gravity of $g_p = 25\,\mathrm{m\,s^{-2}}$, a base radius of $1.25\,R_{Jup}$ at 10 bar, and $T_{eq} = 1250$ K and 1750 K for WASP-45 b and WASP-46 b, respectively. The model displayed with a red line in Fig. 8 was run in an isothermal case taking into account chemical equilibrium and the presence of strong absorbers, such as TiO and VO. The models displayed with blue lines in Figs. 7 and 8 were obtained omitting the presence of the metal oxides.

Looking at the distribution of the experimental points in the two figures, we do not see the telltale increase of the radius at the shortest wavelengths (e.g. see Lecavelier Des Etangs et al. 2008), and therefore we do not expect a strong Rayleigh scattering in the atmosphere. However by studying our data-point quantitatively we can not exclude any

Table 9. Values of k for each of the light curves as plotted in Figs. 7 and 8.

Passband	Central wavelength (nm)	FWHM (nm)	k
WASP-45:			
GROND g'	477.0	137.9	0.11090 ± 0.00111
GROND r'	623.1	138.2	0.11335 ± 0.00090
Bessel R	648.9	164.7	0.11088 ± 0.00062
Gunn r	664.1	85.0	0.10821 ± 0.00099
GROND i'	762.5	153.5	0.11598 ± 0.00103
GROND z'	913.4	137.0	0.11513 ± 0.00089
WASP-46:			
GROND g'	477.0	137.9	0.13950 ± 0.00031
Gunn g	516.9	77.6	0.13961 ± 0.00047
GROND r'	623.1	138.2	0.13943 ± 0.00032
Bessel R	648.9	164.7	0.13990 ± 0.00043
Gunn r	664.1	85.0	0.13815 ± 0.00113
GROND i'	762.5	153.5	0.13871 ± 0.00039
GROND z'	913.4	137.0	0.14059 ± 0.00042

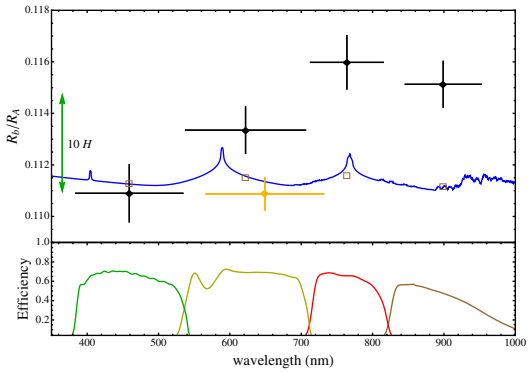

Figure 7. Variation of the radius of WASP-45 b, in terms of planet/star radius ratio, with wavelength. The black points are from the transit observed with GROND, and the yellow point is the weighted-mean results coming from the two transits observed with the Danish telescope. The vertical bars represent the uncertainties in the measurements and the horizontal bars show the FWHM transmission of the passbands used. The observational points are compared to a synthetic spectrum for a Jupiter-mass planet with a surface gravity of $g_{\rm p} = 25\,{\rm m\,s^{-2}}$, and $T_{\rm eq} = 1250\,{\rm K}$. An offset was applied to the model to provide the best fit to our radius measurements. Transmission curves of the filters used are shown in the bottom panel. On the left of the plot the size of ten atmospheric pressure scale heights ($10\,H$) is shown. The small coloured squares represent band-averaged model radii over the bandpasses used in the observations.

hypothesis. From a simple Monte Carlo simulation, we obtained that our data-points would be consistent within 3σ to a slope with a maximum inclination of $m = -1.40 \times 10^{-5}$ for WASP-45 b and $m = -1.17 \times 10^{-5}$ for WASP-46 b (where m is the angular coefficient of the best linear fit). Fitting with a straight line the predictions given at short wavelength by a model with the Rayleigh scattering enhanced by a factor of 1000, we obtained a slope with angular coefficients lower that the ones just mentioned (the angular coefficient for WASP-45 is $m = -2.2 \times 10^{-6}$, and for WASP-46 $m = -3.3 \times 10^{-6}$). Altough pointing in the direction of no strong rayleigh scattering, our data are not sufficient to completely rule out this scenario. More data-points are needed to make any stronger statement regard this this matter.

For the case of WASP-45 b, for which we have only one transit observed with GROND, it is possible to note a radius variation between the g' and i' bands at 2σ, corresponding to roughly $12H$ pressure scale heights. In the case of WASP-46 b, for which we observed four transits with GROND, we noticed a small variation of $\sim 4\,H$ between the i' and z' bands but at only 1.5σ. These detections are too small to be significant – both planets are not well suited to transmission photometry or spectroscopy due to their large impact parameters and high surface gravities.

As stated in A12, the lightcurve of WASP-46 shows a rotational modulation, which is symptomatic of stellar activity. The presence of star spots on the stellar surface, and in general stellar activity, can produce variations in the transit depth when it is measured at different epochs. In particular, we expected that such a variation is stronger at bluer wavelengths and affecting more the lightcurves obtained through the g' band, whereas it is negligible in the i and z bands (e.g., Sing et al. 2011; Mancini et al. 2014). Correcting for this effect, would slightly shift the data point relative to the bluer bands, towards the bottom of Fig. 7. Anyway, since the stellar activity is not particularly high, the expected variation in the transit depth is small and within our errorbars (Fig. 9 shows the effect of the presence of starspots, at different temperatures, on the transit depth with wavelength. The stellar model used to produce the curves are the ATLAS9 by Castelli & Kurucz 2004).

6 SUMMARY AND CONCLUSIONS

We have presented new multi-band photometric light curves of transit events of the hot-Jupiter planets WASP-45 b and WASP-46 b, and new RV measurements of WASP-45. We used these new datasets to refine the orbital and physical parameters that characterise the architecture of the WASP-45 and WASP-46 planetary systems. Moreover, we used the light curves observed through several optical passbands to probe the atmosphere of the two planets. Our conclusions are as follows:

- The radius of WASP-45 b is now much better constrained, with a precision better by almost one order of magnitude with respect to that of A12. We found that WASP-46 b has a slightly lower radius ($1.189 \pm 0.037\,R_{\rm Jup}$) compared to the previous estimation ($1.310 \pm 0.051\,R_{\rm Jup}$). The left panel of Fig. 10 shows the change in position in the planet mass-radius diagram for both WASP-45 b and WASP-46 b.

- Based on our estimates, both planets have a larger density than previously thought (see the right panel of Fig. 10). In particular, WASP-45 b appears to be one of the densest planets in its mass regime (there are only 3

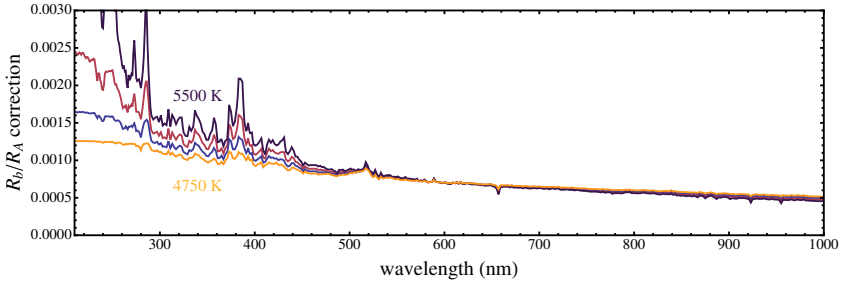

Figure 9. The effect of the presence of unocculted starspot on the surface of the star on the transmission spectrum, considering a 1 per cent flux drop at 600nm. The stellar temperature adopted is $T_{\rm eff}$ = 5600 K, and the spots coverage is modelled using a grid of stellar atmospheric models of different temperature ranging from 4750 (yellow line) to 5500 (purple line), with steps of 250 K.

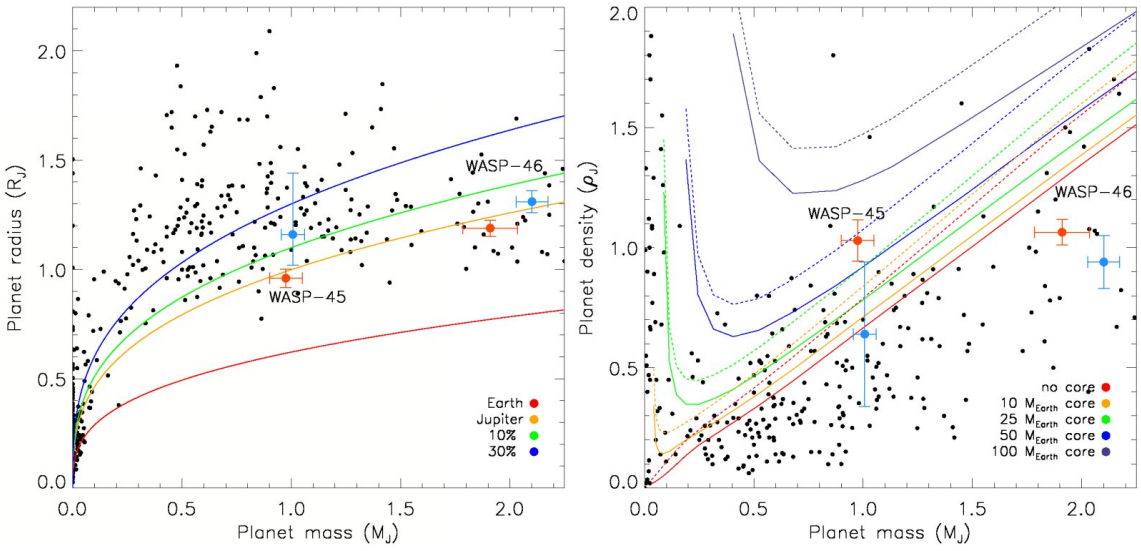

Figure 10. *Left*: the mass versus radius diagram of the known transiting planets. The values for WASP-45 b and WASP-46 b obtained in this work are displayed in orange, and for comparison we also show in light blue the measurements reported in the discovery paper. The coloured curves represent the iso-density lines for planets with the density of Earth and Jupiter, and with a density equal to a Jupiter-like planet with a radius inflated by 10% and 30%. *Right*: the mass versus density diagram of the known transiting planets. As in the left panel, the values obtained for WASP-45 and WASP-46 are highlighted in colour. The superimposed lines represent the expected radius of the planet having an inner core of 0, 10, 25, 50 and 100 Earth masses, and calculated for 10 Gyr old planets at 0.02 au, solid lines, and 0.045 au, dashed lines (Fortney et al. 2007).

other planets with masses between 0.7 and 1.3$M_{\rm Jup}$ that have similar or higher density), suggesting the presence of a heavy-element core of roughly 50 $M_\oplus$ (Fortney et al. 2007).

• By studying the transit times and the RV residuals we did not find any hint for the presence of any additional planetary companion in either of the two planetary systems. However more spectroscopic and photometric data are necessary to claim a lack of other planetary companions, at any mass and separation, in these two systems. In particular a higher temporal cadence for the photometric observations could allow to detect the signature of smaller inner planets, while RV measurements obtained at different epochs separated by several months/years could provide information on the presence of outer long period planets.

• Looking at the radius variation in terms of wavelength, we estimated the upper limit of the slope allowed by our data within 3σ: the angular coefficients of the best linear fit are $m = -1.40 \times 10^{-5}$ and $m = -1.17 \times 10^{-5}$ for WASP-45 b and WASP-46 b respectively. Comparing these values to the slope obtained from a model with 1000 times ehnancement of rayleigh scattering we found that we can not exclude with a high statistical significance the presence of strong Rayleigh scattering in the atmospheres of both planets.

The data of one transit of WASP-45 b, observed simultaneously in four optical bands with GROND, indicate a planetary radius variation of more than 10 H between the g'

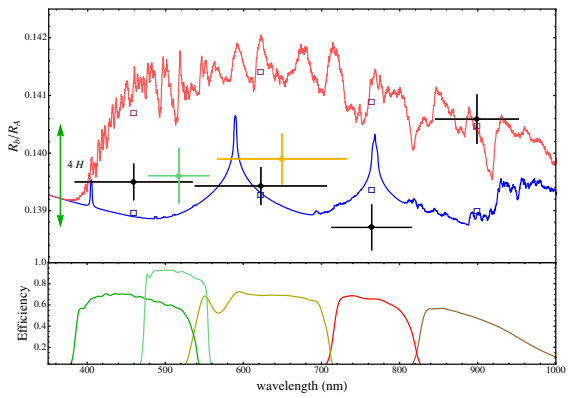

Figure 8. Variation of the radius of WASP-46 b, in terms of planet/star radius ratio, with wavelength. The black points are from the transit observed with GROND, the green point is that obtained with the NTT, and the yellow point is the weighted-mean result coming from the three transits observed with the Danish telescope. The vertical bars represent the uncertainties in the measurements and the horizontal bars show the FWHM transmission of the passbands used. The observational points are compared to two synthetic spectra for a Jupiter-mass planet with a surface gravity of $g_{\rm p} = 25\,{\rm m\,s^{-2}}$, and $T_{\rm eq} = 1750\,{\rm K}$. The synthetic spectrum in blue does not include TiO and VO opacity, while the spectrum in red does, based on equilibrium chemistry. An offset was applied to the models to provide the best fit to our radius measurements. Transmission curves of the filters used are shown in the bottom panel. On the left of the plot the size of four atmospheric pressure scale heights ($4\,H$) is shown. The small coloured squares represent band-averaged model radii over the bandpasses used in the observations.

and the i' bands, but at only a $\sim 2\sigma$ significance level. Such a variation is rather high for that expected for a planet with a temperature below 1200 K, and would require the presence of strong absorbers between 800 and 900 nm. More observations are requested to verify this possible scenario.

In the case of WASP-46 b, by joining the GROND multicolour data of four transit events, we detected a very small radius variation, roughly $4\,H$, between the i' and z' bands, but at only a 1.5σ significance level. This variation can be explained by supposing the absence of potassium at 770 nm and a significant amount of water vapour around 920 nm.

ACKNOWLEDGMENTS

We acknowledge the use of the NASA Astrophysics Data System; the SIMBAD database operated at CDS, Strasbourg, France; and the arXiv scientific paper preprint service operated by Cornell University. This work was supported by KASI (Korea Astronomy and Space Science Institute) grants 2012-1-410-02 and 2013-9-400-00. ASB acknowledges support from the European Union Seventh Framework Programme (FP7/2007-2013) under grant agreement number 313014 (ETAEARTH). TCH acknowledges financial support from the Korea Research Council for Fundamental Science and Technology (KRCF) through the Young Research Scientist Fellowship Program. YD, AE, JSurdej and OW acknowledge support from the Communauté française de Belgique – Actions de recherche concertées – Académie Wallonie-Europe. SHG and XBW would like to thank the financial support from National Natural Science Foundation of China through grants Nos. 10873031 and 11473066. SC thanks G-D. Marleau for useful discussion and comments, the staff and astronomers observing at the ESO La Silla observatory during January and February 2015 for the great, friendly and scientifically stimulating environment.

REFERENCES

Alonso, R., Brown, T. M., Torres, G., et al. 2004, ApJ, 613, 153
Alsubai, K. A., Parley, N. R., Bramich, D. M., et al. 2013, AcA, 63, 465
Anderson, D. R., Collier Cameron, A., Gillon, M., et al. 2012,MNRAS, 422, 1988
Bakos, G. Á., Noyes, R. W., Kovács, G., et al. 2004,PASP, 116, 266
Bakos, G. Á., Csubry, Z., Penev, K., et al. 2013,PASP, 125, 154
Baraffe, I., Chabrier, G., Fortney, J., 2014, Protostar and Planet VI conference proceedings, 763
Barge, P., Baglin, A., Auvergne, M., et al. 2008, A&A, 482, L17
Baruteau, C., Crida, A., Paardekooper, et al. 2014, Protostar and Planet VI conference proceedings, 667
Borucki, W. J., Koch, D., Basri, G., et al. 2011, ApJ, 728, 20
Brahm, R., et al. 2015, in prep.
Butler, R., Marcy, G. W., Fischer, D. A., et al. 1999, ApJ, 526, 916
Castelli, F., & Kurucz, R. L., 2004, (arXiv:sstro-ph/0405087)
Charbonneau, D., Brown, T. M., Noyes, R. W., Gilliland, R. L., 2002, ApJ, 568, 377
Charbonneau, D., Berta, Z. K., Irwin, J., et al. 2009, Nature, 462, 891
Chen, G., van Boekel, R., Wang, H., et al. 2014, A&A, 567, A8
Chen, G., van Boekel, R., Wang, H., et al. 2014, A&A, 563, A40
Claret, A., 2000, A&A, 363, 1081
Claret, A., 2004, A&A, 428, 1001
Demarque P., Woo J.-H., Kim Y.-C., Yi S. K., 2004, ApJS, 155, 667
Dotter A., Chaboyer B., Jevremovic D., et al., 2008, ApJS, 178, 89
Ford, E. B., 2014, PNAS, 111, 12616
Fortney, J. J., Marley, M. S. & Barnes, J. W., 2007, ApJ, 659, 1661
Fortney, J. J., Shabram, M., Showman, A. P., et al. 2010, ApJ, 709, 1396
Gillon, M., Pont, F., Moutou, C., et al. 2006, A&A, 459, 249
Girardi, L., Bressan, A., Bertelli, G., 2000, A&AS, 141, 371

Greiner, J., Bornemann, W., Clemens, C., et al. 2008, PASP, 120, 405
Hellier, C., Anderson, D.R., Collier Cameron, A., et al. 2011, PASP, 120, 405
Holman, M. J. & Murray, N. W. 2005, Science, 307, 1288
Howarth, I. D., 2011, MNRAS, 418, 1165
Izidoro, A., Raymond, S. N., Morbidelli, A., et al. 2015, ApJL, 800, 22
Jones, M. I., Jenkins, J. S., Rojo, P., et al. 2015, A&A, 573, 3
Jordán, A., Brahm, R., Bakos, G. Á., et al. 2014, AJ, 148, 29
Kley, W., & Nelson, R. P., 2012, A&A Rev, 50, 211
Kreidberg, L., Bean, J. L., Désert, J.-M., 2014, Nature, 505, 66
Lendl, M., Anderson, D.R., Collier Cameron, A., et al. 2012, A&A, 544, 72
Lendl, M., Gillon, M., Queloz, D., et al. 2013, A&A, 552, 2
Lendl, M., Triaud, A.H.M.J., Anderson, D.R., et al. 2014, A&A, 568, 81
Lecavelier Des Etangs, A., Pont, F., Vidal-Madjar, A., Sing, D., 2008, A&A, 481, 83L
Lissauer, J. J., Fabrycky, D.C., Ford, E. B., et al. 2011, Nature, 470, 53
McCullough, P. R., Stys, J. E., Valenti, J. A., et al. 2005, PASP, 117, 783
Mancini, L., Southworth, J., Ciceri, S., et al. 2013a, A&A, 551, A11
Mancini, L., Ciceri, S., Chen, G., et al. 2013b, MNRAS, 436, 2
Mancini, L., Southworth, J., Ciceri, S., et al. 2014, MNRAS, 443, 2391
Marcy, G. W., Butler, R. P., Fischer, D., et al. (2001), ApJ, 556, 296
Marsh, T. R. (1989), PASP, 101, 1032
Meschiari, S., Wolf, A. S., Rivera, E., et al. 2009, PASP, 121, 1016
Müller, H. M., Huber, K. F., Czesla, S., et al. 2013, A&A, 560, 112
Mustill, A. J., Davies, M. B., Johansen, A., 2015, submitted to ApJ, (arXiv:1502.06971)
Narita, N., Nagayama, T., Suenaga, T., et al. 2013, PASJ, 65, 27
Penev, K., Bakos, G. Á., Bayliss, D., et al. 2013, AJ, 145, 5
Pepper, J., Pogge, R. W., DePoy, D. L., et al. 2007, PASP, 119, 923
Pietrinferni A., Cassisi S., Salaris M., Castelli F., 2004, ApJ, 612, 168
Pollacco, D. L., Skillen, I., Collier Cameron, A., et al. 2006, PASP, 118, 1407
Richardson, L. J., Deming, D., Wiedemann, G., et al. 2003, ApJ, 584, 1053
Seager, S. & Sasselov, D. D., 2000, ApJ, 537, 916
Seager, S. & Mallén-Ornelas, G., 2003, ApJ, 585, 1038
Sing, D.K., Pont, F., Aigrain, S., et al. 2011, MNRAS, 416, 1443
Southworth, J. 2008, MNRAS, 386, 1644
Southworth, J. 2010, MNRAS, 408, 1689
Southworth, J. 2013, A&A, 557, A119
Southworth, J., Hinse, T. C., Jørgensen, U.G., et al. 2009, MNRAS, 396, 1023
Southworth, J., Mancini, L., Maxted, P. F. L., et al. 2012, MNRAS, 422, 3099
Southworth, J., Hinse, T. C., Burgdorf, M., et al. 2014, MNRAS, 444, 776
Southworth, J., Mancini, L., Ciceri, S., et al.2015, MNRAS, 447, 711
Stetson, P. B., 1987, PASP, 99, 191
VandenBerg D. A., Bergbusch P. A., Dowler P. D., 2006, ApJS, 162, 375
Winn, J. N., Holman, M. J., Bakos, G. Á., et al. 2007, AJ,134, 1707

APPENDIX A: PHOTOMETRIC PARAMETERS

In the two tables in this appendix are presented the photometric results obtained with JKTEBOP from the fit of each light curve presented in the paper.

This paper has been typeset from a TEX/ LATEX file prepared by the author.

Source	$r_A + r_b$	k	i (deg.)	r_A	r_b
Eul 1.2m	0.1218 ± 0.0044	0.1018 ± 0.0018	84.3258 ± 0.2408	0.11052 ± 0.0039	0.011255 ± 0.00053
Dan 1.54m (transit #1)	0.1188 ± 0.0032	0.1130 ± 0.0022	84.6423 ± 0.1809	0.10671 ± 0.0027	0.012061 ± 0.00049
MPG 2.2m (transit g)	0.1165 ± 0.0057	0.1155 ± 0.0063	84.7024 ± 0.3381	0.10444 ± 0.0046	0.012060 ± 0.00116
MPG 2.2m (transit r)	0.1140 ± 0.0036	0.1128 ± 0.0022	84.9141 ± 0.2079	0.10245 ± 0.0030	0.011558 ± 0.00054
MPG 2.2m (transit i)	0.1181 ± 0.0061	0.1234 ± 0.0089	84.6154 ± 0.3761	0.10516 ± 0.0046	0.012979 ± 0.00149
MPG 2.2m (transit z)	0.1198 ± 0.0046	0.1176 ± 0.0035	84.5609 ± 0.2778	0.10719 ± 0.0038	0.012601 ± 0.00079
Dan 1.54m (transit #2)	0.1076 ± 0.0060	0.1097 ± 0.0035	85.2537 ± 0.3657	0.09699 ± 0.0051	0.010640 ± 0.00088
Final results	$\mathbf{0.1172 \pm 0.0017}$	$\mathbf{0.1095 \pm 0.0024}$	$\mathbf{84.686 \pm 0.098}$	$\mathbf{0.1053 \pm 0.0014}$	$\mathbf{0.01172 \pm 0.00026}$
Anderson et al. (2012)	0.1217 ± 0.0098	0.1234 ± 0.0246	$84.47^{+0.54}_{-0.79}$	0.1084 ± 0.0094	0.0134 ± 0.0024

Table A1. Photometric properties of the WASP-45 system derived by fitting the light curves with JKTEBOP. In bold are highlighted the final parameters obtained as weighted mean. The values from the discovery paper are also shown for comparison.

Source	$r_A + r_b$	k	i (deg.)	r_A	r_b
Eul 1.2m (transit #1)	0.1964 ± 0.0190	0.13551 ± 0.00585	82.90 ± 1.31	0.1730 ± 0.0160	0.02344 ± 0.00302
Eul 1.2m (transit #2)	0.1857 ± 0.0099	0.14025 ± 0.00296	83.51 ± 0.70	0.1629 ± 0.0084	0.02284 ± 0.00158
NTT 3.58m	0.1979 ± 0.0044	0.14123 ± 0.00139	82.84 ± 0.30	0.1734 ± 0.0036	0.02449 ± 0.00074
MPG 2.2m (transit #1 g)	0.1996 ± 0.0041	0.14226 ± 0.00127	82.72 ± 0.27	0.1747 ± 0.0034	0.02485 ± 0.00068
MPG 2.2m (transit #1 r)	0.1997 ± 0.0046	0.14229 ± 0.00115	82.77 ± 0.31	0.1748 ± 0.0039	0.02487 ± 0.00072
MPG 2.2m (transit #1 i)	0.1938 ± 0.0042	0.13991 ± 0.00102	83.05 ± 0.30	0.1700 ± 0.0035	0.02379 ± 0.00063
MPG 2.2m (transit #1 z)	0.1925 ± 0.0069	0.14051 ± 0.00119	83.34 ± 0.49	0.1688 ± 0.0059	0.02372 ± 0.00100
Dan 1.54m (transit #1)	0.1901 ± 0.0095	0.14291 ± 0.00310	83.40 ± 0.69	0.1664 ± 0.0080	0.02378 ± 0.00157
MPG 2.2m (transit #2 g)	0.1971 ± 0.0048	0.14185 ± 0.00162	82.85 ± 0.33	0.1726 ± 0.0040	0.02449 ± 0.00082
MPG 2.2m (transit #2 r)	0.1902 ± 0.0037	0.13955 ± 0.00108	83.25 ± 0.25	0.1669 ± 0.0031	0.02329 ± 0.00059
MPG 2.2m (transit #2 i)	0.1968 ± 0.0042	0.14120 ± 0.00117	82.93 ± 0.29	0.1725 ± 0.0036	0.02435 ± 0.00066
MPG 2.2m (transit #2 z)	0.1953 ± 0.0041	0.14135 ± 0.00108	82.96 ± 0.28	0.1711 ± 0.0035	0.02418 ± 0.00064
MPG 2.2m (transit #3 g)	0.1805 ± 0.0103	0.13800 ± 0.00288	84.14 ± 0.80	0.1586 ± 0.0087	0.02189 ± 0.00163
MPG 2.2m (transit #3 r)	0.2067 ± 0.0053	0.14525 ± 0.00169	82.25 ± 0.33	0.1805 ± 0.0044	0.02621 ± 0.00091
MPG 2.2m (transit #3 i)	0.1562 ± 0.0149	0.13543 ± 0.00370	86.30 ± 1.69	0.1376 ± 0.0127	0.01863 ± 0.00213
MPG 2.2m (transit #3 z)	0.1723 ± 0.0093	0.13828 ± 0.00177	84.72 ± 0.76	0.1514 ± 0.0080	0.02093 ± 0.00130
MPG 2.2m (transit #4 g)	0.1971 ± 0.0061	0.13918 ± 0.00209	82.91 ± 0.41	0.1730 ± 0.0051	0.02408 ± 0.00103
MPG 2.2m (transit #4 r)	0.1958 ± 0.0149	0.14121 ± 0.00334	82.79 ± 1.01	0.1716 ± 0.0126	0.02423 ± 0.00231
MPG 2.2m (transit #4 i)	0.1789 ± 0.0113	0.13713 ± 0.00217	84.03 ± 0.82	0.1574 ± 0.0097	0.02158 ± 0.00161
MPG 2.2m (transit #4 z)	0.1945 ± 0.0090	0.14015 ± 0.00298	83.30 ± 0.69	0.1706 ± 0.0075	0.02391 ± 0.00149
Dan 1.54m (transit #2)	0.1959 ± 0.0046	0.14088 ± 0.00153	82.98 ± 0.31	0.1717 ± 0.0038	0.02419 ± 0.00076
Dan 1.54m (transit #3)	0.1930 ± 0.0049	0.14039 ± 0.00136	83.09 ± 0.34	0.1692 ± 0.0042	0.02376 ± 0.00078
Final results	$\mathbf{0.1950 \pm 0.0013}$	$\mathbf{0.14075 \pm 0.00035}$	$\mathbf{82.80 \pm 0.17}$	$\mathbf{0.1709 \pm 0.0011}$	$\mathbf{0.02403 \pm 0.00021}$
Anderson et al. (2012)	0.1992 ± 0.0059	0.1468 ± 0.0017	82.63 ± 0.38	0.1742 ± 0.0057	0.0250 ± 0.0010

Table A2. Photometric properties of the WASP-46 system derived by fitting the light curves with JKTEBOP. In bold are highlighted the final parameters obtained as weighted mean. The values from the discovery paper are also shown for comparison.

Chapter 8

Discussion & Summary

In the last ten years an incredible progress, both in theory and observations, has brought the exoplanet community from the mere detection of a new exoplanet to its accurate characterization. Planets that transit their host star are especially valuable in this framework, thanks to the their orbital configuration that makes a well of information available and measurable.

In this context, the work presented in this thesis is part of three different, ongoing projects, (HAT-South, confirmation of Kepler targets with CAFE and *Homogeneous studies of transiting extrasolar planets*) that are producing extremely interesting results, and contributing to enlargen and deepen the knowledge we have about planetary systems: their formation, dynamics and characteristics.

The ground based transit survey HATSouth aims to detect and characterize a large number of exoplanets transiting nearby stars and explore their diversity. The survey is a network of six identical, completely automated, telescopes positioned in three different locations in the southern hemisphere, providing continuous 24-hour coverage. HATSouth started its operations in 2010 and is now producing a continuous flow of planetary candidates that are awaiting for follow-up observations to confirm their planetary status. Up to now 16, new exoplanets have been discovered.
These planets all have a short period going from roughly 1 to 5 days (HATS-2 and HATS-5, Mohler-Fischer et al. 2013; Zhou et al. 2014). Their masses range from a tenth to three times the mass of Jupiter (HATS-7 and HATS-16, Bakos et al. 2015; Ciceri et al. 2015a), with a wide range in densities that goes from super inflated planets to relatively compact ones.
Of particular interest for future follow-up observations are: HATS-9 b, which lies in one of the fields that will be observed by the *K2* mission (Brahm et al. 2015), HATS-6 b a Saturn-like planet that orbits around a M star showing one of the deepest planetary transit light-curves to date (Hartman et al. 2015), and the two super-Neptunes, HATS-7 b and HATS-8 b (Bakos et al. 2015; Bayliss et al. 2015).

The *Kepler* mission has identified several thousand of planetary candidates, but only a few hundred of those have been confirmed and properly characterized. The CAB–MPIA collaboration aim is to confirm the planetary nature of a properly selected sample of these candidates, mainly massive and/or long period planets around relatively bright stars ($m_V \lesssim 14$) by means of the CAFE spectrograph.
We have confirmed five uncommon planetary systems, with which we are to fill some part of the planetary parameters space previously empty or scarcely populated. Two planets (Kepler-91 b and Kepler-432 b)have been found circling close to their evolved parent star deviating from the trend seen for these kind of systems. Massive planets around evolved stars normally have wider orbits than 0.5 au, the two planets lie therefore in a region of the parameter space that was thought to be empty (e.g. Johnson et al. 2007; Kunitomo et al. 2011). Within our collaboration, we also confirmed the

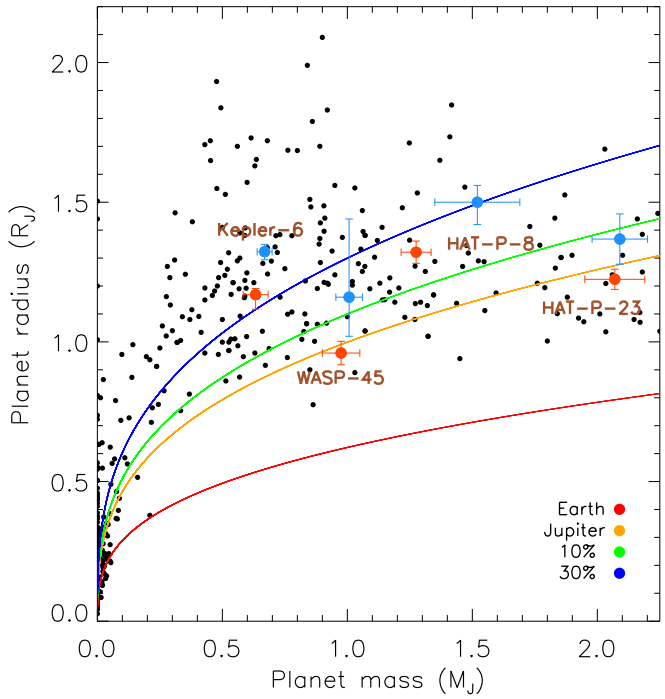

Figure 8.1: Mass–radius diagram of the known transiting planets. The colored curves represent the iso-density lines for planets with the density of Earth and Jupiter, and with a density equal to a Jupiter-like planet with a radius inflated by 10% and 30%. The values for the planets studied within the Homogeneous study project are displayed in orange, for comparison in light blue are reported in the the measurements of the respective discovery papers.

transiting planet with the highest impact parameter, Kepler-447 b. Furthermore, we have confirmed a long period planet and detected a third companion in the same planetary system (KOI-372 *b* and *c*, Mancini et al. 2015b).

The *Homogeneous studies of transiting extrasolar planets* project is a very well established follow-up program targeting transiting planets. Its purpose is to create a large sample of planetary systems that have their properties and characteristics measured in a homogeneous way and are therefore suitable for statistical studies of planetary population. Since the beginning in 2009, more than a hundred planets have been followed up and are therefore free from the diverse kind of systematics that different reduction and analysis algorithms inevitably introduce. Using different observational strategies, such as multi-site or multi-band simultaneous observations, besides obtaining more accurate measurements of the physical parametrs of planetary systems, it is also possible to further characterize them. For instance, the modeling of light curve anomalies due to star spot leads to measure the spin orbit inclination. Or else, studying the variation of the planetary radius in wavelengths gives an insight on the planet atmospheric composition .

In Figure 8.1 a few examples of the results obtained within the project are displayed (Kepler-6, HAT-P-8, HAT-P-23 and WASP-45, Southworth 2011; Mancini et al. 2013; Ciceri et al. 2013; Ciceri et al. 2015b). It is possible to notice the importance of precisely and accurately measured planetary proper-

ties. A small difference in the planetary radius measurement can indeed lead to a diverse bulk density. Therefore, a planet initially compatible with a core-less interior model might instead present an inner rocky core with expected mass around 50 $M_{\oplus}$. The presence of highly inflated planets is still challenging theory. A precise measurement of the radius is essential when trying to model and reproduce the observations in a consistent way.

Suggestion for improvement

The three above mentioned projects are producing fascinating outcomes and, in general, the whole exoplanetary community is making great strides in developing new techniques and isntruments, as well as understanding the astrophysical processes related to planetary systems. However, like in every human project, there is still room for amelioration.
Some suggestion for future development and small changes to the strategies currently used are presented. This is meant not to disparage the work done, but as a way marker to improvement.

- During the years of operation, the HATSouth collaboration has made several improvements in trying to optimize the data collection and the subsequent analysis. Several changes in hardware, software and observational strategy have been carried out resulting in better data-quality and higher throughput in terms of candidate produced.
  Despite the analysis and modeling of the light curve already being performed in the same way for all the light curves, a more homogeneous way to reduce the photometric data of transit follow-ups, may improve our measurements, partially reducing some source of systematic uncertainties. Some steps towards a homogeneous treatment of the spectral follow-up observations have been done, e.g. with the new pipeline for the FEROS and Coralie instruments (Brahm et al. 2015). Nevertheless, a bespoke pipeline for the RV measurements to be used for all the instruments is still missing.

- Given the large number of candidates produced by the HATSouth survey and the limited resources (observing time and instrumentation), it is necessary to prioritize the confirmation of some promising candidates with respect to others. However, in this way it might be possible that some interesting categories of targets that require a great effort both in the follow-up campaign and in the subsequent analysis, are overlooked .
  An example of this, brought to light also from the study on HATS-15 and HATS-16, is the case of transiting planets whose host star is a fast rotator. Given the high rotation velocity, the spectral lines of these stars are broad, making it challenging to perform accurate radial velocity measurements.
  Nonetheless, finding planets around these kind of stars might give an insight on the planet-star dynamics and interactions or contribute to the proper determination of planet occurrence rates for massive stars. Indeed fast rotators are either high mass stars, for which the follow-up of a planet is arduous due to the too few and too broad spectral lines, or solar-like stars that have somehow been spun up by the interaction with some external body (that can be a planet or a stellar companion).

- Another improvement that can be done is to utilize a better observing strategy while following-up *Kepler*'s candidate with CAFE. Even though the instrument has a good stability, the extreme precision required for the project, discloses some small instability that could introduce sensible systematics. By looking at the ThAr calibration frames, it is indeed possible to measure an instrumental shift in radial velocity that in some cases reaches $\sim 150\,ms^{-1}$ during one night.
  Since the exposure times used to collect the spectra are long (up to 1 hour), a small shift in RV might be possible. To properly calibrate the observed spectra, the best option would therefore be to obtain ThAr calibrations both before and right after the science frames. Furthermore, if several calibration spectra are available for one night, it might be possible to interpolate the RV shift creating a function in time and more robustly correct the science spectra.

- The fate of planetary systems in the late stages of the stars lifetime is still not well constrained. Planets around giants are usually found to orbit their expanding star at large distances (a >0.5 au). The discovery of planets such as Kepler-91 b or Kepler-432 b, which orbit their stars close-in, challenges the proposed theory that does not predict such kind of planets.
  It would therefore be of extreme interest to preform dynamical simulations on the stability of these systems taking in account the evolution of the stars. In this way it might be possible to figure out whether we discovered these planets right before they are swallowed by their host stars, or if planets like these survive for much longer than was previously assumed.

- Observing a transit with a multi-band imager allows one to give some constraint on the atmospheric composition of the planet. However, to be able to be able to exclude some of the different atmosphere atmosphere models, requires a very high precision in the measurement of the planetary radius at different wavelengths. It goes without saying, that an extremely good precision in the photometry is needed.
  The multi-band imagers available nowadays, e.g. GROND and BUSCA, do not allow to choose independently the exposure time for the diverse filter used. This results in a non-optimal acquisition of the images in most of the bandpass and therefore a poor constraint on the value of the planetary radius.
  A future instrument where the exposure time for the different filters could be set separately, would permit to obtain precise light curves in all filters. Moreover, allowing a small mechanical motion of the CCD, could provide for a small adjustment to the amount of the defocussing set by the telescope making the observing condition for each band-pass optimal.

- When analyzing all the transit light curves collected for a planetary system, we treat each data-set as a distinct transit, and allow all the photometric parameters to be adjusted separately. A better approach could be to simultaneously fit all the light curves relative to the same transit event. The best fit values for all the parameters should be the same for all the light curves and only the limb darkening coefficients and the transit depth should be allowed to have different values according to the pass-band used for the observations.

- Once the measurements of the planetary radii at different wavelength are obtained, we usually compare them with pre-defined models, adapting them to our case. These models are calculated for a grid of specific values of the parameters, that are often not representative of the case

studied. New atmospheric model codes such as the PETIT code by Mollière et al. (2015) or VSTAR by Bott et al. (2013) can provide a set of planetary radii predictions constructed ad hoc according to the newly measured properties of the planet and its host star. In this way a proper comparison between the data and the different models prediction can be carried out without introducing extra sources of systematics and discrepancies.

Future perspectives

Hot Jupiters show a wide variety of characteristics and properties. A special class of these highly irradiated planets, the bloated ones, is still challenging astronomers who are not yet able to explain the extremely low density that these planets show. Until now, besides inflation, there is not a specific characteristic that clearly distinguishes them from the other planets. It is indeed possible to find planets with similar masses, stellar irradiation or composition that still present very different densities (e.g. HATS-13 and HATS-14 Mancini et al. 2015a). Several theories have been proposed, some of which could explain the scenario of a specific case, but none of them are able to explain the whole set of super-inflated planets. Among the diverse mechanisms, there are tidal friction, enhanced atmospheric opacities, turbulent mixing, Ohmic dissipation, deuterium-deuterium burning, and windshocks (see e.g., Ginzburg & Sari 2015; Ouyed & Jaikumar 2015; Baraffe et al. 2014, and reference therein).

Properly characterizing planetary systems containing hot Jupiters, both via photometric and spectroscopic follow-up, is the first step towards a proper comprehension of the physical mechanism that causes or suppresses the large inflation. However, to discern between the possible causees, a deeper knowledge of the planet is indispensable. In this framework, notions of the planetary atmospheric composition can be of great advantage. The detection of molecules or atoms and the retrival of the chemical abundances in the planet's atmosphere is particularly arduous, especially with ground based facilities, but it is possible as shown by several studies presented in the literature (e.g. Birkby et al. 2013).

The best way to obtain chemical information of these planets is to perform multi-band photometry or transmission spectroscopy during a transit event with multi-band imagers or high-resolution spectrographs. In the past few years, a new technique to detect molecules and constrain the abundances has been introduced by Snellen et al. (2010). This method is the application to the planetary case of the study of a stellar double-line eclipsing binaries. It basically consist of measuring the Doppler shift of the planetary lines after a proper and accurate subtraction of the stellar spectrum. This method, was initially used to measure the mass of planets that do not transit their parent stars, is nowadays also used to measure the absorption lines of a specific molecule such as CO or H_2O (e.g. Rodler et al. 2013; Brogi et al. 2014).

In the context of planets orbiting evolved stars, all the confirmed planets but four orbit their star at relatively large distances and most of them are relatively massive. This and other unknown aspects leads to several unresolved questions: e.g. 'Is the large orbital radius due to a dynamical adjustment of the previous orbit, or are these planets the only ones left of a planetary system where the close-in planets have been swallowed by the expanding star?' or 'Is the lack of planets close-in due to an observational bias?' The expanding star might have indeed removed the atmosphere of those planets

leaving just a small core which is difficult to detect. As already mentioned, the proper characterization, followed by dynamical simulations of the evolution of the known systems could provide some insight on the fate of planetary systems.

Concerning the mass distribution: 'Can the preponderance of massive planets be explained just by invoking an observational bias?'. Besides the obvious fact that lighter planets around a giant might be more difficult to detect or have been already ejected/engulfed by the star, there might also be a formation effect. K and G giants are the evolved stages of F and A-type main sequence stars. If during their main sequence life these kind of stars pose strong observational challenges, in their evolved phase the search for exoplanets around them becomes surmountable. Given the higher mass of the host star it is thought that the initial protoplanetary disk is more massive and the physical conditions can be different leading to a production of more massive planets (e.g., Alibert et al. 2011).

Another possibility might be that the surviving planets might accrete some of the ejected material of the star thereby increasing their mass. However, even taking into account the most favorable scenario, where the star has an incredibly high mass loss rate ($10^{-6}\,M_{\odot}/yr$), the planet accretion would be too small to be detectable. From a rough estimate, given the extreme case of a $R_{\rm p} \sim 2\,R_{\rm Jup}$ planet at 0.5 au from the host star, the planetary accretion rate would be

$$\dot{\rm M}_{\rm p} = \dot{\rm M}_{\star} \left(\frac{\rm R_p}{a}\right)^2 \sim 10^{-12}\,M_{\odot}/yr \sim 10^{-6}\,M_{\oplus}/yr, \tag{8.1}$$

which is roughly 100 times smaller than the mass loss rate due to hydrodynamic escape (Villaver 2011).

Given the relatively small number of planets found orbiting around evolved stars, it is also necessary to look for such kind of systems in order to give some statistically significant results. The best method to detect these planets from ground based facilities is radial velocity. Indeed the radius ratio between a giant star and a planet is very small, and a transit survey targeting those system might be possible only from space, where the required photometric precision might be reached.

8.1 Summary

In the fist part of this thesis the detection of two new planetary systems is presented, HATS-15 and HATS-16, found within the HATSouth collaboration. Both planets are located roughly 700 pc away from our Sun and are composed of a hot Jupiter and a G-type star. The stars are quite evolved ($\sim$ 10 Gyr) and relatively faint with respect to the usual magnitude of the host stars of transiting planets ($V = 14.8$ mag and $V = 13.8$ mag for HATS-15 and HATS-16 respectively).

HATS-15 is a G9 V star hosting a hot Jupiter which completes its orbit in $\sim$ 1.7 days. The planet has a mass of $2.17 \pm 0.15\,M_{\rm Jup}$ and radius of $1.105 \pm 0.040\,R_{\rm Jup}$. Comparing the planet's mass and radius values with those predicted by Fortney et al. (2007), we can exclude the presence of a massive rocky core, giving an upper limit for its mass of $50\,M_{\oplus}$.

HATS-16 b is a massive planet (mass $3.27 \pm 0.19\,M_{\rm Jup}$ and radius $1.30 \pm 0.15\,R_{\rm Jup}$) orbiting around a moderately active G3 V star in $\sim$ 2.7 days. Although pretty massive, HATS-16 b's density is not

extreme and is compatible with a core-less planetary-model.
We found a strong discrepancy in the age values of HATS-16 measured with different methods. This is mainly due to the fact that the star rotates faster than what is expected from its spectral type, having a rotation period of just 12.4 d. Given the mass and distance of the plant, the timescale to tidally spin-up the star is small enough to possibly explain the short period. The activity and period might also be explained invoking planet-star magnetic interaction (e.g. Poppenhaeger & Wolk 2014). However, to properly constrain the origin of the spin-up, more calculations, that take into account all the relevant mechanisms, are required.

The second work presented in this thesis is the confirmation by means of the radial velocity technique of a planetary candidate found by the *Kepler* space-telescope. The new planetary system Kepler-432 is composed of a K giant star, which is ascending the red giant branch, and a massive planet of $M_{\rm p} = 4.87 \pm 0.48\, M_{\rm Jup}$.

The confirmation of the planetary nature of Kepler-432 b has been possible thanks to the accurate measurement of the Doppler shift of the parent star. For this purpose we employed the CAFE spectrograph, fed by the CAHA 2.2 m telescope at the Calar Alto Observatory. By analyzing both the CAFE spectroscopic data and the photometric data provided by the *Kepler* spacecraft, we found that the planet has an eccentric orbit ($e = 0.535 \pm 0.030$) with a period of 52.50097 ± 0.00021 days.

Having a radius just slightly larger than Jupiter ($R_{\rm p} = 1.120 \pm 0.036 R_{\rm Jup}$) but a mass almost five times bigger, Kepler-432 b is somewhat compact $\rho_p = 3.46 \pm 0.48 \rho_{\rm Jup}$, having roughly the same density as the Earth.
By studying already existing high resolution images observed in the near infrared, we spotted a faint companion located at $1.1''$ from Kepler-432. Howbeit, given its faintness, the dilution of the transit depth is very small and is well within the errorbars of the radius measurement. Along with just three other planets, Kepler-432 b occupies an empty region of the stellar radius–semi-major axis parameter space, posing interesting questions and constraints on the evolutionary processes that planetary systems undergo.

The last three chapters of thesis report the results obtained in the context of the *Homogeneous studies of transiting extrasolar planets* project. The observations were performed by means of small-class telescopes located both in the northern and southern hemisphere using the defocusing technique. We obtained improved estimates of the physical parameters of both the star and planet of six planetary systems. In particular, we found that HAT-P-16 is colder, younger and smaller with respect to what was reported in the discovery paper. The measurement of the planetary density suggests to presence of a massive core. As far as it concerns WASP-21, we measured lower values for both the mass and the density of the planet than the initial estimates. HAT-P-23 b has a smaller radius than the one attributed in the discovery paper. As the value of the mass is consistent with the one found in literature, the mean density we found is higher. For WASP-48 we improved the measure for both stellar and planetary radii and masses. Both the star and planet have a smaller radius. WASP-48 b is no longer a highly inflated hot Jupiter but lies in a more populated region of the mass-radius diagram. The value of the planetary radius of WASP-45 b we found is smaller than the discovery paper's one. Among the planets in the same mass regime WASP-45 b is now one of the densest, suggesting the presence of an inner rocky core of about 50 $M_\oplus$ (Fortney et al. 2007). Finally, also for the case of WASP-46 b, we found a slightly

smaller radius and therefore a higher density, that is now greater than Jupiter's one.

In the the case of the HAT-P-16 and WASP-21 systems, we performed simultaneous observations at two different sites. The aim was to detect anomalies in the light curves which might be attributable to astrophysical phenomena. Looking at the residuals of the light curve best fit, small deviations from the expected curve can be detected. However, these anomalies are only in one of the two light curves, hence are imputable to systematics due to instrumental effects, or more likely to atmospheric variations.

The planetary systems HAT-P-23, WASP-48, WASP-45 and WASP-46 have been observed with multiband imagers: the first two with BUSCA, and GROND for the latter two. We measured the planetary radii obtained at the different wavelengthss and we compared them with the predictions made by Fortney et al. (2010), using different molecular compositions. We found that in the case of both HAT-P-23 and WASP-48 the radii of the planets do not show any large variations suggesting that their atmospheres are not affected by a strong Rayleigh scattering. For WASP-45 we detected a radius variation of the order of $10\,H$ (where H is the scale height) between the redder filters and the blue ones. This variation might suggest the presence of strong absorbers in the 800–900 nm regime. Also in the case of WASP-46 b, we found a very mild difference of roughly $4\,H$ between the radii measured in the i' and z' bands. A possible explanation for this variation might be ascribable to the absence of potassium at 770 nm and a significant amount of water vapor around 920 nm.

Acknowledgements

I would like to thank my advisor Thomas Henning, for the great opportunity he gave me to learn and work as a PhD student at MPIA. The few times we met and talked together were always very useful and besides spurring me to gave me the opportunity to see my work as a whole and from a broader prospective. Many thanks also to Luigi Mancini, for being a great guide and the precious advices, hints, suggestions.

A special thank goes to John Southworth, for the precious advices and comments that led me to deepen my knowledge on some important details that I would have otherwise overlooked.I'm also grateful to all the collaborators of HATSouth and CAB-MPIA collaborations, in particular Rafael, Joel and Jorge.

I can't forget, of course, all the friends I met in Heidelberg that support me and make my staying away from home really pleasant and interesting; among all I want to thank my present and past office-mate, for the patience you had with me answering the thousand of questions I made, and joining me in one of ours super interesting chat: thank you Anahi, Dario, Kirsten, Maria, Michael, Thales ad Wilma. A special thanks is also for all the other friends and colleagues met at MPIA for the great company and wonderful time spent together! To cite just a few, thanks Christine, Aiara, Andreas, Paul, Richard, Michael, Taisiya, Paolo, Christina, Roxana and Chiara.

One of the most exciting things of this PhD has been the opportunity to meeting people from all over the world. In particular, it was a great pleasure to get to meet Megan, David, Ati, Sebasien, Richard, Andrius, Aurelian and even more to be able to see you several time more in La Silla and at conferences! I'm also really grateful to all the friends that, even for a short period, made Heidelberg like a home for me: thank you Maria Concetta, Lucia, Claudio, Aldo, Carol, Sara, Giulia, Augusto, Michael, Arianna and Francesco. I can't of course forget all my friends in Italy and now spread around the world that, even from far away, have never stopped believing in me...thanks, without you I would have never make it till the end!

I can't conclude without thanking all my relatives, for their love and support, that has never ceased to reach me. In particular a billion thanks to papa', mamma, Gloria, Davide e Monica.

Bibliography

Abe, F., Bennett, D. P., Bond, I. A., et al. 2004, Science, 305, 1264

Aceituno, J., Sánchez, S. F., Grupp, F., et al. 2013, A&A, 552, A31

Albrecht, S., Winn, J. N., Johnson, J. A., et al. 2012, ApJ, 757, 18

Alcock, C., Akerlof, C. W., Allsman, R. A., et al. 1993, Nature, 365, 621

Alibert, Y., Mordasini, C., & Benz, W. 2011, A&A, 526, A63

Alibert, Y., Mordasini, C., Benz, W., & Winisdoerffer, C. 2005, A&A, 434, 343

Alonso, R., Brown, T. M., Torres, G., et al. 2004, ApJL, 613, L153

Alsubai, K. A., Parley, N. R., Bramich, D. M., et al. 2013, Acta Astronomica, 63, 465

Anderson, D. R., Collier Cameron, A., Delrez, L., et al. 2014, MNRAS, 445, 1114

Armstrong, D. J., Santerne, A., Veras, D., et al. 2015, ArXiv e-prints

Aubourg, E., Bareyre, P., Bréhin, S., et al. 1993, Nature, 365, 623

Bagnasco, G., Kolm, M., Ferruit, P., et al. 2007, in Society of Photo-Optical Instrumentation Engineers (SPIE) Conference Series, Vol. 6692, Society of Photo-Optical Instrumentation Engineers (SPIE) Conference Series, 0

Bakos, G., Noyes, R. W., Kovács, G., et al. 2004, PASP, 116, 266

Bakos, G. A., Csubry, Z., Penev, K., et al. 2013, PASP, 125, 154

Bakos, G. A., Penev, K., Bayliss, D., et al. 2015, ArXiv e-prints

Bakos, G. A., Torres, G., Pál, A., et al. 2010, ApJ, 710, 1724

Baraffe, I., Chabrier, G., Fortney, J., & Sotin, C. 2014, Protostars and Planets VI, 763

Barclay, T., Rowe, J. F., Lissauer, J. J., et al. 2013, Nature, 494, 452

Barge, P., Baglin, A., Auvergne, M., et al. 2008, A&A, 482, L17

Barry, R., Kruk, J., Anderson, J., et al. 2011, in Society of Photo-Optical Instrumentation Engineers (SPIE) Conference Series, Vol. 8151, Society of Photo-Optical Instrumentation Engineers (SPIE) Conference Series, 0

Batalha, N. M., Rowe, J. F., Gilliland, R. L., et al. 2010, ApJL, 713, L103

Bayliss, D., Hartman, J. D., Bakos, G. A., et al. 2015, AJ, 150, 49

Bedell, M., Melendez, J., Bean, J. L., et al. 2015, ArXiv e-prints

Benedict, G. F., McArthur, B. E., Gatewood, G., et al. 2006, AJ, 132, 2206

Benneke, B. & Seager, S. 2012, ApJ, 753, 100

Bennett, D. P. 2010, ApJ, 716, 1408

Beuzit, J.-L., Feldt, M., Dohlen, K., et al. 2008, in Society of Photo-Optical Instrumentation Engineers (SPIE) Conference Series, Vol. 7014, Society of Photo-Optical Instrumentation Engineers (SPIE) Conference Series, 18

Birkby, J. L., de Kok, R. J., Brogi, M., et al. 2013, MNRAS, 436, L35

Black, D. C. & Scargle, J. D. 1982, ApJ, 263, 854

Boley, A. C. & Durisen, R. H. 2010, ApJ, 724, 618

Bond, I. A., Abe, F., Dodd, R. J., et al. 2001, MNRAS, 327, 868

Bond, I. A., Udalski, A., Jaroszyński, M., et al. 2004, ApJL, 606, L155

Borucki, W., Koch, D., Basri, G., et al. 2008, in IAU Symposium, Vol. 249, IAU Symposium, ed. Y.-S. Sun, S. Ferraz-Mello, & J.-L. Zhou, 17–24

Borucki, W., Koch, D., Boss, A., et al. 2004, in ESA Special Publication, Vol. 538, Stellar Structure and Habitable Planet Finding, ed. F. Favata, S. Aigrain, & A. Wilson, 177–182

Borucki, W. J., Koch, D., Basri, G., et al. 2010, Science, 327, 977

Borucki, W. J., Koch, D. G., Batalha, N., et al. 2012, ApJ, 745, 120

Bott, K., Kedziora-Chudczer, L., & Bailey, J. 2013, ArXiv e-prints

Boyajian, T. S., von Braun, K., van Belle, G., et al. 2012, ApJ, 757, 112

Bozza, V. 2010, MNRAS, 408, 2188

Brahm, R., Jordán, A., Hartman, J. D., et al. 2015, AJ, 150, 33

Brahm, R. et al. 2015, in prep.

Broeg, C., Fortier, A., Ehrenreich, D., et al. 2013, in European Physical Journal Web of Conferences, Vol. 47, European Physical Journal Web of Conferences, 3005

Brogi, M., de Kok, R. J., Birkby, J. L., Schwarz, H., & Snellen, I. A. G. 2014, A&A, 565, A124

Brown, T. M. 2003, ApJL, 593, L125

Brown, T. M., Latham, D. W., Everett, M. E., & Esquerdo, G. A. 2011, AJ, 142, 112

Burrows, A., Hubeny, I., Budaj, J., Knutson, H. A., & Charbonneau, D. 2007, ApJL, 668, L171

Casertano, S., Lattanzi, M. G., Sozzetti, A., et al. 2008, A&A, 482, 699

Catala, C. & Plato Team. 2006, in ESA Special Publication, Vol. 1306, ESA Special Publication, ed. M. Fridlund, A. Baglin, J. Lochard, & L. Conroy, 497

Chabrier, G., Johansen, A., Janson, M., & Rafikov, R. 2014, Protostars and Planets VI, 619

Charbonneau, D., Allen, L. E., Megeath, S. T., et al. 2005, ApJ, 626, 523

Charbonneau, D., Brown, T. M., Latham, D. W., & Mayor, M. 2000, ApJL, 529, L45

Chauvin, G., Lagrange, A.-M., Dumas, C., et al. 2004, A&A, 425, L29

Chazelas, B., Pollacco, D., Queloz, D., et al. 2012, in Society of Photo-Optical Instrumentation Engineers (SPIE) Conference Series, Vol. 8444, Society of Photo-Optical Instrumentation Engineers (SPIE) Conference Series, 0

Ciceri, S., Lillo-Box, J., Southworth, J., et al. 2015a, A&A, 573, L5

Ciceri, S., Mancini, L., Southworth, J., et al. 2015b, A&A, 577, A54

Ciceri, S., Mancini, L., Southworth, J., et al. 2013, A&A, 557, A30

Ciceri, S. et al. 2015a, to be submitted to PASP

Ciceri, S. et al. 2015b, submitted to MNRAS

Collier Cameron, A., Guenther, E., Smalley, B., et al. 2010, MNRAS, 407, 507

Collier Cameron, A., Pollacco, D., Street, R. A., et al. 2006, MNRAS, 373, 799

Cosentino, R., Lovis, C., Pepe, F., et al. 2012, in Society of Photo-Optical Instrumentation Engineers (SPIE) Conference Series, Vol. 8446, Society of Photo-Optical Instrumentation Engineers (SPIE) Conference Series, 1

Crepp, J. R., Bechter, A., Bechter, E., et al. 2014, in American Astronomical Society Meeting Abstracts, Vol. 223, American Astronomical Society Meeting Abstracts #223, #348.20

Crossfield, I. J. M., Petigura, E., Schlieder, J. E., et al. 2015a, ApJ, 804, 10

Crossfield, I. J. M., Petigura, E., Schlieder, J. E., et al. 2015b, ApJ, 804, 10

de Bruijne, J. H. J. 2012, Ap&SS, 341, 31

Decampli, W. M. & Cameron, A. G. W. 1979, Icarus, 38, 367

Deming, D., Seager, S., Richardson, L. J., & Harrington, J. 2005, Nature, 434, 740

Demory, B.-O., Seager, S., Lissauer, J., et al. 2013, ArXiv e-prints

Désert, J.-M., Charbonneau, D., Torres, G., et al. 2015, ApJ, 804, 59

Díaz, R. F., Almenara, J. M., Santerne, A., et al. 2014, MNRAS, 441, 983

Dong, S., DePoy, D. L., Gaudi, B. S., et al. 2006, ApJ, 642, 842

Edelson, R., McHardy, I., Jorstad, S., et al. 2015, The Astronomer's Telegram, 7056, 1

Einstein, A. 1936, Science, 84, 506

Etzel, P. B. 1981, in Photometric and Spectroscopic Binary Systems, ed. E. B. Carling & Z. Kopal, 111

Fischer, D. A., Howard, A. W., Laughlin, G. P., et al. 2014a, Protostars and Planets VI, 715

Fischer, D. A., Marcy, G. W., & Spronck, J. F. P. 2014b, ApJS, 210, 5

Fortney, J. J., Marley, M. S., & Barnes, J. W. 2007, ApJ, 659, 1661

Fortney, J. J., Mordasini, C., Nettelmann, N., et al. 2013, ApJ, 775, 80

Fortney, J. J., Shabram, M., Showman, A. P., et al. 2010, ApJ, 709, 1396

Gaudi, B. S. & Winn, J. N. 2007, ApJ, 655, 550

Gillon, M., Jehin, E., Delrez, L., et al. 2013, in Protostars and Planets VI Posters, 66

Gillon, M., Smalley, B., Hebb, L., et al. 2009, A&A, 496, 259

Ginzburg, S. & Sari, R. 2015, ApJ, 803, 111

Gould, A. & Gaucherel, C. 1997, ApJ, 477, 580

Gould, A. & Horne, K. 2013, ArXiv e-prints

Gould, A. & Loeb, A. 1992, ApJ, 396, 104

Gregory, P. C. & Fischer, D. A. 2010, MNRAS, 403, 731

Greiner, J., Bornemann, W., Clemens, C., et al. 2008, PASP, 120, 405

Guillot, T., Santos, N. C., Pont, F., et al. 2006, A&A, 453, L21

Hartman, J. D., Bayliss, D., Brahm, R., et al. 2015, AJ, 149, 166

Hatzes, A. P. 2013, ApJ, 770, 133

Hatzes, A. P. 2014, A&A, 568, A84

Hebb, L., Collier-Cameron, A., Triaud, A. H. M. J., et al. 2010, ApJ, 708, 224

Helled, R., Bodenheimer, P., Podolak, M., et al. 2014, Protostars and Planets VI, 643

Helled, R. & Schubert, G. 2009, ApJ, 697, 1256

Henry, G. W., Marcy, G. W., Butler, R. P., & Vogt, S. S. 2000, ApJL, 529, L41

Hilditch et al. 2001, The Observatory, 121, 389

Hogerheijde, M. 1998, PhD thesis, Department of Astronomy, University of California, Campbell Hall, Berkeley, CA 94720, USA

Holman, M. J., Fabrycky, D. C., Ragozzine, D., et al. 2010, Science, 330, 51

Holman, M. J. & Murray, N. W. 2005, Science, 307, 1288

Hormuth, F. 2007, Master's thesis

Hormuth, F., Hippler, S., Brandner, W., Wagner, K., & Henning, T. 2008, in Society of Photo-Optical Instrumentation Engineers (SPIE) Conference Series, Vol. 7014, Society of Photo-Optical Instrumentation Engineers (SPIE) Conference Series, 48

Howell, S. B., Sobeck, C., Haas, M., et al. 2014, PASP, 126, 398

Hwang, K.-H., Han, C., Choi, J.-Y., et al. 2015, ArXiv e-prints

Jenkins, J. M., Caldwell, D. A., Chandrasekaran, H., et al. 2010, ApJL, 713, L87

Jenkins, J. M., Twicken, J. D., Batalha, N. M., et al. 2015, AJ, 150, 56

Johnson, J. A., Aller, K. M., Howard, A. W., & Crepp, J. R. 2010, PASP, 122, 905

Johnson, J. A., Fischer, D. A., Marcy, G. W., et al. 2007, ApJ, 665, 785

Johnson, J. A., Marcy, G. W., Fischer, D. A., et al. 2006, ApJ, 647, 600

Jordán, A., Brahm, R., Bakos, G. A., et al. 2014, AJ, 148, 29

Kalas, P., Graham, J. R., & Clampin, M. 2005, Nature, 435, 1067

Kaltenegger, L. & Sasselov, D. 2011, ApJL, 736, L25

Kaspi, V. M., Taylor, J. H., & Ryba, M. F. 1994, ApJ, 428, 713

Kasting, J. F. & Catling, D. 2003, ARAA, 41, 429

Kasting, J. F., Whitmire, D. P., & Reynolds, R. T. 1993, Icarus, 101, 108

Kaufer, A. & Pasquini, L. 1998, in Society of Photo-Optical Instrumentation Engineers (SPIE) Conference Series, Vol. 3355, Optical Astronomical Instrumentation, ed. S. D'Odorico, 844–854

Kim, S.-L., Park, B.-G., Lee, C.-U., et al. 2011, in Society of Photo-Optical Instrumentation Engineers (SPIE) Conference Series, Vol. 8151, Society of Photo-Optical Instrumentation Engineers (SPIE) Conference Series, 1

Kipping, D. M., Fossey, S. J., & Campanella, G. 2009, MNRAS, 400, 398

Kipping, D. M., Nesvorný, D., Buchhave, L. A., et al. 2014, ApJ, 784, 28

Knutson, H. A., Charbonneau, D., Noyes, R. W., Brown, T. M., & Gilliland, R. L. 2007, ApJ, 655, 564

Knutson, H. A., Howard, A. W., & Isaacson, H. 2010, ApJ, 720, 1569

Knutson, H. A., Lewis, N., Fortney, J. J., et al. 2012, ApJ, 754, 22

Konacki, M., Torres, G., Jha, S., & Sasselov, D. 2003, ArXiv Astrophysics e-prints

Kopparapu, R. K., Ramirez, R., Kasting, J. F., et al. 2013, ApJ, 765, 131

Kovács, G., Bakos, G., & Noyes, R. W. 2005, MNRAS, 356, 557

Kovács, G., Zucker, S., & Mazeh, T. 2002, A&A, 391, 369

Kreidberg, L., Bean, J. L., Désert, J.-M., et al. 2014, Nature, 505, 69

Kunitomo, M., Ikoma, M., Sato, B., Katsuta, Y., & Ida, S. 2011, ApJ, 737, 66

Kürster, M. & Endl, M. 2004, in Astronomical Society of the Pacific Conference Series, Vol. 321, Extrasolar Planets: Today and Tomorrow, ed. J. Beaulieu, A. Lecavelier Des Etangs, & C. Terquem, 84

Lagrange, A.-M., Bonnefoy, M., Chauvin, G., et al. 2010, Science, 329, 57

Lanotte, A. A., Gillon, M., Demory, B.-O., et al. 2014, A&A, 572, A73

Lenzen, R., Hartung, M., Brandner, W., et al. 2003, in Society of Photo-Optical Instrumentation Engineers (SPIE) Conference Series, Vol. 4841, Instrument Design and Performance for Optical/Infrared Ground-based Telescopes, ed. M. Iye & A. F. M. Moorwood, 944–952

Li, Z.-Y., Banerjee, R., Pudritz, R. E., et al. 2014, Protostars and Planets VI, 173

Liebes, S. 1964, Physical Review, 133, 835

Lillo-Box, J. 2015, PhD thesis

Lillo-Box, J., Barrado, D., & Bouy, H. 2012, A&A, 546, A10

Lillo-Box, J., Barrado, D., & Bouy, H. 2014a, A&A, 566, A103

Lillo-Box, J., Barrado, D., Henning, T., et al. 2014b, A&A, 568, L1

Lillo-Box, J., Barrado, D., Mancini, L., et al. 2015a, A&A, 576, A88

Lillo-Box, J., Barrado, D., Moya, A., et al. 2014c, A&A, 562, A109

Lillo-Box, J., Barrado, D., Santos, N. C., et al. 2015b, A&A, 577, A105

Line, M. R., Zhang, X., Vasisht, G., et al. 2012, ApJ, 749, 93

Lissauer, J. J., Hubickyj, O., D'Angelo, G., & Bodenheimer, P. 2009, Icarus, 199, 338

Loeillet, B., Bouchy, F., Deleuil, M., et al. 2006, in SF2A-2006: Semaine de l'Astrophysique Francaise, ed. D. Barret, F. Casoli, G. Lagache, A. Lecavelier, & L. Pagani, 413

Macintosh, B., Graham, J. R., Barman, T., et al. 2015, ArXiv e-prints

Macintosh, B. A., Anthony, A., Atwood, J., et al. 2012, in Society of Photo-Optical Instrumentation Engineers (SPIE) Conference Series, Vol. 8446, Society of Photo-Optical Instrumentation Engineers (SPIE) Conference Series, 1

Madhusudhan, N., Knutson, H., Fortney, J. J., & Barman, T. 2014, Protostars and Planets VI, 739

Mahadevan, S., Ramsey, L., Redman, S., et al. 2010, in Astronomical Society of the Pacific Conference Series, Vol. 430, Pathways Towards Habitable Planets, ed. V. Coudé du Foresto, D. M. Gelino, & I. Ribas, 272

Mancini, L., Hartman, J. D., Penev, K., et al. 2015a, A&A, 580, A63

Mancini, L., Lillo-Box, J., Southworth, J., et al. 2015b, ArXiv e-prints

Mancini, L., Southworth, J., Ciceri, S., et al. 2013, A&A, 551, A11

Mancini, L., Southworth, J., Ciceri, S., et al. 2014, MNRAS, 443, 2391

Mao, S. & Paczynski, B. 1991, ApJL, 374, L37

Marley, M. S., Fortney, J. J., Hubickyj, O., Bodenheimer, P., & Lissauer, J. J. 2007, ApJ, 655, 541

Marley, M. S., Gelino, C., Stephens, D., Lunine, J. I., & Freedman, R. 1999, ApJ, 513, 879

Marois, C., Lafrenière, D., Doyon, R., Macintosh, B., & Nadeau, D. 2006, ApJ, 641, 556

Matthews, K. & Soifer, B. T. 1994, in Astrophysics and Space Science Library, Vol. 190, Astronomy with Arrays, The Next Generation, ed. I. S. McLean, 239

Mayer, L., Lufkin, G., Quinn, T., & Wadsley, J. 2007, ApJL, 661, L77

Mayor, M., Pepe, F., Queloz, D., et al. 2003, The Messenger, 114, 20

Mayor, M. & Queloz, D. 1995, Nature, 378, 355

McLaughlin, D. B. 1924, ApJ, 60, 22

Meru, F. & Bate, M. R. 2010, MNRAS, 406, 2279

Miller, N. & Fortney, J. J. 2011, ApJL, 736, L29

Mohler-Fischer, M., Mancini, L., Hartman, J. D., et al. 2013, A&A, 558, A55

Mollière, P., van Boekel, R., Petrus Dullemond, C., Henning, T., & Mordasini, C. 2015, ArXiv e-prints

Mordasini, C., Alibert, Y., Benz, W., & Naef, D. 2009, A&A, 501, 1161

Mordasini, C., Mayor, M., Udry, S., et al. 2011, A&A, 526, A111

Movshovitz, N., Bodenheimer, P., Podolak, M., & Lissauer, J. J. 2010, Icarus, 209, 616

Muirhead, P. S., Johnson, J. A., Apps, K., et al. 2012, ApJ, 747, 144

Nayakshin, S. 2010, MNRAS, 408, L36

Nesvorný, D., Kipping, D., Terrell, D., et al. 2013, ApJ, 777, 3

Ofir, A., Dreizler, S., Zechmeister, M., & Husser, T.-O. 2014, A&A, 561, A103

Oppenheimer, B. R., Baranec, C., Beichman, C., et al. 2013, ApJ, 768, 24

Ouyed, R. & Jaikumar, P. 2015, ArXiv e-prints

Paczynski, B. 1986, ApJ, 304, 1

Penev, K., Bakos, G. A., Bayliss, D., et al. 2013, AJ, 145, 5

Pepe, F., Lovis, C., Ségransan, D., et al. 2011, A&A, 534, A58

Pepe, F., Mayor, M., Queloz, D., et al. 2004, A&A, 423, 385

Pepe, F. A., Cristiani, S., Rebolo Lopez, R., et al. 2010, in Society of Photo-Optical Instrumentation Engineers (SPIE) Conference Series, Vol. 7735, Society of Photo-Optical Instrumentation Engineers (SPIE) Conference Series, 0

Pepper, J., Pogge, R. W., DePoy, D. L., et al. 2007, PASP, 119, 923

Perryman, M. 2014, The Exoplanet Handbook

Perryman, M. A. C. 1989, Nature, 340, 111

Pollacco, D. L., Skillen, I., Collier Cameron, A., et al. 2006, PASP, 118, 1407

Pollack, J. B., Hubickyj, O., Bodenheimer, P., et al. 1996, Icarus, 124, 62

Poppenhaeger, K. & Wolk, S. J. 2014, A&A, 565, L1

Queloz, D., Mayor, M., Weber, L., et al. 2000, A&A, 354, 99

Quirrenbach, A., Amado, P. J., Caballero, J. A., et al. 2014, in Society of Photo-Optical Instrumentation Engineers (SPIE) Conference Series, Vol. 9147, Society of Photo-Optical Instrumentation Engineers (SPIE) Conference Series, 1

Racine, R., Walker, G. A. H., Nadeau, D., Doyon, R., & Marois, C. 1999, PASP, 111, 587

Reif, K., Bagschik, K., de Boer, K. S., et al. 1999, in Society of Photo-Optical Instrumentation Engineers (SPIE) Conference Series, Vol. 3649, Sensors, Cameras, and Systems for Scientific/Industrial Applications, ed. M. M. Blouke & G. M. Williams, 109–120

Ricker, G. R., Latham, D. W., Vanderspek, R. K., et al. 2009, in Bulletin of the American Astronomical Society, Vol. 41, American Astronomical Society Meeting Abstracts #213, #403.01

Robertson, P., Mahadevan, S., Endl, M., & Roy, A. 2014, Science, 345, 440

Rodler, F., Kürster, M., & Barnes, J. R. 2013, MNRAS, 432, 1980

Rogers, L. A. 2015, ApJ, 801, 41

Rossiter, R. A. 1924, ApJ, 60, 15

Sánchez, S. F. 2006, Astronomische Nachrichten, 327, 850

Sanchis-Ojeda, R., Rappaport, S., Pallé, E., et al. 2015, ArXiv e-prints

Sanchis-Ojeda, R. & Winn, J. N. 2011, ApJ, 743, 61

Schwartz, J. C. & Cowan, N. B. 2015, MNRAS, 449, 4192

Seager, S. & Mallén-Ornelas, G. 2003, ApJ, 585, 1038

Seager, S. & Sasselov, D. D. 1998, ApJL, 502, L157

Sing, D. K., Désert, J.-M., Fortney, J. J., et al. 2011, A&A, 527, A73

Snellen, I. A. G., de Kok, R. J., de Mooij, E. J. W., & Albrecht, S. 2010, Nature, 465, 1049

Southworth, J. 2006, PhD thesis

Southworth, J. 2008, MNRAS, 386, 1644

Southworth, J. 2011, MNRAS, 417, 2166

Southworth, J., Hinse, T. C., Jørgensen, U. G., et al. 2009, MNRAS, 396, 1023

Southworth, J., Wheatley, P. J., & Sams, G. 2007, MNRAS, 379, L11

Stahl, O., Kaufer, A., & Tubbesing, S. 1999, in Astronomical Society of the Pacific Conference Series, Vol. 188, Optical and Infrared Spectroscopy of Circumstellar Matter, ed. E. Guenther, B. Stecklum, & S. Klose, 331

Stebbins, J. 1920, ApJ, 51, 218

Stetson, P. B. 1987, PASP, 99, 191

Struve, O. 1952, The Observatory, 72, 199

Suzuki, R., Kudo, T., Hashimoto, J., et al. 2010, in Society of Photo-Optical Instrumentation Engineers (SPIE) Conference Series, Vol. 7735, Society of Photo-Optical Instrumentation Engineers (SPIE) Conference Series, 30

Tamuz, O., Ségransan, D., Udry, S., et al. 2008, A&A, 480, L33

Tingley, B. & Sackett, P. D. 2005, ApJ, 627, 1011

Toomre, A. 1964, ApJ, 139, 1217

Torres, G., Fressin, F., Batalha, N. M., et al. 2011, ApJ, 727, 24

Tregloan-Reed, J., Southworth, J., Burgdorf, M., et al. 2015, MNRAS, 450, 1760

Tregloan-Reed, J., Southworth, J., & Tappert, C. 2013, MNRAS, 428, 3671

Tusnski, L. R. M. & Valio, A. 2014, in IAU Symposium, Vol. 293, IAU Symposium, ed. N. Haghighipour, 168–170

Udalski, A., Szymanski, M., Kaluzny, J., Kubiak, M., & Mateo, M. 1992, Acta Astronomica, 42, 253

Villaver, E. 2011, in American Institute of Physics Conference Series, Vol. 1331, American Institute of Physics Conference Series, ed. S. Schuh, H. Drechsel, & U. Heber, 21–32

Wang, J., Fischer, D. A., Barclay, T., et al. 2013, ApJ, 776, 10

Wilken, T., Lovis, C., Manescau, A., et al. 2010, in Society of Photo-Optical Instrumentation Engineers (SPIE) Conference Series, Vol. 7735, Society of Photo-Optical Instrumentation Engineers (SPIE) Conference Series, 0

Winn, J. N. 2009, in IAU Symposium, Vol. 253, IAU Symposium, ed. F. Pont, D. Sasselov, & M. J. Holman, 99–109

Winn, J. N. 2010, ArXiv e-prints

Winn, J. N., Howard, A. W., Johnson, J. A., et al. 2011, AJ, 141, 63

Wolszczan, A. & Frail, D. A. 1992, Nature, 355, 145

Wright, G. S., Bortoletto, F., Bruce, Jr., C. F., et al. 2003, in Society of Photo-Optical Instrumentation Engineers (SPIE) Conference Series, Vol. 4850, IR Space Telescopes and Instruments, ed. J. C. Mather, 493–503

Wyttenbach, A., Ehrenreich, D., Lovis, C., Udry, S., & Pepe, F. 2015, A&A, 577, A62

Zhou, G., Bayliss, D., Kedziora-Chudczer, L., et al. 2015, ArXiv e-prints

Zhou, G., Bayliss, D., Penev, K., et al. 2014, ArXiv e-prints

Zhu, W., Udalski, A., Gould, A., et al. 2015, ApJ, 805, 8